UNIVERSITY OF SOUTHAMPTON

FACULTY OF PHYSICAL SCIENCES AND ENGINEERING

Electronics and Computer Science

Nano-Electronics & Nano-Technology Research Group

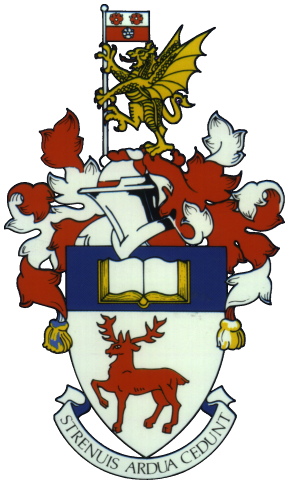

Band-gap Engineering of Germanium Monolithic Light Sources using Tensile Strain and n-type Doping

by

Abdelrahman Zaher Rateb Al-Attili

Thesis for the degree of Doctor of Philosophy

October 2016

UNIVERSITY OF SOUTHAMPTON

FACULTY OF PHYSICAL SCIENCES AND ENGINEERING

Electronics and Computer Science

Nano-Electronics & Nano-Technology Research Group

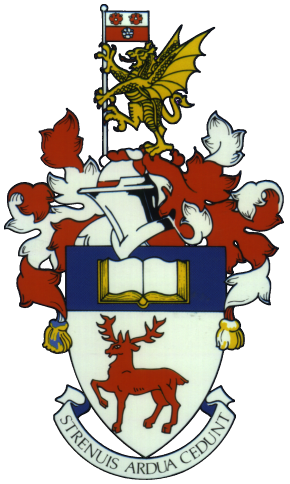

Band-gap Engineering of Germanium Monolithic Light Sources using Tensile Strain and n-type Doping

by

Abdelrahman Zaher Rateb Al-Attili

Jury	**Supervisors**
Dr. Aleksey Andreev	Prof. Shinichi Saito
Prof. James S. Wilkinson	Dr. Frederic Gardes
Dr. Xu Fang	

UNIVERSITY OF Southampton

Thesis for the degree of Doctor of Philosophy

October 2016

UNIVERSITY OF SOUTHAMPTON

ABSTRACT

FACULTY OF PHYSICAL SCIENCES AND ENGINEERING
Electronics and Computer Science

Doctor of Philosophy

BAND-GAP ENGINEERING OF GERMANIUM MONOLITHIC LIGHT SOURCES USING TENSILE STRAIN AND *N*-TYPE DOPING

by Abdelrahman Zaher Rateb Al-Attili

Band-gap engineering of bulk germanium (Ge) holds the potential for realizing a laser source, permitting full integration of monolithic circuitry on CMOS platforms. Techniques rely mainly on tensile strain and n-type doping. In this thesis, we focus on studying diffusion-based phosphorus (P) doping of Ge using spin-on dopants (SOD), and tensile strain engineering using freestanding micro-electro-mechanical systems (MEMS)-like structures. Process development of a reliable SOD recipe was conducted using furnace and rapid-thermal annealing, and successful doping up to $2.5 \times 10^{19}\text{cm}^{-3}$ was achieved, resulting in approximately $10\times$ enhancement in direct-gap emission. A transition in Ge direct-gap photoluminescence (PL) behavior is observed upon doping, from being quadratically dependent on excitation power to linear. We have also demonstrated that the limited doping concentration of P in Ge using SOD is not source limited, but more probably related to the diffusion mechanism. The other part of the project concentrated on Ge strain engineering. Previous works reported high tensile strain values based on freestanding MEMS-like structures made of Ge, yet without embedding an optical cavity (until recently). In this project, we realize this combination by fabricating Ge micro-disks as an optical cavity on top of freestanding SiO_2 structures, utilizing Ge-on-Insulator wafers (GOI). 3D computer simulations were used to understand and optimize the devices, in terms of strain and optical performance. Raman spectroscopy and PL measurements confirmed simulation results showing higher tensile strain for beams with shorter lengths, with a maximum uniaxial strain of 1.3%. Splitting of light and heavy-hole energy bands was observed by PL as the strain increases, agreeing with theoretical models. Direct-gap sharp-peak whispering-gallery modes (WGMs) were confined in 3 μm disks with a maximum quality-factor of ~ 200. Two loss mechanisms could be distinguished, red-shift of the absorption edge, and free-carrier absorption. In order to avoid these excitation-related losses, higher strain values combined with heavy n-type doping are required. A possible implementation using the same GOI platform is proposed for future work.

Contents

List of Figures

List of Tables

Declaration of Authorship

I, Abdelrahman Zaher Rateb Al-Attili , declare that the thesis entitled *Band-gap Engineering of Germanium Monolithic Light Sources using Tensile Strain and n-type Doping* and the work presented in the thesis are both my own, and have been generated by me as the result of my own original research. I confirm that:

- this work was done wholly or mainly while in candidature for a research degree at this University;
- where any part of this thesis has previously been submitted for a degree or any other qualification at this University or any other institution, this has been clearly stated;
- where I have consulted the published work of others, this is always clearly attributed;
- where I have quoted from the work of others, the source is always given. With the exception of such quotations, this thesis is entirely my own work;
- I have acknowledged all main sources of help;
- where the thesis is based on work done by myself jointly with others, I have made clear exactly what was done by others and what I have contributed myself;
- parts of this work have been published as: [1], [2], [3], [4], [5] and [6]

Signed:.....

Date:.....

Acknowledgements

I would like to express my gratitude to my beloved ones, my father and my mother, Zaher and Sahar, and my three dear sisters, Shatha, Layan, and Nour.

I would also like to sincerely thank my respectful supervisor Prof. Shinichi Saito, Saito-Sensei, whom I am honored to be his first PhD student, for his great support, advice and guidance, and for the amazing opportunities he has offered me throughout my MSc and PhD courses, and for being a big brother concerned with my benefits as well as my career.

I am also thankful for my second supervisor Dr. Frederic Gardes for keeping an eye on me, and for all his trust, kindness and support. As well as the respected Prof. James Wilkinson, for his guidance and vast knowledge which he gives generously, from whom I have learned a lot. I have been truly honored to be examined by him for my first year and MPhil vivas.

I am also appreciative for all the academic and staff members who have helped me through my PhD degree, especially in the University of Southampton and the University of Tokyo. I am pleased to mention by name, Dr. Satoshi Kako for his help in the photoluminescence measurements, data analysis, and the enriching conversations that we had. And, Mr. Naoki Higashitarumizu for his help in laser-interference microscopy imaging. As well as, the respected Prof. Yasuhiko Ishikawa, Ishikawa-Sensei, for his academic support and kind encouragement, especially at my first publication and my presentation in SSDM 2015 in Japan. I am also indebted for Dr. Katsuya Oda, Dr. Hideo Arimoto, Dr. Ali Khokhar, Dr. Ahmed Abuelgasim, and Mr. Francesco Martini. And last but not least, my lab. mates, Dr. Muhammad Husain, Dr. Kapil Debnath, Zuo Li, Daniel Burt, Moise Sotto, and Fayong Liu.

Abbreviations

2D, 3D	Two and three dimensional
a-	Amorphous
As	Arsenic
BGN	Band gap narrowing
BOX	Buried oxide
CB	Conduction band
CMOS	Complementary metal-oxide-semiconductor
CMP	Chemical-mechanical polishing
CVD	Chemical vapor deposition
CW	Continuous wave
DBR	Distributed Bragg reflector
DFB	Distributed feedback
EL	Electro-luminescence
erfc	Complementary error function
eV	Electron volt
FCA	Free carrier absorption
FDTD	Finite-difference time-domain
FOx	Flow-able oxide
FP	Fabry-Perot
FSR	Free spectral range
FTTH	Fiber to the home
FWHM	Full-width half-maximum
Ge	Germanium
GILD	Gas-immersion laser doping
GOI	Germanium on insulator
HCl	Hydrochloric (acid)
HF	Hydrofluoric (acid)
HH	Heavy hole
HSQ	Hydrogen silsesquioxane
HT	High temperature
I	Interstitial
i	Intrinsic

IoT	Internet of things
IPA	Isopropyl alcohol
(N)IR	(Near) Infra-red
ITRS	International technology roadmap for semiconductors
LAN	Local area network
LD	Laser diode
LEPECVD	Low-energy plasma-enhanced CVD
LH	Light hole
LIM	Laser interference microscopy
LPE	Liquid phase epitaxy
LT	Low temperature
LTP	Laser-thermal processing
MBE	Molecular beam epitaxy
MEMS	Micro-electro-mechanical systems
MOSFET	Metal-oxide-semiconductor field-effect transistor
NW	Nano-wires
OM	Optical microscopy
P	Phosphorus
Pa	Pascal (MPA, and GPA for Mega and Gigapascal)
PD	Photo-detector
PECVD	Plasma-enhanced CVD
PhC	Photonic crystal
PL	Photo-luminescence
QD	Quantum dots
Q-factor	Quality factor
(M)QW	(Multiple) Quantum wells
RIE	Reactive ion etching
RTA	Rapid thermal annealing
Sb	Antimony
SEM	Scanning electron microscopy
Si	Silicon
SIMS	Secondary-ion-mass spectroscopy
SOD	Spin-on doping
SOI	Silicon on insulator
SRH	Shockley-Read-Hall
TE	Transverse electric
TEC	Thermal expansion coefficient
TM	Transverse magnetic
TMAH	Tetra-methyl-ammonium hydroxide
UHVCVD	Ultra-high vacuum CVD
V^{-2}	Doubly negatively-charged vacancy

VB	Valence band
WG	Waveguide
WGM	Whispering-gallery mode

Nomenclature

A	Radiative recombinations rate
a	Lattice constant
α	Absorption coefficient
α_{FCA}	Free-carrier absorption losses
$\alpha_{c,\Gamma}$, $\alpha_{c,L}$	Deformation potential of Γ and L valleys
B	Non-radiative recombination rate
β	Extraction efficiency
C	Auger recombination rate
C	Concentration
C_s	Source concentration of impurity atoms
°C	Celsius degree
c_{ij}	Stiffness tensor element
c	speed of light
D	Diffusion coefficient (diffusivity)
$d_{material}$	Film thickness
E	Energy
E_a	Activation energy
$E^{\Gamma}_{c,0}$, $E^{L}_{c,0}$	Initial energy of Γ and L
ΔE^{Γ}_{c}, ΔE^{L}_{c}	Energy difference of Γ and L
ϵ_{ij}	Strain tensor element
$\epsilon_{\|\|}$	In-plane strain
$\vec{\mathcal{E}_z}$	Electric field along the z direction
f_c	Quasi-Fermi levels for electrons in CB
f_v	Quasi-Fermi levels for electrons in VB
ϕ	Radial angle
Γ	Direct valley
γ	Photon density
h, $\hbar$	Planck's constant
$\hbar\omega$	Photon energy
$\vec{\mathcal{H}_z}$	Magnetic field along the z direction
$H^{(2)}_m$	Hankel function of the second kind
J	Flux of particles

$J_m^{(1)}$	Bessel function of the first kind
K	Boltzmann constant
$^\circ K$	Kelvin degree
k	Wavenumber
L	Indirect valley
L	Beam length
l	Radial mode number
λ	Free space wavelength
m	Azimuthal mode number
n	Refractive index
$\mathrm{n_{eff}}$	Effective refractive index
n	Total electron density
$n_\circ$	Electron density due to doping
n_i	Intrinsic carrier density
P	Excitation Power
p	Total hole density
ψ	Electromagnetic field
Q	Quality factor
R	Radius
R_c	Radius of curvature
$\mathrm{R_{sh}}$	Sheet resistance
R_{sp}	Spontaneous emission rate
ρ	Radial dimension
S	Raman-strain proportionality constant
S_{dose}	Dose of impurity atoms
$S_{\circ\_max}$	Maximum solid solubility
σ_{ij}	Stress tensor element
T	Temperature
τ_{ex}	Excess-carrier lifetime
τ_r	Radiative lifetime
θ	Circular-sector angle
V	Volume
v	Poisson's ratio
W	Beam width
ω	Anglar frequency
$\Delta\omega$	Raman shift
x_d	Diffusion depth
Y	Young's modulus

Chapter 1

Introduction

"Today, optics is a niche technology. Tomorrow, it's the mainstream of every chip that we build "

Pat Gelsinger, Intel senior VP, 2006

This chapter clarifies the motivation behind realizing a Ge monolithic light source according to historical developments in CMOS industry. The reason behind considering Ge as one of the most promising materials for this purpose is justified in terms of available technologies and materials. Then the engineering approaches utilized for transforming Ge into an optical gain medium are summarized, concluding with the idea behind this project. At the end of this chapter, the organization of research outcomes within this thesis is listed.

The contribution of this project in the form of publications ([1, 2, 3, 4, 5, 6]) and conferences is provided in Appendices C & D.

1.1 Motivation

The prophecy of hand-held computers with face-recognition technology predicted by Feynman [7] in 1959, stimulated research activities towards integrating more and more transistors on integrated circuit (IC) chips [8]. This Complementary Metal-Oxide-Semiconductor (CMOS) technology-node downscaling revolution was enlightened by the famous Moore's law [9], predicting an exponential rise in transistor count by doubling each year and a half. Moore saw the benefits of this downscaling on the performance of integrated circuits, eventually realizing a prosperous market of "Handy home computers". Nowadays hand-held smart-phones have more computational power than the Apollo-11 space-craft [10], which took the first human to the moon in 1969! In fact, it can be stated that the technological boom in the last few decades is driven by CMOS technology, as many aspects of our modern life rely on computers.

This downscaling trend is still being witnessed, with recent realization of 14-nm half-pitch Metal-Oxide-Semiconductor Field-Effect-Transistors (MOSFETs) by Intel [11]. As the density of transistors per chip is approaching that of neurons in human brain [8], many practical challenges are being confronted. These obstacles occur at transistor and system levels; Fabrication limitations and running into new physical phenomena are incorporated with reducing the transistors half-pitch beyond 14-nm. On a system level, issues related to more-dense copper interconnects, such as excessive heating, electromigration, and signal delay due to the increase in parasitic capacitance, overshadow the enhancement in chip performance due to scaling [12, 13]. Heating of dense copper interconnects is an obvious issue that was expected by Moore, yet at integration levels up to 2^{16} devices per chip, it was not considered an issue due to the planar nature of CMOS platforms, providing enough surface area to dissipate heat [9]. However, at recent integration levels, splitting processors with large transistor densities into cores was necessary to dissipate heat efficiently. Moreover, due to the increase in parasitic capacitances of densely-packed metallic interconnects, recent transistors can operate at higher frequencies than permitted by the interconnects [12, 13]. In other words, copper interconnects are imposing a *Bottleneck* on chip performance, and chip-to-chip communications. The dilemma of chip-performance saturation while transistor-density is still increasing, is referred to as Moore's gap.

To get the most out of down-scaling, and cope with the growing demand on bandwidth [1, 5], novel ideas are required to reduce Moore's gap. Although engineering at transistor level may contribute to this, a solution targeting the issues arising from metallic interconnects is more demanding. 3D stacking of current copper and low-k technology, or employing new materials, are being investigated [13]. The ultimate solution, however, would be moving to optical interconnects. Exchanging data using photons is fundamentally better than the electrical representation of bits through metal wiring, utilizing charge carriers [14, 12]. Unlike electrons and holes, photons have neither mass nor charge, resulting in a significant reduction of signal loss, delay, and heating. The main source of power consumption within an optical link is in the light source, and modulation/demodulation stages [14, 12, 13]. Low-threshold high-frequency light-sources are then required to compete with electrical connections [5]. Low-threshold implies lower power consumption at the source, while high-frequency of operation eliminates the necessity of a separate modulation stage. Optical communication links can be installed between different cores on a single chip to enhance the bandwidth. However, chip-to-chip or board-to-board communications are more realistic applications [1, 5].

Literature is rich with mature CMOS-compatible optical components required for realizing full integration of monolithic data-circuitry on Si chips. Waveguides, modulators, photo-detectors [15, 16], and other passive components such as grating couplers are

well-established. In fact, an on-chip optical data link is missing one single component, a monolithic light source [17]. Within-reach integration of optical interconnects on Si chips is feasible using well-established compound-semiconductor lasers [18]. Although this can be realized by the hybrid integration of III-V materials on Si, modification of CMOS production-lines to introduce III-V materials impedes such a solution [18]. A near-term solution can be by using external (on-board) III-V laser diodes (LD), exploiting optical fibers and grating couplers [5]. On the other hand, the ideal manifestation of optical interconnects has to totally rely on mature CMOS infrastructure and exploit Si as an optical medium, or Si Photonics. The key to this new era of electronics and photonics convergence, is a group-IV laser diode. Particularly, Silicon (Si) and germanium (Ge) have captured researchers interest in the last few years for this purpose [1, 8, 5, 19], due to their engineer-able energy-bands structure, and their firm presence in the CMOS industry. Although both being poor light emitters, due to their inherent indirect-gap characteristics, several engineering approaches are proposed to enhance light emission from Si and Ge, and transform them into optical gain mediums [19, 5].

Si is a tempting material, as CMOS industry is Si-based, providing mature understanding of its characteristics and processing techniques. Engineering a Si laser source rely mainly on quantum confinement effects to exploit the carriers in the $\mathcal{X}$ valley for optical recombinations. The fact that Si has an indirect band-gap with a minimum occurring at the $\mathcal{X}$ point in the lower conduction band (CB), and suffers an absence of a local minimum at the direct Γ point [1]. Although this has been demonstrated in porous Si, and Si nano-crystals, there is a trade-off between quantum confinement effects and carrier injection [1]. Moreover, Raman Si lasers, and Er-doped Si lasers are proposed. Several practical issues divert attention away from Si, such as the efficiency and output power, blue-shift of emission wavelength (in quantum structures), leakage of optical modes into the Si wafer, and the necessity of other materials to be used for wave-guiding [1]. Ge is consequently gaining attention as a possible monolithic light source on a CMOS platform [20, 21, 22, 23, 1, 8, 19, 5]. The use of Ge in Si-based electronic devices is widely investigated, such as $Si_{1-x}Ge_x$ virtual substrates for global strain engineering (ITRS roadmap), and high-performance p-MOSFETs. In fact Intel has used Si_xGe_{1-x} alloys as the source and drain material in some transistors [24]. Besides electronics, Ge has been used to demonstrate high-performance photo-detectors (PD) [15, 16], modulators, waveguides, and other optical components. More recently, interest in Ge as a group-IV laser source has rapidly grown after the demonstration of optical gain [20], and lasing using optical [21] and electrical [22, 23] pumping. As a material, Ge has a more-suitable band structure for direct-gap inversion compared to Si, emitting around telecommunications wavelength (1.55 μm) in bulk state. Realizing a Ge laser diode (LD), holds the privilege of full monolithic integration using Ge LDs and PDs, while Si provides high-quality waveguides and modulators.

1.2 Strategies for Realizing Ge Lasers

Ge is an indirect band-gap material with an energy minimum at the L point in the lowest CB. Using the electrons in the L valley for light emission is possible in (111) Ge quantum wells by valley projection onto the Γ point, similar to X valley projection in Si [1]. Superior to Si, Ge has a local minimum at the direct Γ point in the lowest CB, providing a possibility for band-gap engineering in the bulk state [25]. Especially that a small energy difference of 0.136 eV separates L and Γ valleys, which can be reduced to enhance the probability of electrons injection into the Γ valley [25]. Manipulating Ge band-gap in the bulk state has been a more popular pathway.

The idea of Ge band-gap engineering relies on the association of conduction and valence band energies with the crystal lattice [26, 27, 25, 28]. This relation permits manipulating the energy bands by deforming the crystalline structure using tensile or compressive strain. The effect of tensile strain on bulk Ge has been widely studied as a possible approach to convert Ge into a direct-gap material, and recently several groups succeeded in showing this transformation using biaxial [29, 30] and uniaxial [31] strain. Imposing tensile strain deforms the band-gap of bulk Ge (fig. 1.1(a)) by reducing the energies of the Γ and L valleys with different rates [26]. Γ valley being faster than the L valley, reduces the initial energy difference $\Delta E^{\Gamma,L}$ of 0.136 eV until a transformation into a direct-gap material occurs $\Delta E^{\Gamma,L} \rightarrow 0$ at approximately $\sim 2\%$ [32, 25] (4.7% [33, 31]) biaxial (uniaxial) strain. Simultaneously, tensile strain splits the light and heavy-hole bands, shifting the light-hole band upwards and the heavy-hole downwards [25, 28]. n-type doping was proposed [32] to compensate for the remaining energy difference $\Delta E^{\Gamma,L}$, when utilizing modest strain values. As a result of strain and doping, the probability

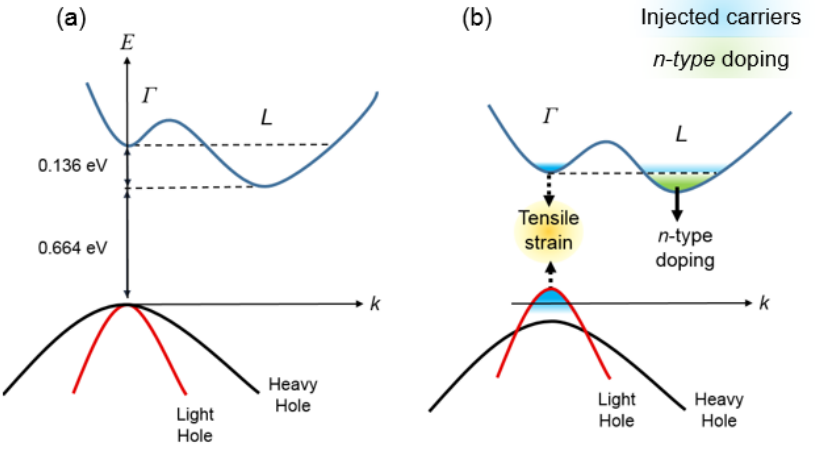

Figure 1.1: Ge band-gap sketch in the case of: (a) bulk Ge, and (b) band-engineered Ge using tensile strain and n-type doping. Tensile strain reduces the energy difference between Γ and L valleys, while n-type doping compensates for the remaining energy difference. Strain also induces splitting of light and heavy hole bands.

of electrons dwelling in the direct Γ valley is increased, consequently enhancing light-emitting recombinations. This band-gap engineering approach is demonstrated in fig. 1.1. Strain and doping target the material itself by manipulating energy-bands structure and carrier dynamics. Optical cavities must also be introduced to manipulate the electromagnetic field within the light emitting device, in order to enhance the light-matter interaction through high quality factors, and increase the total emission efficiency of the device [1, 5].

1.2.1 Aims of this Project

As stated earlier, optical gain [20], and lasing [21, 22, 23] of Ge direct-gap has been recently demonstrated. However, lasing threshold values were extremely high, and reproducing the results is still under investigation. While previous research has greatly contributed to our understanding of Ge direct-gap emission, many steps are to be taken towards a practical integration of a monolithic Ge-on-Si laser diode (LD). Future improvements on Ge light emitting structures will concentrate on reducing lasing threshold. This requires applying higher tensile strain values with optimum uniformity, enhancing n-type donors activation levels, and implementing high quality-factor cavities, with strain being the main factor in this engineering approach. For this purpose, micro-mechanical strain has been proposed as a suitable platform for high tensile strain values [34]. Since then, many groups have reported strain engineering of freestanding structures, similar to Micro-Electro-Mechanical Systems (MEMS) devices [35, 33, 31, 36]. Realization of direct-gap Ge due to uniaxial [31] (biaxial [36]) MEMS-like structures has recently been successful in 2014 (2015). However, such highly strained structures have not been incorporated with optical cavities (until recently [37, 38]). In this project we demonstrate a combination of a simple optical cavity, and a freestanding structure for strain application. This is done using Ge-on-Insulator wafers, providing a flexible platform in which the Ge layer is patterned as an active optical layer providing photons

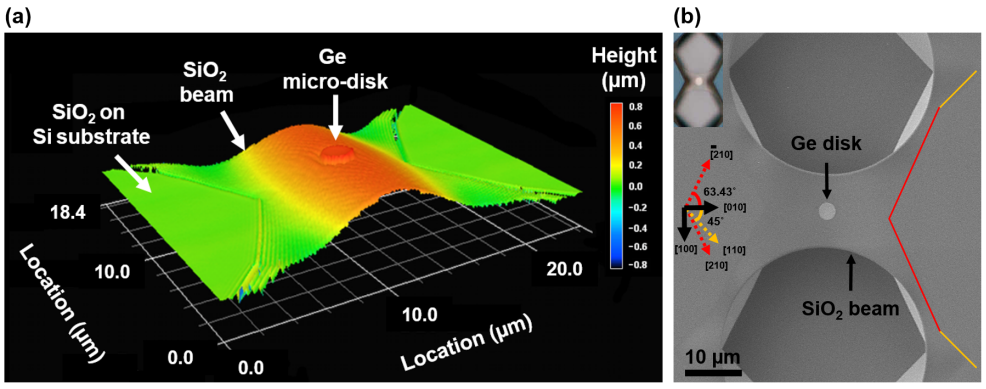

Figure 1.2: Device structure: (a) Laser-interference microscopy, and (b) scanning-electron microscopy images.

confinement, namely micro-disks, while the highly-stressed buried-oxide is released for strain application, in a MEMS-like structure.

1.3 Thesis Outline

This project focuses on tensile strain application on Ge micro-disks using freestanding SiO_2 beams. In addition to investigating diffusion-based n-type doping of Ge using spin-on dopants, and its effect on direct-gap emission. Throughout this thesis, strain and doping issues related to Ge direct-gap emission will be addressed in the following chapters as follows.

- **Chapter2** presents research milestones witnessed towards realizing a practical Ge laser, and accordingly marking the pathway undertaken in this project.
- **Chapter 3** conducts a systematic comparison between two commercially-available spin-on doping solutions for Ge doping. The effect of $\sim 1-2\times10^{19}$ cm^{-3} doping on Ge direct-gap emission was observed in a change in dependency on pumping power, from quadratic to linear, and explained according to holes rate equation.
- A reliable spin-on doping recipe (up to$\sim 2.5\times10^{19}$ cm^{-3}) with minimal surface damage is presented in **chapter 4**. Extremely-high source concentrations have been used, demonstrating that the highest achievable doping concentration is limited due to the diffusion mechanism of phosphorus in Ge, not source limited as previously thought.
- A detailed study of the nature of strain applied using freestanding SiO_2 beams is provided in **chapter 5**. Strain value, orientation, uniformity, and dependency on beam dimensions are examined using finite-element computer simulations, and validated using Raman spectroscopy and photoluminescence measurements. Enhanced energy splitting between light-hole and heavy-hole energy bands is observed by increasing strain in shorter beams, agreeing with theoretical models.
- **Chapter 6** contains the fabrication and characterization of the final device. Sharp whispering gallery modes with quality factors up to 200 were observed from 3-μm-diameter 100-nm-thick Ge disks on freestanding SiO_2 beams. Detailed analysis of the whispering-gallery modes and their behavior at high excitation levels is presented.
- Conclusions of research outcomes and recommendations for future work are given in **chapter 7**. A design is suggested for devices combining tensile strain imposed by the buried oxide, and n-type doping using SOD.

Chapter 2

Background and Literature

"If I have seen further, it is by standing on the shoulders of Giants"
Isaac Newton, a letter to Robert Hooke (1676)

2.1 Introduction

This chapter introduces the main research milestones concerning Ge direct-gap emission and band-gap engineering approaches towards a monolithic light source. Tensile strain, n-type doping, crystalline quality and wafer choices, in addition to optical cavities are discussed in terms of their theoretical role and their implementations in literature. The ideas put into focus in this project are justified accordingly. A summary of reported optical gain values and general aspects of achievable gain is also given in this chapter, providing a comparison between Ge and compound-semiconductor lasers based on the historical improvements in their performance. The last two sections conclude with a brief description of potential applications of Ge light sources, and a brief summary.

Parts of this chapter are published in topical review papers [1] and [5], in the form of figures and tables.

2.2 Ge as a CMOS-Compatible Light Source

An electrically-pumped monolithic light source that is compatible with CMOS technology is considered as the only-missing component to integrate a complete photonic circuitry on a CMOS-based platform [17, 8, 1, 5]. This restricts material choices to group-IV elements, among which Ge appears to be the most suitable; due to its pseudo-direct band-gap that has a flexible difference of 0.136 eV between direct (Γ) and indirect (L) conduction band valleys [25]. This energy barrier can be overcome to promote the probability of electrons injection into the direct Γ valley, consequently enhancing radiative recombinations. Various techniques are reported in literature to induce Ge Γ valleys filling, which can be summarized in applying tensile strain and n-type doping, alloying, utilizing hetero-structures, and quantum confinement effects. However, band-engineering bulk Ge with tensile strain and n-type doping has been the most popular route until now. In fact, optical gain [20], in addition to lasing under optical [21] and electrical [22, 23] pumping have been achieved using Ge. And more recently, low-temperature lasing of GeSn alloy using optical pumping was also reported in FP [39] and micro-disk [40] structures. A practically-implementable combination of a band-engineered Ge structure and an optical cavity has not been reported yet.

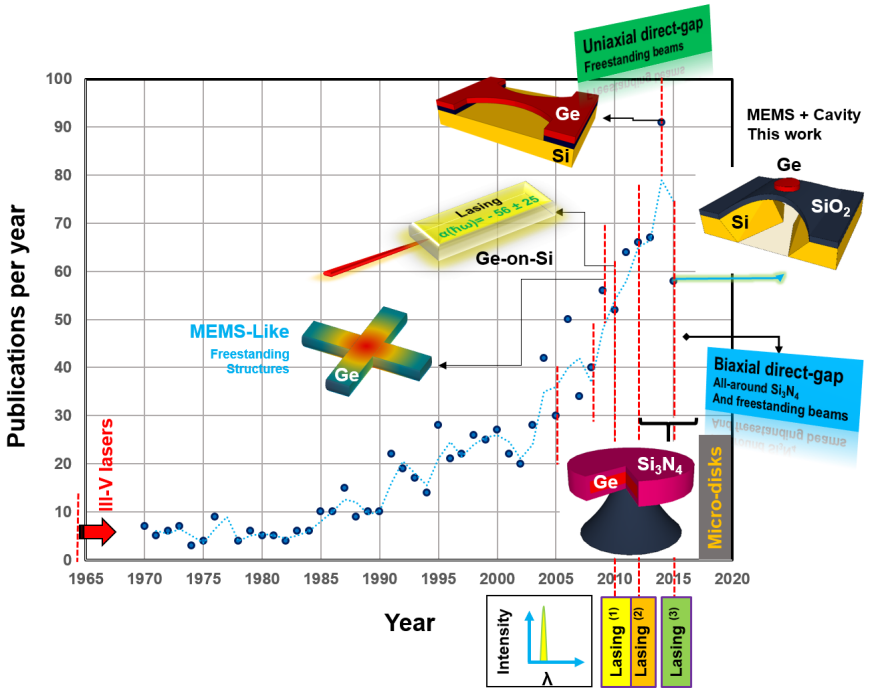

Figure 2.1: Number of publications on Ge direct-gap emission for the last 50 years highlighting recent research milestones. Micro-mechanical strain platforms have been popular since their proposal in 2009 [34]. First transition into a direct-gap material was reported using uniaxial Ge nano-beams in 2014. More recently, direct-gap biaxial Ge beams were demonstrated [36]. Data is extracted from web of science database.

In spite of the first successful optical gain and lasing demonstrations, which contributed generously to our understanding of Ge direct-gap emission, the threshold conditions were extremely high to be implemented in a practical application. First optical gain and lasing reports relied on slight strain values of $\sim 0.25\%$ and heavy n-doping in the range of 10^{19} cm^{-3}, resulting in approximately 56 cm^{-1} optical gain. Although many groups have failed reproducing these results using the same strain and doping levels [41], research efforts across the world are competing to reduce the lasing threshold and enhance the emission efficiency. Ideas are orientating towards an opposite approach of applying higher strain with lower doping levels. Strain reduces the requirements of carrier injection and doping to achieve population inversion, thus reducing the lasing threshold [25]. It is widely agreed upon theoretically that tensile strain has a more significant effect on increasing the optical gain, unlike doping effects which remain controversial. Not only because doping increases free-carriers absorption (FCA) losses, but also due to the limited doping levels of n-type impurities experimentally reported in Ge until now ($\sim 2 \times 10^{19}$ cm^{-3}).

Strain	**Doping**	**Active Structure**	**Crystalline Quality**	**Photonic Cavity**
Thermal	Implantation	Bulk [(b)]	Ge wafer	FP
Buffer layers	*in-situ*	QW	Ge-Si	DBR
Alloying	δ-doping [(a)]	Fins	Ge-GaAs	DFB
Stress liner	Gas-phase [(a)]	NW	GOI	Disks/Rings
MEMS	SOD [(a)]	QD	Ge-SOI	PhC
This work				
MEMS	SOD	Bulk	GOI	Micro-Disk

Table 2.1: Processing pathways to realize a Ge laser source
[(a)] Diffusion based techniques to maintain high crystalline quality.
[(b)] Most of research efforts are targeting bulk Ge by tensile strain and doping.

Approach-wise, two band-gap engineering techniques can be summarized: high strain with low doping, or modest strain with excessive doping. From processing point of view a wide range of challenges have to be overcome before achieving a reliable Ge laser diode. In addition to the practical obstacles of implementing strain and doping, puzzlement extends to include many other factors, such as: crystalline quality or the choice of the wafer, active structure (which has been mostly bulk Ge until now), and embedding a cavity within the device. CMOS standards imposes more restrictions, such as lateral carriers injection [42, 43, 44], being a planar technology. Table 2.1 lists the main factors to consider in designing a Ge laser, which will be discussed throughout this chapter.

2.3 Strain Application

Ge energy bands permit direct-gap emission, although it is an indirect-gap material, mainly due to the local energy minimum at the direct Γ point, and the small energy difference of 0.136 eV between the direct (Γ) and indirect (L) valleys. These properties inspired the growing research efforts for nearly a decade, aiming to transform bulk Ge into a direct-gap optical-gain medium. In this section, the theory behind Ge band-gap engineering using strain, and the utilized straining approaches in literature, are reviewed.

2.3.1 Band-Gap Deformation

Strain nature, being compressive or tensile, uniaxial or biaxial, in addition to its orientation along the crystalline lattice, determine the strain-induced behavior of Γ, L and $\mathcal{X}$ (or Δ) valleys of Ge [45]. This behavior is governed by the deformation potentials, and elastic stiffness coefficients, and can be described using theoretical models such as the deformation potential theory [46, 28, 47, 25]. The deformation potential theory, relates the energy bands minima in the conduction band to the total change in volume through the deformation potentials of the Γ and L valleys, as follows:

$$\Delta E_c^{\Gamma} = \alpha_{c,\Gamma}(\epsilon_{xx} + \epsilon_{yy} + \epsilon_{zz}) \tag{2.1}$$

$$\Delta E_c^{\mathrm{L}} = \alpha_{c,\mathrm{L}}(\epsilon_{xx} + \epsilon_{yy} + \epsilon_{zz}) \tag{2.2}$$

Where, ΔE_c^{Γ} and ΔE_c^{L} are the change in energy (eV) in CB valleys minima relative to the unstrained values $E_{c,0}^{\Gamma}$ and $E_{c,0}^{\mathrm{L}}$, respectively. $\alpha_{c,\Gamma}$ and $\alpha_{c,\mathrm{L}}$ are the hydrostatic deformation potentials for Γ and L valleys, respectively. A transition into a direct-gap material is possible given that $\alpha_{c,\Gamma}$ and $\alpha_{c,\mathrm{L}}$ are both negative, and $\left|\alpha_{c,\Gamma}\right| \gg \left|\alpha_{c,\mathrm{L}}\right|$. ϵ_{xx}, and ϵ_{yy} are the in-plane normal strain components, while ϵ_{zz} is the out-of-plane component. ϵ_{xx}, ϵ_{yy}, and ϵ_{zz} are related to the external stresses applied along the x, y, and z axes, σ_{xx}, σ_{yy}, and σ_{zz}, through the elastic stiffness coefficients. The summation of these normal strain components corresponds to the change of volume for small strain values (as shown in fig. 5.3). Accordingly, equations 2.1 and 2.2 do not consider off-diagonal elements (shear strains) of the strain tensor for simplicity. In the case of biaxial strain, which is the case for Ge grown on Si, the in-plane strain components ϵ_{xx} and ϵ_{yy} are equal. ϵ_{zz} can then be deduced from the generalized Hooke's law for a cubic semiconductor (Cauchy's stiffness tensor), given that the out-of-plant stress component σ_{zz} is zero. More on Hooke's law and deduction of strain components for uniaxial and biaxial strain, and band-gap deformation calculations is provided in Appendix B.

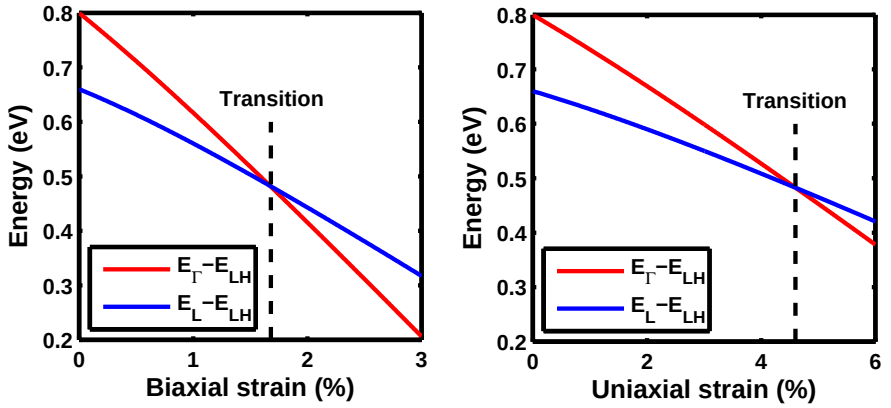

Figure 2.2: Strain-induced band-gap deformation of Ge due to biaxial and uniaxial strain. Transition into a direct-gap materials occurs at $\sim$ 1.7%(4.7%) biaxial (uniaxial) tensile strain along $\langle 100 \rangle$ direction. Deformation potentials in ref. [26] were used, more on calculations is found in Appendix B.

Ge strain-induced band-gap deformation under in-plane biaxial and $\langle 100 \rangle$ uniaxial tensile strain is shown in fig. 2.2. Table B.2 summarizes values of deformation potentials and parameters required for calculating energy-bands deformation of Ge. As can be seen from table B.2, the deformation potential of the Γ valley in the lowest CB is approximately 3 times larger than that of the L valley, making the Γ valley more sensitive to strain. In fact, Γ valley is found to shrink with a rate of -121 meV/$\epsilon_{||}$% compared to -44 meV/$\epsilon_{||}$% for L valley [25]. This interesting feature is the key to transforming Ge into a direct-gap material. Theoretically-predicted transition points differ depending on the parameters values (table B.2) used in calculations, but they are consistent in literature to be around 2% [48, 49, 45, 25, 50, 51] for in-plane biaxial tensile strain (1.7% [52, 45], 1.9% [25]). Such excessive strain values cause a huge red-shift in the emission wavelength away from 1550 nm, the desired wavelength for telecommunications in silica-based fibers. At the direct-gap transition due to biaxial strain, band-gap is equal to $\sim$ 0.47 eV [45] (0.53 eV [25]), corresponding to 2638.29 nm (2339.62 nm) free-space emission wavelength. However, using such high strain values may not be necessary, as modest tensile strain can potentially be used with n-type doping.

Tensile strain has two effects on valence band, a shifting effect due the hydrostatic component, and a splitting effect due to the uniaxial component that degrades the symmetry [25]. The effect of band-splitting appears clearly in the valence band [27, 25, 26, 28], represented in the separation of heavy-hole (HH) and light-hole (LH) bands; shifting the HH band to lower energies, while the LH band is shifted to higher energies reducing the total band-gap. In fact, at high strain values, Γ-LH recombinations dominate the emission spectrum, whereas Γ-HH recombinations have a higher contribution to the emission spectrum at low-strain values before any significant split occurs between LH

and HH bands [53]. Deformation potential theory also models the energy shifts of the HH and LH bands [46, 28, 47, 25], as shown in Appendix B.

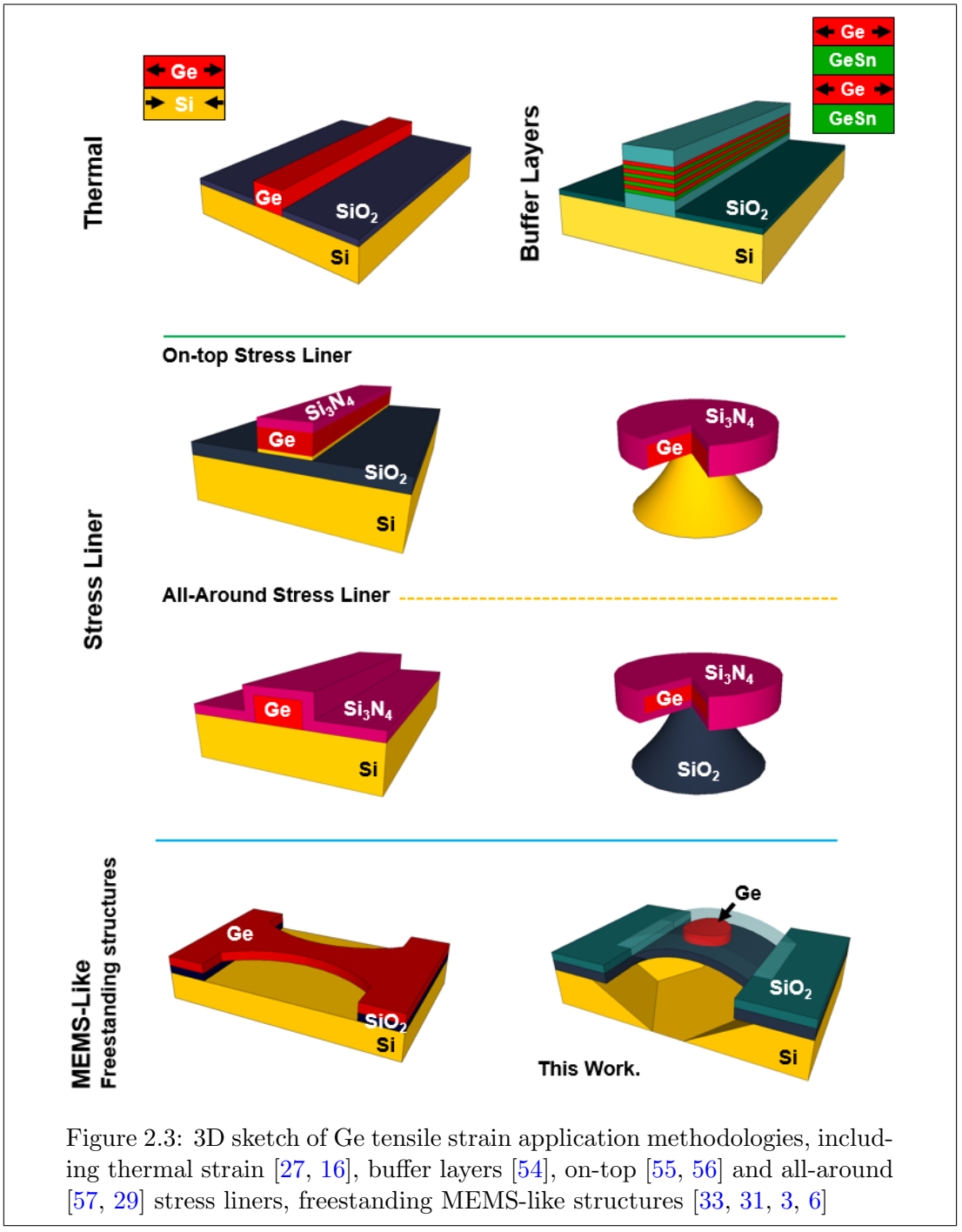

Figure 2.3: 3D sketch of Ge tensile strain application methodologies, including thermal strain [27, 16], buffer layers [54], on-top [55, 56] and all-around [57, 29] stress liners, freestanding MEMS-like structures [33, 31, 3, 6]

2.3.2 Application Methodologies

After introducing the effect of tensile strain on Ge, in this section, the micro-fabrication approaches used to impose tensile strain on Ge are discussed. Strain application methodologies can be summarized as follows: thermally-induced strain by epitaxial growth on Si, buffer layers or virtual substrate, alloying, local stress liners or external stressors, and MEMS-like or freestanding structures. A combination of these approaches can also be utilized to enhance applicable strain values, such as micro-machining and external nitride stress liners as reported in ref. [35]. Figure 2.3 shows three-dimensional sketches of tensile strain application methodologies.

2.3.2.1 Thermal Strain

Epitaxial growth of Ge on Si is expected to result in compressively stressed Ge layers, during the pseudomorphic growth regime for thicknesses below the critical thickness. This is attributed to the larger Ge lattice constant relative to Si [26], resulting in 4.2% lattice mismatch [58]. As Ge thickness exceeds the critical thickness, this stress is expected to relax as the growth is no longer lattice-matched. Relaxation of compressive stress is possible due to stacking faults, misfit and threading dislocations within the Ge lattice [8, 5]. However, it is consistently reported that an epitaxial Ge on Si layer is inherently tensile-strained, with a strain of $\sim 0.2\%$ [59, 16, 8].

This phenomenon was related to the difference in thermal expansion coefficient (TEC) between Ge and Si [27, 16]. It was found that the strain accumulated within the Ge layer depends on the growth and annealing temperatures, and the cool-down or room temperature [16]. As the temperature increases, Ge and Si both expand according to their TECs. Ge having a larger TEC, it goes from being compressively stressed to totally relaxed at a certain temperature. After annealing, when the stack is cooled down to room temperature, Si and Ge shrink again. Ge tends to shrink faster than Si, and, due to the much-thicker Si substrate, Ge shrinkage is prohibited, causing it to acquire tensile strain [27, 16, 8, 1, 5]. The final in-plane strain value depends on the final annealing temperature. For instance, a final annealing temperature of 800 °C results in 0.21% tensile strain [60]. Detailed analysis of the dependency on growth/annealing temperature [1] shows that 530 °C is the critical annealing temperature, below which Ge is compressively stressed as expected due to its larger lattice constant, and above which Ge acquires tensile strain due to its larger TEC.

In-plane thermally-induced strain of Ge-on-Si films is modelled in ref. [16] to be as follows:

$$\epsilon_{||}^{Ge} = \frac{1}{R_c} \frac{Y_{Ge} d_{Ge}^3 + Y_{Si} d_{Si}^3}{6 Y_{Ge} d_{Ge} (d_{Ge} + d_{Si})} \tag{2.3}$$

R_c is the radius of curvature of the wafer, Y_{Ge}, d_{Ge}, and Y_{Si}, d_{Si} are Young's modulus and thickness of Ge and Si, respectively. Theoretical modelling predicts a uniform distribution of strain across the Ge layer thickness, for thin Ge-on-Si layers. Which adds another advantage to this type of strain, in addition to being inherent in Ge grown on Si. This inherent strain is useful for photo-detection applications at telecommunication wavelengths used in silica-based fibers. Due to the shift in detection edge from 1.55 to slightly more than 1.6 μm, increasing the detection sensitivity at 1.55 μm [16].

Thermal strain has also been utilized for Ge optical gain and lasing realization. First experimentally measured optical gain [20] and lasing of Ge using optical [21] and electrical [22] pumping relied on thermally-induced strain with modest 0.2% value. Heavy n-type doping in the order of 1×10^{19} cm^{-3} was used to compensate for this low strain value. Nevertheless, high threshold conditions directed research towards increasing the strain values, to reduce the pumping requirements for transparency. And because of the limitation of thermally-induced strain to $\sim 0.2\%$ [27, 16, 59, 60, 58], due to Ge low melting-point that limits the highest applicable annealing temperature, another straining techniques are proposed in literature, as discussed below.

2.3.2.2 Buffer Layers or Virtual Substrates

Buffer layers with a certain lattice mismatch can be used to impose strain on epitaxially-grown layers on top. It is possible to maintain a single crystal by epitaxial growth for a limited grown-layer thickness, called the critical thickness [61]. Up to the critical thickness, the growth is called pseudomorphic, or lattice-matched [5]. This lattice matching between the grown layer and the substrate imposes a certain in-plane strain on the grown layer, determined by the lattice mismatch. Above the critical thickness, in-plane strain relaxes by forming threading, misfit dislocations and stacking faults [8, 5].

The idea of using Si_xGe_{1-x} buffer layers [62, 63, 61] as a source of stress has been investigated to enhance the performance of Si transistors. An idea referred to as *general strain technology*, which was proposed in ITRS roadmap (2000), and then got overshadowed rapidly by local stress liners [5, 64]. This is attributed to many practical difficulties, starting from the dilemma of growing a good-quality Si_xGe_{1-x} layers on Si with nano-meter uniformity and minimal interface defects, passing through the processing limitations imposed by the lower thermal budget of Si_xGe_{1-x}, higher diffusivity of dopants, and Si-Ge inter-diffusion, to operational issues due to mainly over-heating

because of the lower thermal conductivity of Si_xGe_{1-x} [65]. Although these reasons mitigated the introduction of the global strain technology in CMOS industries, yet in principle, it is useful in terms of enhancing device performance by applying strain. For instance, sub-100-nm MOSFETs with strained Si on $Si_{0.72}Ge_{0.28}$ buffers have shown to enhance the electron (hole) mobility by 110% (45%), due to 1.2% tensile strain [65].

For Ge light emission applications, buffers layers - being limited to the critical thickness - are suitable for multiple-quantum-wells (MQW) [62, 63], hetero-structures [66, 54] and quantum-dot-based (QD) [52] devices. Such lower-dimension structures are the obvious destination of research efforts if bulk Ge fails to satisfy low-threshold operation. It also provides the privilege of tune-ability of the strain by varying the contents of the buffer layer. For example, $In_{0.21}Ga_{0.79}As$ is used to apply up to 1.37% biaxial strain on Ge quantum dots [51]. The value of the strain can be tuned in principle through the indium content. Direct-gap Ge (2.33% biaxial strain) was demonstrated using $In_{0.4}Ga_{0.6}As$ buffer layers deposited using molecular beam epitaxy (MBE) [52]. A transit into a direct-gap was confirmed at 1.7% biaxial strain by low-temperature photoluminescence, and more than 100-times increase in PL intensity was observed from a direct-gap 2.33% strained Ge. Yet, a MQW structure with a thick stack is not preferable for CMOS integration, due to the multiple processing steps and vertical carrier injection [5]. Another issue is the compatibility of the buffers material with CMOS industry, especially that Si_xGe_{1-x} buffers result in compressively-strained Ge in-between them due its larger lattice constant, and provide a negligible difference in the conduction band energies, reducing the significance of Si_xGe_{1-x} hetero-structures for electrons confinement [61]. Another candidate for practical buffer layers are GeSn alloys [54], which are discussed in the next subsection.

2.3.2.3 Alloying

GeSn alloys are being studied for monolithic light emission purposes. The role of GeSn alloys can be either as an active medium [39, 40], or as buffer layers [54] for strain application. It is possible to modify GeSn into a gain medium, the fact that it becomes a direct-gap material with 17% Sn contents [67]. In fact, recent lasing of GeSn alloys fabricated in a Fabry-Perot [39] and micro-disk [40] structures was demonstrated at low temperatures. Other studies considered utilizing GeSn alloys as buffer layers to apply strain onto Ge films grown on top [54, 5]. In both scenarios, the use of GeSn alloys provides a tune-able strain through Sn content [54]. It also provides a suitable platform for carrier confinement structures such as hetero-junctions and MQWs, similar to commercially-available III-V lasers [5]. Obstacles facing alloying resemble in the huge lattice mismatch between Ge and Sn, low solubility of Sn in Ge, the segregation of Sn [67], in addition to the limit it imposes on the processing thermal budget [67, 5].

2.3.2.4 Local Stress Liner or External Stressors

Local stress liners, or external stressors, have succeeded the general strain technology approach which relies on buffer layers [64]. Nowadays stress liners are maturely used in CMOS industry. For instance, Si_3N_4 films are deposited on transistors as local stressors [68, 69], while other films like Si_xGe_{1-x} can be used as source and drain material, performing both strain and band-gap engineering to overcome short-channel effects [70, 24]. In fact, Intel has already invented MOSFETs with Si_xGe_{1-x} source and drain, such as strained Si 90-nm transistors in 2003, and 45-nm high-k metal-gate transistor in 2007 [24].

The idea behind stress liners is to deposit a layer with built-in stresses. Tuning the deposition process by, for example in PECVD Si_3N_4 layers, the radio-frequency to low-frequency power ratio, or H_2 and N_2 percentages in the gas mixture, can be used to tune the value of built-in stresses, in addition to its nature, tensile or compressive [71]. Experimental determination of thin-film in-plane stress is possible using wafer curvature method, according to the famous Stoney's formula (equation 6.1) [72].

Transferring the stress onto the target structure can be done in two ways:

- Local patterning of a pre-stressed layer causing it to expand/shrink depending on its initial condition, dragging along the layer underneath. If the layer is initially compressively stressed, it tends to expand upon patterning to neutralize the built-in stresses. This expansion drags the layers in-touch, causing them to expand as well, or become tensile-strained, and vice versa for initially tensile-stressed layers.
- Deposition of a continuous pre-stressed film without patterning on three-dimensional target structures. Due to the patterned surface of the wafer, and the coverage of the film *all-around* the structures, stresses within the deposited film are transferred onto the structures. In this approach, films with compressive built-in stresses transfer tensile strain onto the three-dimensional structures, due to their tendency to expand.

In both cases, the strain within the structures is generally opposite to the initial stress in the deposited film. Applying this technology to Ge for light emission purposes has been a hot topic for the last few years, mainly using Si_3N_4. Both approaches, patterning Si_3N_4 on the Ge structure [55], or patterning Ge then coating with Si_3N_4 film [71, 73], have been demonstrated. The most commonly used approach was to pattern an initially compressively-stressed Si_3N_4 layer, which tends to expand upon patterning, delivering tensile strain onto Ge [74, 55, 56, 57, 75, 76, 43, 44, 77, 29]. This has been applied to Ge waveguides [74, 75, 76, 43, 44, 1] and micro-cavities [55, 56, 57, 77, 29]. Initial reported tensile strain values were around 1% biaxial [55, 56, 77, 75, 76]. Yet, the main challenge

facing silicon nitride stressors was the uniformity of strain distribution. Strain delivered by a stress-liner is highly non-uniform, especially across Ge thickness [55, 56]. The distribution also depends on the geometry. This non-uniformity is translated into variations in the Ge band-gap, creating local inhomogeneities in optical gain values [55, 56, 57], the fact that charge carriers tend to dwell highly-strained regions due to their smaller band-gap [25]. Inhomogeneity of strain is a serious issue in micro-disks, because of the confinement of whispering gallery modes at the edges of the disks, where the tensile strain is relatively low. The fact that a local Si_3N_4 stress liner fabricated on-top of a micro-disk would result in a maximum tensile strain in the middle. Fabrication of Ge disks on pillars, rather than pedestals was proposed to enhance the uniformity, compromised by optical confinement and maximum strain value [56].

In the case of depositing a continuous film of Si_3N_4 on patterned Ge structures, the film must also have compressive built-in stresses to deliver tensile strain onto Ge [78, 71, 1, 73, 30, 57, 29]. Initial trials demonstrated coating the top and the sides of Ge structures [71, 73, 43, 44]. Both initially compressive [78, 71, 73, 30, 57, 29] and tensile-strained [43, 44] silicon nitride films were used. Tani *et al.* [43, 44] used 250-MPA tensile-strained Si_3N_4 on the top and the sides of a Ge waveguide. This resulted in tensile-strained regions with very low values at the sides of the waveguide, while the top region was compressed. Higher tensile strain values were obtained with initially compressively-stressed layers [78, 71, 73, 30, 57, 29]. Velha *et al.* [71] demonstrated tuneable stress in Ge nano-pillars with high aspect ratio, using initially compressed Si_3N_4 films coated after Ge patterning. The stress in Ge could be varied from 3 GPa compressive to 2GPa tensile and a maximum tensile strain of 2.5% was achieved, with a direct-gap PL peak around 2.2 μm. Such a strain value is expected to convert Ge into a direct-gap material, yet no lasing was observed as the Ge pillars were not in embedded in a cavity. Millar *et al.* reproduced similar results on Ge pillars with emission wavelength extended above 2.25 μm [73].

The up-to-date solution that have developed over the previous few years, was to coat Si_3N_4 all over the Ge structure including the bottom side [71, 43, 44, 57, 73, 30, 29]. The *all-around* deposition criteria has recently become a mark for extremely high tensile strain values with good uniformity [57, 29, 30]. Most recent publications have demonstrated very high tensile strain values on Ge micro-cavities, generally exceeding 2%, resulting in direct-gap Ge resonators [29, 30]. This was firstly done by Ghrib *et al.* [57], by under-etching Ge-on-SiN micro-disks utilizing the bottom silicon nitride as a stressor, then coating the whole structure with initially compressed Si_3N_4. Although this work did not report direct-gap Ge micro-disks, it has proven its ability to increase the strain (up to 1.45%) and its uniformity across the disk thickness and diameter. Recent publications from the same group [29] have demonstrated direct-gap Ge micro-disks.

Transition into a direct-gap material was observed at 1.67% biaxial tensile strain, and a maximum strain of 1.75% was applied. Yet, lasing was not achieved, in fact, quality factors of the resonant modes were not as high as reported by the same group using lower strain values [55, 56, 57]. Millar *et al.* [30] covered Ge micro rings from all sides using 2.45-GPa compressively-stressed Si_3N_4 resulting in more than 2% tensile-strained Ge micro-cavities. The fabrication process relied on making Ge micro-rings, under-etching them using TMAH, and then depositing the stress liner. Although Ge is expected to become a direct-gap material at such strain values, and whispering-gallery modes were clearly observed, lasing was not successful.

2.3.2.5 MEMS-Like Structures

Freestanding structures are widely used in micro-electro-mechanical systems or MEMS devices. MEMS-based pressure sensors, Gyroscopes, accelerometers, and many other examples are based on freestanding structures [79]. Such devices rely on the deformation of freestanding films for sensing or modulating data [79]. Therefore the study of the stress-strain relations in micro-structures has been developed significantly over the past years by the MEMS community [80, 81, 82, 83]. This knowledge can be exploited for Ge direct-gap light emission through strain engineering.

Since the proposal of using micro-mechanical strain by Lim *et al.* [34] in 2009 for Ge band-gap engineering, a growing number of publications from various groups in the world have reported novel ideas on highly-strained MEMS-like structures. Structures including membranes and through-silicon vias by back-etching of bulk Si [84, 85], in addition to other proof-of-concept studies were reported, such as manual application of mechanical strain by high-pressure gas on a Ge membrane [86]. However, the major part of related research have targeted micro-beams or bridges. This can be understood from strain engineering point of view - as discussed below-, resulting in an extremely high tensile strain with good homogeneity, providing carriers confinement in the active region through the strain gradient, and the ability of electrical pumping through the beam material itself.

As previously stated, the growth of a thin film on a substrate with different lattice constant, or different thermal expansion coefficient, builds up stresses within the thin film. Instead of using this property in an external stress liner, it is possible to exploit it in the Ge layer itself, by releasing the Ge layer in a MEMS-like structure. In fact, before this work, most - if not all - MEMS-like structures used Ge as the freestanding beam material. Local under-etching of Ge micro-beams, permits the built-in stresses in Ge to relax. As explained in section 2.3.2.1, Ge on Si films have built-in tensile stresses of

$\sim 0.2\%$. Consequently, Ge films tend to shrink upon suspension, however several adjustments can be done to the freestanding structures in order to impose tensile strain. An interesting design by Suess *et al.* [33] proposed fabricating Ge beams with larger pads. The idea behind this, is that the multiple-section freestanding Ge structure tends to shrink, yet the larger side-pads compared to the smaller middle active-region would exert a higher force as they shrink due to their larger section. This force pulls the smaller middle region, causing it to be tensile strained. Manipulating the beam dimensions, such as the ratio between the side pads and the middle region, can be used to control resulting strain [31]. As this pulling force is in the direction of the beam, the applied strain is uniaxial, which has a less effect on deforming the Ge band gap, due to the lower total change in volume [26]. A maximum uniaxial strain value of 3.1% was achieved by this design, while a transfer into a direct-gap material is predicted at 4.7% uniaxial tensile strain (compared to 2.0% biaxial). An improvement on such structures can be done by adding external silicon nitride stressors at the sides of the beam, to increase the total applied force [35]. This design evolved in later publications into smoothly graded beams with curved edges, resulting in a tight Ge section in the middle of the beam, and large pads on the sides. The gradual decrease of the section towards the middle of the beam, eliminated any pin-point accumulations of high strain, and guaranteed a smooth gradient of strain towards the middle. This improved the homogeneity of the strain in the middle active region of the Ge beam [33, 31, 38]. Moreover, this gradual tightening of the beam section results in a pseudo-heterostructure that confines carriers in the middle active region of the beam [87], due to the higher tensile strain relative to nearby regions [87, 31, 38]. The highest uniaxial strain of 5.7% was reported using 200-nm-wide Ge beams with slightly-curved edges and large side pads [31].

Biaxial strain can be applied by making cross-shaped beams. Such designs have been studied by several groups [35, 36, 88]. A maximum biaxial strain of 1.9% has been recently reported by Gassenq *et al.* [36]. Strain was enhanced by carefully designing the curvature of the beam to eliminate any pin-point high-strain accumulations. In addition to using high-crystalline-quality GOI wafers prepared by bonding, where an enhancement of strain over Ge-on-Si wafers is expected, due to the absence of Si-Ge interface defects [36]. The effect of the wafer on the achievable strain was also reported by other groups. For example, enhancement of strain was reported by fabricating Ge beams using SOI wafers [33], rather than Ge on Si. The reason behind this is not clarified yet, but usually attributed to the lower interface-defect density, in addition to the complex stress profile across the thickness of multiple-stack wafers [33, 36].

Although such strain values are tempting, yet all previous freestanding structures had one common issue, the lack of an optical cavity. Recently, embedding an optical cavity

within a MEMS-based structure was reported by this work (micro-disks), and more recently by Petykiewicz *et al.* [38] and Gassenq *et al.* [37] (DBRs). The fact that etching a light confining structure in a Ge beam, such as a DBR or a photonic crystal (PhC), reduces the achievable strain in the active middle region as the strain gradient along the beam is interrupted by the DBRs [38]. At the same time, high strain values are expected in the DBR or PhC region due to the thinner Ge sections. Petykiewicz *et al.* [38] demonstrated highly-strained (2.3%) uniaxial nano-beams surrounded by much-wider pads having few DBR periods etched in them. Very sharp resonances were observed with the PL emission shifted towards 2 μm. Surprisingly, the sharpest modes were observed from 1.95% strained nano-beams, while Q-factors degraded significantly for 2.3%. This indicates that there is a trade-off between excessive tensile strain and optical gain, although the reason is not obvious yet, it might originate from introducing defects at higher strain values.

Combining a MEMS-like structure and an efficient optical cavity is the idea behind our project. Almost all previously reported MEMS-like structures reported for developing a Ge laser source, have used Ge as the beam material. In this work, we propose using highly-stressed thermal SiO_2 to apply tensile strain on a Ge layer on-top, using GOI wafers. This configuration allows us to separate the optically-active Ge layer, and the stress application mechanism using the buried SiO_2 (BOX) layer. In addition to this flexibility in the cavity and beam designs, Ge with excellent crystalline quality can be studied. The fact that GOI wafers are prepared using a bonding technique, where the high-defect-density Ge-Si interface is removed after bonding. The fabrication and characterization of Ge micro-disk cavities on freestanding SiO_2 beams is presented in later chapters in this report (chapter 6). On the other hand, sensitivity to heating is one of the main disadvantages of this structure. Although freestanding structures are generally prone to heating effects [31, 85, 38], fabricating the Ge layer on top of SiO_2 makes the heat dissipation worse compared to Ge beams, in which the heat can be dissipated through the Ge film. Overcoming this issue in laser-based characterization methods is done by the extrapolation of data-points at several laser-excitation powers, to find the value at the limit of no excitation power (section 5.6). The use of pulsed lasers can be another solution [89]. The difficulty of electrical injection of carriers is another disadvantage, yet, it is not as significant because this study is a proof-of-concept and investigative study. Where optical pumping of the structures is enough in order to understand the behavior of tensile-strained Ge, factors limiting monolithic operation, and the additional required engineering conditions.

Table 2.2 summarizes the straining approaches and their corresponding pros and cons.

2.4 Heavy n-type Doping

Application of strain reduces the required carrier injection to reach transparency, and transform Ge into an optical gain medium [49, 25, 90, 91, 92]. The effect of tensile crystal deformation can be summarized in reducing the energy difference between direct (Γ) and indirect (L) conduction band minima [26, 48, 93], which enhances the probability of electrons' dwelling in the Γ valley [22, 33, 87]. Further enhancement of direct-gap recombinations can be done by n-type doping [27, 50, 49, 15, 58, 94, 52, 95, 87, 55, 43, 96].

Method	Principle	Pros	Cons	Value
Thermally induced	Difference in thermal expansion coefficient (Ge-on-Si)	• Inherent • Uniform	• Limited strain • Interface defects	Limited to ~0.2% on Si
Buffer layers	Difference in lattice constant	• Tuneable • Hetero-structures	• Limited to critical thickness of Ge • Interface defects • Bulky buffer layers and multiple deposition steps	2.33% using $In_{0.4}Ga_{0.6}As$ [52]
Alloying	GeSn alloys	• Tuneable • Hetero-structures	• 14.7% lattice mismatch between Ge and Sn • Low solid solubility of Sn in Ge • high surface segregation of Sn	Ge becomes direct-gap at lim 17% Sn content [67]
External stressor	Deposition of a pre-stressed layer	• Tuneable • Hard mask or contact	• Inhomogeneous • Geometry dependent	Up to 2% using silicon nitride [30]
MEMS	Freestanding structures	• High value • Pseudo hetero-structures • Tuneability	• Heating effects • Embedding a cavity • Large footprint	Up to 5.7% [31] uni-axial

Table 2.2: Strain methodologies

The effects of n-type doping on improving direct-gap emission efficiency and achieving a positive optical gain, can be summarized in two points:

- Filling L valleys with electrons; Heavy n-type doping is expected to fill the indirect valleys in the CB with electrons, as proposed by Liu *et al.* [49]. Consequently, injected electrons have a higher probability of settling in the direct Γ valley. The fact that, filling the L valley will compensate for the remaining energy difference between direct and indirect valleys $\Delta E^{\Gamma,L}$, as shown in fig. 1.1. It is also reported that direct Γ valley get depopulated 5-times faster than L valleys, due to 5 times larger recombination rate, this motivates inter-valley scattering injecting more electrons in Γ valley to maintain equilibrium in CB [53].
- Reducing total free-carrier absorption losses for a certain total carriers concentration, by mainly reducing free-hole absorption [49, 25]. Injected holes contribute to the major component of FCA losses, and by n-type doping population inversion is possible with less injected holes (and less injected electrons).

Although doping might contribute to previous improvements in Ge as a lasing medium, the actual impact of doping is still controversial [5, 41]. Not only because of the theoretically-predicted effects with counter implications on optical gain; such as reducing the excess-carrier lifetime [97, 1]. But also due to the limited doping levels of n-type impurities achieved in Ge. Until now, the exact effects of extremely high doping levels ($> 4 \times 10^{19}$ cm^{-3}) on Ge optical gain are not clarified.

2.4.1 Theoretical Effects of n-type Doping

The effect of doping in increasing the optical gain of Ge can be understood through its contribution in shifting the conduction-band quasi-Fermi level upwards. This favors population inversion with lower pumping levels as described by the Bernard-Duraffourg condition [41]. Theoretically, optical gain is obtained as soon as the conduction-band quasi Fermi level gets into the Γ valley, and the valence-band quasi Fermi level gets within the light-hole band [41]. Although the concentration of electrons injected into the Γ valley is expected to increase super-linearly with doping level, doping can not be increased arbitrarily, the fact that non-radiative processes would also increase and might even counter-balance the privilege of filling the L valleys [49]. These non-radiative processes are mainly dominated by Shockley-Read-Hall recombination as well as FCA [94]. Recently, optical gain measurements of n-doped Ge waveguides have confirmed an increase in the optical gain from to -2200 to -500 cm^{-1} using 2×10^{19} cm^{-3} doping concentration [98]. Even though initial losses due to FCA and band-gap narrowing were higher in the highly-doped waveguides. Initial losses of -2200 cm^{-1} were measured for

2×10^{19} cm^{-3} doped waveguides, compared to -800 cm^{-1} for 2×10^{18} cm^{-3} (at $\lambda = 1600$ nm) [98]. As this study was on doping effect without sufficient strain, no positive gain was observed.

Free-carrier absorption losses of Ge can be calculated as follows [49, 32, 25]:

$$\alpha_{FCA} = -3.4 \times 10^{-25} n\lambda^{2.25} - 3.2 \times 10^{-25} p\lambda^{2.43} \tag{2.4}$$

Where, α_{FCA} are the losses in cm^{-1} due to FCA at a free-space wavelength λ in nm. n and p are total electrons and holes densities. Equation 2.4 indicates that free-hole absorption contributes to the larger percentages of the total FCA [49, 32, 25]. FCA losses increase with carrier injection level (electrons and holes), in fact, FCA losses become dominant at high injection levels so that no net gain is possible [94]. So by reducing the injected density of holes, the total FCA losses can be significantly reduced. And, this is the idea behind using n-type doping, which reduces the required pumping levels to reach population inversion (fig. 2.4).

At the same time doping increases the spontaneous emission rate (R_{sp}) [49, 99] by increasing the electron density, according to the following relation:

$$R_{sp} \propto \alpha(\hbar\omega) \times \frac{1}{\tau_r} \times f_c(\hbar\omega)[1 - f_v(\hbar\omega)] \tag{2.5}$$

Where, $\alpha(\hbar\omega)$ is the absorption spectrum as a function of photon energy ($\hbar\omega$), τ_r is the radiative lifetime, f_c and f_v are the quasi-fermi distributions for CB and VB, respectively. R_{sp} is expected to increase up to 10 times for 2.6×10^{19} cm^{-3} [99]. On the other hand, doping is found to have a significant effect in degrading the excess-carrier lifetime (τ_{ex}) [97, 100, 1]. Not only due to non-activated dopant atoms [101, 102], but also defects generated during the doping process [1, 97, 100], forming non-radiative recombination centers [5, 1, 17]. Excess-carrier lifetime in undoped Ge depends on the layer thickness, where the carrier dynamics are determined by Shockley-Read Hall and surface recombinations processes [97, 100, 1]. While in n-doped Ge, excess carrier lifetime is found to depend on excitation power (unlike undoped Ge) based on SRH non-radiative recombination model [103, 1]. For low excitation conditions, lifetime is mainly limited by holes lifetime, while for high excitation levels, lifetimes is a contribution of electron and hole lifetimes [1]. For example, a study presented in ref. [1] shows that τ_{ex} is reduced from 1ns for undoped Ge, to 0.4(0.14) ns for n-doped Ge under high (low) excitation powers.

Doping has a negligible effect on strain, yet, introducing phosphorus atoms into the Ge lattice is expected to impose slight compressive stress [104] (blue-shift of PL peak).

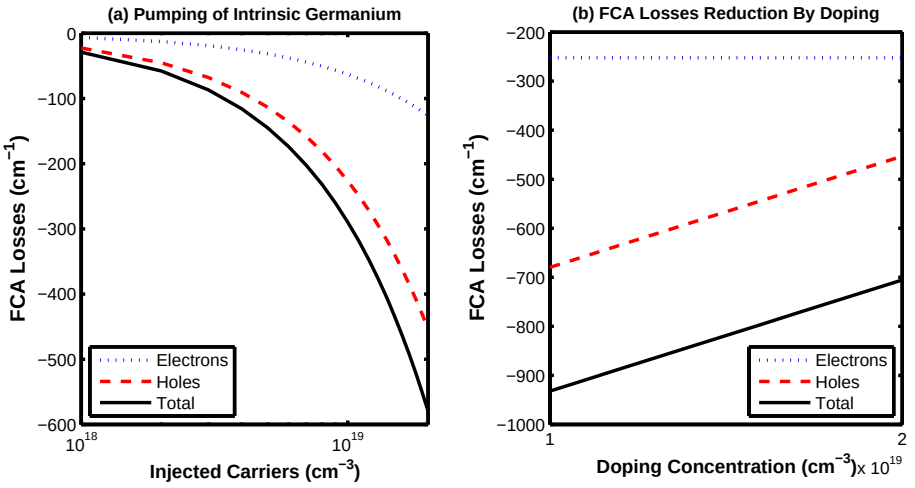

Figure 2.4: Effect of n-type doping of Ge on free-carrier absorption losses: (a) pumping of intrinsic Ge, in which losses by free-holes absorption is dominant. (b) Doping effect on minimizing FCA losses by reducing the contribution of holes. In (b) a fixed total electron density of 4×10^{19} cm^{-3} is assumed, impurity carriers concentration was increased from 1 to 2×10^{19} cm^{-3}, consequently reducing the concentration of injected holes (= injected electrons). The calculations were done at a wavelength of 1700 nm.

However, a slight red-shift in the direct-gap PL peak is expected due to BGN at the same time. This effect is significant for doping concentrations above 2×10^{19} cm^{-3} [105, 106, 107, 32]. For example a doping concentration of approximately 2.5×10^{19} cm^3 results in a direct-gap reduction ΔE^{Γ} of $\sim$ 32 meV, corresponding to a red-shift of 64 nm [73]. While at lower doping concentrations BGN-induced shift in the PL peak is negligible, mainly because the peak corresponding to L valley is affected at such lower doping levels. BGN has a significant effect in increasing losses due to the red-shift in the direct-gap absorption edge [107], as will be shown in chapter 6. Expression of BGN in heavily-doped Ge can be found in refs. [105] and [106]. Jain *et al.* [105] provided a simple expression for BGN of the L-valley at low temperatures. While Camacho-Aguilera *et al.* [106] conducted a room-temperature study of the direct-gap BGN using PL measurements, on Ge doped up to 4.5×10^{19} cm^{-3}. Accordingly, the minimum direct-gap BGN at room temperature can be expressed as follows [106]:

$$\Delta E^{\Gamma} = 8.15\left(\frac{n}{10^{18}}\right)^{0.25} + 2.03\left(\frac{n}{10^{18}}\right)^{0.5} \tag{2.6}$$

2.4.2 Overview of Ge Doping Techniques

Heavy n-type doping of Ge for monolithic light emission purposes has to satisfy two main conditions: achieving high activation levels to contribute to population inversion by filling the L valleys, and maintain crystalline quality. The exact required doping

level is not clearly determined yet [8], especially that it is also dependent on the applied strain. This ambiguity is mainly due to the limited activation levels reported in literature ($\sim 2 \times 10^{19}$ cm^{-3}), making the compromise between heavy doping from one side, and its effects on FCA, lifetime, BGN, and optical gain from another side, vague. The second restriction on the successful doping recipe is that it has to maintain the crystalline quality of Ge. As the crystalline quality is critical to produce efficient radiative recombinations [17].

The maximum achievable active doping concentration depends on the maximum solid-state solubility ($S_{\circ\_max}$) and the diffusion mechanism (depends on the impurity atom), from the materials side [104]. Table 2.3 below shows the maximum solid-solubility ($S_{\circ\_max}$) of different impurity atoms in Ge according to literature [104, 32], which is also temperature dependent. In addition to the method of introducing impurity atoms into the lattice, and activation-temperature profile from the processing side [108]. The mainstream of this research topic concentrated on phosphorus (P) as an impurity. This is attributed to its highest solubility amongst other dopants for widest temperature range, estimated to be 2×10^{20} cm^{-3} at 580 °C and generally above 1×10^{20} cm^{-3} from 500-800 °C [58]. P atoms can be introduced in a solid (P_2O_5), liquid ($POCl_3$), or gaseous (PH_3) sources depending on the doping process. It is estimated that active donors concentration above $5{\times}10^{19}$ cm^{-3} [109, 8] is required to convert slightly-strained Ge into an optical gain material. As the solid solubility of P is much higher, in principle, it is possible use P-doped n^+ Ge as an active layer for a LD. However, P diffusion in Ge suffers from many problems, such as high diffusivity which increases even more with defects density and source concentration. This is attributed to its diffusion mechanism which limits the activation level, and results in a box-like diffusion profile rather than a standard *erfc* or Gaussian profiles [104, 110, 102].

Type	**Impurity**	**S$_{\circ_max}$ (cm^{-3})**	**Temperature** °C
n-type	P	2.0×10^{20}	580 °C
	As	8.7×10^{19}	800 °C
	Sb	1.1×10^{19}	800 °C
p-type	B	5.5×10^{18}	850 °C
	Al	4.3×10^{20}	700 °C
	Ga	5.0×10^{20}	700 °C
	In	4.0×10^{18}	-

Table 2.3: Maximum solid solubility of common dopants in Ge [104]

In this part of the chapter, an overview of research progress towards providing a reliable doping process for a Ge laser is presented.

2.4.2.1 Ion Implantation

Ion implantation is a highly-standard process in CMOS industry, so, having a reliable implantation-based doping recipe for Ge lasing purposes is very tempting. Historical works [111] on P ions implantation in Ge have revealed a lot of issues, such as broadening of the diffusion profile after annealing at temperatures higher than 550°C [111, 104], which is a problem for MOSFETs fabrication requiring shallow junctions, but less important in applications for light emission, requiring a uniform high-activation level across the whole Ge thickness [5]. More importantly, it was found that a large fraction of P out-diffuses from Ge upon annealing [111], putting a limit on the doping concentrations [104]. This out-diffusion is more significant at higher temperatures [111], reaching up to 80%, and can be slightly impeded by using a cap-layer. At the same time, high-temperature annealing is important for the electrical activation of the dopants. 100% activation of dopants is expected at 650 °C, compared to 20% at 400 °C [111]. These two main problems are related to the fast diffusivity of P in Ge, which is governed by its diffusion mechanism. Co-implantation of Sb and P [112] can be used to increase the doping levels up to $\sim 10^{20}$ cm^{-3}, as predicted by theoretical works [102].

Moreover, crystalline quality is the major concern that directed research towards other techniques. Ion-implantation of Ge for laser applications requires a higher dose and power (high activation required across the whole thickness) compared to MOSFET applications (shallow junctions) [5]. At high implantation doses, Ge can easily become amorphous. These crystalline defects will work as non-radiative recombination centers and significantly degrade light-emission efficiency [17]. Multiple-cycle annealing is shown to reduce defects density [113, 27]. Although annealing can be used to retain the crystalline structure, it is not possible for Ge grown on Si. Because while the top Ge surface becomes amorphous due to ion bombardment, the bottom low-temperature-grown Ge layer has a high defect density, which is not suitable as a seed for re-crystallization [5, 100, 16]. This also holds for other wafers with no seed layer, such as GOI. Moreover, annealing for re-crystallization will cause the dopants to out-diffuse. Consequently, investigating the capabilities of *in-situ* and diffusion-based processes gained a lot of interest during the last decade.

2.4.2.2 *in-situ* Doping

in-situ doping relies on introducing electron-donor atoms, usually P, in a gas source (Phosphine PH_3) during Ge growth process [114, 115]. This is advantageous in terms of not requiring any separate doping steps, and can be applied using various growth techniques such as UHVCVD [27, 21], LEPECVD [63], and MBE (Sb doping) [116].

In fact, the first report of Ge lasing [20, 21] have utilized *in-situ* doping of 1×10^{19} cm^{-3}. Two drawbacks can be highlighted in this approach: non-selectivity, or in other words, the whole Ge layer will be doped which is not suitable for integrating another optical components that require less-doping or even intrinsic structures. And the trade-off between crystalline quality and doping concentration. The trade-off exists due to the high diffusivity of *n*-type atoms in Ge, such as P and arsenic (As). This limits the activation levels obtained at high growth temperatures, which are essential to grow high-crystalline-quality Ge [117]. Reducing the temperatures might increase the doping concentration by limiting the diffusion, at the expense of crystalline quality. As a result, it is difficult to introduce more than $2{\times}10^{19}$ cm^{-3} without the degradation of the Ge crystal [114, 115]. The later reason is more serious in limiting the use of *in-situ* doping for a Ge-based monolithic light source.

Delta (δ)-layer doping and Gas-Immersion Laser doping (GILD) are modification proposed on *in-situ* processes to increase the doping levels, they are discussed in details below. Based on the current available technology, ion-implantation and *in-situ* doping are not suitable for a Ge laser and other alternatives have to be explored.

2.4.2.3 Diffusion Based Techniques

The compromise between previous doping techniques and crystalline quality has been the motivation towards diffusion-based processes. δ doping, gas-phase doping, and spin-on doping (SOD) have been proposed in literature as possible approaches towards realizing a heavily doped Ge gain medium. The fact that the source concentration of P atoms can exceed the maximum solid solubility in Ge, so in theory, it is possible to achieve extremely-high doping levels, with minimal effect on crystalline quality by diffusion.

δ-doping

Delta (δ) doping was proposed as a solution to overcome the compromise between doping concentration and crystalline quality of *in-situ* processes. Two different approaches of δ-doping can be spotted in literature, the first one incorporates thin layers of P within the Ge crystal during lattice growth, and this is done using MBE [118], an approach suitable for proof-of-concept studies, and does not rely on diffusion. We will concentrate on the second approach, which is a diffusion-based CMOS-compatible process, and was used in demonstrating the first electrically-pumped Ge laser [22, 119]. The idea is to grow an active intrinsic (or doped up to 1.2×10^{19} cm^{-3} [119]) Ge layer with good crystalline quality, then intentionally deposit multiple mono-layers of P content, separated by thin intrinsic Ge layers, at low temperatures. Low temperature deposition $400 - 450$ °C causes a single layer of P to stick to the Ge surface with no epitaxial growth. *i*-Ge

is chosen rather than doped, due to its higher deposition rate and lower P diffusivity. The stack of alternating P-rich and *i*-Ge layers act as a high-concentration source of P atoms ($\sim 10^{20}$ cm^{-3} [119]), on top of the target high-crystalline-quality Ge layer. The source concentration depends on the number of δ layers used. Active concentration of 4×10^{19} cm^{-3} was demonstrated in ref. [119], using four P-Ge stacks, and annealed afterwards using RTA at 700 °C for 30 seconds. Although the process seems to be based on *in-situ* process, the actual doping of the target layer is done during the consequent annealing step, in which P atoms diffuse from the δ-layers into the target Ge layer. This doping process offers the privilege of compatibility with various growth techniques, being based on *in-situ*, however it requires multiple processing steps. A polishing process, using Chemical-Mechanical Polishing (CMP), is required to remove the depleted stack of δ-layers.

Gas-phase doping

Gas-phase doping is the historical approach of semiconductors doping that utilizes impurity atoms in vapor phase. Although old studies relied on gas-phase doping and demonstrated high doping levels [110], they are not widely investigated nowadays for Ge lasing. Diffusion annealing is done in a furnace with the impurity source being heated separately away from the wafers, resulting in a vapor-phase source of impurity atoms. For P doping, initial studies of P behavior in bulk Ge wafers by Matsumoto *et al.* [110], used red P powder as a solid source which was heated at different temperatures up to 430 °C, to control the vapor-phase source concentration. Doping levels up to 8×10^{19} cm^{-3} were achieved, depending on the source concentration (temperature of the red phosphorus powder). Another possible way is to use $POCl_3$ as a liquid source, which is also heated separately to introduce a vapor-phase P source. Gas-phase doping of Ge using arsenic (As) has been recently demonstrated [117], resulting in a surface concentration of 4×10^{19} cm^{-3}.

Another promising gas-phase doping technique is Gas-Immersion Laser Doping (GILD) [120, 99]. GILD is an *in-situ* doping process during which a precursor gas is introduced to the target wafer (PCl_3 for n-type, BCl_3 for p-type [120]), followed by a laser-thermal processing (LTP) step for dopant activation. LTP provides high ramp rates (10^{10} °K/s), high temperatures, and short annealing durations (10 - 100 ns) [120]. During each few-nano-second LTP step, the top surface of the wafer goes through a melting-crystallization cycle. A certain thickness determined by the laser energy density gets melted upon LTP, causing the dopants diffusivity to become much larger relative to the solid layers underneath. This determines the thickness of the doped layer, as dopant atoms are prevented from diffusing into the solid parts, resulting in a box-shaped doping profile. Then recrystallization occurs in a liquid-phase epitaxy (LPE) process, due to the solid seed layer underneath the melt top surface. Subsequent cycles of gas immersion and LTP are

repeated for several times (up to 400 [120]) in order to increase the doping level. Each full cycle of gas immersion and LTP takes from 0.1 to 1 second [120]. GILD is capable of achieving high-crystalline-quality Ge layers with P concentration up to 5.6×10^{19} cm^{-3} [120, 99]. Although current studies used lasers that can expose few mm^2 areas at a time, this process can potentially be applied in industry with good throughput due to the availability of high-power lasers. Selectivity might be an issue as large areas are exposed at once, the use of reflective hard masks exposing only the target devices is proposed as a possible solution [120].

Spin-on doping

Another simple, yet promising method is spin-on doping (SOD) [58, 2]. SOD is a simple process in which a dopant-rich solution is spin-coated (like a photo-resist) on the wafer and baked to form a silica-based layer with high source concentration. Most of commercially-available spin-on dopants use P_2O_5 nano-powders as a source of P atoms. Source concentrations can be as high as 20×10^{20} cm^{-3} [108], an order of magnitude larger than the maximum solid solubility in Ge [32, 104]. Diffusion step is required afterwards to drive-in and activate dopants, which can be done using furnace or RTA. Being a diffusion-based process, it is possible in theory to achieve very high activation levels, with minimal damage on crystalline quality.

SOD is a relatively cheap doping technique, simple to use, and superior in terms of flexibility; For instance it is possible to pattern the spin-coated layer so as to selectively dope some devices (Ge light emitting diodes) and leave other devices un-doped (Ge modulators and photo-detectors, for example) [58, 32]. SOD has been used in near-infrared (NIR) photo-detectors [121], solar cells [108], and MOSFETs [122]. A detailed study of SOD diffusion profiles in bulk Ge, using secondary-ion-mass spectroscopy (SIMS), is provided in ref. [108]. Ge-on-Si [99], or Ge-on-Insulator (GOI) [99, 123] wafers can be used to impede impurities diffusion out of Ge, since the diffusion of n-type dopants is much faster in Ge, than in Si or the oxide. Recently, extremely high P doping concentration of 10^{20} cm^{-3} was reported by Xu *et al* [123] using GOI wafers, and low-quality-factor resonant whispering-gallery modes were observed in Ge micro-disks at cryogenic temperatures [123]. Although this is a promising achievement, the details of the process are not revealed yet, and the reproduction of such activation levels using SOD is still ongoing.

Regardless of the apparent simplicity of the SOD process, there are many practical issues that complicate its application to Ge, since the existing SOD products are optimized for Si processing [121]. This can be seen in the high temperatures required to extract P atoms out of the SOD film ($\sim$ 1000 °C), which are not suitable for Ge. Two main challenges can be summarized: the formation of non-stable GeO oxide during annealing, the fact that SOD is oxygen-rich especially after the depletion of P atoms. In addition

to stresses imposed by the SOD layer, due to the change of its contents after annealing and the difference in thermal expansion coefficient compared to Ge. These issues are translated into surface damage, and even cracking of Ge layers after SOD [2].

Table 2.4 summarizes common doping processes used for Ge light emission purposes.

Method	Principle	Pros [a]	Cons	Value
in-situ	Introduce a gas precursor (PH_3) during growth process	• Easily implemented • Uniform	• Non-selective • Doping level and Crystal quality trade-off	2×10^{19} cm^{-3} (CVD) 1×10^{20} cm^{-3} (MBE)
Gas phase	Gas Immersion Laser Doping (GILD) using PCl_3 precursor	• Precisely-controlled box-like profile (uniform) • High activation	• Selectivity • Depth and throughput [b] • Multiple LTP cycles	5.6×10^{19} cm^{-3}
Delta layers	Alternating P-rich and intrinsic Ge mono-layers on top of the target Ge layer	• high source concentration • Doping of thick layers (0.6-0.8 µm)	• Multiple processing steps • Non-selective • requires CMP	4×10^{19} cm^{-3}
Spin-on doping (SOD)	Spin coating of dopant-rich silica-based solution	• Simple processing • Selective doping • Cheap	• Non-uniform • Surface damage • Limited dose	4×10^{19} cm^{-3}

Table 2.4: Ge n-type doping techniques for light emission purposes
[a] All processes mentioned in this table maintain crystalline quality, except for *in-situ* doping at activation levels above 2×10^{19} cm^{-3}.
[b] Usually used for shallow junctions (up to $\sim$ 300 nm [120]), and expose few mm^2 areas at a time. Higher throughput by wafer-scale exposure, and doping of thicker layers require lasers with very high energy density.

2.5 Crystalline Quality: Wafer Options

Direct-gap luminescence is significantly affected by crystalline quality [100, 124, 17, 1]. Defects in lattice structure form non-radiative recombination centers [17] which decrease the excess-carrier lifetime. In fact, carrier lifetime is found to be limited by non-radiative recombinations lifetime [1, 5, 100], forcing a limit on the internal quantum efficiency of Ge as an optical material. Reducing defect density by high-temperature or cyclic annealing [1, 113] enhances direct-gap PL intensity, with higher PL intensity obtained for higher annealing temperatures [1].

Ge wafers provide the ideal crystalline structure, yet are not interesting for a practical Ge light emitting device, due to the difficulty of confining an optical mode, and more importantly, the industrial reliance on Si wafers. Ge lasers fabricated from epitaxial Ge-on-Si films are ideal for practical implementation on bulk Si wafers used in CMOS industry. Yet, a fundamental issue arising from the 4.2% lattice mismatch between Si and Ge prevents the growth of high-quality Ge-on-Si films with useful thickness. As a result, regardless of the growth technique, such as LEPECVD [62] and UHVCVD [22, 119, 20, 21, 27], a two-step process is commonly used to grow single-crystal Ge. Starting with a low-temperature LT ($\sim$ 400 °C) growth resulting in a poor-crystalline-quality layer, yet essential to prevent islanding and maintain a uniform thickness across the whole wafer [1, 8, 5]. And a subsequent high-temperature HT step ($\sim$ 700 °C) to deposit the active high-crystalline-quality layer [20, 21, 22, 119, 1, 5]. The LT layer imposes serious issues from carrier-dynamics point of view, as well as photons scattering. Although this is acceptable for photo-detection applications, even for commercial products [1, 5], it is intolerable for lasing purposes due to its impact on carrier lifetime. Virtual substrate technology can be used to grow single-crystal Ge layer on Si, through a series of graded buffer layers with increasing Ge content. A lot of impractical issues arise in such processes, such as maintaining the thickness uniformity across the wafer. In addition to the thick buffer-layer region, and the relaxation of the strain in top Ge layer. Liquid phase epitaxy (LPE) can also be used to crystallize amorphous or poly-crystalline Ge on an insulating layer on Si, through a seed window and rapid melting process [1]. Another solution can be bonding; where a high-quality Ge wafer can be bonded to a handle wafer to transfer a perfect Ge layer [124, 100, 36]. This can be applied to bulk Si in order to override the growth of poor LT layer. For proof-of-concept studies and more engineering flexibility, special wafers such as GOI and Ge-on-SOI can be used. GOI wafers are shown to enhance carrier lifetime significantly, attributed to the absence of the poor LT Ge interface layer [100, 124]. In addition to providing a flexible platform for strain engineering. In the case of using SiO_2 as the insulating layer, GOI wafers lack a good adhesion between Ge and SiO_2, the fact that Ge-O bonds are volatile and soluble in water. Ge-on-SOI can be used to enhance the adhesion by introducing Si as an interface between Ge and SiO_2.

2.6 Photonic Cavity

Manipulating the electromagnetic field through an optical cavity is one of the strategies to enhance photons emission from indirect-gap group-IV materials [1, 5]. This is based on the fact that an optical cavity is capable of increasing the efficiency of light emitting devices, through a three-fold effect of increasing the spontaneous emission rate, extraction, and collection efficiency. Purcell effect is responsible for the first one [125], while preventing the field in certain directions, and directing it to another ones, are responsible for the later two effects [1]. A wide variety of photonic cavities have been demonstrated aiming for Ge lasing, starting from simple Fabry-Perot waveguides (FP) [20, 21, 22, 23, 39] to three-dimensional photonic-crystal cavities [126]. Successful lasing of Ge direct-gap emission has only been reported using FP WGs until now [20, 21, 22, 23]. Such cavities are tempting for practical implementation of a Ge laser for chip-to-chip communications requiring a suitable output power [5]. Similar cavities including distributed-bragg reflectors (DBR) [38], and distributed-feedback cavities (DFB) [17] can be also implemented in a Ge FP WG.

Novel cavities with extremely high quality factors are another tempting choice for proof-of-concept studies, and developing a better understanding on Ge light emission. For example, two-dimensional photonic crystals (PhC) [127, 128, 86] , have been used due to their extremely-high Q-factors, and their planar structure which is advantageous for CMOS-based integration. 2D PhC slabs made of Ge [127, 128, 86], or even Ge quantum dots embedded in 2D PhCs have been demonstrated [129, 130]. Yet, Q-factors of direct-gap Ge resonances were not as high as expected by the design Q-factor, such as 540 reported in [127]. In fact, higher Q-factors were observed using simple micro-disk cavities [131, 55]. Three-dimensional PhCs with embedded Ge quantum islands resulted in 13600 Q-factor [126], such a high Q-factor is expected due to the complete photonic band gap.

Moreover, photonic cavities supporting whispering-gallery-mode (WGM), such as micro-disks [55, 56, 57, 3] and rings [131, 30], are increasingly gaining attention. Being simple circular structures, with compact sizes suitable for dense integration, and providing resonances with high Q-factor exceeding those reported for PhC-based cavities [55]. Tuning resonant modes is simply done by changing the diameter of the cavity, which is a privilege in terms of wavelength-division multiplexing. Moreover, they provide high flexibility in terms of applying and tuning the strain using under-etching and stress liners [6]. For instance, depositing Si_3N_4 stress liners is a common way of applying high tensile strain on Ge micro-disks [55, 56, 57, 29, 30]. This pre-stressed layer can be applied on-top [55, 56], bottom [57], or even all-around the disks after under-etching the circumference [57, 29, 30]. In this project we use simple micro-disk cavities to confine photons,

and engineer the strain within the disks using freestanding SiO_2 beams [2, 6]. Detailed overview of Ge micro-disks and rings, and a brief description of the theory is provided below.

2.6.1 WGM Optical Cavities: Micro-Disks & Rings

Realistic integration of electro-optical data circuitry on CMOS chips requires novel ideas that provide efficient and convincing replacements of pure electrical circuitry. Regarding light emitters, the ability to generate monolithic light that is spatially confined in micron size is crucial for high integration density and complex functionalities [132]. Semiconductor-based WGM cavities provide a promising solution for such requirements.

Ge micro-disks are widely used for optical confinement of direct-gap photons. Resonant modes including lossy FP modes and high-Q WGM were observed by multiple groups in Ge micro-disks [55, 56, 57, 29, 30, 3] and rings [131, 30] by optical [55, 56, 57, 29, 30, 3] and electrical [133] pumping. Diameters of the studied micro-resonators range from 1 to 10 μm, with most of sharp WGMs observed in disks around 3 μm. The highest reported Q-factor of WGMs in Ge micro-resonators on Si (SOI) was 620 using intrinsic micro-rings demonstrated by Lim *et al.* [131]. While, the highest WGMs Q-factor up to now is 1350 and was reported by Ghrib *et al.* [55], by growing Ge micro-disks on GaAs substrate to eliminate interface defects due to approximately similar lattice constant. The disks were tensile-strained up to 1% using a nitride stress liner. Q-factors are degraded by the edge, interface and surface roughness of the micro-resonators, as WGMs interact strongly with these defects causing them to scatter [32]. Ge direct-gap WGMs are considered to be limited by FCA losses [55]. Q-factors have to be enhanced for efficient photons confinement, and this can be done by enhancing the crystalline quality [17, 1], optimizing the etching techniques for roughness reduction [32], eliminating the interface defects at Ge-Si interface [100], and optimizing Ge band-engineering conditions of n-type doping [123, 2] and tensile strain [58, 96, 94].

2.6.1.1 Whispering Gallery Modes

Representation of WGM fields within micro-disk cavities can be done by considering a simple two-dimensional representation of the disk through the effective refractive index method [134, 135]. For an optical mode, a 2D disk with an effective refractive index (n_{eff}) is equivalent to a finitely-thick 3D disk with a refractive index (n). Assuming that the disk height (d) is thin enough to support the fundamental mode in the z direction, it

is possible to write two independent sets of Maxwell's equations for TE and TM modes, by solving the wave equation [134, 135]:

$$\frac{d^2\psi_z}{d\rho^2} + \frac{1}{\rho}\frac{d\psi_z}{d\rho} + \left(\mathrm{n}^2\kappa^2 - \frac{\mathrm{m}^2}{\rho^2}\right)\psi_z = 0 \tag{2.7}$$

Where, ψ_z is the magnetic (electric) component along the z axis field for TE (TM), or $\vec{\mathcal{H}_z}$ ($\vec{\mathcal{E}_z}$), respectively. ρ is the radial distance from the disk center, and κ is free-space wavenumber. n is the refractive index, which can be set to $\mathrm{n_{eff}}$ in a 2D problem within the disk region ($\rho < R$), and equals 1 (air) outside the disk ($\rho > R$), as indicated in fig. 2.5. m is the azimuthal mode number; or the number of full wavelength of the WGM along the disk circumference. Solving equation 2.7, the orthogonal field component can be expressed using Bessel and Hankel functions as follows:

$$\psi_z \propto \begin{cases} J_m^{(1)}\left(\kappa \mathrm{n_{eff}}\rho\right) e^{-i(m\phi-\omega t)} & \rho \leq R \\ \\ H_m^{(2)}\left(\kappa\rho\right) e^{-i(m\phi-\omega t)} & \rho > R \end{cases} \tag{2.8}$$

$J_m^{(1)}$ and $H_m^{(2)}$ are Bessel function of the first kind and Hankel function of the second kind, respectively [134, 135]. Field intensity of the WGMs has three main distinctive regions: (i) volume within the cavity itself and limited by its surface ($\rho < R$), in which WGM fields are described by Bessel functions [136] . (ii) Secondly, waves propagating into low-index region just outside the cavity's surface ($\rho > R$), which are evanescent in nature and decay exponentially with distance. (iii) Free propagating plane waves that are formed by gradual build-up of evanescent waves [132, 136] . All other non-zero field components, $\vec{\mathcal{E}_\rho}$ and $\vec{\mathcal{E}_\phi}$ for TE, $\vec{\mathcal{H}_\rho}$ and $\vec{\mathcal{H}_\phi}$ for TM, can be derived from $\vec{\mathcal{H}_z}$ or $\vec{\mathcal{E}_z}$, respectively [135]. In this report, computer simulations utilizing finite-difference time-domain (FDTD) method was used to solve the 3D Maxwell's equations, for field profile visualization and solving for the resonant frequencies. The final mode representation can be described by the azimuthal number and the radial number l (number of field maxima along the radius), such as $\mathrm{TE}_{m,l}$ or $\mathrm{TM}_{m,l}$. The azimuthal mode number m can be related to the disk radius, and the effective index of the mode using the following simple expression:

$$m \times \frac{\lambda}{\mathrm{n_{eff}}} = 2\pi \times R \tag{2.9}$$

Accordingly, the spacing between supported modes, or the free spectral range (FSR) can be expressed in terms of wavelength as [137] :

$$\Delta\lambda_{FSR} = \frac{\lambda^2}{2\pi \times R \times \mathrm{n_{eff}}} \tag{2.10}$$

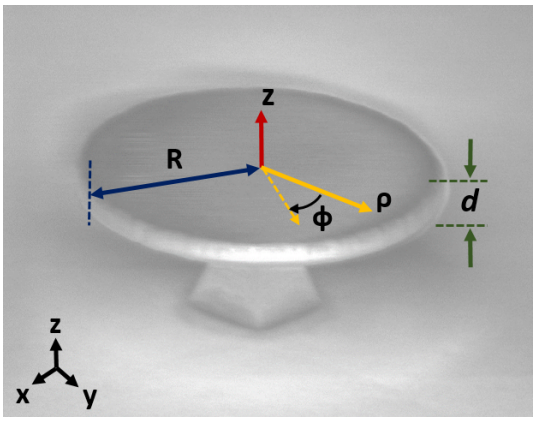

Figure 2.5: A dielectric micro-disk on Si pedestal annotating parameters used in equation 2.8

2.6.1.2 Q-factor

Quality factor (Q-factor) is a measure of the capability of the cavity to confine photons. Looking at the spectral response of a cavity, Q-factor is represented by the sharpness of resonant peaks, and can be estimated as:

$$Q = \frac{\lambda}{\Delta\lambda_{\mathrm{FWHM}}} \tag{2.11}$$

Q-factors of whispering-gallery modes can be decomposed into four main components, as proposed by Gorodetsky *et al.* [138]. The total Q-factor is limited by the lowest component among them, in analogy to electrical resistances connected in parallel:

$$Q_{WGM}^{-1} = Q_{radiation}^{-1} + Q_{scattering}^{-1} + Q_{contaminants}^{-1} + Q_{material}^{-1} \tag{2.12}$$

Radiation or curvature losses of light due to coupling with air modes determine $Q_{radiation}$, which increases exponentially with disk diameter. $Q_{scattering}$ is a measure of side-walls perfection. $Q_{contaminants}$ is also related to scattering, but due to contaminants on the cavity surface. $Q_{material}$ represents material losses, mainly due to absorption. In large micro-disks ($\frac{Diameter}{Wavelength} \gg 15$), $Q_{material}$ is the main limiting factor, where other types of losses become insignificant [138]. For the micro-disks studied in this project, values of all Q-factor components are limited due to high corresponding losses. However, in an active Ge micro-disk, Q-factors of direct-gap resonances are considered to be limited mainly by FCA (material) losses [55].

2.7 Optical Gain

Theoretical modeling of Ge optical gain has been studied using various methods [49, 32, 139, 25, 92, 91, 140]. For example, Liu *et al.* [49] provides a model based on effective mass formalism predicting positive net gain values, where net gain is defined as the difference between material gain and FCA losses. Chang and Chuang [139] and Pizzi. *et al* [141] modeled gain in Ge/SiGeSn quantum wells using tight-binding formalism. While El Kurdi *et al.* used precise 30-band *k.p* formalism to estimate Ge material gain [25]. All mentioned studies agreed that positive material gain of un-strained un-doped bulk Ge is improbable. El Kurdi *et al.* predicted a net optical gain of 3000 cm^{-1} beyond 3 μm wavelength for 3% strained Ge and total carrier density of 1×10^{18} cm^{-3} at low temperatures. While Liu *et al.* estimated a net gain of 400 cm^{-1} for 0.25% biaxial strain with 7×10^{19} cm^{-3} *n*-type doping, and 9×10^{18} cm^{-3} injection, at room temperature.

Experimentally measured optical gain of Ge-based structures can be summarized as follows:

1. Liu *et al.* (2009) [20]: 50 cm^{-1} at 1605 nm emission wavelength measured using pump probe spectroscopy, of a Ge-on-Si mesa structure, with 0.25% thermally-induced strain and a doping level of 1×10^{19} cm^{-3} .

2. De kersauson *et al.* (2011) [142]: 80 cm^{-1} at 1685 nm using variable-strip-length measurement system, of a Ge photonic wire on GaAs substrate capped by a Si_3N_4 stressor imposing an average of 0.4% strain, and 3×10^{19} cm^{-3} doping.

3. Lange *et al.* (2009) [62]: maximum transient gain of $\alpha \times L_{QW} = 8 \times 10^{-4}$ per QW is measured using ultrafast pump-probe spectroscopy (80 fs - low gain lifetime) for compressively strained Ge/Si_xGe_{1-x} quantum wells at room temperature.

4. Xu *et al.* (2015) [143] reported a very high transient optical gain of 5300 cm^{-1} using femto-second transmittance spectroscopy ($<$ 80 fs - low gain lifetime). Ge film was MBE grown and doped using SOD (4×10^{19} cm^{-3}).

5. Okumura *et al.* (2015) [98] have experimentally demonstrated the effect of *n*-type doping (2×10^{19} cm^{-3}) on decreasing the optical losses from 2200 to 500 cm^{-1}. This study have not reported positive optical gain, presumably as no tensile strain was applied.

In addition to strain and doping, other theoretical studies modelled the dependence of gain spectrum on lattice orientation [140]. For instance, it has been proposed that $\langle$ 001 $\rangle$ ($\langle$ 111 $\rangle$) orientation is preferred for large (moderate) strain values in intrinsic (heavily doped $\sim 10^{19}$ cm^{-3}) Ge [140]. Moreover, temperature is expected to enhance

the gain linearly up to a certain pumping level [32], after which the temperature effect is reversed. This was explained by remarking two temperature-dependent factors with opposite influence on optical gain: the amount of excess carriers injected into the direct Γ valley increases with temperature due to the increased probability of occupying higher energy states, while the percentage of electrons contributing to the net gain is inversely proportional with temperature [20, 32].

2.7.1 Strain & Doping: Feedback from Recent Highly-Strained Structures

Theoretically predicted gain values of bulk Ge are quite promising [25]. However, experimentally achieved gain values are still controversial [41, 1, 5]. Reproduction of initial lasing results of slightly-strained and n-doped Ge reported in refs. [21, 22] has been questioned by several groups [41]. Until the recent lasing of unstrained heavily-doped (3×10^{19} cm^{-3}) Ge FP WGs prepared using MBE, and electrically pumped in a $p-n$ structure, reported by Koerner *et al.* [23]. Meanwhile, research efforts have mainly targeted extremely strained structures, following the theory, aiming to reduce the reported lasing threshold values.

Accordingly, it is possible to point out two different routes for developing a Ge laser: utilizing slight strain ($\sim 0.2\%$), similar to initial lasing reports [21, 22] combined with heavy doping ($\sim 10^{20}$ cm^{-3}). Or, increasing the strain significantly ($> 1\%$), with moderate doping ($\sim 10^{19}$ cm^{-3}). Researchers see in the first approach a modest strain that is inherent in Ge layers grown on Si. In addition to maintaining a tempting band-gap energy that emits in the 1550-1650 nm wavelength range, which lies in the standard low-loss transmission window for optical communications. This wavelength range permits using Si as a high-performance transparent waveguide for on-chip signal routing, and silica-based optical fibers for board-to-board communications. However, lasing reported with 0.25% tensile strain [22], or unstrained heavily-doped Ge [23], suffered from very high threshold-current densities (300 [22] and 500 [23] KA/cm^{-2}) making this approach non-realistic. Increasing doping concentration is not trivial according to recent doping trials [2], moreover, the exact effect of higher doping levels on Ge optical gain is not yet elucidated. Ref. [144] provides theoretical calculations for optimum doping concentrations versus tensile strain values for different cavity losses, which simply means that higher doping levels are not always advantageous. It is shown that optimum doping concentration values for different applied strain will vary according to the requirements of either minimizing lasing threshold or maximizing lasing slope efficiency. For instance, increasing strain from 0.25% to 1% reduces optimum doping concentration (for minimum lasing threshold) from 2×10^{20} cm^{-3} to 6×10^{19} cm^{-3} [144].

The significance of the second approach starts from here, where tensile strain will proportionally reduce the required levels of doping and pumping. The main drawback of this approach is the red-shift of the emission peak beyond 2 μm for strain values above 1.1% [144]. This requires modified optical components - such as modulators and photodetectors - for manipulating such wavelengths. One possible way is to introduce strain on currently existing components, such as Ge PDs [27, 16, 15, 94]. However, this solution does not work for global interconnects that use standard silica-based optical fibers as transmission medium, because silica-based fibers impose high absorption losses on signals outside the 1.3 and 1.5 μm low-loss windows. Such communication systems will need more signal amplifying processes compared to standard systems operating in the low-loss regime. Nevertheless, highly strained Ge structures are gaining more attention, as they are a more realistic candidate for low-threshold on-chip lasers.

Recently, strain values have reached extremely high limits resulting in direct-gap bulk Ge [31, 36, 37, 30, 29]. Optical cavities were included in some proposed devices [37, 30, 29, 38], in the form of micro-disks [29], micro-rings [30], and DBRs surrounding freestanding beams [37, 38]. Although transition into a direct-gap material was confirmed in references [29, 30], lasing was not observed. In fact, Q-factors of resonant modes degraded at extremely high strain values [29, 38]. For instance, Ge micro-disks with all-around Si_3N_4 stressors reported by CNRS group [57, 29], had very broad Q-factors for 1.5% [57] and 1.75% tensile-strained Ge [29]. While their previous work of on-top Si_3N_4 stressors resulted in the highest reported Q-factor of 1350 at only 1% tensile strain. Similarly, Petykiewicz *et al.*[38] demonstrated interesting high-quality-factor DBR modes from highly-strained uniaxial nano-beams. Sharp resonances with Q-factors up to 2020 were observed from 1.95% uniaxial tensile-strained nano-beams. Increasing the uniaxial strain to 2.37% degraded the Q-factors significantly and this was attributed to VB losses. We expect that at such high strain values, the defect density in the Ge lattice might increase, consequently increasing the losses. Recent information deduced from literature indicates that even direct-gap Ge ($\epsilon_{||} \sim 2\%$) is not sufficient for lasing [29, 30]. This remarks the importance of doping once again, as a possible solution if combined with high strain. In fact, the exact successful combination of doping and strain is very hard to specify based on current research outcomes [8, 5].

2.7.2 Further Approaches

Considering the reported Ge (or even GeSn [39, 40]) lasing thresholds, and bearing in mind the history of compound-semiconductor lasers, it might be advantageous to target hetero-junctions and lower-dimension structures [145]. Hetero-structures provide charge-carrier confinement in the active layer and have been used to realize lasing of indirect-gap materials and reduce lasing threshold [147]. Si_xGe_{1-x}/Ge hetero-structures

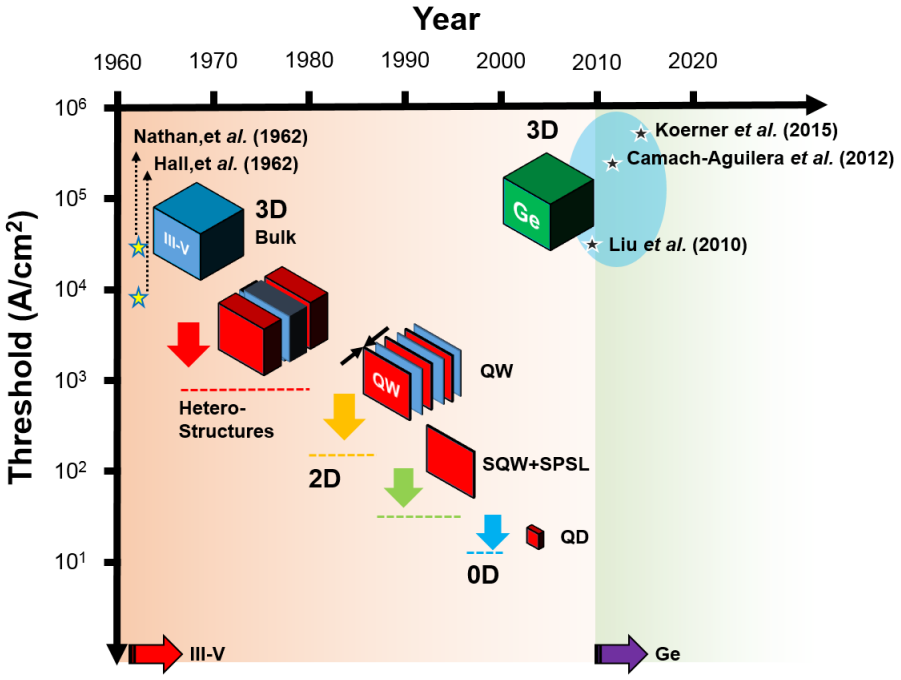

Figure 2.6: Lasing-threshold history of compound-semiconductor lasers & current achievements in Ge lasing. Improvements in lasing threshold were witnessed through reduction in dimensions, from bulk (3D) to quantum wells QW (2D), and quantum dots QD (0D). Lasing threshold of Ge by optical pumping (35 KA/cm^2 [21]) is comparable to first III-V lasing threshold by electrical injection. Ge lasing threshold by electrical injection (280 KA/cm^2 [22], and 500 KA/cm^2 [23]) is more than an order of magnitude higher than first III-V lasing. This figure is inspired from figures in references [145, 146]

might be the most straightforward choice, given that a type-I band alignment is satisfied [61]. Band offset in Si/Si$_x$Ge$_{1-x}$ hetero-structures depends on the strain of Si substrate, in addition to the percentage (x). Type-I band alignment in Ge/Si hetero-structures requires cubic (unstrained) silicon structures surrounding strained Si$_x$Ge$_{1-x}$ layers [61]. However, the obtainable difference between Si and Si$_x$Ge$_{1-x}$ conduction bands cannot exceed 0.02 eV for any Si$_x$Ge$_{1-x}$ composition, which reduces the significance of hetero-structures role in confining electrons in Ge. Another choice to consider is reducing the dimensions of the active region, from bulk or 3D, to 2D (quantum-well, QW) [63], 1D (nano-wires, NW), or even 0D (quantum dots, QD) structures. Historically, a remarkable reduction in lasing threshold have been witnessed in compound-semiconductor lasers by moving towards one less dimension at a time. For instance, the use of QDs reduced threshold values below 20 A/cm^2, compared to $\sim 10^4$ A/cm^2 using bulk structures in 1962 [148, 149, 145]. Introducing QDs took more than 20 years of research. This reduction in threshold is mainly attributed to the confined density of states for lower-dimension structures, implying that electrons are spread over a smaller energy range with higher densities at the band edge [149, 145, 150].

2.8 Applications

Successful implementation of Ge light sources in commercial products relies on CMOS compatibility and cost reduction [5]. Optical components based on tensile-strained Ge already exist in photonics market in the form of efficient PDs [27, 16, 15, 5]. On the other hand, Ge-based light sources - relying also on strain - are still under development with a wide potential market and applications. Possible applications of efficient Ge light sources can be categorized according to power level and operation frequency. For instance, Ge light emitting diodes (LED) are sufficient for short-distance local-area networks (LAN) requiring modest output power and data rates. Such networks are suitable for smart cars and vehicles, or even home and office networks [5]. Another possible target for Ge LEDs would be biomedical technology and lab-on-a-chip devices providing point-of-care services using optical bio-sensors [151]. The increasingly-growing demand on bandwidth creates a wider range of applications for monolithic Ge light sources, or laser diodes (LD). Global networks relying on optical links for high-data-rate communications require efficient monolithic light sources with high operational speed. Networks connecting global data centers, fiber-to-the home (FTTH), future implementation of Internet of things (IoT), cloud computing, and many other practical applications offer a potential market for Ge LDs. In order to compete, Ge LDs have to overshadow the privileges of III-V lasers. In terms of performance, Ge LDs have to provide similar, or higher, internal quantum efficiency. Yet, this condition can be compensated for by offering cost reduction and CMOS compatibility. Another possible route towards more efficient power consumption, rather than competing with III-V materials on internal quantum efficiency, is by realizing Ge LDs with high operational speed. Operating a LD beyond 10 Gbps eliminates the necessity of a dedicated optical modulator, by direct modulation of the LD [5].

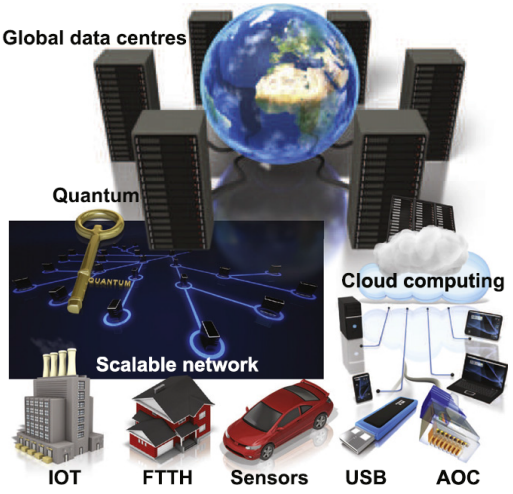

Figure 2.7: Possible markets for Ge light sources [5]

2.9 Summary

Throughout this chapter, main practical approaches towards realizing a monolithic Ge light source are outlined, considering tensile strain, n-type doping, crystalline quality, and optical confinement. Advances in tensile strain application have accelerated in the past few years, resulting in direct-gap Ge. Micro-machining is suitable for such high strain values, where direct-gap uniaxial and biaxial freestanding Ge beams were demonstrated. Graded beams and beams with curved edges were particularly useful for this achievement, maintaining a smooth gradient of strain along the beams and enhancing uniformity. Achievements with regards to n-type doping are less significant. Consistent reports from several groups confirm limited activation levels of P in Ge to $\sim 2 \times 10^{19}$ cm^{-3} by diffusion-based methods. Spin-on doping is being used for Ge light emission purposes as a cheap and simple diffusion-based technique, providing source concentrations above the maximum solid solubility. In addition to strain and doping, crystalline quality is critical for efficient Ge direct-gap recombinations. Wafers prepared by bonding can be used to investigate optical properties of perfect-crystal Ge. A structure satisfying these three requirements, needs to be embedded in a high-quality-factor optical cavity to achieve lasing. Micro-cavities confining whispering-gallery modes, such as micro-disks and rings, have been popular through the last few years. Because of their simple fabrication, small sizes, high Q-factors and flexibility in terms of strain application.

Theoretical and experimental optical gain values reported in literature indicate that Ge holds potential for future low-threshold lasing. Compared to the beginnings of compound-semiconductor lasers, first reported Ge lasing has more than an order-of-magnitude higher lasing threshold. Bearing in mind that those initial lasing experiments relied on 0.2% tensile strain, then in principle, it is possible to reduce the threshold by increasing the tensile strain. More efficient lasing has to utilize lower-dimension structures, following III-V lasers history. Upon realizing efficient Ge light sources, devices can compete based on cost-reduction and integration-ability with CMOS platforms in current data and communications market.

Chapter 3

Spin-on Doping of Thin Germanium-on-Insulator Films using Furnace Annealing

"There are two types of innovation, performance-centric or p-type, and nature-oriented or n-type. Building a sustainable society requires the convergence of the two approaches, as in a p-n junction "

Dr. Ryoji Chubachi, SSDM 2015

3.1 Introduction

As crystalline quality is considered critical to achieve efficient direct-gap emission from Ge, literature is pointing out the necessity of a reliable diffusion-based doping technique. In this chapter we investigate spin-on doping (SOD) as a diffusion-based technology to introduce $n-$type impurity atoms into Ge for light emission purposes. As the commercially-available SOD solutions are optimized for Si processing, many processing obstacles have to be overcome to apply the same products to Ge. In this study, we focus on comparing two main types of commercial SOD solutions, namely, water and alcohol-based solutions containing phosphorus atoms. A general introduction on the diffusion of dopants, highlighting the deviations expected in the case of SOD of Ge, is firstly summarized in section 3.2. Process optimization for both types of dopants is then presented in section 3.4, resulting in a maximum doping concentration of $1 - 2 \times 10^{19}$ cm^{-3}. The effect on crystalline quality and strain within Ge-on-Insulator (GOI) films, and the impact on photoluminescence, are discussed in section 3.5.

Some parts of this chapter were published in ref. [2] in the form of figures and tables.

3.2 Diffusion of Dopants

Diffusion of dopants is the migration of guest atoms through a host material driven by a gradient in concentration [104]. The diffusion behavior is modelled by the diffusion equation, or Fick's second law of diffusion, which can be derived as follows:

Starting with Fick's first law of diffusion, describing the tendency of particles to move from high to low concentration regions, represented by the flux of particles J in $\mathrm{cm}^{-2}.\mathrm{s}^{-1}$ [152, 153].

$$J \propto -\frac{\Delta C(x,t)}{\Delta x} \rightarrow J = -D\frac{\partial C(x,t)}{\partial x} \tag{3.1}$$

Where J is the flux of particles, or the number of particles crossing a unit area per unit time ($\mathrm{cm}^{-2}.\mathrm{s}^{-1}$). C is the concentration of particles (cm^{-3}), and it is a function of space and time, $C(x,t)$. x is the distance from the surface of diffusion (cm). The partial derivate of C relative to space x, represents the spatial concentration gradient. The higher the concentration gradient, the higher the flux of particles, and the negative sign counts for the direction of diffusion opposite to the concentration gradient. D is a proportionality factor, referred to as the diffusion coefficient or diffusivity, describing how fast the diffusion is ($\mathrm{cm}^2.\mathrm{s}^{-1}$), as will be described later.

Applying the continuity of particle flux (or, mass) equation [152, 153]:

$$\frac{\partial C(x,t)}{\partial t} = -\frac{\partial J}{\partial x} \tag{3.2}$$

Denoting that the rate of change of particles concentration with time, is a result of spatial divergence of particle flux. Combining equations 3.1 and 3.2, results in Fick's second law, the *diffusion equation* [152, 153]:

$$\frac{\partial C(x,t)}{\partial t} = \frac{\partial}{\partial x}\left(D\frac{\partial C(x,t)}{\partial x}\right) \tag{3.3}$$

And, assuming that the diffusion coefficient is independence of concentration [152, 153]:

$$\frac{\partial C(x,t)}{\partial t} = D\frac{\partial^2 C(x,t)}{\partial x^2} \tag{3.4}$$

The exact diffusion profile of impurity atoms is obtained by solving the differential equation 3.4 with case-representative boundary conditions. Boundary conditions are imposed by the doping technique, which can be summarized in two main cases, as shown in table 3.1. Atoms diffusing from an infinite source, maintain a constant source concentration

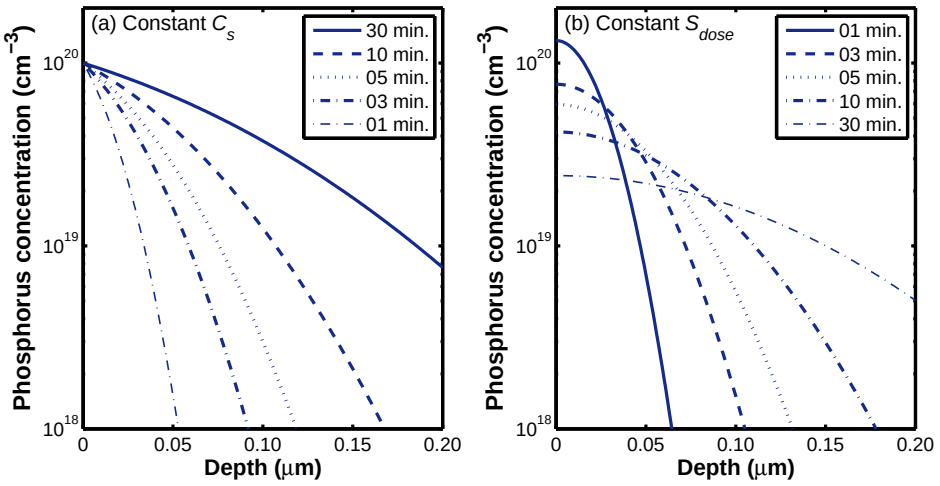

Figure 3.1: Theoretical diffusion profile of P in Ge assuming (a) constant source concentration, and (b) constant total dose (S_{dose}), at 580 °C. Constant S_{dose} represents the case of a spin-on doping source which is a limited source of impurity atoms. Calculations in (b) assume a total dose of 3×10^{14} cm^{-2}, as estimated from experimental data using Filmtronics P507 as a dopant source. Experimental diffusion profiles of P in Ge do not follow this theoretical prediction, due to the extremely fast diffusion of P in Ge, resulting in box-like profile as provided in ref. [108].

C_s at the sample surface, and tend to have a complementary error function (*erfc*) diffusion profile. Such a case is expected, for example, in furnace-based $POCl_3$ doping, with a constant flow of $POCl_3$ vapor. While diffusion from a limited source, providing a certain amount of impurity atoms, results in a Gaussian-shaped diffusion profile. This is the expected diffusion profile in the case of SOD, due to the limited amount of dopant atoms within the spin-coated film. Figure 3.1 plots the expected diffusion profiles for P doping of Ge with constant source concentration (fig. 3.1(a)), and limited total number of dopant atoms (fig. 3.1(b)), at 580 °C. Even though SOD is a limited-source technique, the actual P diffusion profile in Ge deviates from that shown in fig. 3.1(b), mainly due to high diffusivity arising from the diffusion mechanism, as discussed below.

Source	**Diffusion Profile**	**Boundary Conditions**
Limited	$C(x,t) = \frac{S_{dose}}{\sqrt{\pi Dt}} e^{-(\frac{x}{2\sqrt{Dt}})^2}$	$\lim_{x\to\infty} C(x,t) = 0$ $\int_0^\infty C(x,t).dx = S_{dose}$ $C(x,0) = 0$
Infinite	$C(x,t) = C_s \,.\, erfc(\frac{x}{2\sqrt{Dt}})$	$C(0,t) = C_s$ $\lim_{x\to\infty} C(x,t) = 0$ $C(x,0) = 0$

Table 3.1: Theoretical expressions of diffusion profiles for limited and infinite source concentrations [152, 153]

The proportionality factor D, that relates the diffusion flux and the concentration gradient, is referred to as the diffusion coefficient, or diffusivity. Diffusivity has the units of $cm^2.s^{-1}$, mainly indicating how fast the diffusion is, and can be calculated at a certain diffusion temperature as follows:

$$D = D_\circ e^{-\frac{E_a}{KT}} \tag{3.5}$$

Where D is the diffusion coefficient, $D_\circ$ is the pre-exponential factor having the same units as D, and sometimes referred to as the jump frequency factor [104]. E_a is the activation energy (or enthalpy) of diffusion in eV. Fast diffusers have low E_a, and vice versa. K is Boltzmann constant, and T is the temperature. As the fraction within the exponential term is unit-less, if K is in eV/Kelvin, T is in kelvin. Diffusivity is temperature dependent, so it is described by an Arrhenius-like equation [104, 152, 153].

Depending on the route taken by impurity atoms diffusing through a crystalline material, two main diffusion mechanisms can be highlighted, namely: substitutional and interstitial. Substitution requires the impurity atom to take over a place in the lattice and exchange places with direct neighbors, which is unlikely in Ge [104, 154, 101, 102]. While in interstitial diffusion, the impurity simply migrates through the lattice, between the host atoms, from one interstitial site to another, such as some metals in Ge [104]. Dopants diffusing by substitution are expected to have high activation energies, compared to interstitial dopant atoms which tend to have lower activation energies, and consequently fast diffusion even at relatively low annealing temperatures. Intrinsic point defects in crystalline materials affect the diffusion process by providing additional routes for migrating atoms. The higher the defect density, the faster the diffusivity. Defects including vacancies (V) and interstitials (I) offer a possibility for atoms to exchange positions between lattice and interstitial locations. Vacancy-mediated diffusion, in which the migrating atom moves into a neighboring vacant lattice position, is the most common diffusion mechanism in Ge. This is true for self-diffusion and most common dopants [104, 154, 101, 102]. Consequently, diffusivity of impurity atoms depends on the mechanism, size of impurities, and temperature.

Figure 3.2 plots the temperature dependence of common n-type atoms diffusivity in Ge, alongside the diffusivity of oxygen and Si, relative to G self diffusivity, as found in literature [104, 154, 101, 102]. Generally speaking, the diffusion of group IV atoms in Ge, including Ge self-diffusion, is slow compared to n-type (group V) dopants, which are considered fast diffusers in Ge, as shown in fig. 3.2 (a). Compared to group-IV elements, the diffusivity of P, As, and Sb is more than an order of magnitude larger, with P being the slowest amongst them. The choice of P as an n-type doping atom was justified previously in section 2.4.2, mainly due to its highest solid solubility ($S_{\circ\_max}$)

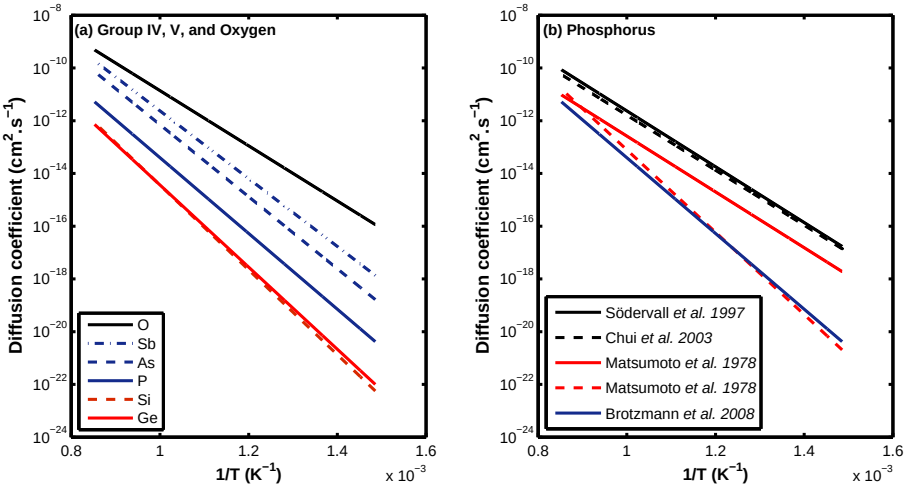

Figure 3.2: Temperature dependence of diffusion coefficients (diffusivity in $cm^2.s^{-1}$) of common impurities in Ge including: (a) Group IV, V, and oxygen. Diffusion of oxygen is faster than all common group V dopants, making Ge oxidation a crucial problem during doping. (b) Summary of P diffusivity in Ge showing a significant increase with higher source concentration (Matsumoto *et al.* [110]) and implantation-originated defect density (Sodervall *et al.* & Chui *et al.* [155] taken from ref. [104]).

as summarized in table 2.3, in addition to its slowest diffusivity among other group V elements (fig. 3.2 (a)). On the other hand, oxygen diffuses approximately one order of magnitude faster than P, and generally faster than all common dopants. This makes Ge doping process very sensitive to active oxygen atoms in the annealing chamber, or in contact to the sample surface. Ge mono-oxide (GeO) is a volatile oxide that is also soluble in water [154], which degrades the quality of the Ge film.

Figure 3.2(b) plots the temperature dependence of P diffusivity in Ge, reported in different references. It is found that the diffusion of P (and other impurities) in Ge is dependent on intrinsic point defects, and impurity concentration. Vacancy-mediated (V) diffusion is dominant in Ge [104, 154, 101, 102], causing the diffusivity of most of the dopants to increase proportional to vacancies concentration (defect density). This can be seen in the high D_P values reported by Sodervall *et al.* and Chui *et al.* [104], for ion-implanted Ge films. While lower values were reported Matsumoto *et al.* [110] and Brotzmann *et al.* [101], who used a diffusion-based doping process. Matsumoto *et al.* [110] used red P powder to study the dependence of D_P on the source concentration (C_s), and demonstrated the transition of the diffusion profile from a standard *erfc* function ($C_s = 3 - 7 \times 10^{18}$ cm^{-3}) to a box-shaped function ($C_s = 5 - 8 \times 10^{19}$ cm^{-3}), indicating a strong dependence on C_s. This increase in diffusivity at higher concentrations limits the activation of P and promotes out-diffusion, as reported by many groups [58, 32, 108, 121, 2].

3.3 Spin-on Doping

Spin-on Doping is being proposed as a promising doping technique for Ge light emission purposes. Having the benefits of low cost, simple processing, tune-ability of doping profile, permitting selective doping by patterning the SOD film, and imposing negligible damage on the crystalline quality being a diffusion-based technology, as will be shown in section 3.5.1. SOD has been used in near-infrared (NIR) photo-detectors (PD) [121], solar cells [108], MOSFETs [122], and more recently for Ge light sources [2, 123]. However, regardless of the apparent simplicity of the SOD process, which is similar to any photo-resist coating process (fig. 3.3), there are many practical challenges that have to be overcome to establish a reliable SOD process of Ge. Since the existing SOD solutions are optimized for Si processing [121]. For instance, SOD films are oxygen-rich with recommended processing temperatures around 1000 °C. Other problems arise from the mechanical stresses of the SOD films after annealing causing Ge films to crack. Such an issue does not occur with Si or SOI films, presumably indicating a difference in thermal expansion coefficient relative to Ge [2]. In fact, as will be shown later in chapter 4, even soft-baking of some SOD solutions is not possible if applied on Ge due to acidity mismatch, which have been tuned to match the surface of Si. Various SOD products are commercially available from suppliers like Filmtronics [156], and Emulsitone [157]. SOD solutions come in a liquid form, based on water or alcohol solvents, in which a nano-powder containing impurity atoms is dissolved. For example, micro or nano-powder of phosphorus pent-oxide (P_2O_5) is used in P SOD sources [156, 157]. Most of the common dopants, such as Sb, As, and P (n-type), in addition to B, Ga, Al (p-type), are available with different source concentrations. Solutions with source concentrations (20×10^{20} cm^{-3}, Filmtronics P509 [108]) exceeding the solid solubility can be used - in principle - to achieve high doping levels.

From theoretical point of view, SOD is expected to result in a constant-dose diffusion profile, because the total amount of impurity atoms in the coating is fixed. Multiple coatings might be used to increase the dose, yet many practical issues arise in such an approach [158]. However, the diffusion profiles reported in literature show a remarkable deviation from theoretical expectations [108]. Diffusion profiles of phosphorus in Ge, for example, can not be described by Gaussian functions, and tend to have a box-like profile. This is often related to the fact that the impurity source film gets exhausted during the annealing process, due to the limited total dose in a $\sim$ 300nm coating, and out-diffusion of dopants into the annealing chamber [159, 108, 32]. It is also attributed to the fast diffusivity of P atoms in Ge, causing the out-diffusion to limit the doping levels, resulting in a box-like profile [58, 32]. Our work presented in chapter 4 agrees with this later explanation, by confirming the extraction of a very high dose from the SOD film using SOI chips. Theoretical models describing the SOD diffusion profiles can be found in literature, such as the model provided in ref. [159] for Zinc SOD.

3.4 Experiment

In this chapter, we investigate the usage of water-based and alcohol-based SOD solutions containing the same concentration of P atoms. Table 3.2 compares the two dopant sources to be used in this experiment. Data was extracted from suppliers information sheets and literature [156, 157, 108]. The main difference between these two products is the solvent; Emulsitone dopant source is aqueous (water-based) with a polymer containing P, while the dopant source provided by Filmtronics is alcohol-based (Ethanol). This reflects on the physical and chemical properties of the solutions, such as viscosity, which is a critical parameter in spin-coating processes. According to the suppliers, viscosity of Emulsitone solution is approximately seven times that of Filmtronics.

Property	**Phosphorosilicafilm**	**P507**
Supplier	Emulsitone	Filmtronics
Solvent	Water	Alcohol (Ethanol)
Soluble in water	Yes	Yes
Flammable	No	Yes
Viscosity (25 °C)	7 cP	0.8 - 1.2 cP
Dopant	Phosphorus	Phosphorus
Dopant Form	Phosphorus Pentoxide	Phosphorus Pentoxide
Source Concentration	5×10^{20} cm^{-3}	5×10^{20} cm^{-3}
Thickness (3000 rpm)	380 nm	230 nm
Group	A	B

Table 3.2: Spin-on dopant sources: comparison between water and alcohol-based solutions

We used commercially available GOI wafers with 70-nm-thick Ge and 145-nm-thick buried-oxide (BOX). Samples were divided into two groups (A & B) according to the dopant source used, as shown in table 3.2. A similar source concentration of $5{\times}10^{20}$ cm^{-3} is provided by the two SOD products. This concentration exceeds the maximum solid solubility of P in Ge, theoretically permitting the achievement of high doping levels with a uniform box-shaped doping profile across the whole Ge thickness [108].

3.4.1 Spin-on Doping Process

A typical SOD process is shown in fig. 3.3, which is similar to the standard coating process of photo-resists [108, 58, 121, 122, 123]. SOD film requires stabilizing at room temperature before usage, and this is done by overnight storage at room temperature.

The process starts by cleaning the Ge wafers using hydrofluoric (HF) and hydrochloric (HCl) acids. Spin-coating process is immediately done after cleaning for each wafer at a time. After placing the clean wafer on the spin-coater chuck, the liquid dopant source is dispensed using a plastic pipette. The coating process starts by rotating the wafer according to an optimized speed profile, allowing the control over film thickness. A final rotational speed of 3000 rpm was used for all samples, resulting in SOD film thicknesses as summarized in table 3.2. Baking is required afterwards to evaporate the solvents out of the film. This step appears to be critical, as any remaining solvent in the film prevents the deposition of a reliable cap layer, and degrades the wafer surface quality after activation. It was found that longer baking durations at higher temperatures generally result in a better surface quality. We have used up to 165 °C for 30 minutes baking for Ge wafers, and this can be extended for Si wafers, with up to 400 °C for 3 hours, resulting in an excellent surface quality. Cracking of the SOD film was observed upon ramping the hotplate too fast, or placing the coated samples on a pre-heated hotplate [108]. So, samples were baked from room temperature with a slow ramping rate of ~ 10 °C/minute. It is possible to pattern this film after baking, in order to selectively dope certain areas of the wafer [58, 32].

Diffusion and activation of dopants is then done immediately using furnace annealing. Leaving a time span between soft-baking and annealing should be avoided as peculiar changes occur to the SOD film, easily recognized by eye. Out-diffusion of dopants from the SOD film into the annealing chamber is expected, especially if no cap layer is used. During the activation, the SOD film solidifies and turns into a glass-like layer, which is subsequently removed using diluted hydrofluoric (HF) acid. 6 - 10 minutes in 20:1 buffered HF is sufficient to remove the glass film completely. The state of the surface after removing the glass layer is a figure of merit to judge the success of the doping process, however, it is rarely mentioned in literature [108, 160]. Formation of etch-resistive particles was observed after activation. The source of this issue was found to be the poor-quality PECVD SiO_2 cap layer, and insufficient baking before activation.

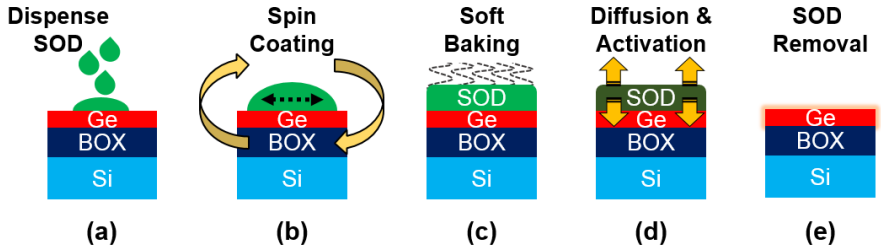

Figure 3.3: SOD process steps: (a) dispense spin-on-dopant source, (b) spin-coating using an optimized speed-profile, (c) soft-baking to solidify SOD layer by evaporating solvents, (d) diffusion and activation by annealing, and (e) removal of depleted SOD film by diluted HF etching

3.4.2 Water-Based Solution

We applied Emulsitone SOD solution to group A samples, by spin-coating at a speed of 3000 rpm. Baking was done afterwards from room temperature to 120 °C with a ramp rate of 10 °C/minute, and the baking duration was 15 minutes at the final temperature. This gradual increase in temperature helps preventing the SOD film from cracking [108]. This film was remarkably non-uniform, represented in line-shaped wrinkles corresponding to thickness variation, as seen in the optical microscopy image in fig. 3.4 (b). A variation of ±60 nm was measured across these wrinkles using a surface profiler. Not only such non-uniformity reflects on the doping profile across the surface of the chip, creating local variations in doping concentration, but also affects the morphology of the GOI layer after annealing represented in cracks. Thermal stresses imposed by the SOD layer, and the weak adhesion between Ge and BOX, are expected to be the reason behind the GOI layer cracking. The thickness non-uniformity of the film has also prevented depositing a reliable cap-layer using PECVD, sputtering, or even spin-on-glass (SOG).

To solve this issue, the SOD solution was diluted using Isopropyl alcohol (IPA) to reduce the viscosity and improve the coating uniformity. Methanol have been used previously to dilute SOD films and control the viscosity [158]. SOD-to-IPA volume ratios of 1:0, 1:1, 1:2, 1:5, and 1:10 were prepared, and the coating process was repeated at 3000 rpm. Resulting film thicknesses of the five samples have changed accordingly, as shown in fig. 3.4 (a). Although the uniformity improves with dilution, as seen in the optical microscopy image in fig. 3.4 (c), the source concentration (C_s), and the total surface dose (S), reduces simultaneously. Activation was then done for the five samples using furnace annealing at 580 °C for 30 minutes in nitrogen (N_2). The sample with the 1:10 diluted

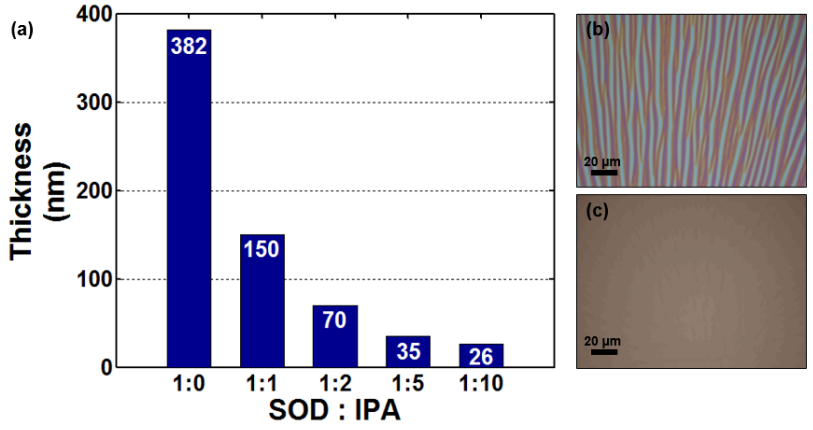

Figure 3.4: Dilution of Emulsitone spin-on dopants using IPA: (a) thickness variation according to dilution percentage, (b) optical microscopy image of Emulsitone (5×10^{20} cm^{-3}) spin-on-dopant coated at 3000 rpm before dilution, and (c) 1:10 SOD:IPA coating using same conditions.

solution was the only non-damaged sample, while the Ge layer has cracked severely in all other samples. Therefore, the 1:10 dilution was necessary to dope Ge using the water-based solution. The sheet resistance (R_{sh}) was measured to be 262 Ω/□ using a 4-point probe [161]. Varying the activation time resulted in lower R_{sh} for reduced annealing durations of 20 and 10 minutes. The corresponding R_{sh} was 211 Ω/□ and 200 Ω/□, respectively. This indicates that annealing for 30 minutes is more than enough for P to diffuse through the whole Ge thickness, and too long such that we observe the effect of out-diffusion. Repetition of the 10-minute SOD process was conducted on the same chip several times to reduce the R_{sh}. R_{sh} values after the second, third, and forth doping repetitions, were 170, 166, and 168 Ω/□, respectively. Although an enhancement of R_{sh} is observed for the first two repetitions, it saturates afterwards to $\sim 170\Omega/\square$. According to conductivity data [162], the maximum doping concentration did not exceed 1×10^{19} cm^{-3}, assuming that P concentration is uniform across the whole thickness of Ge, based on the annealing conditions and the diffusivity of P (fig. 3.2). In spite of the successful doping confirmed by the R_{sh} measurements, the achieved doping level is lower than required for lasing purposes. In fact, we could not observe any photoluminescence signal from group A samples. This low activation level is most probably source-limited, as the dilution reduced the source concentration and the thickness of the SOD film.

3.4.3 Alcohol-Based Solution

Group B samples were coated with Filmtronics P507 dopants, having the same source concentration (C_s) as the solution used above. Manipulating the speed-profile of the spin-coater, a film with good uniformity was obtained, without dilution and consequently maintaining the same C_s. This is expected as the viscosity is low compared to the product used for group A samples. Figure 3.5 shows the effect of the spin-coating acceleration on the uniformity of the film, as observed by optical microscopy. The best uniformity was achieved using 3000 rpm/s acceleration (fig. 3.5 (c)), and is used for all subsequent experiments. Samples were then soft-baked at 120 °C for 15 minutes, and immediately annealed using a furnace at 580 °C for 30 minutes in N_2, similar to group A experiment. In spite of the better coating quality, the Ge layer was completely damaged after annealing, such that R_{sh} could not be measured. The damage was presumably due to SOD layer stresses and the poor adhesion at the Ge-SiO_2 (BOX) interface.

In order to mitigate the stresses during annealing, we have patterned the GOI layer by dry etching Ge micro-disks before the SOD process, as shown in figs. 3.6 (a) and (c). It is expected that thermal stresses could be released in sparse patterned structures, whereas stress relaxation would be difficult in the case of a continuous film without cracking. Then, the SOD layer was coated at 3000 rpm and baked. Annealing was done at 580 °C

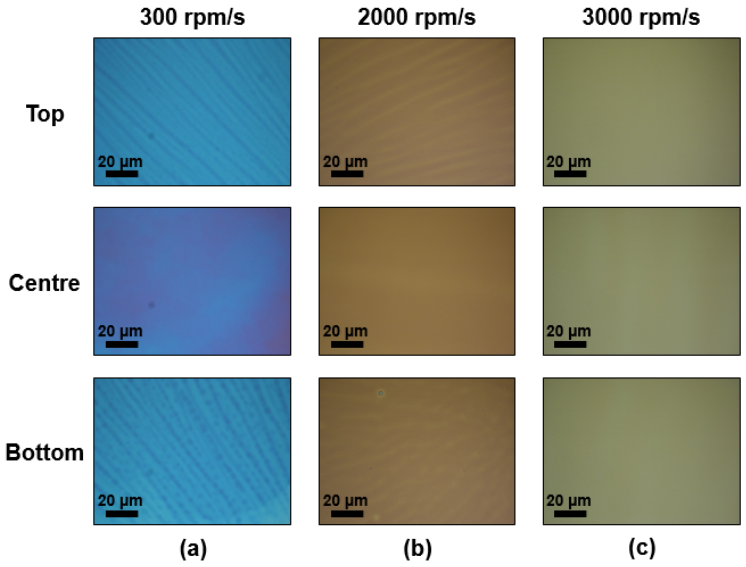

Figure 3.5: The effect of the speed-profile (acceleration) on Filmtronics P507 coating uniformity, with acceleration values chosen as: (a) 300 rpm/s, (b) 2000 rpm/s, and (c) 3000 rpm/s.

in N_2 for 10 and 30 minutes, similar to group A samples. Observing the sample annealed for 10 minutes, gaseous bubbles were dispersed in the SOD layer, whereas this issue was not encountered in the case of 30-minute annealing. These bubbles are most probably due to remnant solvents within the SOD layer, which are still being evaporated during the activation process. This explains not having the same observation with the 30-minute annealed sample, where the longer annealing duration was enough to completely evaporate the solvents and solidify the SOD layer. Figure 3.6 shows optical microscopy images of the 30-minute annealed sample from group B. Figure 3.6 (b) shows that Ge was dissolved in the SOD layer, which clearly demonstrates GOI oxidation during the activation process. Diffusion of oxygen is much faster than P in Ge, as deduced from diffusivity values in fig. 3.2, which imposes a major obstacle on Ge doping. Oxygen is not only in the furnace ambient (although N_2 is purged throughout the process), but also exists in the SOD layer itself. The fact that P is dissolved in the solvent in the form of P_2O_5 nano-powder [108, 156, 157]. Oxidation due to SOD process was confirmed using Silicon-on-Insulator (SOI) wafers, where SOI thickness decreased after the doping process as confirmed by ellipsometry. Upon the SOD layer removal, the Ge patterns were partially peeled off, but some structures survived providing measurable patterns, as shown in fig. 3.6 (d). Although R_{sh} could not be measured as we patterned the Ge layer before applying the spin-on dopant, Raman and photoluminescence (PL) signals were measured and analyzed from the sample annealed for 30 minutes (fig. 3.6 (d)). A maximum doping concentration of 2×10^{19} cm^{-3} was estimated based on the peak position and intensity of the PL spectrum, as shown in section 3.5.2.

3.5 Results and Discussion

Optimizing a reliable SOD recipe for Ge light emission purposes requires overcoming many processing obstacles, because the commercially available products are optimized for Si processing [121]. Si annealing is done at higher temperatures, where the diffusivity of P in Si is lower than in Ge [163, 104]. Additionally, the diffusivity of P in the spin-on dopant film itself, is approximately 3.16×10^{-15} $cm^2.s^{-1}$ at 1000 °C (Filmtronics technical support by email, Feb. 2^{nd}, 2016 [156]). Consequently, the diffusion of P through the SOD film is designed to match annealing temperatures and durations of Si doping, and these conditions are not applicable to Ge, due to the lower melting temperature, and sensitivity to oxygen. Moreover, Si surface is chemically stable with these products, while many issues arise from applying them to Ge, where even soft-baking of some products, like Filmtronics P509 can be an issue, as will be shown later in section 4.4.2. This non-compatibility was related to acidity of the products (Filmtronics technical support by email, Nov. 9^{th}, 2015 [156]), which is suitable for Si surface but not Ge.

Processing obstacles start from obtaining a uniform crack-free coating before annealing, to carefully engineering the annealing process aiming to reduce the effects of out-diffusion and oxidation of Ge. Three main issues can be highlighted: (I) coating a defect-free SOD film with high uniformity is vital for subsequent processing steps. Any defects in this step will be transferred into the target layer during activation, mainly by oxidation. Cracking

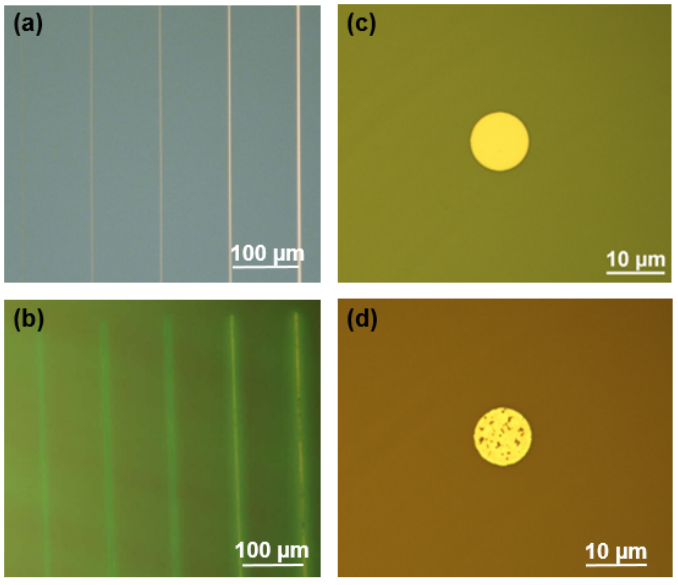

Figure 3.6: Spin-on doped Ge structures from group B samples using Filmtronics P507 and furnace annealing at 580 °C for 30 minutes: Including an array of Ge lines (a) before and (b) after SOD. Image (b) was taken before removing the SOD layer. And a 10 μm Ge micro-disks (c) before and (d) after SOD. Image (d) was taken after removing the SOD layer.

of the dopant layer, which is likely to appear in the case of baking with a fast ramp rate, or due to non-uniformity of coating, will expose Ge to the ambient gas during annealing. This leaves the Ge layer exposed to oxygen, and for temperatures above 450 °C oxidation is likely to occur [108, 104], especially in a furnace chamber with no vacuum applied.

Secondly, (II) The annealing temperature profile, where the diffusion of P in Ge is relatively fast, with oxygen diffusion being even faster. Apart from affecting the diffusion depth, excessive thermal budget will lead to out-diffusion of dopants. Additionally, depleted spin-on dopant layer becomes an oxygen-rich layer, the fact that P exists in the SOD layer as P_2O_5, and any extra annealing time increases the probability of Ge oxidation [121, 108]. This effect is dominant at long annealing durations, where Ge gets consumed by oxidation as shown in fig. 3.6 (b), in which an array of Ge wires is totally consumed by oxidation after 30-minute annealing. This remarks a significant disadvantage of furnace annealing for Ge doping, where the slow ramping rate during the heating up and cooling down of the furnace chamber allows more diffusion and oxidation to occur [108].

Thirdly, (III) thermal stresses affecting the GOI layer that is surrounded with the buried oxide (BOX) and SOD layers, while each layer has a different thermal expansion coefficient. Additionally, SOD layer tends to shrink during annealing due to variations in its contents after the depletion of dopants and solvents evaporation, especially if soft-baking conditions were not sufficient. These thermal stresses are more pronounced in GOI wafers and become more severe for thinner GOI layers, due to poor bonding adhesion between Ge and SiO_2 [100]. To overcome these issues, two approaches were proposed: dilution with IPA, and doping of patterned structures instead of a continuous Ge film. The first approach permits doping GOI easily with minimal damage, however the achieved doping concentration is too low considering Ge light-emission requirements. On the other hand, using the second approach it was possible to dope Ge up to $1 - 2 \times 10^{19}$ cm^{-3} without affecting the crystalline quality, confirmed by Raman and PL data provided below.

3.5.1 Raman Spectroscopy

In this section we investigate the properties of doped Ge micro-disks (Group B samples, fig. 3.6 (d)), relative to intrinsic ones. Namely, crystalline quality and strain values after annealing is our main concern. Raman spectroscopy is used for this purpose, where the intensity, position, and line-width of the Ge Raman peak provides all relevant information. Raman spectrum was measured using a 532-nm laser with a spot size of $\sim$2 μm. A high-resolution grating with 3000 lines/mm groove-density was used to determine the peak position accurately. Laser power at the sample surface and signal accumulation

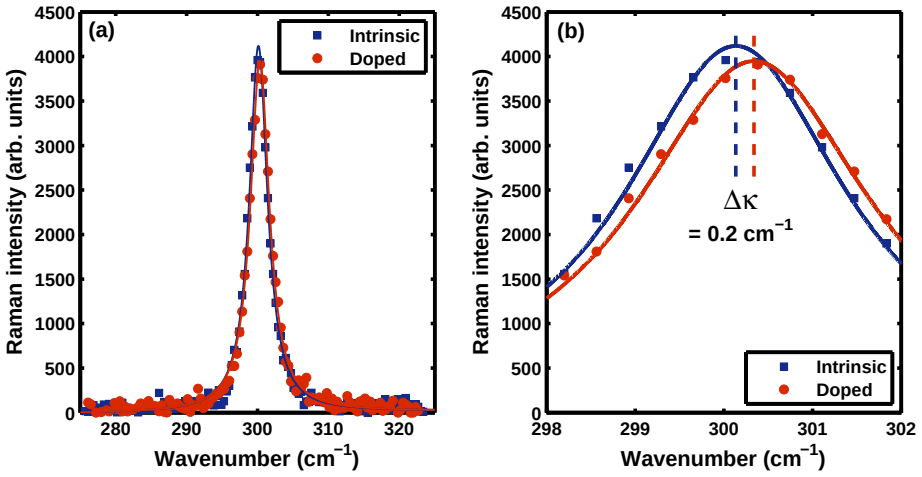

Figure 3.7: Raman spectra of intrinsic (blue) and doped (red) Ge micro-disk, annealed at 580 °C for 30 minutes in nitrogen. Relaxation of tensile stress (Raman blue-shift) is observed after annealing. (a) & (b) Show the same spectra with different x-axis range for a clearer view.

time were set to 275 μW and 5 seconds, respectively. 10 spectra were averaged for each device to enhance the signal-to-noise ratio. Figure 3.7 shows Raman spectra measured at the center of the Ge disk before and after SOD, both figures plot the same spectra with a different range of the x-axis. Experimental data were fitted using Lorentzian functions.

The peak position of the intrinsic Ge disk is at 300.1 cm^{-1}, which indicates accumulation of a slight tensile strain relative to bulk Ge (301 cm^{-1}) [122, 164]. This $\sim$ 0.2% tensile strain is presumably due to Ge growth on Si substrate [16], during the manufacturing process of the GOI wafer by bonding. The peak position of the doped disk dwells at 300.33 cm^{-1}, which is slightly blue-shifted after the thermal treatment at 580 °C for dopants activation. This blue-shift of the Raman peak indicates a slight relaxation of the tensile strain. This is expected especially after thermal annealing [27, 16], especially in patterned micro-structures with relatively free boundaries. Another possible explanation would be the theoretically-predicted lattice compression due to introducing P atoms into the Ge lattice, while other n-type dopants like As and Sb are expected to impose tension [104]. Additionally, the doping-induced change in Raman peak intensity and linewidth is negligible, as seen clearly in fig. 3.7 (b). This implies good crystalline quality of the doped Ge disks, despite the observed voids. The reduction of total excited area due to the voids within the disk might be the reason behind the decrease of Raman intensity.

3.5.2 Photoluminescence Measurements

A study of direct-gap Photoluminescence (PL) was performed to observe the impact of doping. Pumping was done using a 740-nm laser and a 50× objective lens. PL spectra of intrinsic and doped Ge disks are shown in figs. 3.8 (a) & (b), respectively. The PL intensity was remarkably higher in the case of doped disks. Curves colored in red are measured at the same pumping powers for intrinsic (fig. 3.8 (a)) and doped (fig. 3.8 (b)) disks. Approximately, an order-of-magnitude enhancement of PL intensity is observed. This can be explained by the partial filling of L valleys with electrons by doping, increasing the probability of electrons injection into the Γ valleys [32, 99, 109, 165, 106, 166]. Full-Width Half-Maximum (FWHM) linewidths of intrinsic and doped samples were 117 nm and 129 nm, respectively, at 10 mW pumping. Broader line-width after doping is most likely originating from local strain variations due to voids.

The peak position of the doped sample is positioned around ∼1570 nm and is red-shifted by ∼ 5.24 nm relative to the intrinsic sample. This red-shift can not be explained by the relaxation of strain, since a blue-shift is expected according to Raman spectroscopy (fig. 3.7). It is also unlikely to be heat-originated due to laser pumping, because the the peak-position is nearly fixed under different pumping powers. In fact, this red-shift is presumably due to direct band-gap narrowing (BGN) due to doping [106], as have been observed by other groups [99, 109, 106]. Figure 3.9 plots the theoretically-expected narrowing of Ge band-gap due to n and p-type doping [106, 105]. The dashed lines

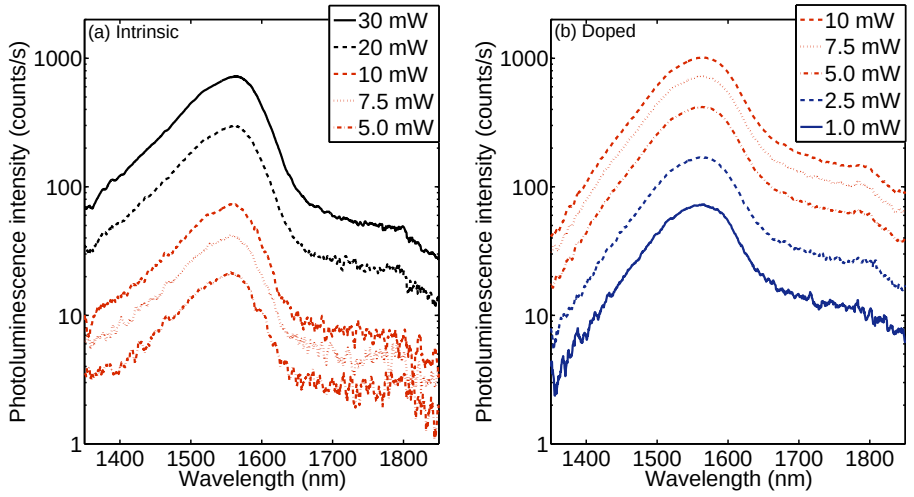

Figure 3.8: Photoluminescence spectra of (a) intrinsic Ge disk and (b) doped Ge disk annealed at 580 °C for 30 minutes in nitrogen. Approximately 10× enhancement of PL intensity is observed due to doping. Broadening of spectra and red-shift were also found, implying carriers or strain non-uniformities (due to voids within the disk) and band gap narrowing.

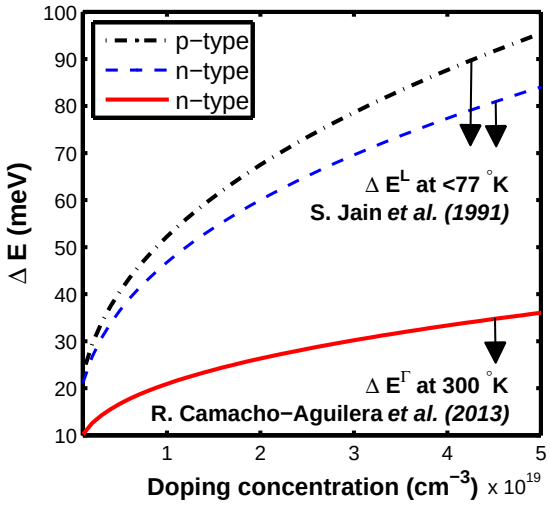

Figure 3.9: Germanium band-gap narrowing (BGN) versus doping concentrations. Dashed lines model the BGN of the L valley at low temperatures [105], while the red solid line calculates minimum BGN of the direct-gap based on ref. [106]. This model works for doping concentrations ranging from 5×10^{18} to 4.5×10^{19} cm^{-3} at room temperature.

correspond to the band-gap narrowing at the L point at low temperatures ($< 77\ ^{\circ}K$) as provided in ref. [105]. The solid red line is the minimum direct-gap narrowing at the Γ point at room temperature, according to equation 2.6. This model has been provided by Camacho-Aguilera *et al.* [106] based on fitting experimental data, and will be used in this discussion. Although some experimental values reported in literature deviate from this model [109], it is fairly accurate considering the red-shift of direct-gap PL peaks reported by several groups [109, 21]. According to this model, the achieved doping concentration in our experiment did not exceed 1×10^{19} cm^{-3}. On the other hand, according to experimental data provided by other groups deviating from this model [99], the doping concentration can be estimated in the range of $1 - 2 \times 10^{19}$ cm^{-3}. However, as the detector cut-off is around 1.6 μm (liquid-nitrogen-cooled InGaAs array) [99], an accurate estimation of doping concentration based on the peak position is unreliable. Comparing the reported PL intensity enhancement factors, a $\sim 10\times$ enhancement of PL intensity is observed due to $\sim 2 \times 10^{19}$ cm^{-3} n-type doping [99, 58, 32]. This agrees with the observed PL intensity enhancement in our experiment. Accordingly, the doping concentration can be estimated to be $1 - 2 \times 10^{19}$ cm^{-3} at maximum.

3.5.3 Excitation-Power Dependence

Studying the dependence of PL intensity on excitation, we observed a change in its behavior from being quadratic ($\propto P^2$) to linear ($\propto P^1$) upon doping. Indicating a better

enhancement of PL intensity with pumping for doped Ge. Figure 3.10 shows the maximum PL intensity versus pumping power (P) for intrinsic and doped Ge disks. The slope of the curve for the doped sample fits to approximately 1 (PL intensity $\propto P^1$). This reflects successful filling of the indirect L valleys in the conduction band by doping, causing a linear increase of the electron-hole pairs population at the direct Γ point by pumping [32, 100, 58]. On the other hand, the slope for the intrinsic sample fits approximately to 2 (PL intensity $\propto P^2$).

This transition in the PL intensity behavior can be understood by considering the steady-state rate equation for the hole density (p) [166].

$$\frac{\partial p}{\partial t} = P - Ap - Bnp \tag{3.6}$$

where A (B) are the non-radiative (radiative) recombination-rate coefficients, and n is the total electron density. We have neglected Auger recombinations in equation 3.6, which are often represented in a separate term in the form of $C_n n(np - n_i^2)$+$C_p p(np - n_i^2)$, or simply Cp^3 at high pumping levels ($n = p \gg n_i$), where C is a coefficient representing Auger recombination rate and n_i is the intrinsic carrier density [46, 103]. Auger recombination is significant in other materials systems, for instance, it is the dominant non-radiative recombination mechanism in InP-based lasers, consuming up to 50% of the threshold current [167]. It is also considered to be one of the main reasons behind the injection-proportional efficiency droop in GaN-based light-emitting devices [167, 168]. The effect of Auger recombination is represented in a higher sensitivity to temperature [169] and degradation of performance at higher pumping levels [168, 169]. However, neglecting Auger recombinations in our case can be justified by the dominant defect-mediated SRH recombinations in Ge ("Ap" term in equation 3.6) [1, 97, 170], in accordance with other theoretical works provided in refs. [1, 97, 170, 100]. Accordingly, γ, the observed PL photon density is

$$\gamma = \beta Bnp \tag{3.7}$$

where β accounts for the extraction efficiency of the detector. Now, considering L-valleys filling in the doped sample with constant doped-electron concentration of $n_\circ$, it is possible to assume that the total electron population is almost constant $n \sim n_\circ$, independent of the pump power ($n_\circ \gg$ photo-induced carriers). Reflecting this assumption on equation 3.6, we get:

$$0 = P - Ap - Bn_\circ p \rightarrow p = \frac{P}{A + Bn_\circ} \tag{3.8}$$

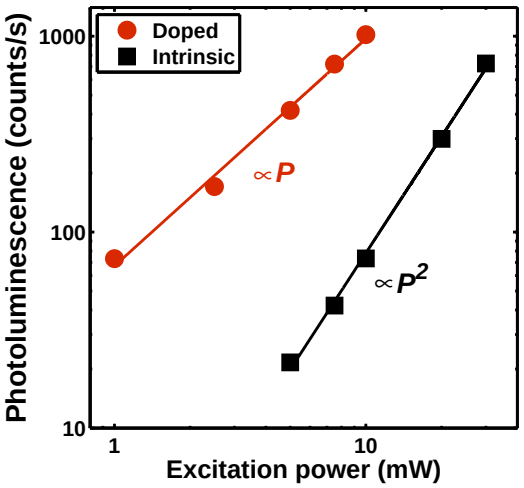

Figure 3.10: The dependence of peak PL intensities on excitation power for intrinsic Ge disk (black) and doped Ge disk (red). The lines are quadratic and linear fits to experimental data.

Where $\frac{\partial p}{\partial t} = 0$ in steady state. Consequently, we obtain a linear power-dependence for the extracted photons density:

$$\gamma = \beta \frac{Bn_0}{A + Bn_0} P \propto P \tag{3.9}$$

Equation 3.12 holes regardless of the magnitudes of A and B, so that the linear dependence can not prove that the radiative recombination dominates over non-radiative processes. The linear dependence of the doped sample is then originating from the linear increase of the hole density by pumping, while the electron density is almost constant. On the other hand, in the case of intrinsic Ge, charge neutrality equates the total electron and hole densities ($n = p$), and assuming dominant non-radiative recombination processes, then the total hole density (p) can be represented in steady state as:

$$0 = P - Ap \rightarrow p = \frac{P}{A} \tag{3.10}$$

and,

$$n = p = \frac{P}{A} \tag{3.11}$$

then,

$$\gamma = \beta \frac{B}{A^2} P^2 \propto P^2 \tag{3.12}$$

Therefore, the product of the photo-induced carrier densities n and p is the reason behind the quadratic dependence, as these densities are linearly dependent on P in the case of intrinsic Ge, assuming a lifetime that is limited by the non-radiative recombinations [1]. The exact enhancement of PL intensity due to doping is then difficult to determine,

the fact that this enhancement is different depending on the pumping power (fig.3.10). Considering linear and quadratic functions, in the region from the limit of zero pumping power ($\mathrm{PL}(P^1) = \mathrm{PL}(P^2) = 0$)), to the point of intersection ($\mathrm{PL}(P^1) = \mathrm{PL}(P^2) \neq 0$), in this region, a linear dependence results in a higher function (PL) value. In other words, doping permits injecting more electrons in the Γ valleys, compared to the intrinsic case, using the same pumping power. Because in the doped case, L valleys are filled allowing more electrons to be injected in the Γ valleys. While in the intrinsic case, initial pumping power is consumed in filling the L valleys, causing a slow (quadratic) increase in electrons population in the Γ valleys. In principle, the intensities of doped and intrinsic samples would eventually be comparable ($\mathrm{PL}(P^1) = \mathrm{PL}(P^2)$, if we excite the samples with the powers high-enough to allow the complete occupation of the L valleys in the intrinsic sample. Our excitation power was not high enough to confirm this, since increasing P above 30 mW (fig. 3.8 (a)) resulted in burning the sample surface. According to these observations, higher doping concentrations are necessary to convert Ge into a gain medium, and achieve population inversion with reasonable threshold.

3.6 Summary

In conclusion, we have examined SOD processes by using two P dopant sources from different suppliers. The study concentrated on comparing water and alcohol-based SOD solutions. It was possible to dope 70-nm-thin Ge layers up to $1 - 2 \times 10^{19}$ cm^{-3} while maintaining the crystalline quality as confirmed by Raman spectroscopy. Up to this point in our research, the exact reason behind this limited activation level was not obvious, especially that the source concentration is more than an order of magnitude higher. This ambiguity is elucidated in the next chapter after eliminating the processing issues, and using two SOD sources with extremely high concentrations. Doping has significantly enhanced the PL intensity, and a change in PL dependence on excitation power was observed from being quadratic (intrinsic) to linear (doped). This observation was explained by the steady-state rate equations for holes density, and indicates that higher doping levels are required for L valleys filling for proper reduction in the population inversion threshold.

We have identified several practical issues for applying commercial SOD products to Ge, which can be summarized in three main points: (I) thermals stresses causing cracking and peeling-off of the Ge layer, (II) Oxidation of Ge during the activation, and (III) limited activation due to the high diffusivity of P in Ge. The proposed solutions to mitigate the first problem include dilution and patterning before applying the SOD layer. Overcoming the oxidation issue requires controlling the gas contents of the annealing chamber, for example, by using rapid-thermal annealing (RTA) instead of furnace. The third issue of fast diffusivity is the main challenge, because it is inherent for P diffusion in Ge. It is vital to overcome the processing issues in order to concentrate on the actual doping levels enhancement and form a better understanding of P doping of Ge. To eliminate such practical challenges, we have proposed using Ge-on-SOI wafers in which a thin Si interface layer between Ge and BOX layers is expected to enhance the adhesion. Using this new stack, and annealing in an RTA chamber, we could reliably dope Ge and form a better idea of P doping limitations and possible solutions, as discussed in the next chapter (chapter 4).

Chapter 4

Optimization of Spin-on Doping using Rapid-Thermal Annealing

"Since the bronze age, early engineers have learned not to accept materials as they are in nature and tinker with them to improve their properties. In the previous century, humans engineered electrical properties of semiconductors by doping, triggering the transistor revolution "

As concluded from:
Photonic Crystals - Modelling the flow of light, Ch. 1, 2nd ed., 2007,
by J. D. Joannopoulos et al.

4.1 Introduction

After the preliminary doping experiments presented in chapter 3, a new wafer stack is used to eliminate the practical issues of Ge film cracking and peeling-off. Rapid-thermal annealing (RTA) is used instead of furnace annealing for multiple reasons as discussed in section 4.2, such as controlling the gas contents in the annealing chamber. In addition to investigating another activation approach of higher-temperature annealing for short durations, as proposed in literature to enhance the doping levels of P [104, 102]. Higher temperatures are also required to efficiently extract the impurity atoms out of the SOD film. In this study we use two Filmtronics products with different source concentrations. A reliable doping recipe with minimal Ge surface damage is developed resulting in up to $\sim 2.5 \times 10^{19}$ cm^{-3} active P concentration. However, this doping level remained the same although a 4× higher source concentration was used (20×10^{20} cm^{-3}). This limited doping concentration is often attributed to the limited source of impurity atoms in the case of SOD [159, 58, 32, 108, 2]. The work in this chapter favors another opinion, attributing the limited doping level to the diffusion mechanism of P in Ge, causing P to diffuse fast through the Ge lattice without being activated [102].

4.2 High-Temperature Short-Duration Annealing

The first experimental approach on Ge doping using the furnace - presented in chapter 3 - relied on relatively low temperatures (580 °C) and long durations up to 30 minutes. Although P is known to have its highest solubility around 580 °C [32], the maximum achieved doping concentration was not higher than 2×10^{19} cm^{-3}. This limit of active P doping of 2×10^{19} cm^{-3} was observed by several groups using SOD [58, 32, 108, 121, 2]. Some of these studies relied on furnace annealing at temperatures ranging from 580 °C [108, 121, 2] to 700 °C [108], for up to 10 minutes [108, 121, 2]. Other studies moved to higher temperatures $>$ 700 °C for up to 5 minutes using rapid-thermal annealing (RTA) [58, 32]. Regardless of the activation profile, the doping concentration was limited to nearly the same level. Secondary-ion-mass spectroscopy (SIMS) shows a limit around 4×10^{19} cm^{-3} [108, 121], while measurements based on electrical activation report a limit around 2×10^{19} cm^{-3} [58, 32, 2].

In theory, it is predicted that high-temperature annealing for short durations is the solution to increase P doping levels in Ge [104, 102]. The fact that P is found to diffuse through a doubly-negatively charged vacancy mechanism (V^{-2}) [104, 102]. This mechanism is the reason behind the extremely-high diffusivity of P in Ge, and consequently the low incorporation of P atoms within the Ge lattice, hence, the limited electrical activation [104, 102]. In fact, this mechanism is initiated for high source concentrations as demonstrated by Matsumoto *et al.* [110] (and observed in multiple experiments [155, 108, 101, 102]), where a transition of the diffusion profile is reported from being a standard *erfc* function into a box-shaped profile by increasing the source concentration

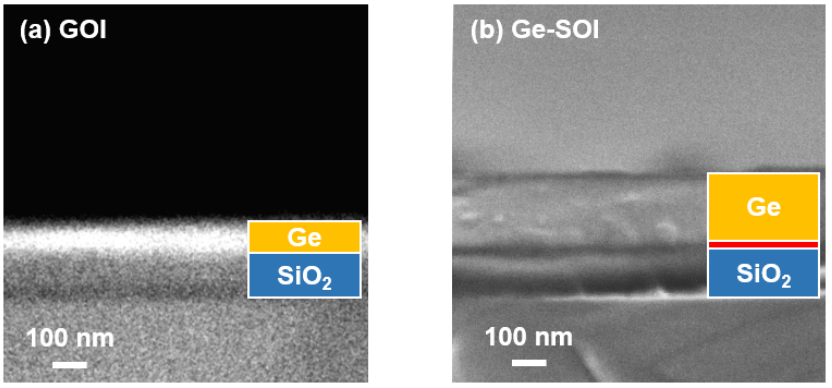

Figure 4.1: Cross-sectional SEM images of (a) GOI wafer with 100-nm-thick Ge, and (b) Ge-on-SOI wafer with 200-nm Ge and 20-nm SOI. Buried-oxide thickness is the same in both wafers (145 nm). The GOI wafer is better in terms of applicable strain by BOX suspension due to thinner Ge (chapter. 5), however very fragile for doping. While the Ge-on-SOI wafer is suitable for doping, yet has a degraded optical performance due to the lower applicable strain by BOX, and high-defect-density Ge-Si interface.

from $C_s = 3-7\times10^{18}$ cm^{-3} to $C_s = 5-8\times10^{19}$ cm^{-3}. This transformation into a box-shaped profile indicates a source-dependent transition in the diffusion mechanism, where the extremely-high diffusivity results in a limited activation. Solutions proposed in theoretical works [104, 102] include flash or laser annealing [120], by using high temperatures for extremely short durations, or co-doping by introducing two different types of impurities simultaneously to mitigate the diffusivity and increase activation [112, 104, 102]. Another possible solution, which is proposed in this thesis for future work (section 7.2.1), is introducing Si atoms to enhance the solubility of P and decrease the diffusivity. Activation levels above 1×10^{20} cm^{-3} have been achieved in Si within this project using SOD (section 4.5). Hence, it is expected that the doping levels within Si_xGe_{1-x} alloys will increase by increasing the Si content (x), gradually moving from the 2×10^{19} cm^{-3} in Ge to $> 1\times10^{20}$ cm^{-3} in Si. Ideally, Ge contents in the Si_xGe_{1-x} alloy has to be as high as possible, where the optical properties of Ge-rich Si_xGe_{1-x} alloys have to be investigated.

In this chapter, RTA is used for high-temperature short-duration processing in an ambient-controlled chamber, moving the activation profile closer to the proposed *flash* annealing conditions [102]. Unlike the previously-reported RTA approach of several-minute annealing time with temperatures around 700 °C [58, 32], higher temperatures up to 900 °C, just below the melting point of Ge, and annealing durations down to 5 seconds are investigated in this chapter. Such temperatures also aid the extraction of more P atoms from the SOD solution, especially that the formation of SiO_2 is expected within the SOD film during activation, impeding the extraction of P. The diffusivity of P atoms within Filmtronics SOD solutions (P507 & P509, table 4.1) is around 3.16×10^{-15} cm^2/s at 1000 °C (Filmtronics technical support by email, Feb. 2nd, 2016 [156]). This indicates that P atoms diffuse with orders-of-magnitude higher diffusivity in Ge compared to the SOD film.

A new wafer stack will be used in this chapter, utilizing a thin Si (SOI) layer to enhance the adhesion between Ge and BOX. The fact that, the previously-used stack with 100-nm GOI has not survived annealing with high ramping rates. In fact, even gentle annealing conditions caused peeling-off of some parts of the Ge structures (fig. 3.6). The new Ge-on-SOI stack consists of 200-nm Ge on 20-nm SOI, and 145-nm BOX (fig. 4.1 (b)). Some disadvantages of this new stack include the high interface-defect density between Si and Ge, degrading the optical performance. In addition to the degradation of achievable strain compared to the initial GOI stack - as shown in section 5.8 -, and the formation of Si_xGe_{1-x} alloys at the Ge-SOI interface after the high-temperature activation (fig. 4.7). However, as will be shown later in this chapter, most of the SOD-related practical issues were overcome using this stack, and a reliable doping recipe with minimal surface damage was developed. A maximum active doping concentration of 2.4×10^{19} cm^{-3} was confirmed by sheet-resistance (R_{sh}) measurements.

4.3 Reference Processing on Silicon

SOD of Si using RTA is done as a reference case to establish a reliable doping process, and compare the behavior of Ge relative to Si. Commercial SOD products are optimized for Si processing [121, 2], in terms of the processing temperatures (typically 1000 °C according to products sheets) and surface compatibility. Based on the outcomes of the comparative study conducted in chapter 3, alcohol-based solutions provided by Filmtronics are to be used in our experiments. Two products are chosen as listed in table 4.1 with different source concentration of P atoms, as found in refs. [158, 108].

Filmtronics Dopants	**P507**	**P509**
Source Concentration	$5 \times 10^{20}\text{cm}^{-3}$	$20 \times 10^{20}\text{cm}^{-3}$

Table 4.1: Phosphorus concentration in Filmtronics products [158, 108]

Experimental work was conducted on Si chips diced from a 6" wafer and cleaned using 20:1 buffered HF to remove the native oxide, and then coated with P507 and P509 SOD layers. Spin-coating was done at 3000 rpm, followed by baking at 165 °C for 30 minutes to ensure the evaporation of solvents. A cap layer of 50-nm SiO_2 was deposited using PECVD at 350 °C to minimize the out-diffusion of P into the RTA chamber [104, 58]. Afterwards, activation was done at different temperatures and durations as shown in fig. 4.2. Figure 4.2 (a) plots the R_{sh} values measured from P507 and P509-doped samples, annealed at 950 °C for 1, 2, 3, and 4 minutes. While fig. 4.2 (b) plots the R_{sh} values for two-minute annealing at $850, 900, 925$, and 950 °C. Although the doping concentration can not be estimated without knowing the exact diffusion profile and depth, the R_{sh} tends to decrease with increasing the diffusion force ($\sqrt{D_P t}$ [104]) consistently [104, 108]. Increasing the diffusion temperature, and consequently increasing the diffusivity D_P, or increasing the diffusion time (t), results in lower R_{sh}. A minimum R_{sh} of approximately 5 Ω/□ was achieved by annealing P509 film on Si at 950 °C for 4 minutes. This decrease in R_{sh} originates from the larger diffusion depth into the wafer [152].

From processing point of view, SOD of Si is much simpler than Ge. An issue to be mentioned, is the formation of etch-resistant particles on the surface of Si upon activation. By examining the Si surface after each processing step, this issue was related to the use of PECVD SiO_2 cap layer. Especially if the baking conditions before annealing were not hard enough to drive all the solvents out. The association of these particles with the SiO_2 cap layer is not understood yet, but they are absent in the case of annealing without a cap layer. Hard baking of the SOD layer before activation using the furnace at 430 °C for an hour can also be used to prevent the formation of such particles. Using flowable oxide (FOx) or HSQ as a cap layer are also possible solutions.

4.4 Germanium Spin-on Doping using RTA

After initializing a reliable doping process on Si using RTA, we applied the same recipes on Ge. Ge was found to react differently to P507 and P509, compared to Si. Doping process of Ge using P507 is generally stable with less practical issues compared to P509. Detailed discussion of the processing, activation conditions, and results is provided below.

4.4.1 Filmtronics P507

Experimental work was conducted on Ge-on-SOI chips, with 200-nm Ge / 20-nm SOI / 145-nm BOX (fig. 4.1 (b)). Doping solution was left to stabilize at room temperature overnight, then coating was done following the process described in section 3.4.3. Coating speed is fixed at 3000 rpm for all experiments, and baking was done at 165 °C for 30 minutes. Baking is an essential step to get rid of all solvents in the SOD layer before activation. No cap layer was used in order to avoid the formation of the particles discussed earlier (section 4.3). Annealing was done at temperatures ranging from 650 - 900 °C and durations between 5 and 300 seconds. Then the SOD layer was removed using 20:1 BHF for 6 minutes. A clean crack-free Ge layer was successfully maintained as shown in fig. 4.3. Figure 4.3 (a) shows the heavily-doped (2.4×10^{19} cm^{-3}) Ge layer after the SOD layer removal, with the inset sketching the wafer stack. Figure 4.3 (b) shows a heavily-doped Ge micro-disk fabricated using this wafer. The annealing conditions for the chip in fig. 4.3 were 700 °C for 15 seconds. The surface condition and the doping level of this micro-disk is significantly better than the previously achieved one using the furnace and GOI wafers (fig. 3.6). It is worth mentioning that even though Ge surface was in a good condition, oxidation of Ge due to oxygen atoms in the SOD

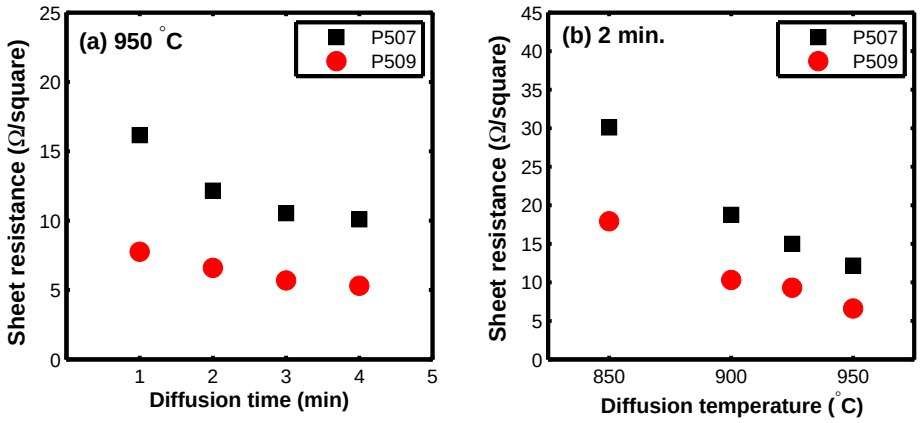

Figure 4.2: Sheet resistance R_{sh} values of spin-on doped bulk Si wafers using Filmtronics P507 and P509: (a) R_{sh} dependence on annealing time at 950 °C, and (b) R_{sh} dependence on annealing temperature for 2 minutes.

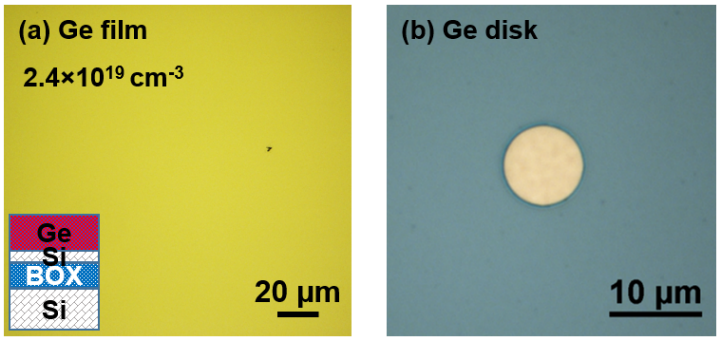

Figure 4.3: Optical microscopy images of a heavily-doped (a) Ge film and (b) Ge micro-disk using Filmtronics P507: (a) 2.4×10^{19} cm^{-3} doped Ge film, inset shows the Ge-on-SOI stack. (b) Shows a heavily-doped Ge micro-disk with good surface quality. The e-beam resist (HSQ) is still on top. The annealing conditions were 700 °C for 15 seconds.

film was confirmed by measuring the thickness of Ge using ellipsometry. For instance, annealing at 750 (800) °C for 5 seconds resulted in thinning down the Ge layer to 173 (160) nm. This favors avoiding extremely high temperatures or too-long durations [58].

Annealing of the Ge-on-SOI wafers was done at different temperatures and durations, aiming to find the optimum activation condition. The annealing process starts with multiple cycles of purging the chamber with N_2 gas at a flow rate of 2000 sccm for few seconds then evacuating the chamber to vacuum level. Afterwards, N_2 is purged continuously with the same rate until the end of the process. This ensures a dominant nitrogen ambient in the chamber, to reduce any probable oxidation by atmospheric oxygen. The temperature profile is ramped to the target annealing temperature in two steps, starting with an initial ramp to 400 °C at 25 °C/second [121]. The chamber is left at this temperature for 30 seconds to stabilize, then the final ramp is done with the same rate. This profile has been optimized after several experiments, and it is fixed for all RTA SOD processes. Figures 4.4 (a) and (b) show the resulting R_{sh} values for different annealing conditions. Each R_{sh} value is an average of three experimental values, measured at different positions on the doped chip. Figure 4.4 (a) presents the dependence of R_{sh} values on the annealing time for 650 and 700 °C. It is found that there is an optimum annealing time at each temperature resulting in the lowest R_{sh} , or highest activation level. This optimum annealing time is shorter for higher annealing temperatures, for instance, the lowest R_{sh} values of approximately $56 - 59\ \Omega/\square$ were obtained by 15 seconds and 100 seconds annealing at 700 and 650 °C, respectively. The maximum resulting doping concentration was estimated to be 2.4×10^{19} cm^{-3} [162], assuming a uniform doping profile across the Ge thickness (178 nm after 700 °C for 15 seconds). This agrees with the basic understanding of diffusion processes, where the diffusion coefficient increases with temperature, requiring less time for P atoms to diffuse through the same thickness.

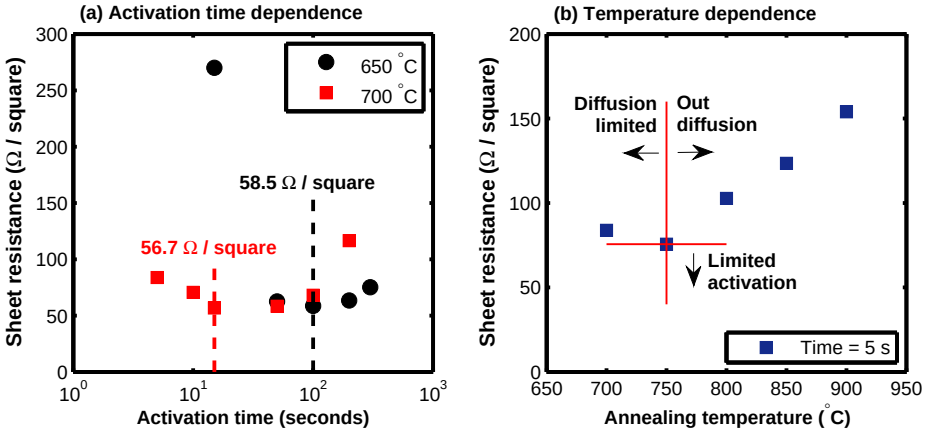

Figure 4.4: Ge sheet resistance (R_{sh}) dependence on RTA activation conditions using Filmtronics P507: (a) the effect of activation duration, showing the minimum R_{sh} occurring at shorter times for higher annealing temperatures. (b) The effect of activation temperature, indicating three regions of diffusion-limited R_{sh} , out-diffusion-limited R_{sh} , and limited-activation of dopants. This behavior also applies to data points in (a). Each value in these figures is an average of three experimental values.

The tendency of R_{sh} to increase before and after the optimum annealing time, splits the curve into two main regions: for annealing times shorter than the optimum, the sheet resistance is diffusion-limited, where the diffusion force ($\sqrt{DPt}$ [104]) is not enough for P to diffuse through the Ge thickness. At the minimum R_{sh} value, the annealing duration is sufficient for P to diffuse through the whole layer, resulting in the minimum R_{sh}. Approximately, the minimum R_{sh} point occurs within 15 - 50 seconds annealing at 700 °C (fig. 4.4 (a)), indicating an extremely-high diffusivity of P. Assuming a uniform diffusion across the whole Ge thickness (∼170 nm by ellipsometry) after 50 second annealing, the diffusion coefficient can be calculated as $\sim 3 \times 10^{-12}$ cm^2/s using the equation $t \simeq \frac{x_d^2}{2D_P}$ [153]. Where t is the diffusion time, x_d is the mean diffusion depth [153], and D_P is the diffusivity of P in Ge. This value agrees to a good extent with values reported in literature [171, 155] (fig. 3.2 (b)). While for longer annealing times, out-diffusion starts to dominate the R_{sh} behavior, especially that the SOD source of impurity atoms is finite. SIMS data available in literature [123] provides an evidence of P atoms accumulation at the top and bottom Ge interfaces by out-diffusion.

Figure 4.4 (b) shows the dependence of R_{sh} values on the annealing temperature, for a fixed activation time of 5 seconds. The behavior of the R_{sh} curve against temperature is similar to its behavior against time, as shown in fig. 4.4 (a). Initially, increasing the diffusion force ($\sqrt{DPt}$) by increasing the temperature from 700 °C to 750 °C, and consequently increasing the diffusion depth of P, results in decreasing the R_{sh}. A minimum R_{sh} value of 75 Ω/□ is measured at 750 °C for 5-second annealing. Afterwards,

R_{sh} tends to increase again, as a sign of out-diffusion due to the excessive diffusion force.

According to data in figs. 4.4 (a) and (b), a limit on the minimum R_{sh} value exists, reflecting a limited doping concentration. The achieved doping concentration is consistent with the work of other groups [108, 58, 32, 121]. This limit is imposed by the high diffusivity of P in Ge, as a consequence of the source-dependent diffusivity and diffusion mechanism [104, 102, 154]. Up to this point, there is a doubt wither this limited achievable doping concentration using SOD is simply source-limited [159, 58, 32, 2, 108], or there is an actual limit impose by the diffusion mechanism regardless of the source concentration. In the case of a source-limited activation, the minimum achievable R_{sh} value corresponds to the maximum amount of P atoms extracted from the SOD film, and driven into the Ge film. In order to form a better understanding of the limited P concentration in Ge, a higher source concentration was used in the next section.

4.4.2 Higher Source Concentration: Filmtronics P509

Aiming to investigate whether the activation levels are source limited, a higher source concentration was used. P509 SOD solution provided by Filmtronics is a suitable option for such purpose, containing P atoms with a concentration of 20×10^{20} cm^{-3}, four times higher than P507 [108]. Ge doping using P509 has required innovating new processing ideas to overcome serious compatibility issues. Although P509 works smoothly with Si, and very low sheet resistances down to 5 $\Omega/\square$ were obtained, a lot of processing obstacles emerged when applying it to Ge. Such problems were not encountered with P507.

Coating P509 on Ge immediately as shown in fig. 4.5 (a), baking it, and then annealing results in a severely damaged surface as shown in fig. 4.5 (b). The exact nature of the damaged surface is not known, but it is comparable to burnt polymer particles. In order to determine the reason behind this problem, a comparative study was conducted by applying P509 on Ge-on-SOI wafers and bulk Si, and carefully observing the surface state of each wafer after each processing step. It was found that the P509 SOD layer on Ge was not hard-baked even after an hour baking using hotplate at 165 °C. This can be observed by eye due to the transparent color of the SOD coating, while on Si, the SOD layer starts to solidify forming a silver-colored layer after 10 - 15 minutes. We tried increasing the baking temperature and time. Extreme baking conditions using the furnace at 400 °C for 1 hour have also failed solidifying the P509 layer on Ge, and annealing afterwards resulted in a damaged Ge surface as shown in fig. 4.5 (b). Contacting the technical support of the provider (Filmtronics) by email, they suggested that the acidity of the solution is most likely to cause this problem when coated on Ge, the fact that it was optimized for Si processing (Filmtronics technical support by email, Feb. 2nd,

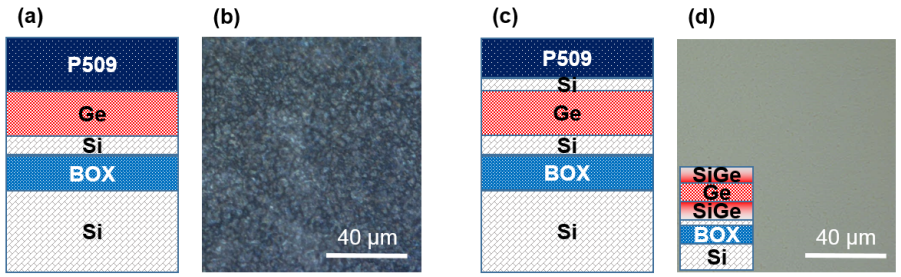

Figure 4.5: Optical microscopy images of P509-doped Ge films before (a)&(b) and after (c)&(d) applying a Si interface layer: (a) shows the stack when applying P509 directly and (b) shows the resulting surface after annealing at 850 °C for 6 minutes. (c) shows the stack when applying P509 using a Si interface layer and (d) shows the resulting surface after annealing at 850 °C for 6 minutes. Inset in (d) shows the expected stack after annealing and the formation of Si_xGe_{1-x} alloys at Ge interfaces.

2016 [156]). Accordingly, a compatibility issue is causing this problem, and no matter the baking conditions, the product (P509) in its current state could not be solidified on Ge. To mitigate these issues, we proposed using a thin Si interface layer between Ge and P509, as sketched in fig. 4.5 (c). This layer was efficient as an interface, permitting doping using P509 and resulting in a high-quality Ge surface after annealing. The details of this Si layer and its consequences on processing are discussed in the following section.

4.4.2.1 Thin Si Interface Layer to Overcome Compatibility Issues

A reliable thin Si interface layer is required to overcome compatibility issues between the P509 SOD layer and Ge. As the crystalline quality of this Si layer is irrelevant as long as it provides a reliable interface, amorphous Si (a-Si) deposition using PECVD was used. Adding this layer requires applying higher temperatures, to allow for P diffusion through the thin Si interface, because the diffusivity of P in Si is significantly lower than Ge [163, 104, 172, 173]. Temperatures above 900 °C are proposed for Si processing by SOD-solution specifications sheet [156]. As such temperatures are too high for Ge processing, especially for few-minute annealing durations, $800 - 850$ °C will be used. The formation of Si_xGe_{1-x} alloys is expected at the top (due to a-Si layer) and bottom (due to SOI layer) interfaces of the Ge film, due to Si and Ge inter-diffusivity at high temperatures. Yet, applying such high temperatures allow for more extraction of P atoms from the SOD film. So, this layer has to be thin enough to keep the annealing conditions suitable for Ge, and thick enough to provide a reliable interface, permitting the solidification of the P509 solution. Being thin reduces the required annealing time for P atoms to diffuse through it into Ge. It also reduces the effect of Si-Ge inter-diffusion because a thinner a-Si layer results in a lower x value in the Si_xGe_{1-x} alloy. For instance, if Ge thickness is 200 nm, and the top (PECVD a-Si) and bottom (SOI) Si layers are 10

and 20 nm, respectively, and a complete inter-diffusion occurs during annealing, then a $Si_{0.15}Ge_{0.85}$ layer is expected to form. In reality, the diffusion time is insufficient for a complete inter-diffusion, as the diffusivity of Si in Ge is much less than that of P (fig. 3.2).

The recipe used to deposit a-Si layers on Ge is shown in table A.2. It was modified from an existing recipe that is used for a-Si deposition on Si using PECVD. Layers down to the thickness of 8 nm were deposited without any optically-observable voids. When P509 is coated on >8-nm-thick a-Si on Ge, it solidifies within 10 to 15-minute baking at 165 °C and transforms into a silver-colored layer, similar to being coated on bulk Si. Such thicknesses were enough to provide a reliable interface layer, and dope Ge using P509 with minimal surface damage, as shown in fig. 4.5 (d). For thinner films of 5 nm thickness, baking of the P509 film and doping was successful as confirmed by the low R_{sh} values, however surface damage was severe and optically observable. Proof-of-concept experiments were done on Ge-on-Si wafers using 10-nm-thick a-Si interface layers, and R_{sh} values down to 14 Ω/□ were measured, yet the exact doping concentration within Ge can not be determined due to the Ge-Si stack, and ambiguity of the diffusion profile. In order to accurately estimate the doping concentration, Ge-on-SOI wafers (used with P507) were doped using the same technique as discussed below.

4.4.2.2 Ge-on-SOI Doping with 10-nm Si Interface Layer

After establishing a reliable a-Si interface layer between Ge and P509 solution, the same experiment was conducted on Ge-on-SOI wafers. Ge-on-SOI wafer has the same stack used before with P507 solution, consisting of 200-nm Ge on 20-nm SOI and 145-nm BOX. This way we can roughly estimate the doping concentration by assuming a uniform doping profile across the Ge thickness. This assumption is valid based on the annealing conditions (850 °C for few minutes), which are more than enough for P to diffuse through the a-Si and Ge layers. After cleaning the samples, a 10-nm a-Si interface layer was deposited using PECVD process shown in table A.2. Coating was then done using P509 solution at 3000 rpm and baked at 165 °C for 30 minutes. Solidification of the P509 layer was recognizable by optical observation, due to the change of the film color. Diffusion and activation of dopants was then done at 850 °C for 2, 6, and 10 minutes, justified by the required time for P to diffuse through the a-Si based on the diffusivity values described in the next section. The remaining glass layer was removed afterwards using 20:1 BHF for 6 minutes, and the remaining a-Si was etched using TMAH for 2 minutes. The R_{sh} values were nearly fixed around 90 Ω/□ as shown in fig. 4.6. The corresponding doping concentration does not exceed $\sim 1.5 \times 10^{19}$ cm^{-3}, given that the remaining Ge thickness is ∼160 nm. A similar doping concentration was confirmed by doping another Ge-on-SOI wafer with thicker Ge using the same technique.

4.5 Results and Discussion

Even though compatibility issues between Ge and P509 were overcome using a thin a-Si interface layer, a modest doping concentration was achieved, comparable with previously achieved concentration using P507, the lower-concentration source. This indicates that the limiting factor of the maximum doping level of P in Ge is not the source concentration, as initially suspected [58, 32, 108, 159]. In order to confirm this, doping of SOI wafers using P509 was done to estimate the total concentration of impurity atoms extracted from the SOD film and diffused into the wafer. SOI layer thickness was around 300 nm, and annealing was done at 850 °C for 2, 6, and 10 minutes, similar to the annealing conditions used for Ge-on-SOI. The resulting R_{sh} values are also summarized in fig. 4.6, alongside R_{sh} values of the Ge-on-SOI wafers. Each point in fig. 4.6 is an average of three experimental values. The results are consistent and fairly reproducible, for instance, the data points for Ge can be written as ∼88±2, 102±1, and 95±1 Ω/□ for 2, 6, and 10 minutes annealing. While the corresponding values for the Si sample are ∼ 91±7, 38±1, and 26±2 Ω/□, respectively. A remarkable difference of the R_{sh} dependence on annealing time can be spotted between Si and Ge. Where increasing the annealing time corresponds to a reduction in the R_{sh} value in Si, while it nearly has no effect in this annealing-duration range for Ge. This difference in R_{sh} behavior can be related to the difference in the diffusivity and diffusion mechanism, as the source concentration is similar in both cases [104, 172]. For instance, such annealing times are sufficient for P atoms to diffuse across the whole Ge thickness, while this is not the case for Si resulting in lower R_{sh} values due to the increase in diffusion depth with time.

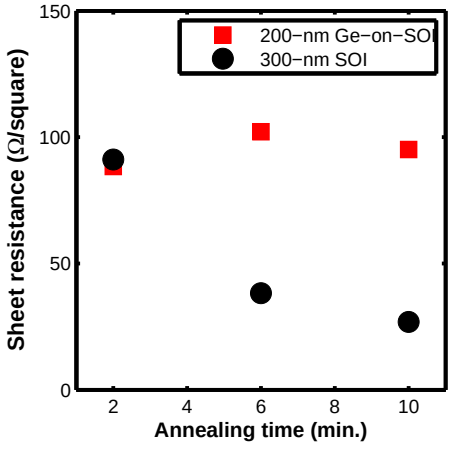

Figure 4.6: Sheet resistance (R_{sh}) values for Ge-on-SOI (with a-Si interface layer) and SOI wafers doped at 850 °C using Filmtronics P509. Estimated doping concentrations in the SOI wafer is around $\sim 1 \times 10^{20}$ cm^{-3} based on the highest reported diffusivity value, indicating that the activation in Ge is not limited by the source.

In order to estimate the doping concentration in the SOI wafers, a rough estimation of diffusion depth was done by using the formula $t \simeq \frac{x_d^2}{2D_{P,Si}}$ [153]. The diffusivity of P in Si ($D_{P,Si}$) at 850 °C is $\sim 2 \times 10^{-16}, 2 \times 10^{-15}$, and 3×10^{-13} cm^2/s, for source concentrations in the order of $10^{19}, 10^{20}$, and 10^{21} cm^{-3}, respectively [163]. The last value of $D_{P,Si}$ was used to estimate the mean diffusion depth (x_d), as it matches the source concentration and results in the lowest estimation of doping concentration (highest mean diffusion depth (x_d)) for a certain R_{sh} value. R_{sh}values were measured experimentally using a four-point probe [161]. Doping concentration (C_{doping}) values were extracted from resistivity-concentration tables provided in literature [174, 175]. Table 4.2 lists the values of diffusion depth (x_d), doping concentration (C_{doping}) and dose (S_{dose}) in cm^{-2}, for the three SOI chips processed with different activation times. It was found that the total dose is in the order of $\sim 10^{15}$ cm^{-2}, and the total concentration of P atoms extracted from the SOD layer and diffused into the wafer is around $\sim 1 \times 10^{20}$ cm^{-3}, using P509. Even if we assume a total diffusion of P atoms through the 300-nm-thick SOI layer after 10 minutes annealing, the doping concentration is approximately 9.7×10^{19} cm^{-3} based on an R_{sh} value of 26 Ω/□. This confirms that the limited doping levels of P in Ge are not source limited in the case of SOD.

Activation		x_d	$R_{sh}^{(a)}$	$C_{doping}^{(b)}$	**Dose (S_{dose})**
Temp.	Time	(nm)	(Ω/□)	(cm^{-3})	(cm^{-2})
850 °C	2 min.	84	94	9.6×10^{19}	8.0×10^{14}
	6 min.	146	38	1.44×10^{20}	2.1×10^{15}
	10 min.	189	26	1.6×10^{20}	3.0×10^{15}

Table 4.2: Total phosphorus dose estimation using P509 spin-on dopants on SOI wafers
(a) Each R_{sh} value is an average of three experimental values.
(b) C_{doping} extracted from tables in refs. [174, 175].

This limited doping level of P in Ge is often related to extremely-high diffusivity originating from its diffusion mechanism, which is mainly driven by a doubly-negatively-charged vacancy (V^{-2}) [104, 102]. The fast diffusion of P impedes the incorporation of its atoms into the Ge lattice, resulting in a box-shaped diffusion profile with an upper limit of the achievable doping [110, 108, 102]. This causes the accumulation of P atoms at the top and bottom interfaces of Ge layer by out-diffusion [123]. This issue can be overcome by non-equilibrium doping by several ion-implantation cycles [102], or MBE δ-doping [5]. Co-doping of P and other atoms such as As or Sb is another possible solution [104, 102]. It is also expected that flash or laser annealing with high-power short-duration pulses might mitigate this issue [102, 120, 99].

4.5.1 Raman Spectroscopy and Photoluminescence

In conclusion, similar active doping concentrations were achieved using P507 and P509 SOD solutions, with a much simpler and more reliable process in the case of P507. A better understanding of Ge quality and the effect of P507 doping can be formed through Raman spectroscopy and Photoluminescence (PL). Figure 4.7 shows Raman and PL spectra of a Ge-on-SOI sample doped using P507 at the optimum conditions of 700 °C for 15 seconds, with an estimated active doping of 2.4×10^{19} cm^{-3} (fig. 4.3). Excitation was done using a green laser for both tests, and a power of 550 μW and 2.5 mW was used for Raman and PL, respectively. Raman signal was accumulated for 10 s and averaged for 10 times, using a 50× lens and a 3000-lines/mm grating. Characterization using Raman spectroscopy confirms maintaining good crystalline quality, as the line-width has not degraded after the doping process. The Raman peak properties relative to the original peak before doping is not shown as it is similar to previous results in fig. 3.7. A new observation in the Raman spectrum is the Si_xGe_{1-x} peak at 396.9 cm^{-1}, which results from the Si-Ge inter-diffusion at the Ge-SOI (bear in mind that a-Si cap was not used in the P507 doping process, and it is expected to contribute to Si_xGe_{1-x} formation in samples doped with P509). If a linear interpolation is assumed from Ge Raman peak (301 cm^{-1}) to Si (521 cm^{-1}), then this peak corresponds to approximately $Si_{0.4}Ge_{0.6}$. This peak is also observed in the PL spectrum around 1480 nm. The PL spectrum from intrinsic Ge-on-SOI films was undetectable using the same exposure conditions, indicating a significant enhancement of direct-gap emission from the doped sample. The

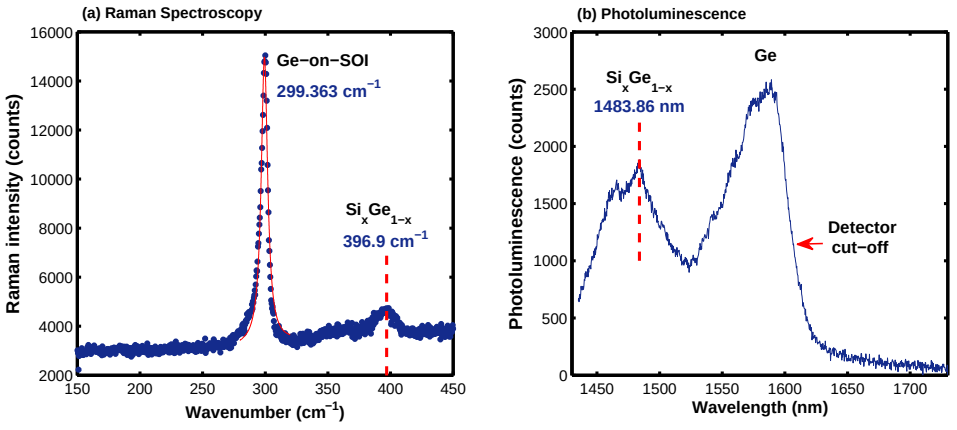

Figure 4.7: (a) Raman spectroscopy and (b) photoluminescence spectra of a heavily-doped Ge-on-SOI micro-disk using Filmtronics P507 (fig. 4.3): Raman spectrum indicates a good crystalline quality based on the line-width which is comparable with the initial wafer before doping (not shown, presented previously in fig. 3.7). It also shows the formation of Si_xGe_{1-x} alloys at the Ge- a-Si and Ge-SOI interfaces. PL spectrum shows a significant enhancement of direct-gap emission intensity as the spectrum of intrinsic samples was undetectable using the same conditions. The Si_xGe_{1-x} peak is also captured in the PL spectrum with a relatively high intensity.

signal was accumulated for 2 minutes using a fiber-coupled microscope set-up and a 150 lines/mm grating. The Si_xGe_{1-x} peak appears to have a relatively high intensity relative to Ge, especially that the initial Ge layer is 200-nm thick, while the SOI layer is only 20 nm, and is further away from the excitation surface.

4.6 Summary

In this chapter we have demonstrated a reliable Ge n-type doping recipe for up to 2.4×10^{19} cm^{-3} active doping concentration. Previous problems of surface damage and peeling-off of Ge were overcome. This was done using a new wafer stack of Ge-on-SOI instead of the previously used GOI (chapter 3) for a better adhesion between Ge and BOX layers, with Filmtronics P507 SOD solution as the dopant source, and using a high-temperature short-duration RTA process. Repeating the recipe with a higher source-concentration (P509) was done in order to increase the doping concentrations. The use of a-Si interface layer between Ge and P509 was proposed to overcome compatibility issues. The minimum applicable a-Si thickness was found to be 8 - 10 nm, sufficient to solidify the P509 solution and protect the Ge layer during the extreme annealing conditions. Although the doping levels were not increased using P509, this experiment helped us form a better understanding of the limiting factor in the case of P doping of Ge. Accordingly, the limited doping levels were attributed to the diffusion mechanism, rather than a limited source concentration. Co-doping or extremely-fast high-power annealing is proposed in literature as a solution to overcome this problem [112, 102]. Moreover, the use of Ge-rich Si_xGe_{1-x} alloys can be used to increase the solubility of P and slightly modify the diffusion mechanism, as proposed for future work (section 7.2.1). Although the possibility of achieving an optical gain in Si_xGe_{1-x} alloys is another topic that needs exploration, yet it is worth mentioning in this report, as this approach was found to provide many advantages, such as the relatively high emission intensity compared to Ge (fig. 4.7), while maintaining an emission peak around 1.55 μm.

Chapter 5

Study of Strain Application using Freestanding SiO_2 Beams

"Men pass away, but their deeds abide"
Augustin-Louis Cauchy, his last words.

5.1 Introduction

The application of tensile strain on germanium (Ge) for light emission purposes can be implemented in various ways. In this chapter we focus on the utilization of freestanding SiO_2 beams for tensile strain application on Ge micro-disks placed on top. This configuration is possible by using the Ge-on-insulator (GOI) wafers (used in chapter 3 with 100-nm-thick Ge on 145-nm-thick buried-oxide). After a brief theoretical introduction in sections 5.2 & 5.3, an investigation of strain dependency on the beam design, considering the resulting orientation, uniformity, and value, is then conducted by means of 3D finite-element computer simulations in section 5.4. Fabrication of the actual devices, and their experimental characteristics obtained by Raman spectroscopy and Photoluminescence (PL) measurements, are provided in sections 5.5, 5.6, and 5.7. Device characterization results are consistent with simulations outcomes of higher tensile strain for shorter beams. Splitting of light and heavy-hole bands is observed in the PL spectra as an indication of tensile strain. A comparative study is then conducted on the strain within similar structures fabricated using Ge-on-SOI wafers, used for doping in chapter 4. Final results promote GOI wafers for higher strain values, and consequently will be used for the final devices in chapter 6.

Parts of this chapter are published in [5] & [6].

5.2 Freestanding MEMS-Like Structures for Strain Application

Utilizing strain was the key for several innovations in electronic and photonic devices such as the realization of low threshold QW lasers [145], enhanced-performance MOSFETs [68, 70, 24], and high-efficiency Ge photodetectors [27, 16, 15, 5]. Such manipulation is possible due to the association of lattice deformation, represented by strain, with the band-gap structure and carrier dynamics [26, 25]. Strain is also considered as the key for realizing a Ge-based monolithic light source that can be introduced onto Si chips in a conventional CMOS fabrication line.

An inherent tensile strain of ~ 0.2 % is accumulated with Ge grown on Si due to the difference in thermal expansion coefficients between Si and Ge [27, 16]. This strain is biaxial in nature due to the stretching stresses acting in-plane of the thin Ge film [16]. Many straining techniques are proposed in literature to enhance this strain value, consequently deforming the band-gap and promoting the direct-gap radiative recombinations. Some straining techniques might enhance the strain uniformly along in-plane directions, maintaining the biaxial entity of strain, or alternatively, enhance the strain along a single direction causing the strain to become uniaxial. Biaxial strain results from applying stresses on both in-plane directions (x and y), while the out-of-plane direction is stress-free (z). In this case, if the two in-plane directions are tensile strained, then the out-of-plane direction will be compressed according to Young's modulus and Poisson's ratio, represented in the elastic stiffness constants (Appendix B.1) . On the other hand, uniaxial strain results from applying stress along a single direction (x), consequently causing the stress-free directions (y and z) to be compressed. Accordingly, uniaxial and biaxial strains have a different effect on Ge band gap, because the energy-bands deformation is related to the total change in volume, or volumetric strain, rather than the values of single strain components [26, 25]. The most straightforward implementation of these two approaches is by fabricating freestanding beams along one direction (uniaxial), or two perpendicular cross-shaped beams (biaxial). Although both of these structures have been studied for Ge band-gap engineering [31, 33, 36, 88], yet, uniaxial freestanding beams have initially been more popular in the research of highly-strained Ge structures. This is mainly due to the simpler engineering and possibility of optical mode confinement by, for example, DBR mirrors on the sides [38]. In fact, direct-gap transformation of Ge using uniaxial beams [31] was reported earlier than biaxially-strained beams [36].

Theoretically predicted direct Γ-light hole (LH) and indirect (L $-$ LH) band-gaps of strained Ge are shown in fig. 2.2. A uniaxial (biaxial) strain of $\sim$4.7% ($\sim$2.0%) is required to transform Ge into a direct-gap material. These results are reproduced from theoretical works provided in literature [25, 176, 28, 33], as summarized in Appendix B.

5.3 Strain by Freestanding SiO_2 Beams

The mechanism of tensile-strain application by releasing a Ge layer relies on the tendency of Ge to shrink upon suspension, in order to relax the initial tensile stresses. This has been exploited by designing Ge beams supported from the sides by wider-section pads [33, 31, 36, 38, 88]. By under-etching the Ge beam and the wider-section pads, they both shrink as they get suspended. However, due to this difference in the cross-sectional area, the wider-section pads (boundaries) impose a larger force compared to the weaker Ge beam, effectively "pulling" the Ge beam (middle region) outwards. Eventually, the pads are expected to relax their initial tensile stresses, on behalf of tensile-straining the Ge beam (middle region). Novel designs implementing a gradual decrease of the Ge beam section from the boundaries towards the middle, permit a smooth gradual increase of tensile strain towards the middle of the beam [33, 31]. The interest in freestanding Ge beams is evident in literature due to the high achievable tensile-strain values [33, 31, 35, 36, 1, 5] . Strain values up to 3.1% [33], or even 5.7% [31], were reported using uniaxial beams, yet without the implementation of an optical cavity within these structures. Recent works by Gassenq *et al.* [37] and Petykiewicz *et al.* (2016) [38] demonstrated the fabrication of focusing distributed-Bragg reflectors (DBR) on the sides of unixial Ge beams. Addition of the DBR mirrors degraded the achievable strain values to 2.2% [37] and 2.37% [38]. This is expected as the pads - being the source of the tensile forces exerted on the Ge beam - are being weakened by etching the DBRs. In fact, accumulation of high tensile strain values is expected in the DBR region, comparable or even higher than the Ge beam itself, due to the thinner Ge sections.

The mechanism is different in the case of releasing a thermally-grown SiO_2 layer. This is due to the different initial built-in stresses compared to Ge, which are compressive (tensile) in the case of SiO_2 (Ge). Growing SiO_2 films by thermal oxidation of Si accumulates compressive stresses within the dioxide film due to the high growth temperatures, and the difference in thermal expansion coefficients between SiO_2 and Si [81, 79, 6]. Such compressive stresses are less-pronounced in Plasma-Enhanced CVD (PECVD) SiO_2 films due to the lower deposition temperatures [81]. Compressive stresses are not uniform across the thickness of thermally-grown SiO_2 layers, where higher compressive stresses are accumulated at the interface between SiO_2 and Si substrate [79]. Consequently, SiO_2 tends to expand upon suspension, while Ge tends to shrink. Releasing a compressively-stressed film causes it to expand in order to relax the average residual stresses within the film, while the stress gradient across the film thickness and the boundary conditions cause it to deflect or deform in order to reduce the stress-gradient across the film thickness [79], as shown in fig. 5.1. Expansion of SiO_2 beams upon suspension can be exploited to impose tensile strain on a Ge structure placed on top, while the deflection of the beam exerts an additional component by bending and affects the strain distribution.

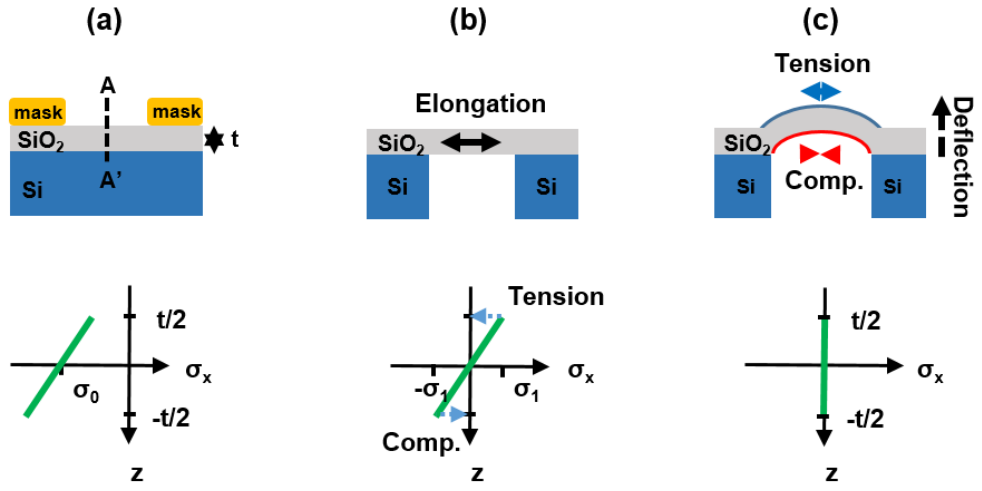

Figure 5.1: Stress diagram of a doubly-clamped SiO_2 beam (a) as grown on Si, (b) after releasing by under-etching, and (c) after deflection (assuming a stress-free beam). Due to upwards deflection, the top side of the beam is tensile strained while the bottom side is compressed. Higher initial built-in stresses in the film result in higher tensile strain upon suspension.

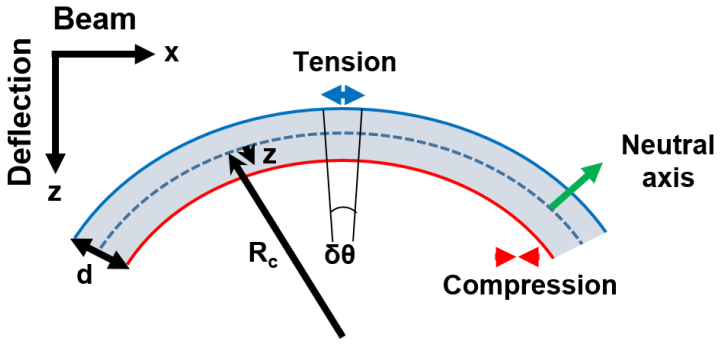

Figure 5.2: Deflected-beam profile showing the formation of tensile and compressive strains above and below the neutral axis, respectively. In an ideal defect-free beam, the neutral axis is located in the middle of its thickness. Adding a Ge disk on-top of an SiO_2 beam shifts the neutral axis.

Assuming an ideal single-layered beam, and a beam length much larger than its width and thickness [79], the origin of bending-induced strain can be describe as follows. Referring to fig. 5.2, if a beam with a thickness of d μm is deflected towards the negative z direction with a radius of curvature of R_c μm, three regions across the thickness of the beam can be identified according to the type of strain: The upper part experiencing an increasing tensile strain towards the top surface, while the bottom side faces an opposite, and equal, compressive strain. The strain between these regions varies linearly for small deflections, such that at the middle of the beam thickness no strain exists, forming a neutral axis which has the same length of the original beam before suspension [79]. Adding any structure on the beam, such as a micro-disk on top for example, will shift and deform this neutral axis.

Consequently, a general description of strain accumulated in upwards-bent beams can be related to the radius of curvature (R_c) as follows: The length of a differential segment defined by $\partial\theta$ after bending is dependent on the segment's position relative to the neutral axis (z). So, if we denote this differential length with ∂L, we can calculate:

$$\partial L = (R_c - z)\partial\theta \tag{5.1}$$

Where $\partial\theta$ is in Radians. By definition, a differential length of a segment at the neutral axis is equal to its original length before bending (∂x), so:

$$\partial x|_{z=0} = R_c.\partial\theta \tag{5.2}$$

Combining equations 5.1 and 5.2, we get:

$$\partial L = \partial x - \underbrace{(\frac{z}{R_c}).\partial x}_{\text{strain}} \tag{5.3}$$

Bearing in mind that original length is ∂x, we can identify the second term in equation 5.3 as the strain (ϵ_x) along the beam direction (x) [79].

$$\epsilon_x = -\frac{z}{R_c} \tag{5.4}$$

The direction of z is chosen to result in a positive sign for tensile strain, and a negative sign for compressive strain, where z equals zero at the neutral axis. It can be concluded that tensile strain accumulation is expected at the far-most part of the beam relative to the center of curvature. Moreover, the strain value is inversely proportional to the radius of curvature. Consequently, it is expected that beams with reduced lengths are capable of delivering higher strain values due to the lower radius of curvature (R_c). Multi-layered beams with finite and comparable dimensions are complex structures, in which the strain distribution can not be described by such simple equations, and 3D computer simulations can be used instead. This applies to the structures studied in this project, which consist of Ge micro-disks on freestanding SiO_2 beams with few-micron dimensions. Detailed analysis of the strain distribution and its dependency on the beam design are provided in the following sections, based on 3D finite-element simulations (section 5.4) in addition to Raman and photoluminescence measurements (sections 5.6 & 5.7).

5.4 Finite-Element Simulations

Finite-element computer simulations can be used to visualize strain distribution within micro-mechanical devices. COMSOL Multyphics software is an appropriate software for such purposes, allowing good flexibility in structures design and results derivation. Built-in solid-mechanics model was used to make a stationary study on our structures, which are mainly Ge micro-disks on freestanding SiO_2 beams using the GOI stack described before (100-nm Ge / 145-nm BOX). Modelling the strain within Ge micro-disks on freestanding SiO_2 devices can be done using various approaches, such as observing the first eigenmode deflection of the devices. This agrees with the upward deflection scenario, and gives a good idea of the strain distribution within the structure [79]. However, this method is not realistic in terms of strain values, as the initial built-in stresses of the BOX layer are not taken into account. These built-in stresses are the actual source of strain in our devices, and the value of the resulting strain is mainly determined by them. Another way of modelling the devices would be by applying a force on the bottom side of the beam, causing it to deflect upwards into the first eigenmode shape. This assumption is proposed in ref. [79] justified by the fact that an upward-deflected SiO_2 beam is affected by compressive stresses from the surrounding BOX layer at the boundaries imposing a downward-directed force, and for the beam to be stable in its upward-deflected position, a counter force has to be affecting the beam in the opposite direction, or pushing the beam upwards [79]. This force value can then be tuned to match the fabricated devices. A value of ~ 700 μN was estimated in our case by matching the simulated and experimental strain values of a 20-μm-long uniaxial beam.

A more accurate approach, imitating the actual mechanism in reality, is by assuming initial stresses and strains within the structure. Then in a stationary study, the resulting deformation and consequent strains are calculated based on the resulting mechanically-stable state of the geometry. For instance, the initial stresses within a thermally-grown SiO_2 layer can be calculated using Stoney's formula (equation 6.1 [72]) by measuring the bending radius of the wafer. This has been done experimentally in this project for thermal and PECVD SiO_2 (fig. 6.3). Or, for crystalline micro-structures, initial strain can be measured locally by Raman spectroscopy. This can be used to estimate the initial strain in Ge micro-disks before releasing the SiO_2 beams. Typical values are in the order of 1 GPa compressive in-plane stresses for 145-nm BOX layer, grown at 1000°C by dry oxidation (section 6.3.2), and 0.2% tensile strain in Ge which is the inherent thermally-originated strain [27, 16]. These values can be used as an input to the COMSOL model in order to observe the beam deformation in steady state and estimate the resulting strain values, distribution, and uniformity. Regardless of the approach used for modelling, Ge elastic stiffness constants have to be input into the material library (table B.1).

5.4.1 Normal Strain Components and Volumetric Strain

Before presenting the simulation results, a brief explanation of the measured strain values is summarized in this section. Normal strain components ϵ_{xx}, ϵ_{yy} and ϵ_{zz} (or simply, ϵ_x, ϵ_y and ϵ_z) are identified as the ratio between the extension (or change in length), and the original length of the object along the same axis, x, y, or z, respectively. These components are the diagonal elements in the strain tensor, and their summation represents the relative change in volume, or volumetric strain $\frac{\Delta V}{V_\circ}$. These components, and their contribution to the volumetric strain, are sketched in fig. 5.3. Assuming three normal forces affecting a cubic object (a unit cell of a semiconductor lattice) with a side length (lattice constant) of (a) nm, exerting normal stresses σ_{xx}, σ_{yy} and σ_{zz} along x, y, and z axes. These normal stresses will induce corresponding normal strain components, note that being normal means perpendicular to each face of the cube. Shear stresses acting parallel to the cube faces are neglected. The initial volume of the cube ($V_\circ$) increases to $V' = V_\circ + \Delta V$. The new volume V' can be calculated by multiplying the side lengths of the new cube represented by normal strain components ($a.(1+\epsilon_{xx}), a.(1+\epsilon_{yy})$, and $a.(1+\epsilon_{zz})$). The result of this multiplication is shown in the equation on top of fig. 5.3. It is possible to de-assemble the new volume into a summation of three main components: its initial volume $V_\circ$ (volume (1) fig. 5.3), the change in volume due to normal strain components (volume (2) fig. 5.3), and the change in volume do to higher-order terms resulting from multiplying the normal-strain components (volume (3) fig. 5.3). For small

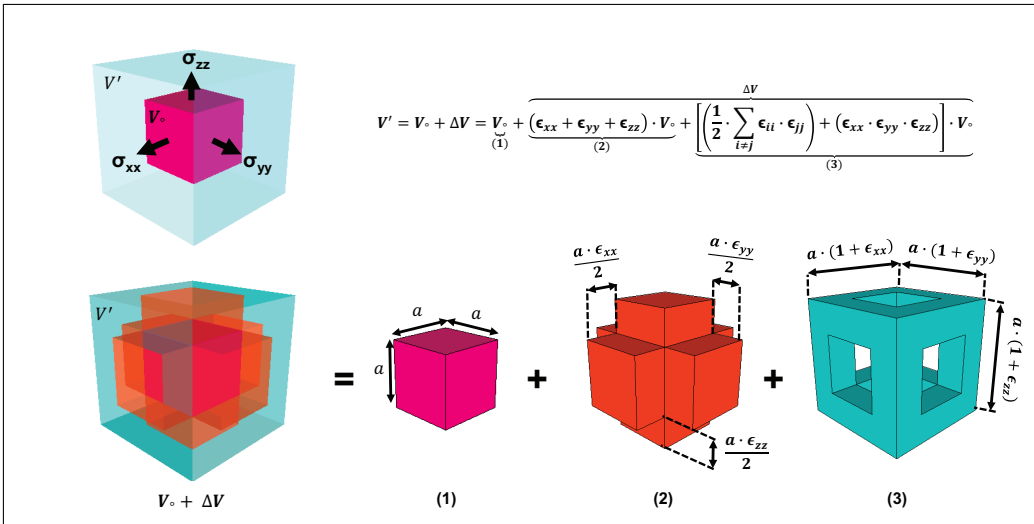

Figure 5.3: Normal strain components and volumetric strain: the new volume of a tri-axially strained cube is the summation of the original volume (component (1)) and the change in volume due to first-order (2) & higher-order (3) terms in the equation shown above. This equation represents the new volume of the cube by multiplying the strained side-lengths shown on sketch (3). For small strains, component (3) is negligible.

strain values, the third volume component ((3) in fig. 5.3) is negligible. Consequently, the summation of the normal strain components, is approximately $\frac{\Delta V}{V_\circ}$. In this report, normal strain components are considered to create a simple argument on uniaxial and biaxial strains. ϵ_{xx} is always in the direction of the beam, ϵ_{yy} is the other in-plane normal strain component, which is also along one of the beams in biaxial structures, and ϵ_{zz} is the out-of-plane component. Volumetric strain is the summation of these components.

5.4.2 Manipulation of Strain Orientation by Beam Design

The target devices as mentioned before are Ge micro-disks on freestanding SiO_2 beams with various designs. Modelling the dependence of strain characteristics on the beam type, namely uniaxial and biaxial beams, requires the dimensions to be fixed and matched to the fabricated devices. As an example, 3D geometries of 20-μm-long and 4-μm-wide uniaxial and biaxial beams, with 2-μm-diameter Ge disks on top, were created using COMSOL software. Ge and BOX thicknesses were chosen to be 100 and 145 nm, respectively. Fixed boundary conditions were assumed neglecting the effect of any displacement. Figure 5.4 shows 3D distributions of normal strain components within the structures after deflection. Normal strain components ϵ_{xx}, ϵ_{yy}, and ϵ_{zz}, are defined as the relative change in length along the principal x, y, and z axes, respectively, as discussed in the previous section 5.4.2. Figures 5.4 (a)-(c) show the distribution of strain components for uniaxial beams, while figs. 5.4 (d)-(f) show the distribution of the same strain components for biaxial beams. In uniaxial beams, a single tensile strain component (ϵ_{xx}) exists, which is along the beam direction (x), dominating in value over the other in-plane and out-of-plane components (ϵ_{yy} and ϵ_{zz}), which are mainly compressive within the disk region. On the other hand, the two in-plane components (ϵ_{xx} and ϵ_{yy}) are symmetric and tensile in biaxial beams within the disk region, while compression is observed along the out-of-plane direction (ϵ_{zz}). Comparing uniaxial and biaxial beams with similar dimensions, the strain component along the beam direction (ϵ_{xx}) has a larger value in uniaxial beams. However, the total tensile change in volume is higher in biaxial beams due to the tensile nature of the other in-plane component (ϵ_{yy}). Accordingly, biaxial beams are expected to have a more significant impact on the band structure of the Ge disk.

Figures 5.5 (a) & (c) show a 3D representation of the total change in volume, or volumetric strain, within the same structures shown in fig. 5.4, indicating a slightly higher total tensile strain within the Ge disk for biaxial beams. Volumetric strain is identified as the summation of normal strain components ($\epsilon_{xx} + \epsilon_{yy} + \epsilon_{zz}$), as discussed in section 5.4.1. Figures 5.5 (b) & (d) plot the corresponding individual strain components at the top surface of the Ge disk, mapped across the disk diameter (line $A - A'$) along the beam

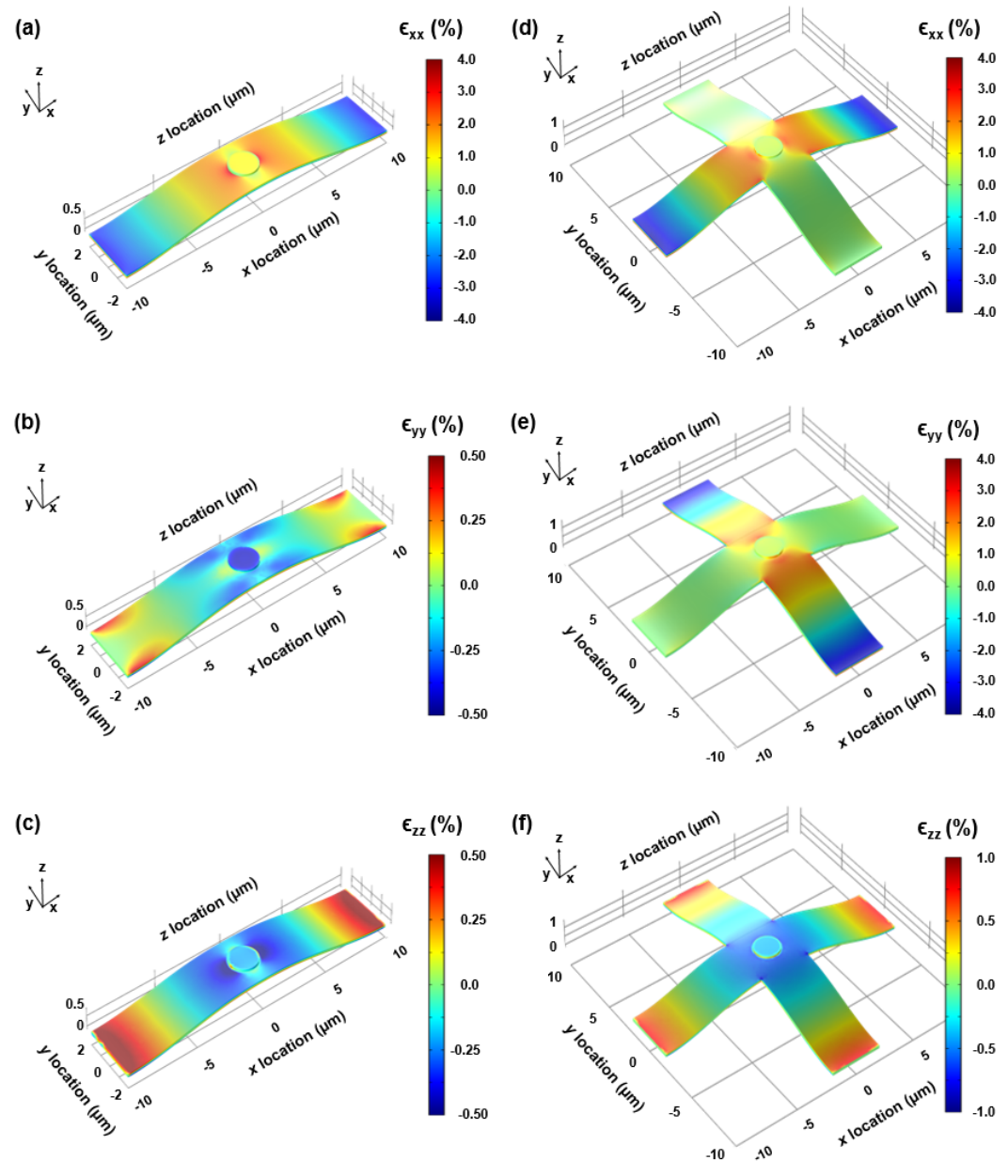

Figure 5.4: 3D maps of strain components within uniaxial and biaxial freestanding beams with Ge micro-disks on top. (a), (b), & (c) plots of normal strain components ϵ_{xx}, ϵ_{yy}, and ϵ_{zz} for a 20-μm-long uniaxial beam and a 2-μm Ge disk. Tensile strain across the Ge disk is only due to the component along the beam direction ϵ_{xx}, while the other in-plane and out-of-plane components are compressive. (d), (e), and (f) show the same components on a biaxial structure with similar dimensions. Both of the in-plane components (ϵ_{xx} & ϵ_{yy}) are tensile in this case and symmetric, while only the out-of-plane component is compressive.

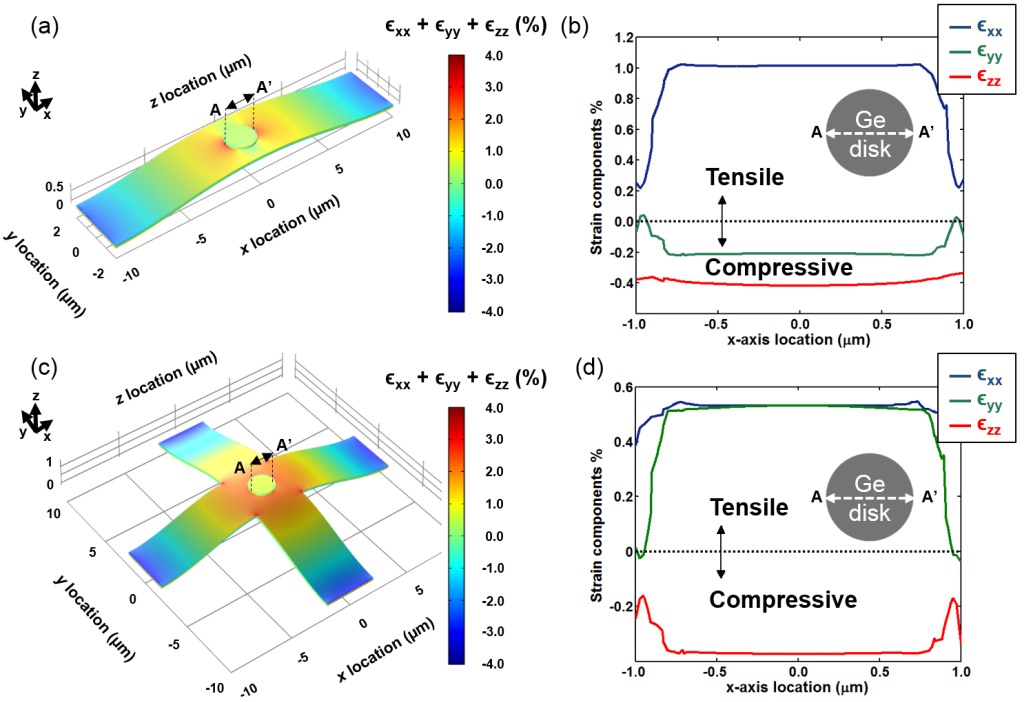

Figure 5.5: Volumetric strain across uniaxial and biaxial beams with Ge micro-disks on top: (a) & (c) are 3D maps of volumetric strain distribution for uniaxial and biaixial beams with similar dimensions, showing higher total change in volume for biaxial structures. (b) & (d) show the profile of normal strain components measured at the top surface and across the diameter of the Ge disk along the $A - A'$ line ($x = [-1.5 : 1.5], y = 0, z = 0.1$).

direction (x). The higher value of ϵ_{xx} is evident in uniaxial beams compared to ϵ_{xx} and ϵ_{yy} in biaxial beams. Yet, the summation yields a higher total strain of approximately $\sim$0.6% in the biaxial beam, compared to $\sim$0.4% in the uniaxial one. The corresponding direct band-gap values are calculated to be 0.693 eV and 0.775eV, respectively.

5.4.3 Strain Uniformity

Uniformity of strain distribution is important from carrier-dynamics point of view, which eventually affects the net optical gain within the Ge disk. Highly-strained regions have lower direct-valley (Γ) energies, and consequently higher electron population compared to less strained regions [25]. This fluctuation in the band gap eventually creates corresponding optical gain and loss regions within the same Ge disk [55, 56, 57]. To examine the uniformity of strain distribution within the structures, cross-sectional map of the total strain ($\epsilon_{xx} + \epsilon_{yy} + \epsilon_{zz}$) is simulated. Figure 5.6 shows an example of 10 μm (fig. 5.6 (a)) and 20 μm-long (fig. 5.6 (b)) uniaxial beams. Simulations indicate that tensile strain is accumulated throughout most of the disk with relatively good uniformity. Accumulation of tensile strain on the top side of the beam is confirmed, while the bottom

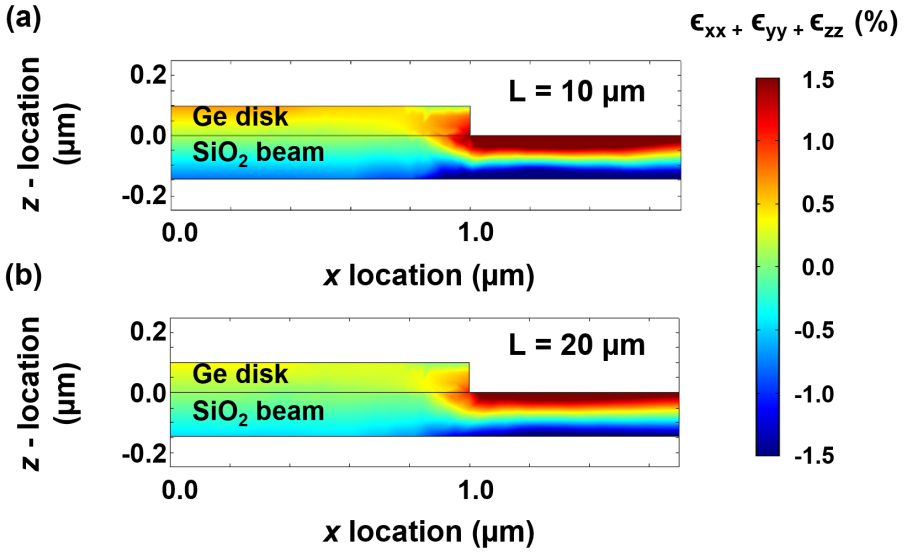

Figure 5.6: Cross-sectional distribution of volumetric strain for (a) 10 and (b) 20-μm-long uniaxial beams. Higher tensile strain is observed at the edges, which is advantageous for whispering-gallery modes confinement.

side is mainly compressed. This agrees with the theoretical model presented in section 5.3. Strain values are found to be higher in shorter beams, as appears in fig. 5.6, yet, the uniformity of its distribution is degraded. Nevertheless, this non-uniformity is mainly represented by a higher tensile strain at the edges of the disk, which is advantageous for whispering gallery modes (WGM) confinement. This distribution of higher strain values at the disk edges are the main advantage of this structure over the standard disks-on-pedestals structures, which tend to have lower tensile-strain values at the edges [55, 56]. Huge efforts have been witnessed in the last few years aiming to enhance the tensile strain at the edges of micro-disks on pedestals by engineering the coverage of external Si_3N_4 stress liners [55, 56, 57, 29, 30]. Another possible approach of squeezing the optical WGM away from the edges and towards the inner highly-strained regions of the micro-disks on pedestals is proposed in this thesis for future work (section 7.2.2). It is worth mentioning that the simulations assume fixed boundary conditions at the edges of the beam, and this condition might differ in reality, affecting the actual strain distribution within the disk. Other factors that may affect the strain distribution are the adhesion between Ge and BOX layers, where the poor adhesion would cause a loss of strain at the interface due to the relaxation of the Ge layer. And the actual deflection profile of the beam, which might not be a simple first eigenmode deflected upwards.

5.4.4 Effect of Beam Dimensions on Strain Value

In the previous two sections, it is shown that the orientation and distribution of the strain can be manipulated by the beam design. This manipulation is directly correlated

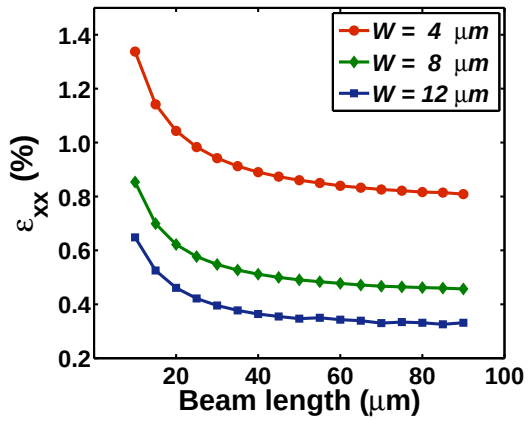

Figure 5.7: The effect of beam dimensions on the strain component along the beam direction (ϵ_{xx}) for uniaxial beams. Tensile strain is enhanced as the beam dimensions decrease.

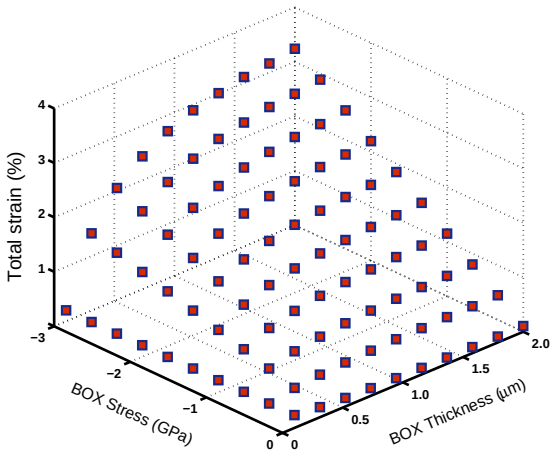

Figure 5.8: Manipulating the total strain through the buried-oxide thickness and initial built-in stresses. This assumes the possibility of tuning the built-in stresses of any thickness of SiO_2. Practically, an increase of BOX thickness results in lower built-in stresses, as shown in fig. 6.3

with the values of applicable strain. This is visualized in fig. 5.7 which summarizes the effect of beam length (L) and width (W) on the resulting strain. A uniaxial beam is considered as an example, and the strain value is represented by measuring the strain component along the beam direction (ϵ_{xx}) at the center point of the top Ge-disk surface. Shorter beams impose higher tensile strain, as expected in the previous section (5.4.3), and this effect is pronounced for beams shorter than 20 μm. Dependency on beam length becomes less significant for longer beams, where the strain value becomes nearly fixed independent of the beam length. Beam width (W) has a similar effect on ϵ_{xx}, yet having a slightly less impact compared with L. This agrees with previous results reported in MEMS-related studies on doubly-clamped SiO_2 beams, for example as summarized in

chapter 2 in ref. [135]. Demonstrating that reducing the length of doubly-clamped SiO_2 beams increases tensile strain, with a similar but less-significant effect for the beam width.

5.4.5 Strain Enhancement by BOX Layer Manipulation

As concluded from the previous section, for certain thicknesses of Ge and BOX, and certain built-in stresses in the BOX layer, there is a maximum achievable tensile strain value. Thin-film stress measurements of doubly-clamped SiO_2 beams made of thermally-grown and PECVD SiO_2 films confirm the accumulation of higher tensile strains in thermal-oxide beams after suspension, due to the higher initial built-in stresses (chapter 2 in ref. [177]). According to simulations, this maximum value is achieved using the minimum beam dimensions. Hence, it is possible to further increase the strain by engineering the stack ratio. For instance, using a thinner Ge layer permits the application of higher strain on the entire disk with better uniformity. Additionally, increasing the thickness of the BOX layer (and maintaining the built-in stress level) is expected to have a similar effect.

Figure 5.8 is a 3D representation of total strain measured at the top middle point of a Ge micro-disk on a uniaxial freestanding beam. All parameters were fixed (beam length is 10 μm, Ge thickness is 100 nm, and disk diameter is 3 μm) except the initial built-in stress and the thickness of the BOX layer. Initial stresses were varied from -1 MPa to -3 GPa (the minus sign indicating compressive stress), and the thickness was changed from 100 nm to 2 μm. This simulation assumes that we are able to control the built-in stresses for each thickness of the BOX layer. According to fig. 5.8, higher strain is applied on the Ge disk if both the thickness and the stress are increased. In other words, if the thickness of the BOX layer is fixed, highest built-in stresses are required. Similarly, if the built-in stresses can be controlled independent of thickness, highest thickness is required. Data presented in chapter 6 (fig. 6.3) shows that this is not the case experimentally, in fact, built-in stresses decrease as the SiO_2 thickness increases. Consequently, a compromise has to be engineered between BOX thickness and initial built-in stresses. A point of merit that can be concluded from fig. 5.8, is that BOX thickness has to be larger than that of Ge. This is evident in the 100-nm-thick BOX data points. In this case, the BOX thickness is equal to that of Ge, and this results in a significant reduction in the effect of BOX stresses on the resulting strain within the Ge disk. For instance, increasing the built-in stress from -1 MPa to -3 GPa, enhances the strain from 0.2 to 0.23% only. This effect is demonstrated experimentally in section 5.8 using Ge-on-SOI wafers, in which the BOX layer (145 nm) is thinner than Ge (200 nm), resulting in a degraded strain upon suspension, and negligible dependence on beam dimensions. Implying the necessity of a BOX layer thicker than Ge, with highest possible built-in stresses.

5.5 Beam Designs

Multiple designs of SiO_2 beams were included in our e-beam mask, aiming to investigate the most appropriate designs from strain and stability point of view. Designs can be categorized into two main groups, as shown in fig. 5.9: (I) Rectangular or straight-edge beams (figs. 5.9 (a), &(b)). In addition to (II) curved beams (fig. 5.9 (c)). Each category of beams can be implemented in a uniaxial (fig. 5.9 (a)) or biaxial (fig. 5.9 (b)) form, imposing uniaxial or biaxial strain respectively as discussed in section 5.4.2. Doubly-clamed uniaxial rectangular beams are widely investigated for MEMS applications [80, 135], and consequently we will concentrate on devices with similar uniaxial designs. Anisotropic wet-etching of bulk Si can be exploited to determine the beam boundaries with minimal under-etch, restricting the resulting strain to the beam suspension, which is suitable to form a basic understanding of strain characteristics. More complex structures, namely curved beams (fig. 5.9 (c)), are utilized in this work to enhance the stability upon suspension, by reducing the stresses on beam joints. Moreover, the curved edges allow a smooth gradient of strain along the beam direction, preventing any pin-point accumulations of stress at sharp corners [35, 33, 31]. Such pin-point concentrations of stress at the boundaries cause a loss of total strain in the beam, as they do not contribute to the strain along the beam direction [33, 31]. Curved-edge beams will be used for the final device structures demonstrated in chapter 6. Although no precise statistical data is available on the deflection direction of the beams, most of the beams deflect upwards in the GOI devices (downwards bending was significant in Ge-on-SOI devices due to PECVD capping, as discussed later in section 5.8). Beam deflection affects the strain distribution within the Ge disks, as will be shown later in this chapter. More on the fabrication process can be found in section 6.3.

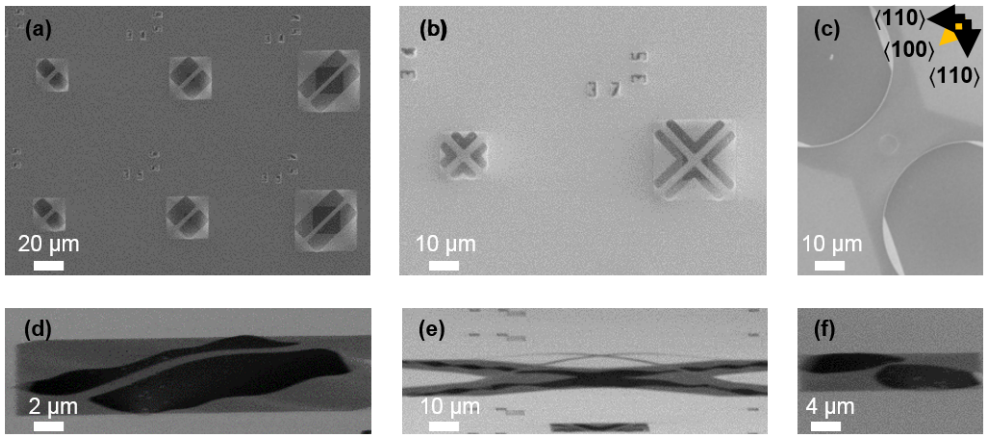

Figure 5.9: Scanning-electron microscopy (SEM) images of freestanding SiO_2 beams. (a), (b), and (c) show top-view images of uniaxial, biaxial, and curved-edge uniaxial beams. (d), (e), and (f) show birds-eye view images of the same structures. Beams are aligned with ⟨100⟩ directions.

5.6 Strain Characterization by Raman Spectroscopy

Experimental estimation of strain values in Ge can be done using Raman spectroscopy. Strain is proportional to the Raman shift in cm^{-1} relative to bulk Ge, and can be calculated using the linear relation:

$$\Delta\omega = S \times \epsilon \tag{5.5}$$

Where $\Delta\omega$ is the Raman shift relative to bulk Ge in wavenumbers, ϵ is the strain, and S is a proportionality factor. The value of this proportionality factor depends on the strain type and orientation. Table 5.1 lists some reported values for various strain orientations. The S value used for uniaxial beams in this project is 152 cm^{-1} [33, 31], while 390 cm^{-1} is used for biaxial beams [75, 76].

Strain	**Orientation**	S (cm^{-1})	**Ref.**
Uniaxial	⟨100⟩	152	[33, 31]
	⟨110⟩	202	[164]
	⟨100⟩	135	This Work
	⟨111⟩	434	[178]
		438	[178]
Biaxial	(100) Ge wafer	390	[75, 76]
		424	[73]
		415	[57]

Table 5.1: Values of Raman-strain proportionality factor (S) for different orientations

Figures 5.10 (a), (c), and (e) show examples of Raman spectra for bulk Ge, GOI, and a Ge disk on a freestanding SiO_2 beam. Measurement conditions are listed in table 5.2, which are always used for Raman characterization in this report, unless stated otherwise. The red-shift of the GOI and the Ge disk spectra relative to bulk Ge indicates the accumulation of tensile strain. More detailed analysis is provided below.

5.6.1 Power Dependence of Raman Shift

Due to the sensitivity of freestanding structures to heating by laser excitation, power dependence of Raman signal was investigated to optimize exposure conditions. Generally speaking, heating is expected to shift the Raman peak position resulting in misleading estimations of strain values. This effect is more pronounced in freestanding structures,

Parameter	Value
Excitation source	CW
Excitation wavelength	532 nm
Max. Power [(a)]	55 mW
Objective lens	50×
Spot size	∼2 μm
Grating	3000 lines/mm
Exposure time	10 s
Averaging	50 times
Data fit	Lorentzian

Table 5.2: Raman spectroscopy characterization conditions
[(a)] Maximum power measured at sample surface.

because the heat leakage path through the substrate is eliminated and replaced with air, which is a relatively poor thermal conductor. Considering a GOI wafer, heat generated by laser excitation can be dissipated across the top Ge layer, and through the BOX layer into the substrate. Meanwhile, patterning the top Ge layer into micro-disks and suspending the BOX layer by removing the bulk Si underneath, cuts off the heat dissipation path. This is expected to increase heat confinement within Ge which is surrounded by air and SiO_2; both being good thermal insulators compared to Ge.

Figure 5.10 compares the power-dependence of Raman signals from bulk Ge, un-patterned GOI, and a 2 μm Ge disk on a freestanding SiO_2 beam. The beam length and width are 10 and 3 μm, respectively. Figures on the left show the actual Raman spectra using different excitation powers, while figures on the right summarize peak positions and spectrum line-width in each case. Increasing the excitation power from 0.055 to 5.5 mW at sample surface, a negligible heat-induced shift in the Raman peak position was observed in the case of Ge and non-patterned GOI wafers. Fitting the peak positions recorded against different excitations powers was possible using linear functions. The slope of the best-fit line is -0.45×10^{-4} cm$^{-1}/\mu$W for bulk Ge, and -0.64×10^{-4} cm$^{-1}/\mu$W for the GOI wafer. This slightly higher sensitivity of Raman peak position towards excitation in the case of GOI can be explained by the heat insulation imposed by the BOX layer, which impedes the dissipation of heat through the bulk substrate. Extrapolating this linear relation, and finding the peak position value at the limit of zero excitation power, permits the estimation of strain value without the effect of heat. For instance, a shift of approximately -0.8 cm^{-1} exists for the GOI film relative to bulk Ge, which corresponds to a biaxial tensile strain of $\sim 0.2\%$. This strain is presumably due to the growth of Ge on Si during the process of GOI manufacturing. A slight increase in spectrum line-width was also observed for both Ge and GOI wafers at higher excitations. The difference in line-width behavior against excitation power between Ge and GOI wafers is nearly negligible.

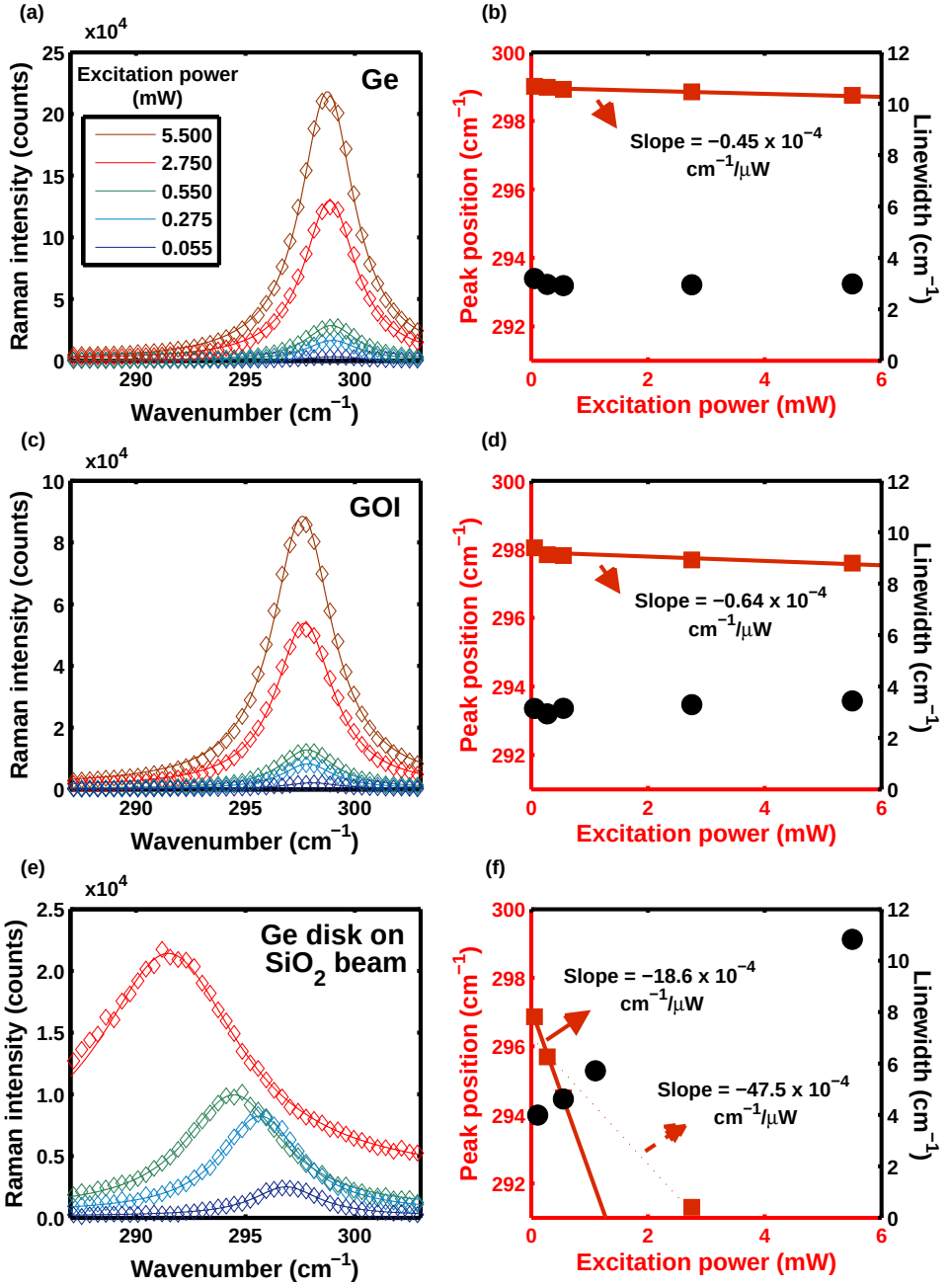

Figure 5.10: Dependence of Raman signal on the excitation power for (a) & (b) bulk Ge, (c) & (d) un-patterned GOI, and (e) & (f) Ge micro-disks on freestanding uniaxial SiO_2 beams. Excitation power was increased from 0.055 to 5.5 mW, and the effect on the peak-position and line-width was summarized for each case. Sensitivity to excitation is maximum for free-standing structures, mainly due to the absence of heat dissipation path through bulk Si, as the case in GOI and Ge. GOI wafers are slightly more sensitive to excitation power compared to bulk Ge, due the BOX layer providing some heat insulation. Extrapolation of peak positions against power is used to find strain values for freestanding structures.

The 2 μm Ge disk is expected to heat up more severely with excitation power compared to the continuous Ge blanket in the GOI wafer, in which heat can be dissipated across the Ge film and through the Si substrate. Especially that the 2 μm Ge disk is comparable to the spot-size of the excitation laser. This is demonstrated in figs. 5.10 (e) & (f), where a severe heat-induced red-shift of the Raman peak and line-width broadening are observed in the freestanding structure. Peak positions are plotted against excitation power in fig. 5.10 (f). Fitting the first three peak positions (up to 0.55 mW) using a linear relation yields a heat-induced shift of $-18.6.45 \times 10^{-4}$ cm$^{-1}/\mu$W , while including the fourth point (2.75 mW) yields a sensitivity of -47.5×10^{-4} cm$^{-1}/\mu$W, and a larger Raman shift. It is possible that the power-dependence of the Raman peak position tends to become non-linear at higher powers, in the case of freestanding structures, as appears in fig. 5.10 (f). So, for peak-position extraction in this report, fitting of the first three peak positions using a best-fit linear relation is used. The fact that including higher-power points will cause a higher estimation of strain values, which is not likely, as will be shown using photoluminescence (PL) data. For instance, a shift of approximately -1.88 cm^{-1} (-2.68 cm^{-1}) is calculated by fitting the first three (four) peak-position points in fig. 5.10 (f), corresponding to a uniaxial strain of 1.2 % (1.7 %). The slight red-shift in PL peaks - shown in section 5.7 - does not correspond to 1.7% tensile strain [25]. Spectrum line-width is also significantly affected by laser excitation compared to Ge and GOI line-widths, where it increased from approximately 4 cm^{-1} to 10.8 cm^{-1} upon increasing the excitation power from 0.055 to 5.5 mW. This can be explained by local strain variations induced by heating from laser-excitation, resulting in broad Raman emissions at various wavenumbers. Heating effects on Raman spectrum are expected to be similar for all investigated beam dimensions under the excitation conditions described above (table 5.2). Beam dimensions varied in length from 10 to 100 μm, and from 3 to 12 μm in width. This was confirmed experimentally by measuring similar sensitivity of Raman-peak position to excitation power, represented by a slope value in the range of approximately -20×10^{-4} cm$^{-1}/\mu$W for all freestanding devices.

5.6.2 Effect of Beam Dimensions

Characterization procedure presented in the previous section is used to estimate the resulting strain values of various beam designs. Rectangular beams with straight edges and boundaries determined by anisotropic wet-etching are fabricated, with lengths varying from 10 to 100 μm, and widths of 3, 4, 5, and 6 μm. Resulting Raman shift values are shown in fig. 5.11 (a). Enhancement of tensile strain upon suspension relative to non-patterned GOI wafer is evident due to the higher negative Raman shift. Agreeing with simulations presented in section 5.4.4, shorter beams impose higher tensile strain values (higher negative Raman shifts), with a maximum tensile strain of approximately

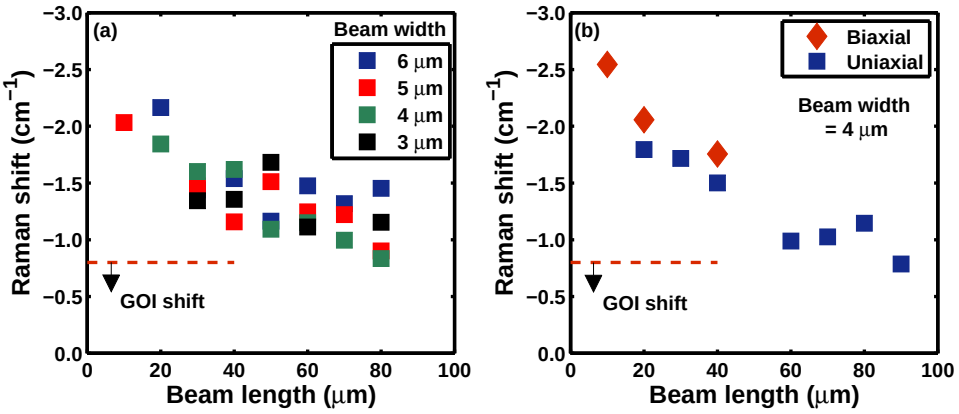

Figure 5.11: Experimental values of Raman shift (strain) for beams with (a) different dimensions and (b) different designs. (a) Red-shift of the Raman peak relative to bulk Ge increases as the beam length decreases, indicating higher tensile strain values. The effect of beam width is less significant. (b) Biaxial beams have a slightly higher negative Raman shift compared to uniaxial beams with similar dimensions.

1.3 %. For longer beams, strain values decrease and approach the initial state of the non-patterned GOI wafer. The effect of beam width is less significant compared to length within the studied width values. These results agree with previous studies conducted on doubly-clamped SiO_2 beams for MEMS applications, such as reported in chapter 2 ref. [177]. It is agreed upon that shorter beams have higher tensile stain, while the beam width effect is less significant. Achievable strain values are mainly dependent on the initial stresses of the BOX layer, where for example, thermally-grown oxide will result in higher tensile strain compared to PECVD oxide after suspension [177]. It is important to note that the penetration depth of the green laser (532 nm) used in Raman characterization is approximately $\sim$ 20 nm, hence mainly representing the value of accumulated strain in the top part of the Ge disk [179, 180].

5.6.3 Uniaxial and Biaxial Beams

As proposed by simulations in section 5.4.2, a different type of strain can be imposed on the Ge disk through designing the beam in a uniaxial or a biaxial form. Biaxial beams are shown to results in a higher total strain compared to uniaxial beams with similar dimensions, due to the symmetry of the in-plane strain components ϵ_{xx} and ϵ_{yy}. Experimental Raman shift values agree with simulation results as shown in fig. 5.11 (b). Biaxial beams result in higher negative Raman shift compared to uniaxial beams with similar dimensions.

5.7 Photoluminescence Measurements

Photoluminescence (PL) measurements were conducted to examine the effect of beam suspension on the direct-gap luminescence of the Ge disks. PL characterization was done at room temperature using a microscope setup, in which pumping and signal collection is done through the same objective lens from top. Testing conditions are listed in table 5.3, which are used for PL data in this report unless stated otherwise.

Parameter	Value
Excitation source	CW TI:S
Excitation wavelength	730 nm
Power [(a)]	400 μW
Objective leans	50×
Spot size	~2 μm
Exposure time	1s
Averaging	1000 times

Table 5.3: Photoluminescence characterization conditions
[(a)] Measured at sample surface.

Figure 5.12 (a) shows the PL signal of a non-patterned GOI wafer taken as a reference, alongside the PL signal from a freestanding Ge-on-SiO_2 beam (fig. 5.12 (b)), in which a continuous film of Ge is suspended, not patterned into a disk. While fig. 5.13 plots PL spectra of a 2 μm Ge disk on 10-μm-long uniaxial freestanding SiO_2 beam. The PL signal around 1580 nm corresponds to the direct-gap of Ge [25, 32, 3]. This peak has a different behavior as the excitation power increases according to the structure, as discussed below.

5.7.1 Power Dependence of Photoluminescence Spectrum

Power dependence of the PL signal allows us to investigate the effects of laser excitation, mainly heating, on the direct-gap spectrum, before examining the effect of strain. We studied the effect of excitation power on a non-patterned GOI wafer (fig. 5.12 (a)) and freestanding structures. Freestanding structures include non-patterned Ge films (freestanding Ge-on-SiO_2 beams) (fig. 5.12 (b)) and Ge micro-disks on a freestanding SiO_2 beams (fig. 5.13). Based on the previous power-dependence study conducted on Raman signal (section 5.6.1), heating effects are expected to be most pronounced in the case of freestanding Ge micro-disks, followed by the freestanding Ge films. While heating effects should be less significant in the non-patterned GOI wafer.

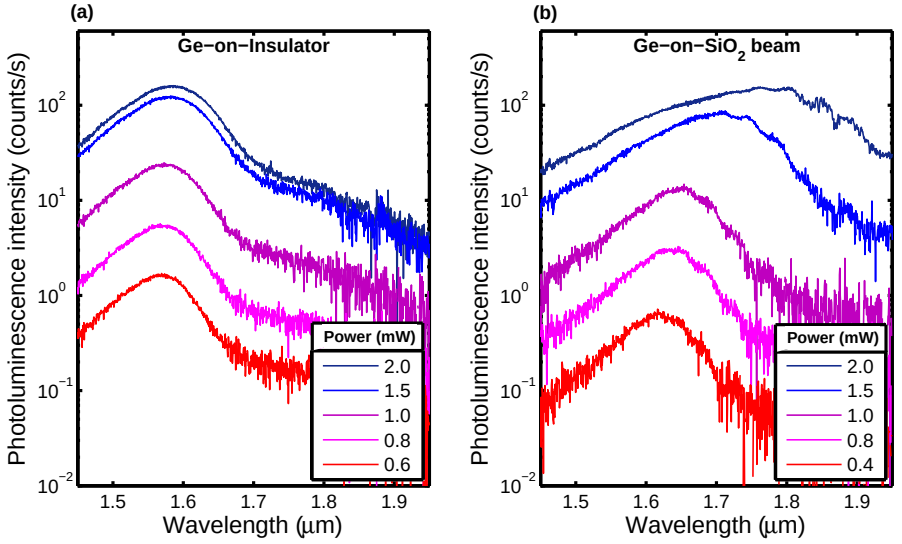

Figure 5.12: Power dependence of the PL spectrum for (a) GOI wafer, and (b) Ge-on-SiO_2 freestanding film. The legend is pumping power in mW.

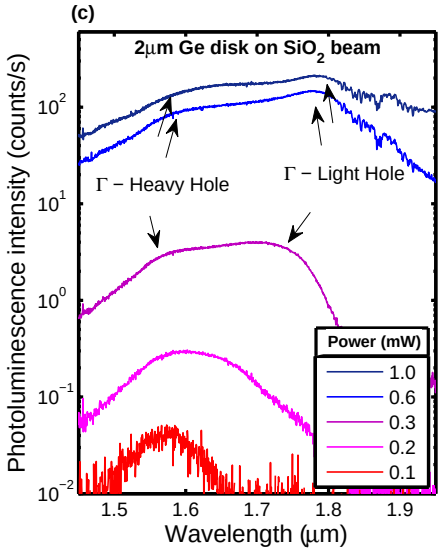

Figure 5.13: Power dependence of the photoluminescence spectrum of a 2 μm Ge disk on a freestanding SiO_2 beam. Sensitivity to excitation power increases in freestanding structures. Splitting of light-hole and heavy-hole bands is observed. The legend is the pumping power in mW.

Pumping power was increased from 100 μW to 2000 μW on the stacks with a continuous Ge film (fig. 5.12), and up to 1000 μW on the freestanding micro-disks (fig. 5.13). In the case of the non-patterned GOI wafer (fig. 5.12 (a)), the position of the direct-gap peak is nearly unaffected by pumping power. This indicates that the temperature increase of the local Ge film within the excitation area is negligible [105]. It is also noticed that the shape and line-width of this peak is nearly the same regardless of pumping power. This direct-gap peak of intrinsic slightly-strained Ge corresponds mainly to Γ-heavy

hole (HH) recombinations [26, 25, 32, 176]. Releasing the Ge-on-SiO_2 stack by local etching of bulk Si, forming a freestanding beam of a continuous Ge film, makes the structure slightly more sensitive to laser excitation (fig. 5.12 (b)). This is expected due to the absence of the heat dissipation path through bulk Si. Heating effect is seen as a red-shift upon pumping due to band-gap narrowing, and line-width broadening [3, 106]. It is worth mentioning that the direct-gap peak position of this freestanding Ge film is red-shifted compared to the non-patterned GOI wafer, due to the additional tensile strain gained upon suspension [4, 6].

Sensitivity to excitation power becomes more critical if the Ge film is patterned into isolated micro-structures, especially if the sizes are comparable to the laser spot size. This is noticed in fig. 5.13 for a 2-μm disk on a freestanding beam. Excitation power could not be increased above 1000 μW as the micro-disks get instantly burnt. As the pumping power is increased, the PL spectrum splits into two main peaks, as seen in fig. 5.13. These peaks can be attributed to Γ-HH and Γ-LH recombinations, according to their energy. Such a split in LH and HH bands is expected in strained Ge [25]. Lower-wavelength peak, corresponding to Γ-HH, is nearly fixed in position, indicating a negligible increase in disk temperature. Meanwhile, the higher-wavelength peak, mainly attributed to Γ-LH transitions, is red-shifted significantly. This split of the spectrum into LH and HH peaks is reported by other groups due to uniaxial [176] and biaxial [57, 88] strain. This band splitting is more pronounced under uniaxial strain due to the reduced symmetry [25, 176]. We expect that it is even more pronounced in freestanding structures, because additional strain might be created by the deformation of the beam due to severe heating, causing an additional split in the LH and HH bands [88]. This additional strain explains the red-shift of the Γ-LH peak with pumping, causing the spectrum to broaden. No sharp-peak resonances were observed from 2 μm disks. This might be due to the low Q-factors of whispering-gallery modes (WGMs) associated with the small-radius disks [138], mainly due to the pronounced interaction between the WGM and the rough circumference. Disks with diameters $\leq$2 μm are more prone to heating, because their size is comparable to the laser spot size (chapter 6).

5.7.2 Effect of Beam Dimensions

Figure 5.14 shows PL spectra for 2 μm Ge disks on uniaxial SiO_2 beams with different lengths. Excitation conditions were set as shown in table 5.3. As the power is fixed, and beam lengths (10 - 90 μm) are much larger than the laser spot-size ($\sim$ 2 μm), heating effects are expected to be similar in all devices. This has been confirmed previously by the study of Raman dependence on excitation power (section 5.6.1). All the Spectra consisted of two distinctive peaks as discussed above, and get slightly broadened as the

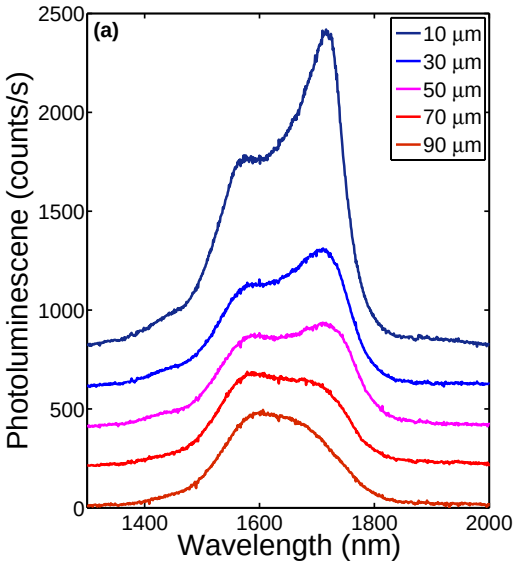

Figure 5.14: Photoluminescence of Ge micro-disks on freestanding SiO_2 beams with different lengths. Beam width (W) is fixed for all devices and equals 4 μm. Lower and higher-wavelength peaks are attributed to Γ-HH and Γ-LH, respectively. PL broadening is observed as the beam length decreases represented in higher Γ-HH and Γ-LH energy-splitting.

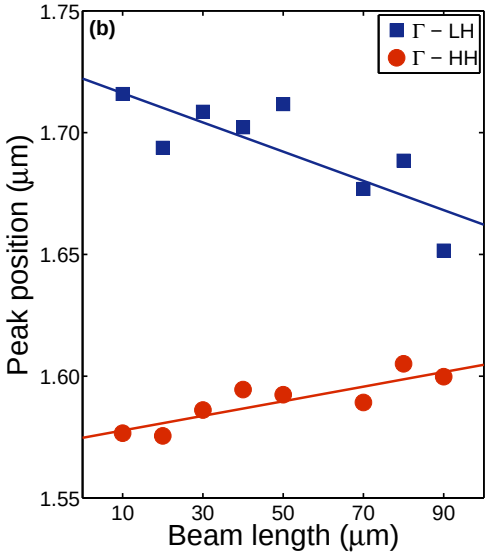

Figure 5.15: Γ-Light hole (LH) and Γ-heavy hole (HH) PL peak positions for Ge micro-disks on freestanding SiO_2 beams with different lengths. The energy difference between LH and HH bands increases for shorter beam lengths, indicating additional accumulation of tensile strain as explained by theoretical models [25].

beam length decreases. Broadening is a consequence of the Γ-HH band blue-shift, and Γ-LH band red-shift, in consistence with the theoretical effects of tensile strain [25, 26]. The blue-shift of the Γ-HH band eliminates any possible impact of heating in creating this band splitting, as a red-shift of this peak is expected as the temperature increases [32, 165]. By extracting the Γ-HH and Γ-LH peak positions, the separation between these bands is confirmed to increase for shorter beams. For instance, a separation of approximately 87 nm (139 nm) is observed for a 70 μm (10 μm)-long beam. As the split of LH and HH bands is associated with strain [25], this indicates an enhancement of tensile strain as the beam length decreases. This agrees with the previous results of computer simulations and Raman spectroscopy.

Another possible way to interpret these results is from strain-homogeneity point of view. Strain inhomogeneity contributes to broadening of the PL spectrum, as a certain shift in the Ge peak is expected for each strain value [25, 26]. Consequently, as the range of strain values increases (more inhomogeneity), emissions at a wider range of wavelengths (energies) is expected. And this inhomogeneity, or non-uniformity, is coupled with the increase of tensile strain in our structures, as demonstrated in the cross-sectional maps in fig. 5.6. The reason for considering this interpretation of PL spectra broadening is the position of the main Γ-HH peak (lower wavelength). Where the estimated tensile strain values based on Raman spectroscopy are up to $\sim 1\%$ uniaxial. Such tensile strain is expected to red-shift the main Ge peak (Γ-HH) to ~ 1.6 μm. Although a red-shift up to ~ 1.58 μm is observed in the PL spectra, there is a slight mismatch with Raman estimations. A possible reason might be the different excitation-laser wavelengths used for Raman spectroscopy and PL measurements. The penetration depth (α^{-1}) of a green light (532 nm) used for Raman characterization is approximately 20 nm in Ge, thus reflecting an idea of strain values mainly within the top regions of the Ge disk, which is 100 nm thick. According to theory (fig. 5.2) and simulations (fig. 5.6), higher tensile strain values are expected at the top side of the disk, in the case of upwards-bent beams. Hence, Raman spectroscopy reads the maximum tensile strain values within the structures. On the other hand, the laser penetration depth is larger in the case of PL measurements, where α^{-1} is more than 145 nm for a 730-nm-wavelength laser. Accordingly, PL represents the strain across the whole Ge-disk thickness, not only the top surface as observed by Raman. As can be seen in the cross-sectional strain maps (fig. 5.6), lower tensile strain values, or even compressive regions, exist within the bottom layers of the Ge disk. This might explain the relatively low red-shift in the main Ge peak in the PL spectra. However, the broadening is evident (fig. 5.15), and even if it is attributed to strain inhomogeneity, it also indicates higher tensile strain values within some regions of the Ge disk. The fact that higher tensile strain is correlative with more inhomogeneity, or non-uniformity of its distribution.

5.8 A Comparative Study with Ge-on-SOI Wafers

In chapter 4, a modified stack of Ge-on-SOI was proposed to combine n-type doping and apply strain using the buried-oxide (BOX) layer. In this section we investigate this stack as a possible platform to fabricate Ge-on-SOI micro-disks on freestanding SiO_2 beams, in comparison with the previously discussed GOI stack, in terms of tensile strain. Instead of using a 100-nm Ge / 145-nm SiO_2 GOI wafer, a Ge-on-SOI stack of 200-nm Ge / 20-nm Si / 145-nm SiO_2 was used (fig. 4.1). Both wafers are commercially available. In the case of GOI, volatile Ge mono-oxide (GeO) which is soluble in water may from at the Ge-BOX interface, thus making the Ge layer very fragile [154, 100]. While in the Ge-on-SOI wafer, the thin ($\sim$ 20 nm) SOI layer between Ge and BOX promotes adhesion and prevents the formation of Ge-O bonds. The significance of this Si layer appears, for instance, in Ge doping by rapid-thermal-annealing (RTA), where as shown in chapter 4, Ge-on-SOI layers survive high-ramping-rate annealing conditions while GOI layers do not. It is also expected to deliver the strain from the BOX layer to Ge more efficiently, due to the improved adhesion. Moreover, it can be used for electrical injection of carriers [43, 44]. Two drawbacks associated with this SOI layer can be highlighted though: interface defects with Ge, and the necessity of a cap layer to protect it from alkali etching of bulk Si, which degrades the strain significantly as will be shown in this section.

Structures similar to previously discussed GOI devices were fabricated using the Ge-on-SOI wafer (fig. 5.16). Devices include uniaxial and biaxial beams with straight and curved edges. Compared to GOI devices, two main differences can be pointed out: dry-etching of Ge-on-SOI micro-disks instead of Ge, and an obligatory 200-nm-thick PECVD SiO_2 layer capping the devices. In the case of GOI, this PECVD cap layer can be totally or mostly removed, as described in section 6.3.3. In addition to degrading the tensile strain, this cap layer increased the probability of beams down-bending upon suspension. More details on the fabrication process are provided in section 6.3.

5.8.1 Finite-Element Simulations

Strain simulations using COMSOL Multiphysics software were done to visualize the strain distribution and values within the structures. Built-in solid-mechanics model was used to make a stationary study on our structures, using the calculated initial stress values for BOX and PECVD oxides, presented in fig. 6.3. Initial Values of -0.4 GPa and -1.0 GPa were used for the 200-nm PECVD SiO_2 (cap layer) and 145-nm thermal SiO_2 (BOX). While Ge was set to be initially 0.2% tensile strained, and fixed boundary conditions are assumed at the beam edges. The beam deformation in steady state, resulting strain values, distribution, and uniformity are discussed below.

5.8.1.1 Strain Distribution

Germanium layer (200 nm) being thicker than the BOX (145 nm), and the passivation PECVD SiO_2 layer on top, are found to have major impacts on the strain distribution. As a case for study, a 10-μm-long freestanding beam with a 3-μm Ge-on-SOI disk on top is considered. Figure 5.17 shows cross-sectional maps of the uniaxial (ϵ_{xx}) and volumetric ($\epsilon_{vol.}$) strain distributions. Ge-on-SOI micro-disks without (first column) and with (second column) PECVD SiO_2 passivation layer are shown, given that the disks without the passivation layer are taken as a reference, to mark the effect of the PECVD oxide, and not fabricated in real devices. Figures 5.17 (a) and (b) present the strain distribution for upwards and downwards-bent beams, respectively. Downwards bending is considered in this section because a significant number of Ge-on-SOI devices were

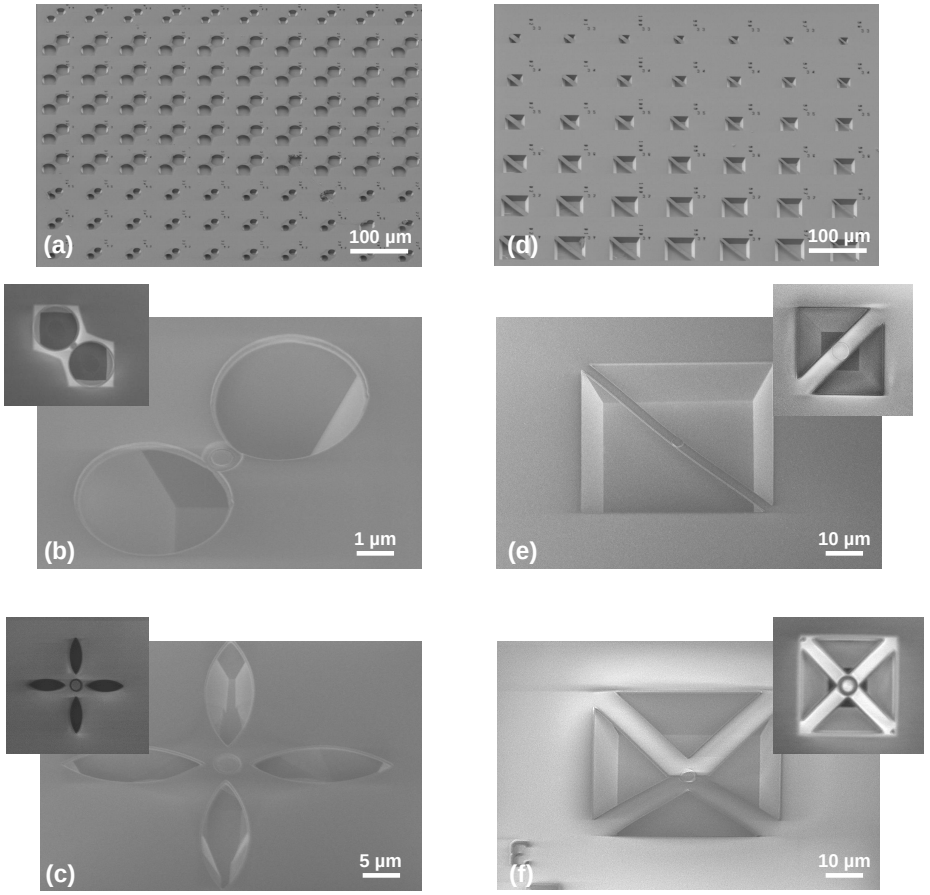

Figure 5.16: Scanning-electron microscopy (SEM) images of Ge-on-SOI micro-disks on freestanding SiO_2 beams. (a), (b), and (c) show uniaxial and biaxial beams with curved edges, while (d), (e), and (f) show similar beams with straight edges. Significant number of devices are bent downwards. Devices are capped with 200-nm-thick PECVD SiO_2.

downwards-bent, presumably due to the PECVD passivation layer (figs.5.16 (e) & (f)).

If we consider upwards bending, we can summarize the following. It is found that in the reference case, without adding the PECVD oxide on top of the structure (fig. 5.17 (a) left column), higher tensile strain values are obtained at the lower side of the micro-disk, while the top of the disk faces more compression. This is due to the larger Ge thickness compared to the BOX, opposite to previously obtained distribution using the GOI stack with Ge being thinner than the BOX. It can be stated that the BOX thickness and stress are not enough to impose tensile strain throughout the whole Ge disk thickness. This can be clearly noticed on the top side of the disk which has a total strain of nearly 0.2% which is the initial strain value before suspension. In fact, Ge being thicker than the BOX affects the distribution of the strain within the BOX layer, due to the initial tensile strain within the Ge disk ($\sim 0.2\%$) causing it to shrink after releasing the structure. This effect can be seen in the strain distribution within the BOX layer, where upwards bending is expected to result in compressive strain at the bottom side of the beam. However, underneath the disk region the bottom side of the beam is tensile-strained, while everywhere else, the bottom side of the beam is compressed. Adding the PECVD SiO_2 layer flips the strain distribution across the Ge thickness, such that the top side of the disk is tensile strained (fig. 5.17 (a) right column). Additionally, with the PECVD layer, the bottom side of the beam is compressed, while the top is tensile-strained. A maximum volumetric strain of 0.4% is estimated at the top side of the disk. The tensile strain values are higher in the case of using a PECVD layer in this Ge-on-SOI stack, yet not as high as required, and even lower than the previously achieved values using the GOI wafer. Considering the case of downwards bending, the beam is expected to be tensile-strained at the bottom side and compressed on top, and this holds for both cases with and without depositing the PECVD layer (fig. 5.17 (b)). The tensile strain values are also higher in the case of using the PECVD layer (fig. 5.17 (b) right column), similar to the upwards-bending case. However, this enhancement is not useful, because it occurs within the Ge-SOI interface region, which is full of defects.

To sum up, figs. 5.18 (a) and (b) plot linear maps of strain across the thickness of Ge, measured at the center of the disk ($x = 0$), for upwards and downwards bending, respectively. Black lines are used for Ge disks with no PECVD cap layer on top, while red lines represent the case of using a 200-nm PECVD SiO_2 cap layer, with an initial built-in 0.4 GPa compressive stress. Dotted, solid, and dashed lines are used for BOX layers with initial built-in compressive stresses of 0.5, 1, and 1.5 GPa, respectively. For upwards bending, adding the PECVD layer flips the tensile strain distribution from being higher at the bottom side of the disk, to being higher at the top side. While for downwards bending, the tensile strain is higher at the bottom side of the Ge disk in both cases.

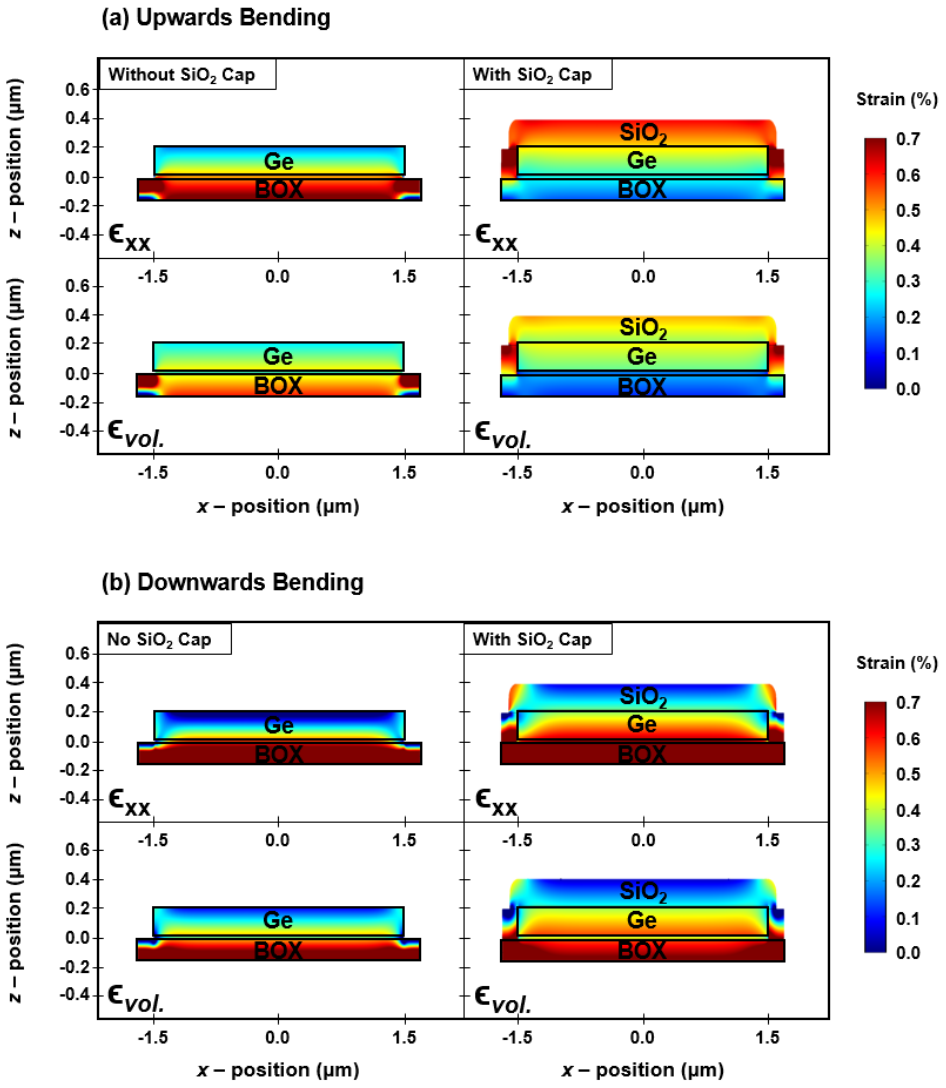

Figure 5.17: Cross-sectional strain maps based on computer simulations of Ge-on-SOI micro-disks on freestanding uniaxial SiO_2 beams. Ge disk diameter is 3 μm and beam length is 10 μm for all cases. All figures in (a) represent upwards-bent devices, while figures in (b) represent downwards-bent devices. Figures on the left column demonstrate the case of not using a PECVD cap, which is not fabricated and taken only as a reference. Figures on the right column demonstrate the actual devices with 200-nm PECVD SiO_2 on top required to protect the SOI layer. Mapped strain values are ϵ_{xx} and $\epsilon_{vol.}$ which are the normal strain component along the beam direction, and the volumetric strain, respectively.

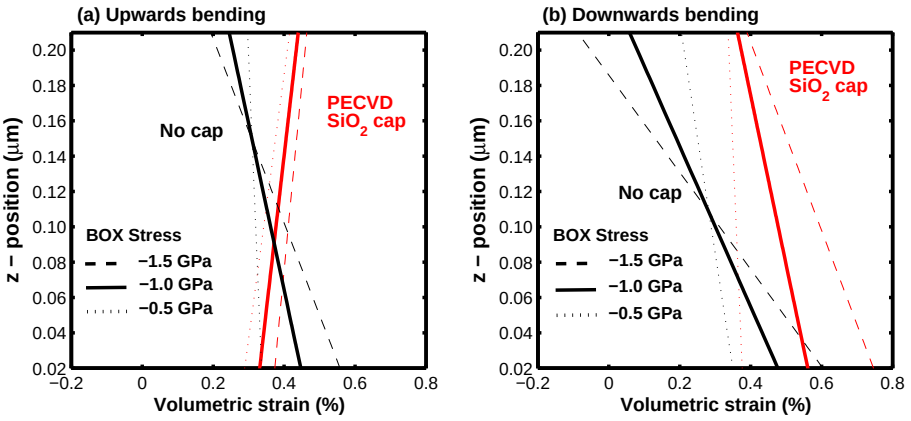

Figure 5.18: Linear-map of volumetric strain across the thickness of a Ge-on-SOI micro-disk on a freestanding SiO_2 beam, showing the effect of adding a PECVD SiO_2 cap layer. Ge disk diameter is 3 μm and beam length is 10 μm for all cases. The strain is mapped across the Ge layer, at the center of the disk ($x = y = 0$). Figure (a) considers upwards-bent beams, while (b) considers downwards-bent beams. Black lines are before adding the PECVD cap, with dotted, solid, and dashed lines are for the cases of 0.5, 1.0, and 1.5 GPa of initial compressive stresses assumed in the BOX layer. Red lines represent the same conditions after adding a 200-nm PECVD SiO_2 layer with -0.4 GPa stress.

An important outcome to remark, is that adding the PECVD layer slightly enhances the tensile strain compared to the non-capped case, but at the same time, limits the effect of the BOX layer as a stressor, or in other words, counter-acts its effect in straining the Ge disk. This is expected as the PECVD SiO_2 and the BOX layers both tend to expand after suspension, having the same fixed boundaries at both sides of the beam, while the Ge disk dwells in the middle of the stack, within the neutral-axis region. In fact, being within the neutral-axis region, some parts across the thickness of the disk might be tensile strained, while the other parts are being compressed, as shown in fig. 5.18 (b) (-1.5 GPa BOX stress). Counter-acting the effect of the BOX is also evident in figs. 5.18 (a) and (b), in which dotted (-0.5 GPa) and dashed (-1.5 GPa) lines account for the cases of slightly and heavily stressed BOX layers, respectively. It is noticed considering the black lines (without PECVD cap) that increasing the initial stresses in the BOX layer correspond to increasing the maximum tensile strain. However, increasing the maximum achievable tensile strain is accompanied with a degradation of strain homogeneity, represented in an increase in the slope of these lines. For instance, considering the upward bending case without PECVD, and the lowest-stress BOX shown in the dotted line, it is obvious that the strain is nearly fixed across the Ge thickness ranging from $\sim 0.32 - 0.35\%$. Increasing the BOX stresses to -1.5 GPa shown in the black dashed line, increases the maximum strain value to approximately 0.55%, yet, accompanied with a significant variation of strain values ranging from 0.55% down to $\sim$0.2%. This variation in the resulting strain values is decreased by using a PECVD cap layer. For instance,

considering the same case of upwards bending, and assuming an initial BOX stress of -1.5 GPa, the variation of strain reduces to a range from 0.38 - 0.47% when the PECVD cap is used. This effect is also true for downwards bending, indicating that the PECVD cap forms a limiting factor on the resulting strain, and results in an enhancement of its uniformity. This effect will be clearly observed in the next section on the strain dependence on the beam length.

5.8.1.2 Beam Length Dependence

The effect of the beam dimensions, namely beam length, on the resulting strain is studied in this section. Concentrating on the upwards-bending case, simulations were done for three cases of different BOX built-in stresses. Figure 5.19 shows the resulting volumetric strain (%) for different beam lengths, varying from 10 to 90 μm. Red lines represent the case of using a PECVD cap layer, while the black dashed lines represent the case of no cap layer used, taken as a reference. Figures 5.19 (a), (b), and (c) are simulation results assuming BOX built-in stresses of 0.5, 1.0, and 1.5 GPa, respectively. On each dataset, there are three lines labeled as 1, 2, and 3, corresponding to three positions across the Ge-disk thickness at which the value of the strain is measured. Inset in fig. 5.19 (a)

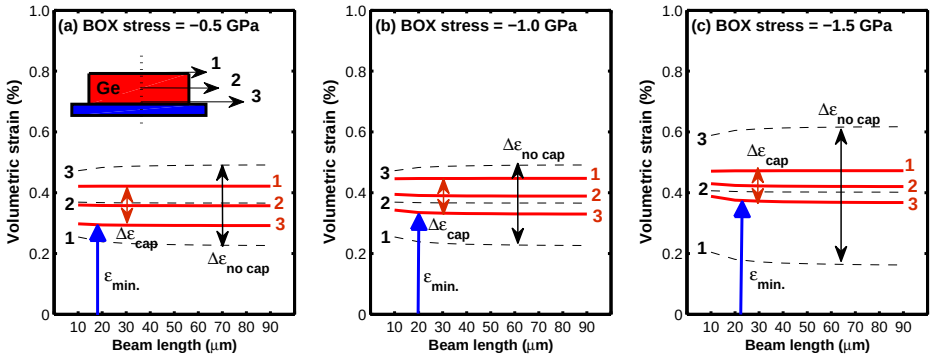

Figure 5.19: The effect of beam length on the resulting total strain value within Ge-on-SOI micro-disks on upwards-bent freestanding SiO_2 beams. (a), (b), and (c) assume different initial compressive stress values in the BOX layer of 0.5, 1.0, and 1.5 GPa, respectively. Black lines represent the case before adding the PECVD cap, while red lines show the effect of adding the cap. Strain is measured at three locations on-top (1), middle (2), and bottom (3) points across the Ge disk thickness ($x = 0$). Adding the cap flips the strain distribution upside-down (for upwards bending fig. 5.18 (a)), and enhances the uniformity ($\Delta\epsilon_{cap} < \Delta\epsilon_{nocap}$), but it limits the maximum strain value within the disk consequently. Higher BOX stress results in higher possible tensile strain values within the disk (higher $\epsilon_{min.}$). The effect of beam length is negligible using Ge-on-SOI stack due to the thicker Ge layer, and the limited effect of BOX due to PECVD capping.

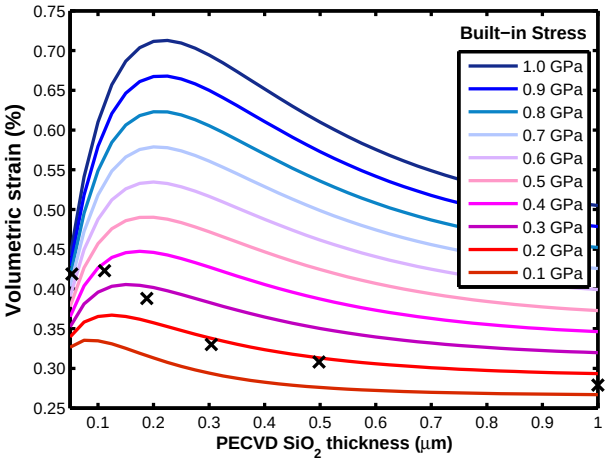

Figure 5.20: Parametric sweep using finite-element simulations summarizing the effect of the thickness and initial built-in stresses of the PECVD cap layer on the maximum resulting volumetric strain. Volumetric strain is measured at the top middle point on the Ge micro-disk. Cross points are estimated volumetric strain values based on experimental values of built-in stresses for PECVD SiO_2 layers with different thicknesses.

shows the position of these points across the Ge disk thickness. The separation between these lines gives an idea of the uniformity of strain distribution ($\Delta\epsilon_{cap}$ and $\Delta\epsilon_{nocap}$). While $\epsilon_{min.}$ indicates the minimum achievable tensile strain value.

It can be concluded from fig. 5.19 that beam-length dependence is negligible in the new wafer stack. This trend is true independent of the BOX built-in stresses within the studied range (figs. 5.19 (a) to (c)), even though, by increasing the BOX stresses, tensile strain values within the Ge disk are increased ($\epsilon_{min.}$). Homogeneity of strain distribution is enhanced in the case of using a PECVD layer, as seen in the red lines separated by $\Delta\epsilon_{cap}$ compared to the black lines (no cap) separated by the higher-value $\Delta\epsilon_{nocap}$. However, beam-length dependence is also negligible in the case of using a PECVD cap layer. This was not the case in the GOI devices, where the Ge disks are on-top of the beams, not in the middle of two counter-acting layers within the neutral-axis region, and having a lower thickness compared to the BOX layer.

5.8.1.3 PECVD Layer Engineering

In order to visualize the effect of built-in stresses and the thickness of the PECVD SiO_2 cap layer, a parametric sweep was done on those two factors while fixing the BOX stress to -1 GPa. From fig. 5.20, it is obvious that in our stack, a PECVD cap-layer thickness around 200 nm is optimum for achieving higher tensile strain, for all built-in stress values.

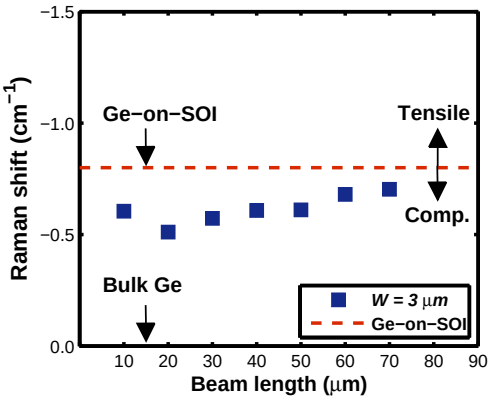

Figure 5.21: Raman shift values of Ge-on-SOI micro-disks on freestanding SiO_2 beams with different lengths. Beam width (W) is fixed at 3 μm. Ge-on-SOI stack experiences a reduction in tensile strain (lower Raman shift) upon suspension. The corresponding tensile strain is $\sim 0.4\%$ uniaxial.

This thickness was used in the fabricated devices. Thicker PECVD layer is not useful as it cancels the effect of the BOX and restricts the beam bending. In addition, thicker PECVD SiO_2 films have less built-in stresses (fig. 6.3), resulting in lower tensile strain values, as indicated by (x) marks on fig. 5.20 based on experimental values. Increasing the built-in stresses is not straightforward, especially that it is associated with degrading the optical properties of the film. Moreover, annealing is required after deposition to enhance the film quality, contributing to further reduction of built-in stresses (fig. 6.3).

5.8.2 Raman Spectroscopy

Strain characterization of Ge-on-SOI micro-disks on freestanding SiO_2 beams with different lengths was conducted. Beam width (W) is 3 μm for all devices. Excitation conditions are shown in table 5.2, and exposure under three excitation powers was done to eliminate the effect of heating as discussed in section 5.6.1. Degradation of strain in Ge-on-SOI freestanding structures is confirmed as shown in fig. 5.21. In fact, tensile strain after beams suspensions is lower than the initial tensile strain in the Ge-on-SOI wafers, indicating that the disks are mostly compressed relative to the initial 0.2% state. This is also concluded from simulations, where the initial tensile strain of the Ge disk before suspension was set as 0.2% biaxial, corresponding to approximately 0.4% volumetric strain ($\epsilon_{xx} = \epsilon_{yy} = 0.2\%$). However, the maximum resulting volumetric strain after releasing the structure is around 0.4%, while most of the disk regions are strained below this value, as demonstrated in the cross-sectional maps in fig. 5.17. A Raman shift value of 0.7 cm^{-1} corresponds to a uniaxial strain of 0.46%, in good agreement with the volumetric strain values $\epsilon_{vol.}$ predicted by simulations (fig. 5.17). Moreover, the dependency on beam length is negligible, in consistence with simulation results presented in section 5.8.1.2.

5.9 Summary

In this chapter, the origin of the tensile strain obtained by freestanding SiO_2 beams is elucidated using simple theory and computer simulations. Finite-element simulations were conducted to form a better understanding on the strain orientation, distribution, and value within Ge micro-disks on freestanding SiO_2 beams, fabricated using GOI wafers (100 nm Ge / 145 nm BOX). The impact of uniaxial and biaxial beams on the strain orientation was clarified, showing more total change in volume in the case of biaxial beams. Examining the uniformity of strain distribution indicates higher tensile strain accumulation at the disk edges, which is preferable for whispering-gallery modes confinement. Enhancement of strain value, accompanied by a reduction in uniformity is expected for shorter beam lengths, in the studied beam-length range. As the strain in our structures originate from the initial built-in stresses in the buried-oxide layer, the impact of BOX stress and thickness was investigated. Higher BOX stress and thickness are required to increase the tensile strain values in the Ge disk on top. A wide variety of beam designs were fabricated, including uniaxial and biaxial beams, and characterized using Raman spectroscopy and photoluminescence (PL) measurements. A maximum uniaxial tensile strain of 1.3% was measured experimentally. Dependency of strain on beam design was confirmed to coincide with simulation results, with higher strain obtained using shorter beam lengths. Splitting of light and heavy-hole bands due to strain was observed through the PL spectra of Ge disks on beams with variable lengths, such that the splitting increases with higher strain as the beam length decreases.

The last section provides a comparison between previous results, and the same devices fabricated on Ge-on-SOI wafers used for doping (200 nm Ge / 20 nm SOI / 145 nm BOX) in chapter 4. It was shown that tensile strain values are degraded in the new stack, with negligible dependency on the beam dimensions. This behavior was confirmed using Raman spectroscopy, and can be attributed to two main reasons: firstly, Ge layer being thicker than the BOX, and usage of PECVD SiO_2 as a passivation layer. Initially-stressed PECVD layer counter-acts the effect of BOX, due to fixed boundaries at both sides of the beam while the Ge disk being encapsulated in the middle of the stack. This cap layer was found to enhance the uniformity of strain within the Ge disk, but reducing at the same time the maximum strain value. In conclusion, GOI wafers are better in terms of strain application, while Ge-on-SOI wafers are more suitable for doping. As the strain is the main factor in transforming Ge into an optical gain medium, GOI wafers will be used in optimizing the final devices, as presented in chapter 6.

Chapter 6

Germanium Micro-disks on Freestanding SiO_2 Beams

"Electromagnetic waves are like living creatures, they sense the surroundings and get affected by the boundaries, then they adapt to ensure their survival"
Prof. Muhammed Kamil Abd Al-Azeez

6.1 Introduction

In this chapter we demonstrate the main devices in this project, implementing a combination of a simple cavity and a freestanding MEMS-like structure, motivated by the highly-strained freestanding structures proposed in literature, yet, lacking an optical cavity. Ge micro-disks were fabricated on freestanding SiO_2 beams using GOI wafers, and investigated in details for potential monolithic operation due to tensile strain. Device structures are introduced with a detailed description of the fabrication process. This study is supported by computer simulations and experimental characterization of tensile strain and optical performance of the devices. Laser microscopy imaging, Raman spectroscopy, and photoluminescence measurements were conducted and the results are discussed thoroughly. Concentrating on the behavior of whispering-gallery-mode (WGM) resonances to form a better understanding of the limiting factors that prevent monolithic operation, and the additional requirements for an efficient band-engineered bulk Ge. Sharp-peak WGMs were observed within the direct-gap of 100-nm-thick intrinsic Ge micro-disks, due to $\sim 0.7\%$ uniaxial strain.

Parts of this chapter are published in references [3, 4, 6].

6.2 Ge Micro-Disks & Rings

Ge micro-disks have gained a lot of attention during the last few years for lasing purposes, due to their simple structure, high-quality-factor (Q-factor) whispering-gallery modes (WGM), and there flexibility in terms of strain engineering. Previous works concentrated on engineering the strain of Ge micro-disks on pillars [56], pedestals [55, 57, 89, 29, 30], or on thick insulating films [131, 181]. In this work, we propose and demonstrate fabricating Ge micro-disks on freestanding beams using Ge-on-insulator (GOI) wafers. GOI wafers provide a flexible platform, allowing separate engineering of Ge as an optically-active layer, and manipulating the buried oxide (BOX) as a source of tensile strain. Several groups have reported observing WGMs within the direct-gap of Ge micro-disks and rings, excited by optical [131, 89, 181, 55, 56, 57, 29, 123] or electrical [181] pumping. Other low-quality-factor modes within micro-resonators, often attributed to Fabry-Perot (FP) modes, were also reported [55, 56, 57]. Sharp-peak WGMs are usually observed in 2 μm to 4 μm-diameter disks. Disks with smaller diameters are expected to suffer from very high losses, considering the wavelength range of Ge direct-gap [138]. On the other hand, for larger disks, the absence of sharp WGMs can be either due to the lower power-density of the pumping laser as the diameter increases, or a degraded strain distribution compared to smaller structures.

Confinement of sharp-peak WGMs has been reported in intrinsic [131, 89, 181] and doped [55, 56, 123] Ge micro-disks. However, Q-factors have a general trend towards degradation upon pumping, no matter being pumped optically [89, 55, 3] or electrically [181]. The highest reported WGM Q-factor of Ge direct-gap emission is 620 [131] (1350 [55]) for intrinsic (doped) structures. The highest Q-factor of 1350 [55] was attributed to the extremely low defect-density of Ge grown on GaAs substrates, in addition to the high 1% biaxial tensile strain imposed using Si_3N_4 stress liner, and $\sim 1 \times 10^{19}$ cm^{-3} *in-situ* doping [55]. Enhancement of Q-factors requires improving crystalline quality [17, 1], eliminating the surface roughness [138] and applying proper surface passivation, for example by thermal oxidation [182]. In addition to reducing the defects density especially at the Ge-substrate interface, although this is quite challenging for epitaxially-grown Ge-on-Si, it can be done for proof-of-concept studies by, for example, bonding of Ge rather than growing it [100]. Moreover, optimizing the band-engineering conditions through proper n-type doping [123] and tensile strain [57, 30] to increase the optical gain.

In this chapter we use 100-nm-thick Ge micro-disks, which are the thinnest compared to other works in this research area, as an optical cavity. This has two main advantages in terms of strain and single-mode confinement; Dielectric layers thinner than $\frac{\lambda_o}{2\times n_{eff}}$ are expected to support the lowest order modes of TE and TM polarization [132, 86]. TM modes get filtered out if the layer is thinned down below $\frac{\lambda_o}{4\times n_{eff}}$ [132, 86], providing a

dominant low-order TE modes confinement capability. This reduces unwanted spectral resonances that are confined within the cavity and enhances the probability of single mode confinement. From strain point of view, thinner sheets of the material are capable of handling higher strain values without fracturing [86]. Table 6.1 summarizes the research efforts targeting WGMs confinement within Ge micro-cavities, comparing this work with others in terms of the diameter ($2R$), strain, doping, and Q-factors relative to Ge thickness. Strain values indicate that extremely high tensile strain is not ultimately advantageous as previously thought, represented in the absence of sharp-peak WGMs in direct-gap ($> 1.7\%$ biaxial tensile strain) Ge micro-disks and rings [29, 30]. A Q-factor of 200 was achieved in this work, which is promising considering the thickness of Ge used.

		$2R$ (μm)	**Strain(%)**	**Ge** (nm)	**Q**	λ (μm)	**Ref.**
Doped	Disk	4	1%	300	1350	1.744	[55]
		4	1%	300	1000	1.998	[55]
		6	1.45%	500	Broad	~ 2.1	[57]
		9	0.72%	250	100	~ 1.7	[183]
		6	1.75%	190	Broad	~ 2.2	[29]
	Ring	4-6	2%	380	Broad	2.3	[30]
Intrinsic	Disk	3 μm	0.7% —	100	200	1.8	This work
		3.6	-	1000	700	1.565	[89]
		6	-	900	477	1.578	[181]
	Ring	1.22 μm	-	300	620	~ 1.63	[131]

Table 6.1: Review of Ge direct-gap whispering-gallery-mode resonances
‡ Notes:
- $2R$ is the diameter of the disk/ring (2×radius)
- The symbol — indicates uniaxial strain.
- 'Broad' indicates broad-peak resonances with low Q-factor and no exact value mentioned in the publication.
- Doped devices have a concentration of 1×10^{19} cm^{-3}, except for [30] 2.5×10^{19} cm^{-3}.
- All doped devices use *in-situ* doping.
- Some works grow Ge on GaAs to reduce dislocations [55, 183].
- All reported Q factors are measured at room temperature.
- Pumping is optical for all reported values except for [183].

6.3 Structure Layout and Fabrication

An overview of the fabrication process used throughout this project is summarized in this section. The target is to realize a combination of Ge micro-disks, with diameters ranging from 1 - 10 μm, on freestanding SiO_2 beams for strain applications. Wafers used in this chapter are GOI wafers with a stack of 100-nm Ge/ 145-nm SiO_2. A detailed description of the processes is given below, including Ge cleaning, patterning using Reactive Ion Etching (RIE), surface passivation using PECVD SiO_2 and its effect on strain, SiO_2 patterning using RIE and wet-etching, and Si anisotropic wet-etching using Tetramethyl-ammonium hydroxide (TMAH). A sketch of the fabrication process is shown in fig. 6.1. Details of some fabrication processes are given in Appendix A.

Eight-inch commercially-available GOI wafers were coated with thick optical photo-resist and diced into 4 cm× 3 cm chips. Initial cleaning of the chips was done starting with a solvent cleaning step using Acetone and IPA, to dissolve any remnant photo-resist or organic contamination. Acid cleaning is also necessary to remove any native oxide on the surface and etch few atomic layers off of the top Ge layer (step (1) fig. 6.1).

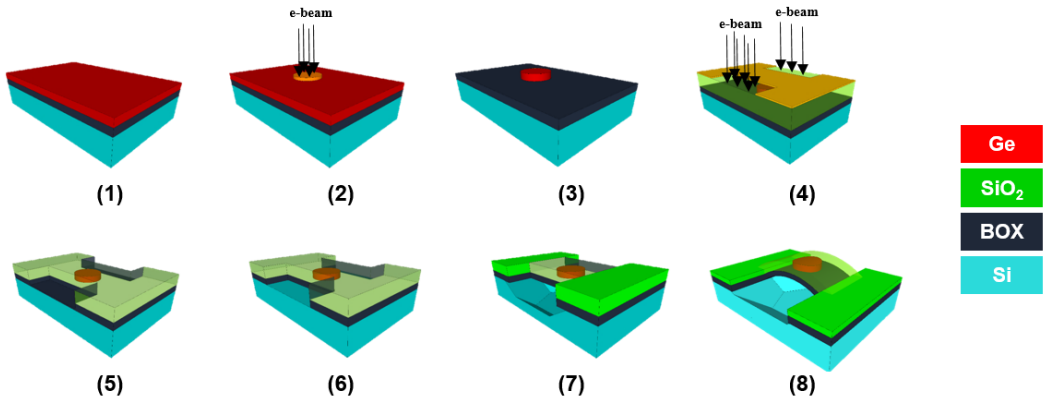

Figure 6.1: 3D sketch of the fabrication process[(a)]: (1) Cleaning the wafers using Acetone, IPA, HF, and HCl, (2) e-beam exposure of HSQ as a patterning mask for Ge structures, (3) transferring the patterns onto the Ge layer using dry RIE, acid cleaning steps are done afterwards, (4) surface passivation using PECVD SiO_2 and e-beam exposure of ZEP520A as a patterning mask for SiO_2 beams, (5) PECVD and buried SiO_2 patterning using dry RIE down to the thickness of $\sim$ 20 nm, followed by (6) wet-etching of the left-over BOX using HF [(b)], and finally (7) releasing the SiO_2 structures by local anisotropic wet-etching of bulk Si using TMAH. (8) Shows the final structure with the beam deflected upwards.
[(a)] This process is shown for GOI wafers, it also applies for Ge-on-SOI wafers given that Ge-on-SOI micro-disks are etched in steps 2 and 3.
[(b)] Less than 10 nm PECVD SiO_2 remains after this step in the case of GOI, while 200 nm is left in the case of Ge-on-SOI to protect the SOI layer (section 5.8).

This is important especially before any dopant diffusion process. Hydrofluoric (HF) and Hydrochloric (HCl) acids were used, in the form of 20:1 diluted buffered HF and 36% diluted HCl. A typical processing duration is 10 and 30 seconds, respectively. These acids are typically used in literature, and their effect on surface termination and roughness has been studied [184]. Oxide-free, Hydrogen or Chlorine-terminated surface is obtained by using HF and HCl, respectively, with a reduced surface roughness in case of HCl compared to HF [184]. Table 6.2 lists the etching rates of the commonly used chemicals throughout the fabrication process, including HF and HCl. Cleaning processes are expected to etch away $2-3$ nm Ge at most.

Process	**Material**	**Chemicals**	**Etch Rate** (nm/min)
Cleaning	Ge	Acetone & IPA 20:1 BHF HCl 36%	- 1.5 2
SOD Removal	SOD	20:1 BHF	180
Disks Dry Etching	Ge HSQ	SF_6 & O_2	200 50
Beams Dry Etching	PECVD SiO_2 Thermal SiO_2 ZEP520A	CHF_3 & Ar	28 25 29
	PMMA950-A11 [(a)]		46
Beams Wet Etching	PECVD SiO_2 PECVD SiO_2 [(b)] Thermal SiO_2	20:1 BHF	90 60 30
Suspension	Si	TMAH 22%	9

Table 6.2: Summary of etching rates
[(a)] 4-μm-thick resist used for thick BOX (2 μm) patterning.
[(b)] Annealed at 650 °C for 10 minutes. Note that the dry-etching rate is the same for PECVD SiO_2 before and after annealing, while wet-etching rates differ.

6.3.1 Ge Patterning

Ge layer is to be patterned into micro-disks with diameters ranging from 1 - 10 μm. Ge patterning is done immediately after cleaning, where a layer of a negative-tone e-beam resist, namely, HSQ is spin-coated on Ge. HSQ, or Hydrogen SilsesQuioxane, is a high-resolution e-beam resist that is suitable as a dry-etching mask [185]. Especially that it tends to form an SiO_x film upon exposure, which gets hardened using oxygen plasma during dry etching, providing significant selectivity against Ge (table 6.2) [185]. We have used 2% and 6% HSQ solutions, resulting in 30 nm and 120 nm film thicknesses when spin-coated at 3000 rpm. Choice of HSQ thickness depends on the thickness of Ge to be etched, for instance, 50 nm HSQ is enough to etch approximately 200 nm of Ge. For GOI wafers with 100-nm-thick Ge, 2% HSQ was used. Soft baking at 80 °C

is required before exposure for 4 minutes. A dose test have been conducted initially to optimize e-beam exposure conditions for micro-disks patterning. A base dose of 1800 $\mu C/cm^2$ was found to be suitable for 2% HSQ (30 nm). Table 6.3 lists the optimum doses for various types of resists, used throughout fabrication processes in this project. Each value was found using a separate dose test. Development of HSQ is done using MF-319 developer for 1:40 minutes followed by DI water rinsing (step (2) fig. 6.1). Hard baking is also required before dry-etching, which is done at 240 °C for 4 minutes.

Material	**E-beam Resist**	**Thickness** (nm)	**Dose** ($\mu C/cm^2$)
Ge	HSQ 2%	30	1800
	HSQ 6%[(a)]	120	1400
SiO_2	ZEP520A	460	270
	2× ZEP520A[(b)]	840	388
	PMMA950-A11[(c)]	4000	750

Table 6.3: Summary of e-beam exposure doses
[(a)] 6% HSQ is thicker than 2% HSQ, however the required dose is less, and this is due to the higher percentage of HSQ in the solution, making it more sensitive to electrons exposure.
[(b)] Double coating of ZEP520A, soft-baking is done after the first and second coating at 180 °C .
[(c)] This resist is suitable for up to 2-μm-thick SiO_2 etching.

Dry RIE is then used to transfer the patterns onto the target Ge layer (step (3) fig. 6.1). A gas mixture of 36 sccm O_2 and 36 sccm SF_6 is introduced in a 30 mT vacuum chamber. Exact details of the etching recipe are provided in Appendix A.3. As shown in table 6.2, the etching rate is approximately 200 nm/minute, with a selectivity of $\sim 4:1$ relative to HSQ. After dry etching, removal of remnant HSQ is done by dipping the samples in 20:1 BHF for few seconds (3-5 seconds), etching off only 1.5-2.5 nm of BOX. 36% HCl cleaning is then used for 30 seconds, aiming to reduce surface roughness after etching [185]. Then the surface is immediately passivated by SiO_2 deposited using PECVD, as discussed below.

6.3.2 Surface Passivation

Surface passivation is required to protect Ge from the following wet-etching steps, although TMAH etching rate of Ge is insignificant. In fact, Ge can be used as a hard mask for Si etching using TMAH. Though, this passivation is necessary due to the week adhesion between Ge and BOX in GOI wafers, where Ge-O bonds at the interface are unstable and may dissolve in water, peeling off the Ge structures [100]. In the case of Ge-on-SOI wafers, it is required to protect the SOI layer during the wet-etching of bulk

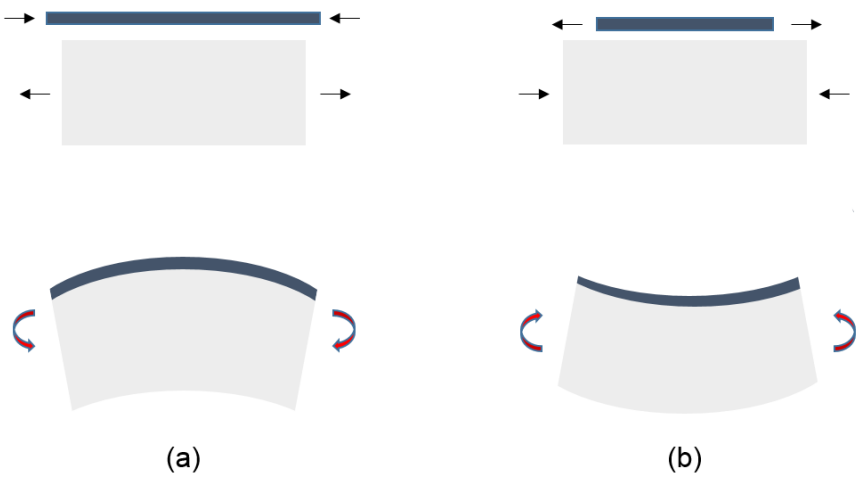

Figure 6.2: The effect of residual stresses of thin films on substrate curvature: (a) Residual compressive stresses within the deposited/grown film, the film tends to expand when patterned. (b) Residual tensile stresses, the film tends to shrink when patterned.

Si. 100-nm-thick SiO_2 layer is deposited on top of the structures using PECVD at 350 °C (step (4) fig. 6.1). However, there are two main consequences of this layer on our devices. Firstly, is the associated stress within this film which will affect the final strain distribution in our devices. It is found that in our devices, lower built-in stresses in the PECVD dioxide are preferable to obtain higher tensile strain in the Ge disks (chapter 5). The fact that the Ge disks are embedded between highly-stressed BOX, which is the main source of tensile strain after suspension, and the PECVD SiO_2 layer. And as has been previously shown in section 5.8, built-in stresses in the PECVD SiO_2 work on counter-acting the stresses in the thermally-grown BOX, eventually cancelling its effect in straining the Ge disks. And, secondly, the poor quality of the film degrades the optical properties, and provides voids for chemicals to attack Ge (and SOI) during wet-processing. Consequently, annealing at relatively high temperatures for defects curing is required.

Built-in stresses were studied for SiO_2 films with different thicknesses, grown thermally and deposited using PECVD for comparison. Thermal oxidation was done at 1000 °C, while PECVD SiO_2 was deposited at 350 °C. In-plane stresses affect the wafer curvature, depending on being compressive or tensile, and proportional to stress value, as shown in fig. 6.2. Built-in stresses can be calculated using Stoney's formula 6.1 [72], given the radius of curvature ($R_{c'}$) of the wafer induced by depositing a film of thickness (d_f):

$$\sigma_{built-in} = \frac{Y_s}{1-v_s} \cdot \frac{d_s^2}{6d_f} \cdot \left[\frac{1}{R_{c'}} - \frac{1}{R_c} \right] \tag{6.1}$$

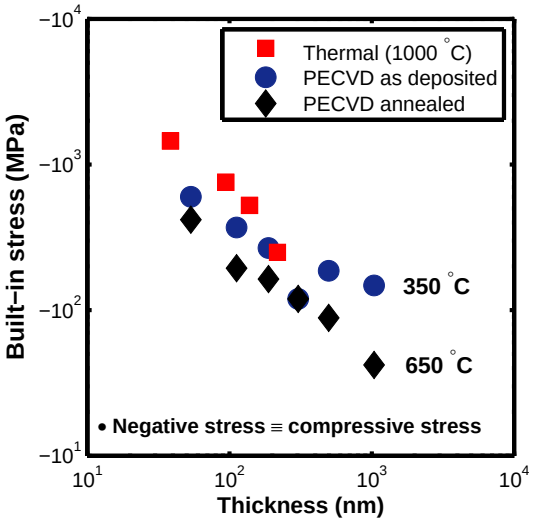

Figure 6.3: Calculated built-in stresses of thermally-grown and PECVD SiO_2 films with different thicknesses on Si. Thermal dry oxidation was done at 1000 °C, while PECVD films were deposited at 350 °C. Annealing of the wafers with PECVD oxide was done at 650 °C for 10 minutes in Nitrogen, which are the exact conditions used to cure the PECVD dioxide films in the final devices.

$\frac{Y_s}{1-v_s}$ is the biaxial elastic modulus of the substrate, where Y_s and v_s are Young's modulus and Poisson's ratio, respectively. The biaxial elastic modulus of a $\langle 100 \rangle$ Si wafer is found in literature to be 1.805×10^{11} Pa [186]. d_s and d_f are substrate and film thicknesses. R_c and $R_{c'}$ are the radius of curvature before and after film deposition. Radius of curvature was measured using Tencor FLX-2908 thin-film stress-measurement tool, which plots the wafer curvature using the reflection of a laser beam. Figure 6.3 plots the calculated in-plane stress values within SiO_2 films with different thicknesses. Thermal oxide has higher built-in stresses compared to PECVD-deposited oxide, due to the higher growth temperature [81, 177]. This agrees with previously-reported results in literature, such as MEMS-related studies on doubly-clamped SiO_2 beams for sensors, as in chapter 2 in ref. [135]. For PECVD dioxide, film stress was measured as deposited, and then re-measured after annealing at 650 °C for 10 minutes in Nitrogen ambient. Higher temperatures are expected to further enhance the film quality, however, applicable temperatures are limited to avoid damaging the Ge quality. Annealing appears to reduce build-in stresses in the PECVD films (fig. 6.3), indicating an enhancement in film quality, which also reflects on better optical properties. Although this annealing step is necessary to enhance the passivation film quality, it will have a negative effect on dopants distribution if doped-Ge is used, or Si-Ge inter-diffusion in the case of Ge-on-SOI wafers. This inter-diffusion effect forming Si_xGe_{1-x} alloys within the Ge micro-disk is confirmed using Raman spectroscopy, as presented in section 4.5.1.

It seems that increasing the SiO_2 film thickness decreases the built-in stresses. This relaxation of in-plane stresses in the thin film, are balanced by an increase in stresses within the Si wafer. This result also agrees with previous MEMS-related studies on thin SiO_2 films, reporting an increase of in-plane stresses for thinner films [80, 177]. For our devices, because Ge is on-top of the BOX layer, PECVD SiO_2 layer has to be ideally with no stress and as thin as possible to allow for beam bending to induce strain within the devices. Accordingly, for the final devices, a 100-nm-thick PECVD layer was deposited and annealed at 650 °C for 10 minutes in Nitrogen. And in later processing stages discussed below, this layer was exposed to HF to reduce its thickness below 10 nm, where it has nearly no effect in terms of strain on the Ge disks, as confirmed by Raman spectroscopy and photoluminescence measurements later in this chapter, and previously in chapter 5.

6.3.3 Beam Patterning and Suspension

After SiO_2 deposition, patterning of the beams is then done in subsequent dry and wet etching processes. To dry-etch the beams, patterns are first exposed on a positive-tone e-beam resist (step (4) fig. 6.1). A 460-nm layer of ZEP520-A is spin-coated on the chips and baked at 180 °C. This thickness is enough to etch approximately 500 nm SiO_2, where the dry etching rates of PECVD and thermal oxide are nearly the same. A dose of 270 $\mu C/cm^2$ is used after several dose tests to expose the beam patterns. A dual coating of ZEP520-A can be used to get an 840 nm layer, to etch thicker dioxide layers, yet a higher dose of 388 $\mu C/cm^2$ should be used. Patterns development is then done using ZED-N50 for 2 minutes, followed by IPA for 30 seconds. Dry RIE etching is then done using CHF_3 and Ar gases, leaving approximately 20-40 nm BOX un-etched (step (5) fig. 6.1). This way an undamaged bulk Si surface will be exposed by wet HF etching of the remaining 20-nm-thick SiO_2. This is important for the next alkali (TMAH) wet-etching step, because TMAH etching of Si is sensitive to surface roughness. The dry etching rate of thermal oxide was 25 nm/minute, while the PECVD dioxide is etched with a rate of 28 nm/minute. Remaining resist is then stripped using oxygen plasma ashing. The final stage of suspending the structures is done using wet processes. Starting with 20:1 BHF to remove the remnant BOX, and expose the surface of bulk Si (step (6) fig. 6.1). This step is critical because the PECVD SiO_2 layer that encapsulates the Ge structures is also etched during this step, with two to three-times higher etching rate. This step can be engineered to reduce the PECVD SiO_2 thickness for strain enhancement, where $<$ 10-nm-thick PECVD SiO_2 remains on top of the devices. Immediately after the BHF etching, TMAH is used to locally etch bulk Si and suspend the structures (step (7) fig. 6.1). The etching rate at room temperature is $\sim$ 9 nm/minute. For the structures to be suspended, they have to by aligned with $\langle 100 \rangle$ directions, because of the anisotropy of TMAH etching along the $\langle 110 \rangle$ directions. In other words, the beams have to be rotated

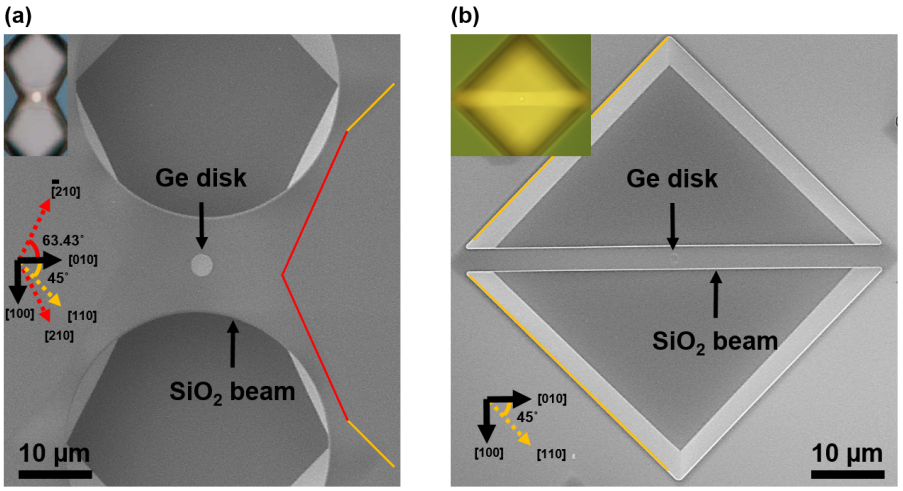

Figure 6.4: Scanning electron microscopy (SEM) images of Ge micro-disks on freestanding SiO_2 beams with different designs highlighting the stable crystal orientations after TMAH etching: (a) Curved-edge beams, and (b) rectangular beams. Insets are optical images of similar devices. The device shown in (a) is the 3-μm-disk device characterized in the later sections of this chapter (sections 6.6.2.2 & 6.6.2.1), in which sharp-peak whispering-gallery modes were observed.

45° relative to the ⟨110⟩ notch.

Residual compressive thermal stresses within the BOX layer get partially relieved upon beams suspension [79]. Built-in compressive stresses exist due to thermal oxidation process, given that the thermal expansion coefficients of Si and SiO_2 are different [81]. Stresses are partially relieved by elongation of the dioxide layer, and consequently the beams tend to deflect out-of-plane because of the fixed boundaries [81, 79] (step (8) fig. 6.1). BOX layer expansion will also expand the Ge layer on top, yet the total strain within the Ge layer will be less than that of SiO_2 due to germanium's higher Young's modulus, or in other words, lower length expansion due to unit stress applied. At the same time, beam deflection will affect the strain distribution within the Ge disk and the beam. Upward bending is expected to impose tensile strain on the top side of the beam, while the bottom side gets compressed. Somewhere in the middle between these regions, exists a plane with no change in length, often referred to as the neutral plane. The position of the neutral plane is exactly in the middle in a simple single-layer defect-free beam. Yet, this is not the case in our devices as the Ge disk would also shift this neutral plane. Cross-sectional distribution of the resulting strain is discussed in details in chapter 5.

6.4 Final Device Structure

Devices with various beam designs were fabricated, as summarized in section 5.5, including simple rectangular beams and beams with curved edges (fig. 6.4). After scanning-electron-microscopy (SEM) and Raman spectroscopy characterization, curved-edge beams (fig. 6.5) were found to be advantageous over standard rectangular beams in terms of stability and deflection profile. Rectangular beams are more susceptible to fatigue, torsion and deflecting in complicated profiles deviating from the first eigen-mode shape. While beams with curved edges are more consistent in their deflection profile, as shown in fig. 6.6, yet, being either upwards or downwards. Wider-section boundaries (pads) are presumably the reason behind this improved mechanical stability. Downwards-bending is expected to originate from stiction effects due to the wet-etching processes. Gas-etching is expected to mitigate this issue, such as Xenon di-fluoride (XeF_2) used for MEMS devices, however, such processes are isotropic and aggressive, reducing the control over the boundaries. Such techniques are not necessary as most of the devices were upwards bent. Another privilege of curved beams, which is the motivation behind their design, is the smooth stress gradient along the beam direction, consequently avoiding stress-concentration points at sharp boundaries [33, 31], as the case in rectangular beams [35]. This enhances the survivability of the beam after suspension, and concentrates the resulting tensile strain within the disk region [33, 36].

Although curved-beams can be designed in uniaxial and biaxial forms, our study will concentrate on the uniaxial design. Because of its simpler design and manipulation, and less required optimization for strain distribution and profile [31, 38], which - in the case of biaxial beams - has to be carefully designed based on computer simulations [36, 85]. Deflection profiles of biaxial beams are also more difficult to control due to the multiple boundaries. Consequently, most of the recent work on freestanding MEMS-like structures have concentrated on uniaxial beams for similar reasons [35, 33, 87, 31, 38]. In fact, as stated in the literature review (fig. 2.1), direct-gap Ge was first achieved by uniaxial Ge beams [31]. The work on optimizing strain distribution within biaxial-strained freestanding structures is still undergoing [36, 85], and will be taken into consideration for future continuation of this work (section 7.2.2). The final device structure is shown in fig. 6.5 (a) in which Ge micro-disks are dry-etched on SiO_2 beams with curved edges. SiO_2 beams were defined by circular holes centered around the micro-disks (fig. 6.5). Manipulating beam dimensions and suspension area to control the strain is done by changing the diameter of the holes' openings (L in fig. 6.5 (a)). Diameters of the holes define the beam length (L) and the minimum separation between them defines the beam width (W). Beam design parameters, L and W, were set to 36 μm and 12 μm respectively. The choice of the holes separation, or beam width (W), is based on varying the disks diameters up to 10 μm, hence the beam width was designed slightly wider by 2 μm for alignment tolerance and beam stability with large disks on top. When the Ge

disk diameter is comparable to the beam width, a remarkable deformation of the beam is expected, the fact that Ge is initially tensile strained tending to shrink upon releasing the structure. This is obvious in laser-interference microscopy (LIM) images of 9 and 10 μm disks, fig. 6.6. While this deformation is less likely in the case of smaller disks (1 - 3 μm disks, fig. 6.6). And accordingly, the holes diameter, or L, is chosen such that the resulting freestanding beam length is larger than the beam width (12 μm), and as short as possible based on the privilege of shorter beams in terms of strain. The circular-holes with 36 μm diameter result in a total freestanding length of < 20 μm, due to the anisotropy of TMAH etching as explained below.

Beams were aligned with $\langle 100 \rangle$ directions of the Si substrate, as marked in the optical microscopy image in fig. 6.5 (b). It was found that the anisotropy of TMAH etching of Si through circular holes is pronounced along two directions: the standard $\langle 110 \rangle$ at 45°, and $\langle 210 \rangle$ at 63.4° relative to the beam direction $\langle 010 \rangle$, as shown in fig. 6.5 (b). Consequently, $L = 36$ μm results in less than 20 μm final beam length due to TMAH anisotropy. Beams were suspended after TMAH etching, and deflected mostly upwards, as confirmed by SEM and LIM images (fig. 6.6). According to theory, Ge micro-disks are mostly tensile strained in the case of upwards bending [79], as confirmed by cross-sectional strain maps (fig. 5.6). Remarkably, even if the beam is bent downwards, tensile-strained regions might exist within the bottom side of the disk, while the top side gets compressed. As a result, it can be stated that a mixture of tensile and compressively-strained regions exist within the disks, no matter the bending direction. Yet, upwards bending is expected to result in higher total tensile strain distribution within the disk [79]. According to the 3D height maps created by LIM imaging (fig. 6.6), most the disks, especially with diameters smaller than 6 μm, deflected upwards. For instance, in the case of the 3 μm disk, the SiO_2 beam was bent upwards with a maximum deflection of approximately 0.8 μm. Height variation due to bending (< 0.2 μm) contributes to strain inhomogeneity, which creates optical gain and loss regions within the same disk [55, 56, 57]. The effect of bending becomes significant for larger disks, as the disk might also affect the beam deformation, as seen for example for the 10 μm disk (fig. 6.6).

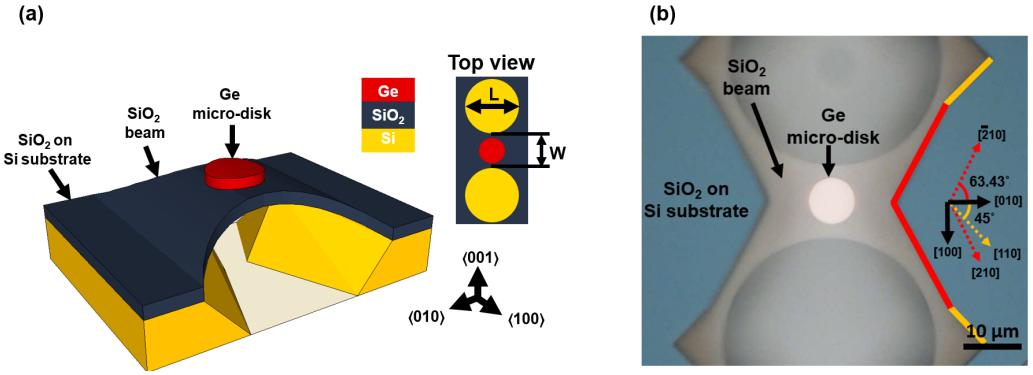

Figure 6.5: (a) 3D sketch, and (b) optical microscopy image of the final devices using GOI wafers.

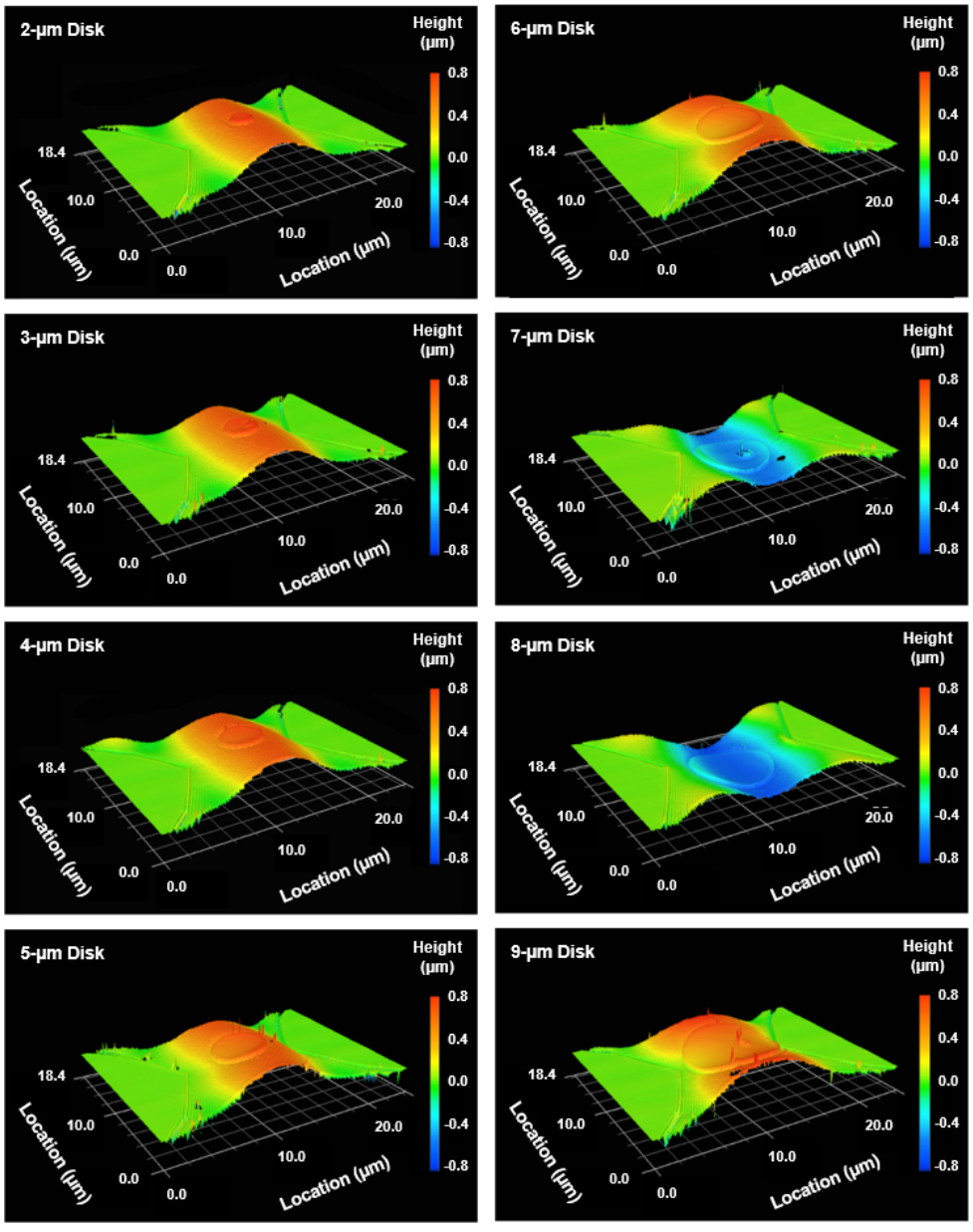

Figure 6.6: Laser-interference microscopy (LIM) images of Ge micro-disks on freestanding SiO_2 beams with curved edges (L=36 and W=12 μm).

6.5 Strain Characterization by Raman Spectroscopy

Raman spectroscopy is used to estimate the strain values within the Ge micro-disks. High resolution 3000 lines/mm grating is used for this test to determine the peak position accurately. This is based on the red-shift of the Raman peak of bulk Ge (301 cm^{-1}) due to tensile strain, according to the relation:

$$\Delta\omega = S \times \epsilon, \tag{6.2}$$

Where $\Delta\omega$ is the relative shift in wavenumbers, ϵ is the strain, and S is a proportionality factor. S depends on the strain orientation, and several values have been reported as summarized in table 5.1. A value of 152 cm^{-1} [31, 33] (390 cm^{-1} [75, 76]) will be used in our case, which has been reported for uniaxial (biaxial) strained Ge structures. Heating must be considered in freestanding structures as it induces additional red-shift in the Raman peak position, resulting in over-estimating the tensile strain value, as demonstrated in section 5.6.1. This can be accounted for by checking the power dependence of Raman peak positions, and extrapolating the values to find the limit at zero excitation point. Excitation was done using a green laser (532 nm) with 2 μm spot size, and exposure was accumulated for 10 seconds and averaged over 50 times. Experimental data points were fitted by Lorentzian functions to estimate the peak positions. A linear red-shifting with the rate of -0.18×10^{-4} $cm^{-1}/\mu W$ (-6.3×10^{-4} $cm^{-1}/\mu W$) was found for

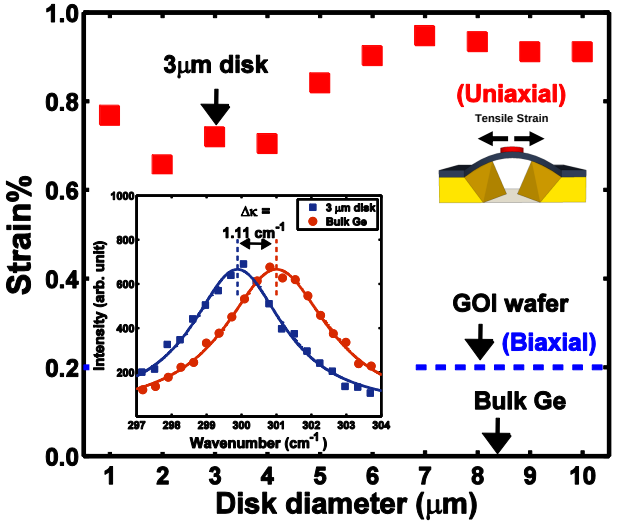

Figure 6.7: Tensile strain values of Ge micro-disks with different diameters on freestanding SiO_2 beams with curved edges (fig. 6.6, L=36 and W=12 μm for all devices). These values were calculated assuming a uniaxial tensile strain, while the GOI wafer strain value is biaxial. Inset shows the actual Raman spectra for bulk Ge and the 3 μm disk.

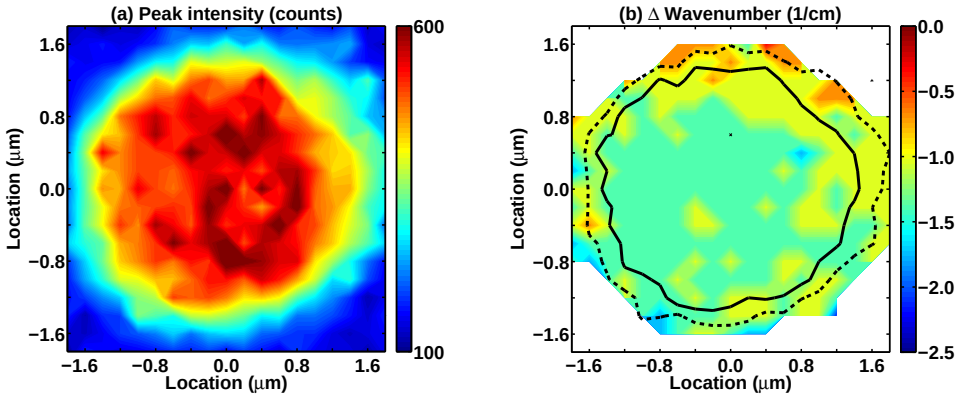

Figure 6.8: 2D Raman spectroscopy map of a 3μm Ge disk on a freestanding beam with curved edges, showing: (a) peak intensity that defines the disk region, and (b) actual Raman shift across the Ge surface.

the un-patterned GOI (3 μm Ge micro-disk on freestanding beam with curved edges), indicating more than 30$\times$ sensitivity to heating after suspension. Before releasing the SiO_2 beams, Ge disks were slightly tensile-strained ($\epsilon \approx 0.2\%$), presumably due to Ge-on-Si growth during the GOI wafer fabrication process by bonding. After suspension, tensile strain was enhanced for all disk diameters, as shown in fig. 6.7. Beam dimensions are the same for all the disks as clarified in the previous section. $S = 152$ cm^{-1} was used to calculate the values in fig. 6.7, assuming a uniaxial strain based on the outcomes of chapter 5. For example, a uniaxial strain of 0.78, 0.73, and 0.92% is estimated for disks with 1, 3, and 10 μm diameter. This corresponds to 0.29, 0.28, and 0.35% biaxial tensile strain, assuming $S = 390$ cm^{-1}. The maximum measured strain was 1.13% for the 8 μm disk. This value is mainly determined by the initial built-in stresses in the BOX layer, and the adhesion between Ge and BOX.

Besides the strain enhancement, its homogeneity is vital for Ge direct-gap emission. Inhomogeneity of strain is reflected onto variations in band-gap energies [26, 25]. Electrons accordingly have a higher probability of dwelling higher-strained regions, thus, having a larger optical gain value compared to less-strained regions. As a result, a mixture of optical gain and loss regions may exist within the same Ge structure, causing a reduction in the total overlap between resonant modes and gain regions [55, 56, 57]. A 2D Raman scan (200 nm resolution) was conducted on a 3 μm disk on a curved beam (fig. 6.4 (a)). Figures 6.8 (a) & (b) plot the Raman intensity and Raman shift across the top surface of the disk, respectively. Contour lines (6.8 (b)) with solid (dotted) black lines specify the disk regions with highest-intensity Raman peaks, above 400 (350) counts. These maps indicated a fairly uniform tensile strain of 0.73% (-1.11 cm^{-1}) distributed over the top surface of the $3-\mu$m disk. Stress relaxation at certain points, especially at the edges, might be originating from the poor adhesion between Ge and BOX.

6.6 Whispering-Gallery-Mode Resonances

Whispering-gallery-mode (WGM) resonances of Ge direct-gap emission were observed from a 3-μm-diameter disk on a freestanding SiO_2 beam with curved edges. An SEM images of this device is shown in fig. 6.4 (a), and an LIM image is shown in fig. 6.6. Here, we present a detailed study of these sharp-peak WGMs using computer simulations and room-temperature photoluminescence (PL) measurements.

6.6.1 Finite-Difference Time-Domain Simulations

3D Finite-difference time-domain (FDTD) simulations were conducted to understand the nature of optical modes existing in a 3 μm Ge disk on a freestanding SiO_2 beam, as shown in the inset of fig. 6.9. The choice of the disk dimensions was based on observing WGM resonances from the actual device. Stack thicknesses were also set to match the actual device (100-nm Ge on 145-nm SiO_2). Built-in material models use wavelength-dependent refractive indexes based on the famous E. Palik measurements [180], which are around 4.2 and 1.45 for Ge and SiO_2, respectively, around 1.7 μm.

Assuming the wave-guiding of transverse-electric (TE) modes only in 100-nm-thick Ge [132, 86], an in-plane electric field source $\vec{\mathcal{E}_{x,y}}$ was used to excite the structure. A Gaussian pulse centered around 1.7 μm was launched into the disk to mimic direct-gap emission of slightly-strained Ge. Simulation time was sufficient to ensure correct resonant modes monitoring. The simulated spectrum of the freestanding 3 μm disk is shown in fig. 6.9, with the surface plots of the out-of-plane magnetic field component $\vec{\mathcal{H}_z}$ of the resonant modes shown on top. Accordingly, the resonances can be identified as WGMs at 1506.8, 1559.9, 1625.4, 1707.2, and 1809.9 nm. Following the notation of $TE_{m,l}$, where m is the azimuthal number and l is the radial number of the WGMs. These modes can be labelled as $TE_{13,1}$, $TE_{12,1}$, $TE_{11,1}$, $TE_{10,1}$, and $TE_{9,1}$, respectively. Table 6.4 lists the effective refractive index values (n_{eff}) for these modes.

Mode	λ(nm)	n_{eff}	$^{(a)}n_{eff,calc}\|_{R=1.5\mu m}$
$TE_{9,1}$	1809.9	2.5125	1.729
$TE_{10,1}$	1707.2	2.57275	1.812
$TE_{11,1}$	1625.4	2.64574	1.898
$TE_{12,1}$	1559.9	2.746	-
$TE_{13,1}$	1506.8	2.837	-

Table 6.4: Effective refractive index of WGMs in fig. 6.9
$^{(a)}$ n_{eff} calculated using equation 2.9, assuming R = 1.5 μm and azimuthal mode numbers (m) extracted from simulations.

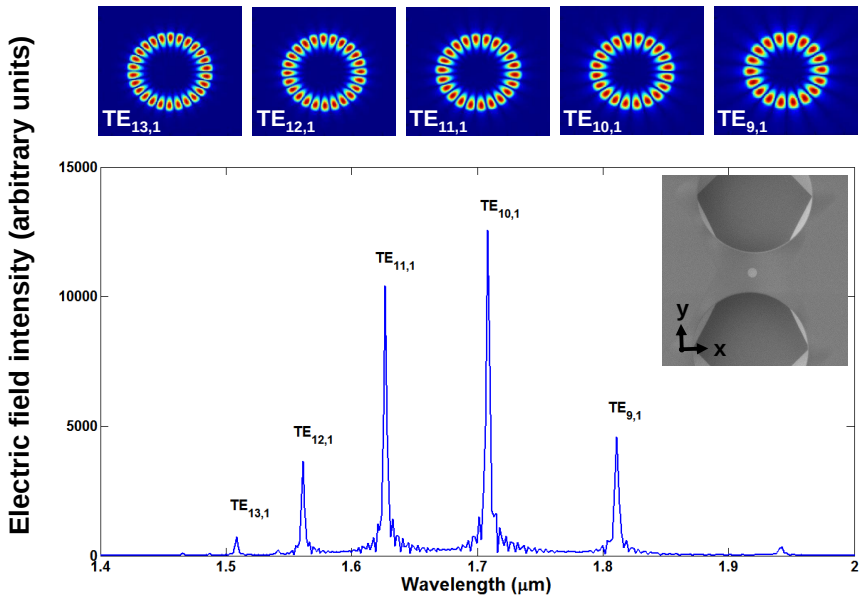

Figure 6.9: Spectrum of electric field ($\vec{\mathcal{E}}_{x,y}$) resonances in-plane of a 3 μm disk on a freestanding SiO_2 beam (shown in the SEM image inset). Confined modes with sharp peaks are whispering gallery modes as confirmed by surface plots (top) of magnetic field component ($\vec{\mathcal{H}}_z$).

6.6.2 Photoluminescence Measurements

Direct-gap photo-Luminescence (PL) of the devices was measured at room-temperature, using a free-space microscope set-up in which pumping and PL signal collection is done from top, and guided into a liquid-nitrogen-cooled extended InGaAs detector. Excitation was done using a continuous-wave laser with a wavelength of 730 nm, and using the exposure conditions listed in table 5.3. The laser beam is focused into a $\sim$2 μm spot at the sample surface using a 50$\times$ objective lens, at 400 μW excitation power. PL spectra of Ge disks with different diameters on freestanding beams with curved edges (fig. 6.6) are shown in fig. 6.10. The peak around $1.6 - 1.7$ μm corresponds to the direct-gap of slightly-strained Ge [17, 1, 165, 32, 95]. A red-shift in the spectra is observed relative to bulk Ge ($\sim$ 1.55 μm), as expected due to tensile strain confirmed by the Raman measurements. Measured strain values contribute to red-shifting the Ge direct-gap peak up to $1.63 - 1.64$ μm [26, 25]. Additional red-shift is mainly due to heating effects from laser excitation (figs. 5.12 & 5.13) [105, 16, 131, 107].

As appears from the spectra of different disk sizes (fig. 6.10), sharp-peak resonant modes were confined only in the 3 μm disks. Based on simulations, these resonances can be attributed to $TE_{11,1}$, $TE_{10,1}$, and $TE_{9,1}$ WGMs, as shown in fig. 6.11. Maximum

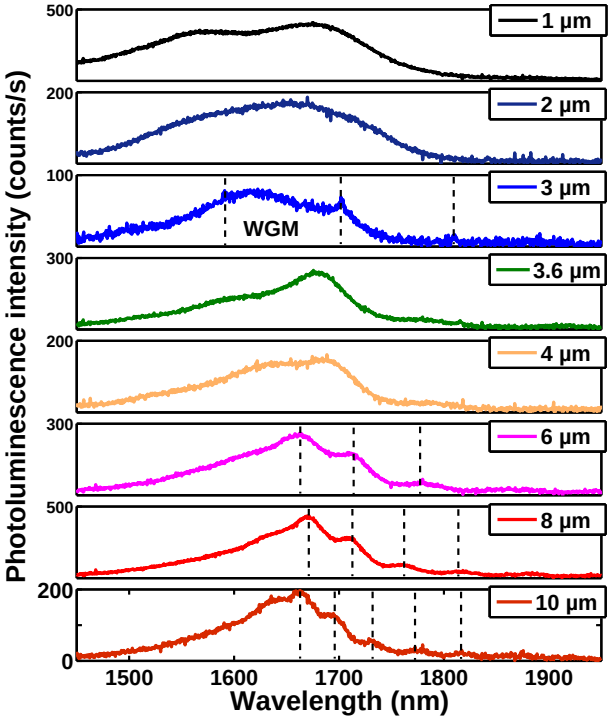

Figure 6.10: Photoluminescence spectra of Ge micro-disks with different diameters ranging from 1 to 10 μm on freestanding SiO_2 beams with curved edges. Sharp WGMs are observed in 3 μm disks, while broad-peak resonances are observed in 6, 8, and 10 μm disks.

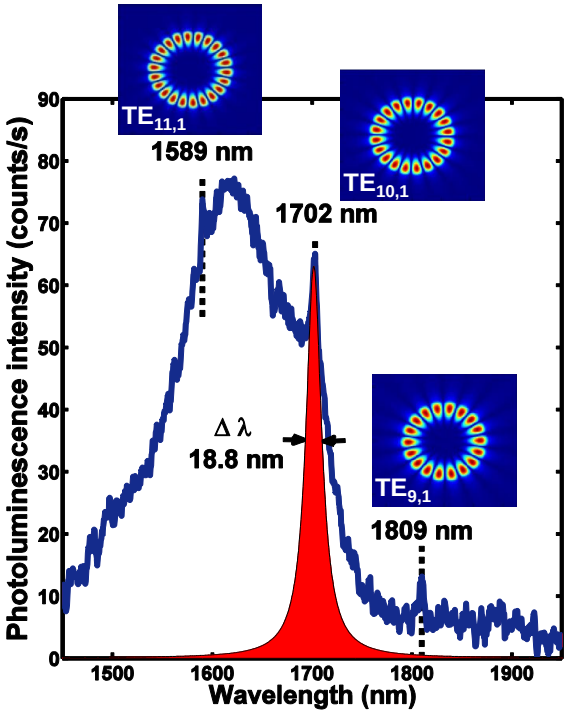

Figure 6.11: Whispering-gallery modes as observed in the photoluminescence spectrum of a 3 μm Ge disk on a freestanding SiO_2 beam with curved edges. Lorentzian function fit of $TE_{10,1}$ is shown in red, which is used to estimate Q-factors and peak positions.

Q-factors were 67, 182, and 191.8, respectively, estimated by dividing the central wavelength by the full-width half-maximum (FWHM), equation 2.11. On contrary, spectra of smaller disks (1 and 2 μm diameters) were extremely broadened, without any significant modulation by cavity resonances (fig. 6.10). This broadening can be explained by severe heating, especially that the disks are smaller than the laser spot size. Q-factors of WGMs are expected to be lower in smaller disks due to higher interaction between the mode and the surface [138]. On the other hand, the cavity modulation was apparent in larger-disks spectra which had broad-peak resonances, as can be seen for 6, 8, and 10-μm disks in fig. 6.10. Free spectral range (FSR) decreases as the disk diameter increases, resulting in more broad-peak resonances within the same wavelength range. The absence of sharp-peak resonances in larger disks can also be related to the laser spot size, as a 2 μm beam is not sufficient to pump the whole disk area. Such resonances are not as significant for monolithic operations as those observed in the 3 μm disks, which will be discussed further below.

6.6.2.1 Excitation Power Dependence

To form a better understanding of WGMs behavior, we excited the 3 μm disk with different power levels as shown in fig. 6.12. On a log-scale figure, $TE_{11,1}$ WGM is nearly invisible due to its low intensity and Q factor. Its vicinity to the direct-gap absorption edge [16, 107] imposes high losses on the confined mode, which explains the lowest Q-factor relative to the other two confined modes at higher wavelengths. So, discussions below will concentrate on $TE_{10,1}$, and $TE_{9,1}$. Increasing the excitation power up to 800 μW causes the direct-gap emission to increase accordingly, as expected due to the increase of injected carriers. Considering the intensity of each mode separately, $TE_{10,1}$ and $TE_{9,1}$ modes are proportional to $P^{2.28}$ and $P^{1.98}$, respectively, where P is the excitation power. This quadratic ($\propto P^{\sim 2}$) dependence is shown in fig. 6.13, and it is expected based on our previous study of the PL of intrinsic Ge presented in chapter 3.

Figure 6.14 (a) plots Γ-HH PL-peak positions (from fig. 6.13), while fig. 6.14 (b) plots the Raman peak positions of the same structure, against the laser excitation power for the 3 μm disk device. Matching these two sets of data can be used to estimate a value for the proportionality factor S used in the Raman-strain equation 6.2. Γ-HH peak evaluated at the limit of no excitation power corresponds to a band-gap energy of ~ 0.778eV, and using theoretical calculations (Appendix B, parameters in ref. [26]), this energy is due to $\sim$0.82% (0.3%) uniaxial (biaxial) tensile strain. Inserting these values in equation 6.2, where $\Delta\omega$ is -1.11 cm^{-1} for the same device, and solving for S yields a value of 135 (370) cm^{-1} for uniaxial (biaxial) strain. These values agree to a very good extent with the reported values of 152 [31] (390 [75, 76]).

6.6.2.2 Quality Factors

Resonant peaks in fig. 6.12 were fitted with Lorentzian functions to determine the Q-factors and peak positions for $TE_{10,1}$, and $TE_{9,1}$, as summarized in figs. 6.15 & 6.16, respectively. A trend of Q-factors degradation and red-shifting of resonant peaks upon increasing the pumping levels is evident for both WGMs. Similar results have been reported by several groups using optical [89, 55, 56, 57] and electrical [181] carriers injection, given that lasing has not been reported from a Ge micro-disk yet. This degradation of Q-factors at higher carrier-injection levels can be attributed to two main reasons: Firstly, heating-induced band-gap narrowing causing a shift of Ge direct-gap absorption edge towards higher wavelengths [27, 16, 60, 59]. This increases the absorption coefficient at lower wavelengths imposing pumping-proportional loses. Higher-energy (shorter-wavelength) modes are more affected by this loss mechanism, according to their position relative to the vicinity of the Ge direct-gap absorption edge [16, 131, 107]. Another main loss mechanism responsible for Q-factors degradation is free-carrier absorption (FCA) losses which increase with pumping due to additional photo-induced

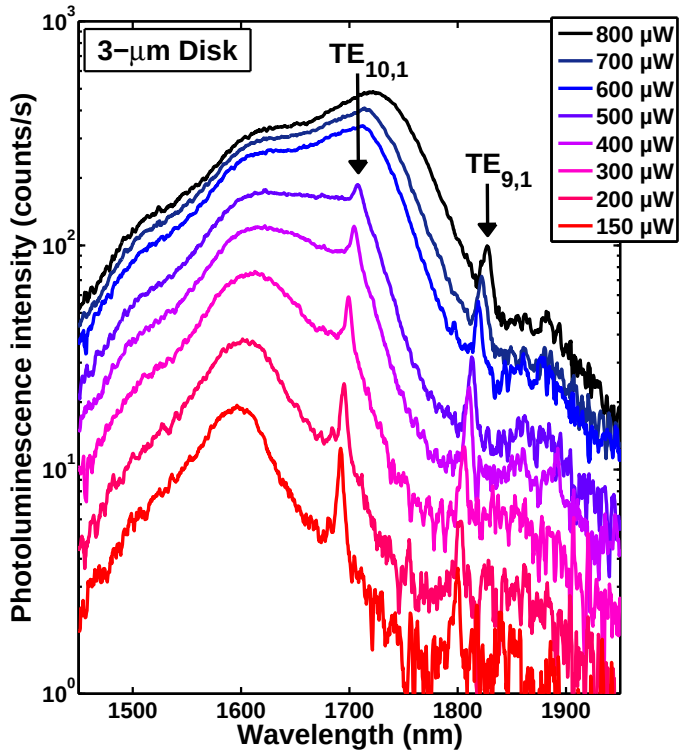

Figure 6.12: Photoluminescence power-dependence of the whispering-gallery modes observed in the 3 μm Ge micro-disk. Red-shift of the spectrum, and degradation of Q-factors is observed at higher excitation levels.

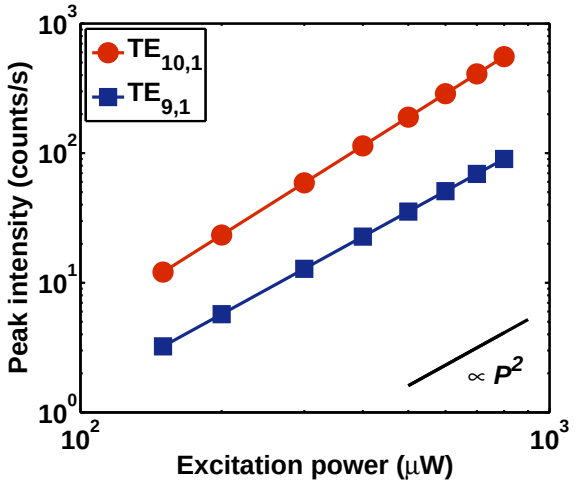

Figure 6.13: Quadratic dependence of the whispering-gallery-modes intensity on excitation power. This result agrees with our previous results shown in chapter 3 for intrinsic Ge PL power dependence.

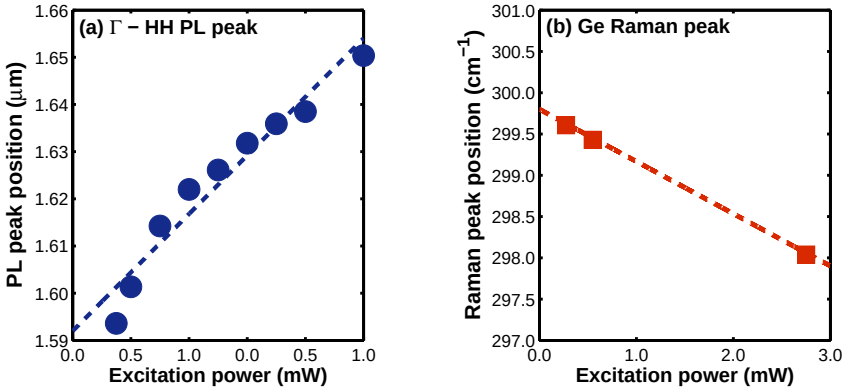

Figure 6.14: Raman and photoluminescence peak positions at the limit of no excitation power, found by extrapolating the peak positions at different power levels. (a) shows the main Γ-HH peak positions, and (b) shows the Ge Raman peak position. This data results in a Raman-strain proportionality coefficient S of 135 (370) for uniaxial (biaxial) strain.

carriers [49, 32, 25, 89]. The effect of FCA is more pronounced for lower-energy (higher-wavelength) resonances [49, 32, 25], as indicated by equation 2.4. As these loss mechanisms are associated with the density of injected carriers, Q-factors of the WGMs are affected by pumping levels, until they become barely detectable at 800 μW, (fig. 6.12).

Examining $TE_{10,1}$ and $TE_{9,1}$ WGMs separately (figs. 6.15 & 6.16), a difference in their degradation trend is evident. It can be seen that up to 300 μW pumping, both modes are broadened in a similar manner (Q-factor $\downarrow$). For higher excitation levels, the Q-factor of $TE_{10,1}$ (fig. 6.15) starts to decline with a much higher rate compared to $TE_{9,1}$ (fig.

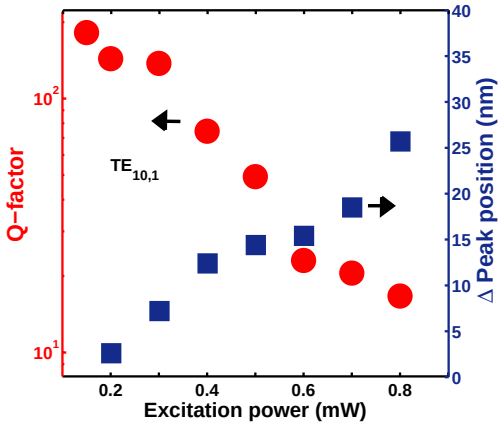

Figure 6.15: The effect of excitation power on the Q-factor and peak position of $TE_{10,1}$. Increasing the power contributes to degradation in Q-factor and a red-shift in peak position. Significant drop in Q-factor after 0.3 mW is attributed to the red-shift in Ge direct-gap absorption edge due to heating.

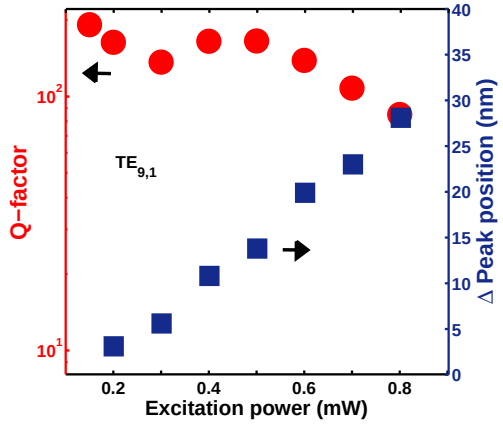

Figure 6.16: The effect of excitation power on the Q-factor and peak position of $TE_{9,1}$. Increasing the power also contributes to degradation in Q-factor and a red-shift in peak position. A steady degradation rate of the Q-factor is attributed mainly to free-carrier absorption, as the red-shift of the absorption edge is not sufficient to approach this mode at such power levels.

6.16), which undergoes a nearly constant degradation rate. This can be understood by considering that both modes are initially affected by FCA, up to 300 μW. Up to this power level, the red-shift in the direct-gap absorption edge is not enough to affect $TE_{10,1}$ yet. At higher power levels, the heating-originated red-shift of the direct-gap absorption edge continues, overshadowing the lower-wavelength mode ($TE_{10,1}$) until it becomes non-detectable above 600 μW. Up to this excitation power, the higher-wavelength mode ($TE_{9,1}$) remains at a safe distance from the direct-gap absorption edge, suffering only from the increase in FCA. This higher-wavelength peak is observed even at 1000 μW. This indicates that absorption due to the red-shift in the absorption edge (heating) is

more significant than the FCA in preventing lasing. In order to avoid high injection levels, higher tensile strain and *n*-type doping are required. *n*-type doping [123] is expected to reduces FCA losses, by allowing inversion with reduced levels of injected holes, which have a higher contribution to the total FCA compared to electrons [32], as demonstrated earlier in fig. 2.4.

6.6.2.3 Optical Losses & Required Improvements

According to the data in fig. 6.16, the Q-factor of $TE_{9,1}$ WGM can be considered FCA limited ($Q^{-1}_{material}$ term is dominant in equation 2.12). FCA losses (α_{fca} in cm^{-1}) can then be estimated using the following equation provided in refs. [138, 55]:

$$Q_{FCA} = \frac{2\pi n_{eff}}{\alpha_{fca}\lambda} \tag{6.3}$$

Q_{FCA} is the FCA-limited Q-factor, which can be used as 192 for $TE_{9,1}$, at a free-space wavelength (λ) of 1809 nm (1809×10^{-7} cm). n_{eff} is the effective refractive index which has an experimentally calculated (simulated) value of 1.73 (2.51), as summarized in table 6.4. According to these vales, α_{fca} losses is on the range of 312(453) cm^{-1}. With strain values similar to ones in our devices, extreme doping in the order of $\sim 10^{20}$ cm^{-3}, and high injection density in the order of $\sim 10^{19}$ cm^{-3}, might be required to overcome such optical loss values [92], assuming no additional losses are added to the system due to the doping and injection. And because such conditions are too extreme, higher tensile strain values are required for practical applications. An equivalent combination of 1.2% biaxial strain, $\sim 10^{19}$ cm^{-3} doping, and $\sim 10^{19}$ cm^{-3} injection density, can be used [92]. Additional improvements can be applied by a suitable passivation layer to terminate the active bonds at the surface of dry-etched Ge and enhance the carriers lifetime [1, 6]. Thermal oxidation of Ge after dry-etching is one possible approach [117, 182].

In conclusion, introducing higher tensile strain, and *n*-type doping is necessary to overcome optical losses. Although optimizing the beam structure in our devices might slightly enhance the strain, the maximum achievable tensile strain values are limited by the initial built-in stresses in the BOX layer. Consequently, *n*-type doping must also be incorporated, and as the current GOI wafers could not be doped without peeling-off the Ge layer (chapter. 3), the successfully-doped Ge-on-SOI stack (chapter 4) has to be used instead. Slight modifications of the designs are proposed for the future work (section 7.2.2) modifying the strain into biaxial and permitting the use of external stress liners.

6.7 Summary

In this chapter, we have demonstrated a combination of an optical cavity and a MEMS-like freestanding structure for strain application. The effect of strain for Ge monolithic emission purposes was investigated and discussed based on computer simulations, Raman spectroscopy, and photoluminescence measurements. We have shown that it is possible to accumulate tensile strain by using freestanding structures as confirmed by Raman spectroscopy, however tensile strain values were limited by the initial built-in stress in the BOX layer. Further optimization of the stack, to enhance the adhesion between Ge and BOX, or the structure itself has to be undertaken. Raman spectroscopy was also used to check the homogeneity of strain distribution within the Ge disks, and a relatively uniform distribution was confirmed. Sharp-peak resonances were observed from 3 μm Ge disks on freestanding SiO_2 beams with curved edges, and were attributed to whispering-gallery modes based on computer simulations. A maximum Q-factor of ~ 200 was estimated. Broad-peak resonances were also found in the photoluminescence spectra of larger disks, while smaller disks suffered from severe heating represented in significant spectrum broadening. Power-dependence of the WGMs was studied in details, revealing a quadratic power dependence of intensity, explained by the intrinsic nature of the disks, coinciding with our previous results presented in chapter 3. Combining the Raman and PL peaks positions we could estimate a proportionality factor relating the Raman shift with the strain value, agreeing to a good extent with previously reported values from other groups. Excitation-related loss mechanisms such as the red-shift of direct-gap absorption edge and free-carrier absorption were predominant and prevented monolithic operation. Higher strain and n-type doping are required to overcome losses, and avoid high-pumping conditions. Further optimization and an improved structure based on the n-type-doped Ge-on-SOI stack (chapter 4) is proposed in the next chapter for future work.

Chapter 7

Conclusions and Future Work

"That is the way to learn the most, that when you are doing something with such enjoyment that you dont notice that the time passes."
Albert Einstein, from an advice letter to his son.

7.1 Conclusions & Contribution

This project is a step taken on the road towards realizing a Ge laser source, for a complete integration of photonic circuitry on CMOS platforms. Related to a relatively new topic, our study focused on the formation of a better understanding of Ge direct-gap emission and proof-of-concept investigations. We have contributed with two topical review papers, summarizing the necessity of group-IV laser sources [1] and the research milestones undertaken in this aspect. In addition to clarifying research approaches and methodologies towards a Ge laser in specific [5]. Experimental work concentrated on two main engineering routes, tensile strain and n-type doping, in order to enhance Ge direct-gap light-emission efficiency. The contribution in the form of published articles and conferences is given in appendices C & D.

Chapters 3 and 4 presented the work on n-type doping of Ge using phosphorus (P) atoms. Spin-on doping (SOD) was investigated as a simple and cheap approach of introducing high concentrations of impurities to Ge. Initial doping trials were done on 70-nm-thick GOI films using different types of spin-on dopants (water and alcohol-based) and furnace annealing at relatively low temperatures (chapter 3). Although a maximum doping of $1 - 2 \times 10^{19}$ cm^{-3} was achieved, film quality was degraded during the doping process [2, 4]. This degradation was represented in Ge layer peeling-off and cracking, attributed to the fragile nature of the thin GOI films, due to the weak adhesion between Ge and the buried oxide. We could successfully detect $\sim$10$\times$ enhancement in the direct-gap photoluminescence (PL) signal compared to intrinsic Ge. A transformation of

the PL intensity dependence on pumping power was observed, switching from quadratic (intrinsic) to linear (doped). This result was explained by the steady-state rate equation of the holes density, confirming the role of n-type doping in filling the L valleys in the conduction band [2]. Subsequent experimental work (chapter 4) used a specific type of spin-on dopants (alcohol-based) based on the initial results, and focused on developing a doping recipe with high activation level and minimal damage on Ge crystalline quality. As Ge peeling-off and cracking problems were attributed to the fragile GOI films, a new stack of Ge-on-SOI was used for a better adhesion. A reliable doping recipe was successfully developed at relatively high temperatures and shorter durations using rapid-thermal annealing (RTA), resulting in an electrically-active doping concentration of $\sim 2.5 \times 10^{19}$ cm^{-3}. Although some resources in literature predicted that the reason behind the limited doping levels achieved using SOD is due to the limited source of P atoms, the experiments in chapter 4 contradict this claim. More probably, the limit on doping level is originating from the diffusion mechanism of P in Ge, agreeing with some theoretical works which proposed this explanation. The extremely fast diffusivity of P in Ge, which also increases rapidly with source concentration, causes P atoms to diffuse through or out of the Ge layer instead of being incorporated into the crystal. Achieving extremely high doping levels in Ge has to overcome this fast-diffusivity issue.

On the other hand, the other part of this project concentrated on tensile strain engineering, which has the major impact on enhancing the radiative recombinations of Ge. The use of Ge-on-insulator (GOI) wafers is proposed as a suitable platform providing flexibility in patterning the Ge layer as an active optical layer, meanwhile utilizing the buried oxide (BOX) as a source of stress. Ge layer was patterned into micro-disks providing optical confinement, while freestanding beams made of the BOX layer were used to exert tensile strain on the Ge disks on top. Consequently, a proper study on the nature of strain obtained by releasing the BOX layer was conducted in chapter 5. 3D finite-element computer simulations, Raman spectroscopy and PL measurements, were used to understand and optimize the tensile strain within Ge micro-disks on freestanding SiO_2 beams [6, 4, 5]. It was shown that the orientation, value, and homogeneity of the strain can be controlled through the beams design. Effects of design parameters on the strain were discussed in details, such as the beams length and width and the properties of the buried-oxide. Results of computer simulations, Raman and PL measurements coincided in observing higher tensile strain values within shorter freestanding SiO_2 beams. Tensile strain effect on splitting the light and heavy-hole bands was observed in the PL spectra of uniaxial beams, agreeing with theoretical predictions. A comparative study of strain using wafers with different stacks based on simulations and Raman measurements, promoted GOI wafers over Ge-on-SOI wafers for higher achievable tensile strain, and consequently the GOI stack has been used in the fabricating the main devices.

For the final devices, beams with curved edges and optimized design parameters were fabricated. Devices were characterized using laser-interference microscopy, Raman spectroscopy, and room-temperature PL measurements. Accumulation of tensile strain with fairly-acceptable uniformity was confirmed by Raman spectroscopy. An average tensile strain value of $\sim 0.7\%$ uniaxial was achieved. By matching the data from Raman spectroscopy and PL measurements, we estimated the value of the Raman-strain proportionality coefficient S, which agrees to a good extent with values reported by other groups. Sharp-peak whispering-gallery modes within the Ge direct-gap emission were observed from 3-μm disks on freestanding beams with curved edges. A quality factor of 200 was obtained in 100-nm-thick intrinsic Ge, indicating the potential of achieving high Q-factors. Performing a detailed study on the power dependence of the resonant modes, we could highlight two excitation-related loss mechanisms preventing monolithic operation, which are the red-shift of the direct-gap absorption edge and free-carrier-absorption (FCA) losses. The study has shown the necessity of avoiding high pumping levels, where losses due to the red-shift of Ge direct-gap absorption edge were found to be more significant compared to FCA losses. Assuming an FCA-limited Q-factors we could estimate the optical losses to be ~ 312 cm^{-1}, and additional engineering requirements have been discussed accordingly.

In conclusion, Ge band-gap engineering by tensile strain and n-type doping holds the potential of realizing a low-threshold Ge laser. The current research level has not achieved this goal yet, but it is rapidly progressing. Although tensile strain has the main impact on the optical gain of Ge, outcomes of this project and recent feedback from literature indicate the necessity of combining tensile strain and heavy n-type doping in the same device, for a practically-implementable Ge laser. In the next section, several ideas are proposed for this aim as a future work.

7.2 Future Outlook

There is plenty of room for device optimization in order to further increase Ge material gain. This can be planned in three separate routes as proposed below.

7.2.1 Techniques for Higher Doping Levels

A limit on phosphorus (P) doping concentrations exists presumably due to the diffusion mechanism. As low-temperature long-duration (chapter 3), and high-temperature short-duration (chapter 4) processes have been investigated with extremely-high source concentrations, in addition to repeated doping of the same chip for multiple times, other doping approaches has to be considered. The use of other types of impurities, such as Arsenic (As) might be possible, especially that full activation of As atoms is possible even at 500 °C [104], in addition to its high solubility (table 2.3). However, in spite of the larger atom size of As compared to P, it diffuses with a higher velocity through the Ge lattice (fig. 3.2) through a doubly-negatively-charged vacancy (V^{-2}) mechanism, with a quadratic increase of diffusivity proportional to concentration, similar to P [104]. This raises doubts around moving towards As, instead of P. The use of As is often restricted in educational facilities due to its potential hazards. Antimony (Sb) is a less-tempting option because it has the highest diffusivity among these three elements (fig. 3.2), and the lowest solubility at the same time (table 2.3). Another possible approach that has recently caught the interest of several groups is co-doping of P and other impurity atoms, aiming to alter the diffusion mechanism of P and control the doping level [112, 102, 187]. This approach is also tempting as a standard ion-implantation process, although requiring defect-reduction annealing steps afterwards.

Another interesting idea that is worth exploring, is introducing a slight percentage of Si atoms into the Ge layers, forming Si_xGe_{1-x} alloys with extremely high Ge content. Moving from pure Ge ($x = 0$) to pure Si ($x = 1$) is expected to gradually increase the solubility of P, and modify the diffusion mechanism, represented by a lower diffusivity [172, 104, 173]. This is deduced from the experimental work presented in chapter 4, in which a doping level of $\sim 10^{19}$ ($\sim 10^{20}$) cm^{-3} is achieved in Ge (Si) doped using the same source. Ideally, the target of such experiment is to achieve heavily-doped ($\sim 10^{20}$ cm^{-3}) Ge-rich Si_xGe_{1-x} alloy, with an extremely-low Si percentage (x). Although this has not been widely studied yet, from optical point of view, the resulting Ge-rich alloy is expected to be more similar to Ge, rather than Si. Emission of Si_xGe_{1-x} alloys, as shown in fig. 4.7, has a relatively high intensity compared to Ge, and positioned slightly below 1.55 μm, permitting the introduction of strain and heavy doping, while maintaining the emission wavelength within the desirable telecommunication range.

7.2.2 Optimization of Strain and Cavity

The proposed platform of GOI is highly flexible due to the separation of strain and optical layers engineering. Although the obtainable strain is mainly dependent on the built-in stresses in the buried-oxide (BOX) layer, and the Ge/BOX thickness ratio, a slight enhancement of tensile strain is expected through design optimization. Mainly, the reduction of pin-point build-ups of strain due to sharp beam edges is recommended [33, 36]. Moreover, reducing the width of the beam, especially in the middle, is expected to enhance the strain. This is limited by the Ge disk size on top of the beam, however, a change of the cavity design - for example - to circular bragg grating [188] (circular 1D photonic crystal [189]) with a middle pillar diameter of $\sim 200 - 400$ nm permits this improvement. In theory, very high Q-factors are expected in such periodic structures [188, 189]. This design has another advantage of better strain uniformity within such a small pillar, compared to a few-micron-sized disk, bearing in mind that the optical mode mostly dwells the middle region of the central pillar, instead of a whispering-gallery mode requiring high strain at the edges.

However, as concluded from this work, taking the performance a step forward requires incorporating n-type doping and tensile strain at the same time. To achieve this, Ge-on-SOI wafers have to be used instead of GOI wafers (chapters 3 & 4). This requires modifying the designs of the freestanding beams, as they degrade the tensile strain in the case of Ge-on-SOI wafers, as deduced from section 5.8. The reason behind strain degradation was the encapsulation of the Ge-on-SOI disks between the pre-stressed BOX and PECVD cap layers, which are constrained by fixed boundaries from two sides causing them to counter-act each other upon suspension. A simple manipulation of the boundary conditions can be done to exploit the PECVD cap layer as a stress-liner for strain enhancement, instead of counter-acting the BOX. This is done by fabricating Ge-on-SOI micro-disks on pedestals, instead of beams, encapsulated *all-around* by the BOX (bottom side) and PECVD cap (top and sides) layers; After patterning, these pre-stressed SiO_2 layers expand and because of the free circular boundaries all around the disk, they will both contribute to tensile-straining the Ge disk. This scenario is similar to interesting works by other groups on Ge micro-disks and rings strained by *all-around* stress liners [57, 29, 30], which have resulted in the highest biaxial tensile strain values up to now. In fact, *all-around* stress-liners have been proposed after the initial studies on stress-liners deposited on-top of Ge micro-disks [55, 56], in order to solve a major issue of the low-tensile-strain regions at the disk edges, which is not suitable for whispering-gallery modes (WGM) confinement. Although *all-around* coverage of the disks enhanced the strain at the edges, tensile strain is still higher within the inner regions of the disks. Here, we propose another approach to enhance the overlap between the highly-tensile-strained regions and the optical mode by "squeezing" the WGM into the inner regions of the disk, instead of engineering the coverage of the stress-liner. This

can be done by etching a grating around the circumference of the disk, resulting in a micro-gear shape [190, 191]. Consequently, the low-strain regions at the edges will be within the grating periods, while the WGM is pushed inwards, moving closer to the middle regions of the disk. A detailed study of the expected emission spectrum and mode profiles in micro-gear structures can be found in references [190, 191], which have been proposed previously to filter-out some resonances from the emission spectrum of III-V micro-disks, in order to reduce the lasing threshold. In addition to combining tensile strain and doping, another advantage of this structure is being less prone to heating compared to the freestanding beams, because of the Si pedestal forming a heat dissipation path into the substrate.

7.2.3 Lower-Dimensions using the Same Platform

Considering the history of III-V semiconductor lasers, as summarized in fig. 2.6, reducing the dimensions of the gain material from bulk into quantum structures have been the key to realize extremely-low-threshold operation. An enhancement in threshold was achieved by each reduction in dimensions. Theoretical models predict that using the electrons of the L valleys by fabricating Ge quantum-well (2D) structures is not advantageous [1]. Further reduction in dimensions by utilizing 1D nano-wires (NW) or 0D quantum dots (QD), worth examining. It would be possible to investigate Ge quantum dots, for example, using our GOI platform. Ge quantum dots can be fabricated in a top-down process, on freestanding SiO_2 structures for strain enhancement. Wet processes, ideally anisotropic, can be tuned to fabricate sub-Bohr-radius Ge quantum dots. A cavity is also required in this structure, and this can be done by depositing a layer of low-loss silicon nitride on top, then pattern it into micro-disks, or even photonic-crystals, embedding the Ge QDs. Initial compressive stresses can be introduced into this Si_3N_4 layer, such that it expands after patterning to impose tensile strain on the QDs. Generally speaking, most of the research efforts up to now targeted bulk (3D) Ge structures, and further studies are required to explore lower-dimension Ge structures as a possible gain medium.

Appendix A

Selected Fabrication Processes

This Appendix contains summaries of important fabrication parameters used for various processes mentioned in the report.

A.1 Amorphous Si Deposition using PECVD

Process	Parameter	Value	Unit
Stabilize chamber	Temperature	200	°C
Pre-deposition purge [a]	H_2 flow	100	sccm
	Pressure	400	mT
	Time	1	min.
Pre-deposition plasma	Power	20	W
	Time	3	min.
Silane purge	SiH_4 flow	100	sccm
	H_2 flow	100	sccm
	Ar flow	300	sccm
	Pressure	400	mT
	Time	2	min.
Deposition	Pressure	400	mT
	Power	10	W
	Time [b]	30	sec.
Inert gas purge	Ar flow	100	sccm
	Pressure	400	mT
	Time	2	min.

Table A.1: Amorphous Si deposition recipe using PECVD
[a] Organic contamination cleaning and surface activation.
[b] 10 nm a-Si.

A.2 SiO_2 Deposition using PECVD

Process	Parameter	Value	Unit
Stabilize chamber	Temperature	350	°C
Gas purge	SiH_4 flow	4.2	sccm
	N_2 flow	80	sccm
	N_2O flow	350	sccm
	Pressure	1000	mT
	Time	2	min.
Deposition	Pressure	1000	mT
	Power	20	W
	Time [(a)]	1 : 40	min.
Inert gas purge	N_2 flow	100	sccm
	Pressure	1000	mT
	Time	2	min.

Table A.2: SiO_2 deposition recipe using PECVD
[(a)] Results in 100-nm-thick SiO_2.

A.3 Ge Dry Reactive-Ion Etching

Process	Parameter	Value	Unit
Gas purge	SF_6 flow	36	sccm
	O_2 flow	36	sccm
	Pressure	30	mT
	Time	30	sec.
Silane purge	SF_6 flow	36	sccm
	O_2 flow	36	sccm
	Pressure	30	mT
	Power	100	Watt
	Rate [(a)]	200	nm/min.

Table A.3: Ge dry reactive-ion etching recipe
[(a)] Ge etching rate per minute, selectivity with SiO_2 is 5 (Ge) : 1 (SiO_2).

Appendix B

Generalized Hooke's Law and Band-Gap Deformation Calculations

B.1 Generalized Hooke's Law

Hooke's law in its one-dimensional form states that if a force (F) is applied on a spring, then it is displaced for a certain distance (x) determined by the stiffness of th e spring, or the spring constant (k), as follows [186, 79]:

$$F = k \times x \tag{B.1}$$

This one-dimensional law can be generalized for any three-dimensional elastic object, using a formula referred to as Cauchy's stiffness tensor [186, 79]:

$$\sigma_{ij} = c_{ijkl}.\epsilon_{kl} \tag{B.2}$$

σ_{ij} is F per unit area, c_{ijkl} are elastic stiffness tensors replacing the spring constant in Hooke's law. ϵ_{kl} is the corresponding fractional change of length, or the strain tensor. This formula can be written in the matrix form, where c_{ijkl} is a 9×9 matrix with 81 elements [186]. Making use of symmetry, by considering an isotropic cubic semiconductor lattice which is the case for Ge or Si, the stiffness tensor reduces to a 6×6 matrix as it reduces to an order of two (c_{ij}) [186]. This is a result of having only three independent stiffness components in a symmetric material, namely, c_{11}, c_{12}, and c_{44} Consequently, we can write the generalized Hooke's law as follows [186]:

$$\begin{pmatrix} \sigma_{xx} \\ \sigma_{yy} \\ \sigma_{zz} \\ \sigma_{yz} \\ \sigma_{xz} \\ \sigma_{xy} \end{pmatrix} = \begin{pmatrix} c_{11} & c_{12} & c_{12} & 0 & 0 & 0 \\ c_{12} & c_{11} & c_{12} & 0 & 0 & 0 \\ c_{12} & c_{12} & c_{11} & 0 & 0 & 0 \\ 0 & 0 & 0 & c_{44} & 0 & 0 \\ 0 & 0 & 0 & 0 & c_{44} & 0 \\ 0 & 0 & 0 & 0 & 0 & c_{44} \end{pmatrix} \begin{pmatrix} \epsilon_{xx} \\ \epsilon_{yy} \\ \epsilon_{zz} \\ 2\epsilon_{yz} \\ 2\epsilon_{xz} \\ 2\epsilon_{xy} \end{pmatrix} \tag{B.3}$$

Neglecting shear stresses represented by c_{44} stiffness elements, this reduces to:

$$\begin{pmatrix} \sigma_{xx} \\ \sigma_{yy} \\ \sigma_{zz} \end{pmatrix} = \begin{pmatrix} c_{11} & c_{12} & c_{12} \\ c_{12} & c_{11} & c_{12} \\ c_{12} & c_{12} & c_{11} \end{pmatrix} \begin{pmatrix} \epsilon_{xx} \\ \epsilon_{yy} \\ \epsilon_{zz} \end{pmatrix} \tag{B.4}$$

In the case of uniaxial stress application, the values of σ_{yy} and σ_{zz} are zero. Substituting this in Equation B.4 and eliminating the 2^{nd} and 3^{rd} lines results in [186]:

$$\epsilon_{yy} = \epsilon_{zz} = -\frac{c_{12}}{c_{11} + c_{12}} \epsilon_{xx} \tag{B.5}$$

On the other hand, for biaxial stresses, σ_{xx} and σ_{yy} are equal, while σ_{zz} equals zero in equilibrium. Substituting in Equation B.4 and solving results in:

$$\epsilon_{yy} = \epsilon_{xx} \qquad \text{and} \qquad \epsilon_{zz} = -2\frac{c_{12}}{c_{11}} \epsilon_{xx} \tag{B.6}$$

Similar results can be reached by inverting previous equations B.2, and solve for ϵ_{kl} [186]:

$$\epsilon_{ij} = c^{-1}_{ijkl} . \sigma_{kl} = s_{ijkl} . \sigma_{kl} \tag{B.7}$$

Where, s_{ijkl} is called the compliance tensor, the inverse of the stiffness tensor c_{ijkl}. Typical values of elastic stiffness constants of Ge and Si are summarized in table B.1.

B.2 Band-Gap Deformation

Relative values of normal strain components deduced in equations B.5 and B.6 are used with deformation-potential theory equations [25, 26, 28], to see the impact of strain on the band gap. The only variable input in these equations is one of the normal strain components, in our case ϵ_{xx}. It is possible to plot the energy of Γ and L valleys in the conduction band, in addition to heavy and light-hole bands in the valence band. Direct and indirect band-gaps are defined by the energy difference between the light-hole band, and Γ and L valleys, respectively. As the parameters used in calculations have different reported values - summarized in table B.2 -, energy-bands behavior against strain is slightly affected. Below is a summary of equations modelling the behavior of main energy bands in Ge, as found in the references in table B.2. The energy difference of the lowest conduction band at the Γ and L points due to a change in volume can be calculated as:

$$\Delta E_c^{\Gamma} = \alpha_{c,\Gamma}(\epsilon_{xx} + \epsilon_{yy} + \epsilon_{zz}) \tag{B.8}$$

$$\Delta E_c^{L} = \alpha_{c,L}(\epsilon_{xx} + \epsilon_{yy} + \epsilon_{zz}) \tag{B.9}$$

Where, ΔE_c^{Γ} and ΔE_c^{L} are the change in energy (eV) in CB valleys minima relative to the unstrained values $E_{c,0}^{\Gamma}$ and $E_{c,0}^{\mathrm{L}}$, respectively. $\alpha_{c,\Gamma}$ and $\alpha_{c,\mathrm{L}}$ are the hydrostatic deformation potentials for Γ and L valleys, respectively, with values summarized in table B.2. The shifts in LH and HH energies relative to the unstrained states ($\mathrm{E_v^{HH}} = \mathrm{E_v^{LH}} = 0$), can be calculated as follows [28]:

$$\Delta E_v^{HH} = -\mathcal{P}_\epsilon - \mathcal{Q}_\epsilon \tag{B.10}$$

$$\Delta E_v^{LH} = -\mathcal{P}_\epsilon + 0.5(\mathcal{Q}_\epsilon - \Delta_0 + \sqrt{\Delta_0^2 + 2\mathcal{Q}_\epsilon\Delta_0 + 9\mathcal{Q}_\epsilon^2}) \tag{B.11}$$

Given that,

$$\mathcal{P}_\epsilon = -\alpha_v(\epsilon_{xx} + \epsilon_{yy} + \epsilon_{zz}) \tag{B.12}$$

$$\mathcal{Q}_\epsilon = -0.5\beta_v(\epsilon_{xx} + \epsilon_{yy} - 2\epsilon_{zz}) \tag{B.13}$$

Where, α_v, β_v, Δ_0 are the hydrostatic and shear deformation potentials, and the spin-orbit splitting, respectively. Values of parameters listed in these equations are summarized in table B.2.

Material	Parameter	Value	Unit	Ref. [a]
Ge	c_{11}	131.5	GPA	[26]
	c_{12}	49.4		
	c_{44}	68.4		
Si	c_{11}	167.5		
	c_{12}	65		
	c_{44}	80.1		

Table B.1: Elastic stiffness constants for Ge & Si
[a] Other values can be found in refs. [192, 88, 186].

Parameter	Symbol	Value	Unit	Ref.
Initial direct-gap [a]	$E^{\Gamma}_{c,0}$	0.8	eV	[25]
		0.802		[28]
		0.89		[26]
Indirect-gap [a]	$E^{L}_{c,0}$	0.664		[25]
		0.661		[28]
		0.74		[26]
CB Γ def. pot. [b]	$\alpha_{c,\Gamma}$	-9.75		[25]
		-8.24		[26, 28]
CB L def. pot.	$\alpha_{c,L}$	-3.6		[25]
		-2.34		[28]
		-1.54		[26]
VB hydrostatic def. pot.	α_v	1.24		[26, 28]
VB shear def. pot.	β_v	-2.16		[28]
Spin-orbit splitting	Δ_0	0.29		[28, 25]
		0.3		[26]

Table B.2: Summary of parameters used for calculating Ge strain-induced band-gap deformation
[a] Band gap values are at room temperature.
[b] def. pot. ≡ deformation potential.

Appendix C

List of Publications

1. **Authors**:
   S. Saito, F. Y. Gardes, A. Z. Al-Attili, K. Tani, K. Oda, Y. Suwa, T. Ido, Y. Ishikawa, S. Kako, S. Iwamoto, Y. Arakawa.
   Article:
   "Group IV Light Sources to Enable the Convergence of Photonics and Electronics."
   Journal:
   Frontiers in Materials: Optics and Photonics, **1**, 15 (2014).
   DOI:
   10.3389/fmats.2014.00015

2. **Authors**:
   A. Z. Al-Attili, S. Kako, M. K. Husain, F. Y. Gardes, H. Arimoto, N. Higashitarumizu, S. Iwamoto, Y. Arakawa, Y. Ishikawa, and S. Saito.
   Article:
   "Spin-on Doping of Germanium-on-Insulator Wafers for Monolithic Light Sources on Silicon."
   Journal:
   Japanese Journal of Applied Physics, **54**, 052101 (2015).
   DOI:
   10.7567/JJAP.54.052101

3. **Authors**:
   A. Z. Al-Attili, M. Husain, F. Gardes, H. Arimoto, S. Saito, N. Higashitarumizu, Y. Ishikawa, S. Kako, S. Iwamoto, Y. Arakawa.
   Article:
   "Fabrication of Ge Micro-Disks on Free-Standing SiO_2 Beams for Monolithic Light Emission."
   Journal:
   Proceedings of the IEEE 15^{th} International Conference on Nanotechnology (IEEE NANO), pp. 1274-1277, 2015, Rome, Italy.
   DOI:
   10.1109/NANO.2015.7388863

4. **Authors**:
   A. Prasmusinto, A. Z. Al-Attili, H. Arimoto, and S. Saito.
   Article:

"Impacts of Atomically Flat Si (111) Surfaces on Novel Photonic Crystal Designs."
Journal:
Proceedings of the IEEE 15th International Conference on Nanotechnology (IEEE NANO), pp. 963-966, 2015, Rome, Italy.
DOI:
10.1109/NANO.2015.7388778

5. **Authors**:
Hideo Arimoto, M. K. Husain, A. Prasmusinto, K. Debnath, A. Z. Al-Attili, R. Petra, H. M. H. Chong, G. T. Reed, and S. Saito.
Article:
"Low-Loss Silicon Rectangular Waveguides Fabricated by Anisotoropic Wet Etching for Roughness Reduction."
Journal:
Proceedings of the IEEE 12th International Conference on Group IV Photonics (GFP), pp. 90-91, 2015, Vancouver, BC.
DOI:
10.1109/Group4.2015.7305962

6. **Authors**:
A. Z. Al-Attili, S. Kako, M. K. Husain, F. Y. Gardes, N. Higashitarumizu, S. Iwamoto, Y. Arakawa, Y. Ishikawa, H. Arimoto, K. Oda, T. Ido, and S. Saito.
Article:
"Whispering Gallery Mode Resonances from Ge Micro-Disks on Suspended Beams."
Journal:
Frontiers in Materials: Optics and Photonics, **2**, 43 (2015).
DOI:
10.3389/fmats.2015.00043

7. **Authors**:
A. Z. Al-Attili, S. Kako, M. K. Husain, F. Y. Gardes, S. Iwamoto, Y. Arakawa, and S. Saito.
Article:
"Tensile Strain Engineering of Germanium Micro-Disks on Free-Standing SiO_2 Beams."
Journal:
Japanese Journal of Applied Physics, **55**, 4S (2016).
DOI:
10.7567/JJAP.55.04EH02

8. **Authors**:
S. Saito, A. Z. Al-Attili, K. Oda, and Y. Ishikawa.
Article:
"Towards Monolithic Integration of Germanium Light Sources on Silicon Chips."
Journal:
Semiconductor Science and Technology, **31**, 4 (2016).
DOI:
10.1088/0268-1242/31/4/043002

9. **Authors**:
K. Debnath, H. Arimoto, M. K. Husain, A. Prasmusinto, A. Z. Al-Attili, R. Petra, H. M. H. Chong, G. T. Reed, and S. Saito.

Article:
"Low-Loss Silicon Waveguides and Grating Couplers Fabricated Using Anisotropic Wet Etching Technique."
Journal:
Frontiers in Materials: Optics and Photonics, **3**, 10 (2016).
DOI:
10.3389/fmats.2016.00010

Appendix D

List of Conferences

1. **Authors**:
   A. Z. Al-Attili, M. Husain, F. Gardes, and S. Saito.
   Article:
   "Group IV Photonics: Ge Light Emission."
   Conference:
   Nano Group Workshop (University of Southampton), 2014, Southampton, UK.
   Presentation::
   Poster Presentation [Best Poster Award].

2. **Authors**:
   S. Saito, F. Y. Gardes, A. Z. Al-Attili, K. Tani, K. Oda, Y. Suwa, T. Ido, Y. Ishikawa, S. Kako, S. Iwamoto, and Y. Arakawa.
   Article:
   "Group IV Light Sources to Enable the Convergence of Photonics and Electronics."
   Conference:
   The 4^{th} International Symposium on Photonics and Electronics Convergence - Advanced Nanophotonics and Silicon Device Systems (ISPEC), 2014, Tokyo, Japan.
   Presentation::
   Oral Presentation [Invited].

3. **Authors**:
   A. Z. Al-Attili, M. Husain, F. Gardes, H. Arimoto, S. Saito, N. Higashitarumizu, Y. Ishikawa, S. Kako, S. Iwamoto, Y. Arakawa.
   Article:
   "Fabrication of Ge Micro-Disks on Free-Standing SiO_2 Beams for Monolithic Light Emission."
   Conference:
   The 15^{th} IEEE International Conference on Nanotechnology (IEEE NANO), 2015, Rome, Italy.
   Presentation::
   Oral Presentation.

4. **Authors**:
   A. Prasmusinto, A. Z. Al-Attili, H. Arimoto, and S. Saito.
   Article:
   "Impacts of Atomically Flat Si (111) Surfaces on Novel Photonic Crystal Designs."

Conference:
The 15th IEEE International Conference on Nanotechnology (IEEE NANO), 2015, Rome, Italy.
Presentation::
Poster Presentation.

5. **Authors**:
Hideo Arimoto, M. K. Husain, A. Prasmusinto, K. Debnath, A. Z. Al-Attili, R. Petra, H. M. H. Chong, G. T. Reed, and S. Saito.
Article:
"Low-Loss Silicon Rectangular Waveguides Fabricated by Anisotoropic Wet Etching for Roughness Reduction."
Conference:
The 12th IEEE International Conference on Group IV Photonics (GFP), 2015, Vancouver, BC.
Presentation::
Poster Presentation.

6. **Authors**:
A. Z. Al-Attili, S. Kako, M. Husain, F. Gardes, S. Iwamoto, Y. Arakawa, and S. Saito.
Article:
"Tensile Strain of Germanium Micro-Disks on Freestanding SiO_2 Beams."
Conference:
The International Conference on Solid State Devices and Materials (SSDM), 2015, Sapporo, Japan.
Presentation::
Oral Presentation.

7. **Authors**:
A. Prasmusinto, A. Z. Al-Attili, K. Debnath, and S. Saito.
Article:
"Photonic Crystal Nanocavity with Atomically Flat Si (111) Interfaces."
Conference:
MRS Spring Meeting, 2016, Phoenix, Arizona.
Presentation::
Oral Presentation.

References

[1] S. Saito, F. Y. Gardes, A. Z. Al-Attili, K. Tani, K. Oda, Y. Suwa, T. Ido, Y. Ishikawa, S. Kako, S. Iwamoto, and Y. Arakawa. Group iv light sources to enable the convergence of photonics and electronics. *Front. Mater.*, 1(15), 2014. ISSN 2296-8016. doi: 10.3389/fmats.2014.00015.

[2] A. Z. Al-Attili, S. Kako, M. K. Husain, F. Y. Gardes, H. Arimoto, N. Higashitarumizu, S. Iwamoto, Y. Arakawa, Y. Ishikawa, and S. Saito. Spin-on doping of germanium-on-insulator wafers for monolithic light sources on silicon. *Jpn. J. Appl. Phys.*, 54(5):052101, 2015. doi: 10.7567/JJAP.54.052101.

[3] A. Z. Al-Attili, S. Kako, M. Husain, F. Gardes, N. Higashitarumizu, S. Iwamoto, Y. Arakawa, Y. Ishikawa, H. Arimoto, K. Oda, T. Ido, and S. Saito. Whispering gallery mode resonances from Ge micro-disks on suspended beams. *Front. Mater.*, 2(43), 2015. doi: 10.3389/fmats.2015.00043.

[4] A. Al-Attili, M. Husain, F. Gardes, H. Arimoto, S. Saito, N. Higashitarumizu, Y. Ishikawa, S. Kako, S. Iwamoto, and Y. Arakawa. Fabrication of Ge micro-disks on free-standing SiO_2 beams for monolithic light emission. In *Proc. 15th IEEE Conf. Nanotechnology* (IEEE NANO), pages 1274–1277, 2015. doi: 10.1109/NANO.2015.7388863.

[5] S. Saito, A. Z. Al-Attili, K. Oda, and Y. Ishikawa. Towards monolithic integration of germanium light sources on silicon chips. *Semicond. Sci. Technol.*, 31(4):043002, 2016. doi: 10.1088/0268-1242/31/4/043002.

[6] A. Z. Al-Attili, S. Kako, M. K. Husain, F. Y. Gardes, S. Iwamoto, Y. Arakawa, and S. Saito. Tensile strain engineering of germanium micro-disks on free-standing sio_2 beams. *Jpn. J. Appl. Phys.*, 55(4S):04EH02, 2016. doi: 10.7567/JJAP.55.04EH02.

[7] R. P. Feynman. There's plenty of room at the bottom (the transcript of a talk in 1959 at the annual meeting of the american physical society (aps)). *IEEE J. Microelectromech. Syst.*, 1(1):60–66, 1992. doi: 10.1109/84.128057.

[8] Y. Ishikawa and S. Saito. Ge-on-si photonic devices for photonic-electronic integration on a si platform. *IEICE Electron. Expr.*, 11(24):20142008, 2014. doi: 10.1587/elex.11.20142008.

[9] G. E. Moore. Cramming more components onto integrated circuits. *Electronics*, 38(8):114–117, 1965. doi: (Republished-identifier)0018-9219(98)00753-1.

[10] J. Tomayko. *Computers in spaceflight: the NASA experience*, book Chapter 2: Computers on board the Apollo spacecraft. NASA, 1987. URL http://history.nasa.gov/computers/Ch2-5.html.

[11] Intel. 14 nm transistor explained - following the path of Moores law, 2016. URL http://www.intel.com/content/www/us/en/silicon-innovations/standards-14nm-explained-video.html.

[12] D. A. B. Miller. Rationale and challenges for optical interconnects to electronic chips. *Proc. IEEE*, 88(6):728–749, 2000. doi: 10.1109/5.867687.

[13] D. A. B. Miller. Optical interconnects to electronic chips. *Appl. Opt.*, 49(25): F59–F70, 2010. doi: 10.1364/AO.49.000F59.

[14] D. A. B. Miller. Physical reasons for optical interconnection,. *Special Issue on Smart Pixels, Int. J. Optoelectronics*, 11(3):155–168, 1997. doi: 10.1093/0198293569.003.0006.

[15] J. Michel, J. Liu, and L. C. Kimerling. High-performance Ge-on-Si photodetectors. *Nat. Photonics*, 4(8):527–534, 2010. doi: 10.1038/nphoton.2010.157.

[16] Y. Ishikawa, K. Wada, J. Liu, D. D. Cannon, H. C. Luan, J. Michel, and L. C. Kimerling. Strain-induced enhancement of near-infrared absorption in Ge epitaxial layers grown on Si substrate. *J. Appl. Phys.*, 98(1):013501, 2005. doi: 10.1063/1.1943507.

[17] S. Saito, K. Oda, T. Takahama, K. Tani, and T. Mine. Germanium fin light-emitting diode. *Appl. Phys. Lett.*, 99(24):241105, 2011. doi: 10.1063/1.3670053.

[18] D. A. B. Miller. Hybrid seed-massively parallel optical interconnections for silicon ics. In *Proc. 2nd Int. Conf. Massively Parallel Processing Using Optical Interconnections* (MPPOI), pages 2–7. IEEE, 1995. doi: 10.1109/MPPOI.1995.528621.

[19] R. Geiger, T. Zabel, and H. Sigg. Group iv direct band gap photonics: methods, challenges and opportunities. *Front. Mater.*, 2(52), 2015. doi: 10.3389/fmats.2015.00052.

[20] J. Liu, X. Sun, L. C. Kimerling, and J. Michel. Direct-gap optical gain of ge on si at room temperature. *Opt. Lett.*, 34(11):1738–1740, 2009. doi: 10.1364/OL.34.001738.

[21] J. Liu, X. Sun, R. Camacho-Aguilera, L. C. Kimerling, and J. Michel. Ge-on-Si laser operating at room temperature. *Opt. Lett.*, 35(5):679–681, 2010. doi: 10.1364/OL.35.000679.

[22] R. E. Camacho-Aguilera, Y. Cai, N. Patel, J. T. Bessette, M. Romagnoli, L. C. Kimerling, and J. Michel. An electrically pumped germanium laser. *Opt. Express*, 20(10):11316–11320, 2012. doi: 10.1364/OE.20.011316.

[23] R. Koerner, M. Oehme, M. Gollhofer, M. Schmid, K. Kostecki, S. Bechler, D. Widmann, E. Kasper, and J. Schulze. Electrically pumped lasing from Ge fabry-perot resonators on Si. *Optics Express*, 23(11):14815–14822, 2015. doi: 10.1364/oe.23.014815.

[24] M. Bohr and K. Mistry. Intel's revolutionary 22-nm transistor technology, 2016. URL https://newsroom.intel.com/. The article PDF file can be found at http://download.intel.com/newsroom/kits/22nm/pdfs/22nm-details_presentation.pdf [Accessed 2016].

[25] M. El Kurdi, G. Fishman, S. Sauvage, and P. Boucaud. Band structure and optical gain of tensile-strained germanium based on a 30 band k.p formalism. *J. Appl. Phys.*, 107(1):013710, 2010. ISSN 0021-8979. doi: 10.1063/1.3279307.

[26] C. G. Van de Walle. Band lineups and deformation potentials in the model-solid theory. *Phys. Rev. B*, 39(3):1871, 1989. doi: 10.1103/PhysRevB.39.1871.

[27] Y. Ishikawa, K. Wada, D. D. Cannon, J. Liu, H. C. Luan, and L. C. Kimerling. Strain-induced band gap shrinkage in Ge grown on Si substrate. *Appl. Phys. Lett.*, 82(13):2044, 2003. doi: 10.1063/1.1564868.

[28] C. Boztug, J. R. Sanchez-Perez, F. Cavallo, M. G. Lagally, and R. Paiella. Strained-germanium nanostructures for infrared photonics. *Acs Nano*, 8(4):3136–3151, 2014. doi: 10.1021/nn404739b.

[29] M. El Kurdi, M. Prost, A. Ghrib, S. Sauvage, X. Checoury, G. Beaudoin, I. Sagnes, G. Picardi, R. Ossikovski, and P. Boucaud. Direct band gap germanium microdisks obtained with silicon nitride stressor layers. *ACS Photonics*, 3(3):443448, 2016. doi: 10.1021/acsphotonics.5b00632.

[30] R. W. Millar, K. Gallacher, J. Frigerio, A. Ballabio, A. Bashir, I. MacLaren, G. Isella, and D. J. Paul. Analysis of Ge micro-cavities with in-plane tensile strains above 2%. *Opt. Express*, 24(5):4365–4374, 2016. doi: 10.1364/OE.24.004365.

[31] D. S. Sukhdeo, D. Nam, J. H. Kang, M. L. Brongersma, and K. C. Saraswat. Direct bandgap germanium-on-silicon inferred from 5.7% ⟨100⟩ uniaxial tensile strain. *Photon. Res.*, 2(3):A8–A13, 2014. doi: 10.1364/PRJ.2.0000A8.

[32] J. Liu, L. C. Kimerling, and J. Michel. Monolithic Ge-on-Si lasers for large-scale electronic-photonic integration. *Semicond. Sci. Technol.*, 27(09):094006, 2012. ISSN 0268-1242. doi: 10.1088/0268-1242/27/9/094006.

[33] M. J. Süess, R. Geiger, R. A. Minamisawa, G. Schiefler, J. Frigerio, D. Chrastina, G. Isella, R. Spolenak, J. Faist, and H. Sigg. Analysis of enhanced light emission from highly strained germanium microbridges. *Nat. Photonics*, 7(6):466–472, 2013. doi: 10.1038/nphoton.2013.67.

[34] P. H. Lim, S. Park, Y. Ishikawa, and K. Wada. Enhanced direct bandgap emission in germanium by micromechanical strain engineering. *Opt. Express*, 17(18):16358–16365, 2009. doi: 10.1364/OE.17.016358.

[35] J. R. Jain, A. Hryciw, T. M. Baer, D. A. B. Miller, M. L. Brongersma, and R. T. Howe. A micromachining-based technology for enhancing germanium light-emission via tensile strain. *Nat. Photonics*, 6(6):398–405, 2012. doi: 10.1038/NPHOTON.2012.111.

[36] A. Gassenq, K. Guilloy, G. Osvaldo Dias, N. Pauc, D. Rouchon, J. M. Hartmann, J. Widiez, S. Tardif, F. Rieutord, J. Escalante, I. Duchemin, Y. M. Niquet, R. Geiger, T. Zabel, H. Sigg, J. Faist, A. Chelnokov, V. Reboud, and V. Calvo. 1.9% bi-axial tensile strain in thick germanium suspended membranes fabricated in optical germanium-on-insulator substrates for laser applications. *Appl. Phys. Lett.*, 107(19):191904, 2015. doi: 10.1063/1.4935590.

[37] A. Gassenq, S. Tardif, K. Guilloy, N. Pauc, J. Escalante, I. Duchemin, Y. M. Niquet, F. Rieutord, V. Calvo, G. O. Dias, D. Rouchon, J. Widiez, J. M. Hartmann, D. Fowler, A. Chelnokov, V. Reboud, R. Geiger, T. Zabel, H. Sigg, and J. Faist. Distributed bragg reflectors integration in highly strained Ge micro-bridges on 200 mm GeOI substrates for laser applications. In *IEEE 12th Int. Conf. Group IV Photonics* (GFP), pages 51–52, 2015. doi: 10.1109/Group4.2015.7305999.

[38] J. Petykiewicz, D. Nam, D. S. Sukhdeo, S. Gupta, S. Buckley, A. Y. Piggott, J. Vukovi, and K. C. Saraswat. Direct bandgap light emission from strained germanium nanowires coupled with high-Q nanophotonic cavities. *Nano Lett.*, 16(4):2168–2173, 2016. doi: 10.1021/acs.nanolett.5b03976.

[39] S. Wirths, R. Geiger, N. von den Driesch, G. Mussler, T. Stoica, S. Mantl, Z. Ikonic, M. Luysberg, S. Chiussi, J. M. Hartmann, H. Sigg, J. Faist, D. Buca, and D. Grützmacher. Lasing in direct-bandgap GeSn alloy grown on Si. *Nat. Photonics*, 9(2):88–92, 2015. ISSN 1749-4893. doi: 10.1038/nphoton.2014.321.

[40] S. Wirths, R. Geiger, C. Schulte-Braucks, N. von den Driesch, D. Stange, T. Zabel, Z. Ikonic, J. M. Hartmann, S. Mantl, H. Sigg, D. Grutzmacher, and D. Buca. Direct bandgap gesn microdisk lasers at 2.5 μm for monolithic integration on si-platform. In *IEEE Int. Electron Devices Meeting* (IEDM), pages 2.6.1–2.6.4, 2015. doi: 10.1109/IEDM.2015.7409615.

[41] L. Carroll, P. Friedli, S. Neunschwander, H. Sigg, S. Cecchi, F. Isa, D. Chrastina, G. Isella, Y. Fedoryshyn, and J. Faist. Direct-gap gain and optical absorption in

germanium correlated to the density of photoexcited carriers, doping, and strain. *Phys. Rev. Lett.*, 109(5):057402, 2012. doi: 10.1103/PhysRevLett.109.057402.

[42] K. Tani, S. Saito, S. Oda, T. Okumura, T. Mine, and T. Ido. Lateral carrier injection to germanium for monolithic light sources. In *IEEE 9th Int. Conf. Group IV Photonics* (GFP), pages 328–330, 2012. doi: 10.1109/GROUP4.2012.6324176.

[43] K. Tani, K. Oda, J. Kasai, T. Okumura, T. Mine, S. Saito, and T. Ido. Germanium waveguides on lateral silicon-on-insulator diodes for monolithic light emitters and photo detectors. In *IEEE 10th Int. Conf. Group IV Photonics* (GFP), pages 134–135, Seoul, 2013. doi: 10.1109/Group4.2013.6644407.

[44] K. Tani, K. Oda, T. Okumura, T. Takezaki, J. Kasai, T. Mine, and T. Ido. Enhanced electroluminescence from germanium waveguides by local tensile strain with silicon nitride stressors. In *Int. Conf. Solid State Devices and Materials (SSDM)*, pages K–6–3, Fukuoka, 2013.

[45] H. Tahini, A. Chroneos, R. Grimes, U. Schwingenschlgl, and A. Dimoulas. Strain-induced changes to the electronic structure of germanium. *J. Phys.: Condens. Matter*, 24(19):195802, 2012. doi: 10.1088/0953-8984/24/19/195802.

[46] S. L. Chuang. *Physics of photonic devices*, volume 80. John Wiley & Sons, 2012. ISBN 1118585658.

[47] I. Balslev. Influence of uniaxial stress on the indirect absorption edge in silicon and germanium. *Phys. Rev.*, 143(2):636–647, 1966. doi: 10.1103/PhysRev.143.636.

[48] M. V. Fischetti and S. E. Laux. Band structure, deformation potentials, and carrier mobility in strained Si, Ge, and SiGe alloys. *J. Appl. Phys.*, 80(4):2234, 1996. doi: 10.1063/1.363052.

[49] J. Liu, X. Sun, D. Pan, X. Wang, L. C. Kimerling, T. L. Koch, and J. Michel. Tensile-strained, n-type Ge as a gain medium for monolithic laser integration on Si. *Opt. Express*, 15(18):11272–11277, 2007. doi: 10.1364/OE.15.011272.

[50] J. Menéndez and J. Kouvetakis. Type-I Ge/$Ge_{1-x-y}Si_xSn_y$ strained-layer heterostructure with a direct Ge bandgap. *Appl. Phys. Lett.*, 85(7):1175, 2004. doi: 10.1063/1.1784032.

[51] Y. Bai, K. E. Lee, C. Cheng, M. L. Lee, and E. A. Fitzgerald. Growth of highly tensile-strained Ge on relaxed $In_xGa_{1-x}As$ by metal-organic chemical vapor deposition. *J. Appl. Phys.*, 104(8):084518, 2008. doi: 10.1063/1.3005886.

[52] Y. Huo, H. Lin, R. Chen, M. Makarova, Y. Rong, M. Li, T. I. Kamins, J. Vučković, and J. S. Harris. Strong enhancement of direct transition photoluminescence with highly tensile-strained Ge grown by molecular beam epitaxy. *Appl. Phys. Lett.*, 98 (1):011111, 2011. doi: 10.1063/1.3534785.

[53] X. Sun, J. Liu, L. C. Kimerling, and J. Michel. Toward a germanium laser for integrated silicon photonics. *IEEE J. Select. Topics Quantum Electron.*, 16(1): 124–131, 2010. doi: 10.1109/jstqe.2009.2027445.

[54] Y. Y. Fang, J. Tolle, R. Roucka, A. V. G. Chizmeshya, J. Kouvetakis, V. R. D'Costa, and J. Menéndez. Perfectly tetragonal, tensile-strained Ge on $Ge_{1y}Sn_y$ buffered Si(100). *Appl. Phys. Lett.*, 90(6):061915, 2007. doi: 10.1063/1.2472273.

[55] A. Ghrib, M. El Kurdi, M. de Kersauson, M. Prost, S. Sauvage, X. Checoury, G. Beaudoin, I. Sagnes, and P. Boucaud. Tensile-strained germanium microdisks. *Appl. Phys. Lett.*, 102(22):221112, 2013. doi: 10.1063/1.4809832.

[56] A. Ghrib, M. El Kurdi, M. Prost, M. de Kersauson, L. Largeau, O. Mauguin, G. Beaudoin, S. Sauvage, X. Checoury, G. Ndong, M. Chaigneau, R. Ossikovski, S. David, I. Sagnes, and P. Boucaud. Strain engineering in germanium microdisks. volume 8990, pages 89901C–89901C–7, 2014. doi: 10.1117/12.2037307.

[57] A. Ghrib, M. El Kurdi, M. Prost, S. Sauvage, X. Checoury, G. Beaudoin, M. Chaigneau, R. Ossikovski, I. Sagnes, and P. Boucaud. All-around SiN stressor for high and homogeneous tensile strain in germanium microdisk cavities. *Adv. Optical Mater.*, 3(3):353–358, 2015. ISSN 2195-1071. doi: 10.1002/adom.201400369.

[58] J. Liu, R. Camacho-Aguilera, J. T. Bessette, X. Sun, X. Wang, Y. Cai, L. C. Kimerling, and J. Michel. Ge-on-Si optoelectronics. *Thin Solid Films*, 520(8): 3354–3360, 2012. doi: 10.1016/j.tsf.2011.10.121.

[59] J. Liu, D. D. Cannon, K. Wada, Y. Ishikawa, S. Jongthammanurak, D. T. Danielson, J. Michel, and L. C. Kimerling. Tensile strained Ge *p-i-n* photodetectors on Si platform for C and L band telecommunications. *Appl. Phys. Lett.*, 87(1):011110, 2005. doi: 10.1063/1.1993749.

[60] D. D. Cannon, J. Liu, Y. Ishikawa, K. Wada, D. T. Danielson, S. Jongthammanurak, J. Michel, and L. C. Kimerling. Tensile strained epitaxial Ge film on Si(100) substrate with potential application to L-band telecommunications. *Appl. Phys. Lett.*, 84(6):906, 2004. doi: 10.1063/1.1645677.

[61] R. People and J. C. Bean. Band alignments of coherently strained Ge_xSi_{1x}/Si heterostructures on $\langle 001 \rangle$ Ge_ySi_{1y} substrates. *Appl. Phys. Lett.*, 48(8):538, 1986. doi: 10.1063/1.96499.

[62] C. Lange, N. S. Köster, S. Chatterjee, H. Sigg, D. Chrastina, G. Isella, H. von Knel, M. Schäfer, M. Kira, and S. W. Koch. Ultrafast nonlinear optical response of photoexcited Ge/SiGe quantum wells: Evidence for a femtosecond transient population inversion. *Phys. Rev. B*, 79(20):201306, 2009. doi: 10.1103/PhysRevB.79.201306.

[63] K. Gallacher, P. Velha, D. J. Paul, J. Frigerio, D. Chrastina, and G. Isella. 1.55 μm electroluminescence from strained n-Ge quantum wells on silicon substrates. In *IEEE 9th Int. Conf. Group IV Photonics* (GFP), pages 81–83, 2012. doi: 10.1109/group4.2012.6324093.

[64] ITRS. International technology roadmap for semiconductors, 2013. URL http://www.itrs.net.

[65] K. Rim, J. Chu, H. Chen, K. A. Jenkins, T. Kanarsky, K. Lee, A. Mocuta, H. Zhu, R. Roy, J. Newbury, J. Ott, K. Petrarca, P. Mooney, D. Lacey, S. Koester, K. Chan, D. Boyd, M. Ieong, and H. S. Wong. Characteristics and device design of sub-100 nm strained Si N- and PMOSFETs. In *Tech. Dig. Symp. VLSI Technology*, pages 98–99, 2002. doi: 10.1109/VLSIT.2002.1015406.

[66] S. Cho, B. G. Park, C. Yang, S. Cheung, E. Yoon, T. I. Kamins, S. B. Yoo, and J. S. Harris. Room-temperature electroluminescence from germanium in an $Al_{0.3}Ga_{0.7}As$/Ge heterojunction light-emitting diode by Gamma-valley transport. *Opt. Express*, 20(14):14921–14927, 2012. doi: 10.1364/OE.20.014921.

[67] M. Oehme, J. Werner, M. Gollhofer, M. Schmid, M. Kaschel, E. Kasper, and J. Schulze. Room-temperature electroluminescence from GeSn light-emitting pin diodes on Si. *IEEE Photon. Technol. Lett.*, 23(23):1751–1753, 2011. doi: 10.1109/LPT.2011.2169052.

[68] C. Ortolland, Y. Okuno, P. Verheyen, C. Kerner, C. Stapelmann, M. Aoulaiche, N. Horiguchi, and T. Hoffmann. Stress memorization technique—fundamental understanding and low-cost integration for advanced CMOS technology using a nonselective process. *IEEE Trans. Electron Devices*, 56(8):1690–1697, 2009. doi: 10.1109/TED.2009.2024021.

[69] F. Ootsuka, S. Wakahara, K. Ichinose, A. Honzawa, S. Wada, H. Sato, T. Ando, H. Ohta, K. Watanabe, and T. Onai. A highly dense, high-performance 130 nm node CMOS technology for large scale system-on-a-chip applications. In *IEEE Int. Conf. Electron Devices Meeting* (IEDM), pages 575–578, 2000. doi: 10.1109/IEDM.2000.904385.

[70] A. Nishiyama, K. Matsuzawa, and S. Takagi. SiGe source/drain structure for the suppression of the short-channel effect of sub-0.1-μm p-channel MOSFETs. *IEEE Trans. Electron Devices*, 48(6):1114–1120, 2001. doi: 10.1109/16.925236.

[71] P. Velha, D. C. Dumas, K. Gallacher, R. Millar, M. Myronov, D. R. Leadley, and D. J. Paul. Strained germanium nanostructures on silicon emitting at $> 2.2\mu$m wavelength. pages 142–143, 2013. doi: 10.1109/Group4.2013.6644411.

[72] G. G. Stoney. The tension of metallic films deposited by electrolysis. *Proc. Royal Society of London A: Mathematical, Physical and Engineering Sciences*, 82(553):172–175, 1909. doi: 10.1098/rspa.1909.0021.

[73] R. W. Millar, K. Gallacher, A. Samarelli, J. Frigerio, D. Chrastina, G. Isella, T. Dieing, and D. J. Paul. Extending the emission wavelength of Ge nanopillars to 2.25 μm using silicon nitride stressors. *Opt. Express*, 23(14):18193–18202, 2015. doi: 10.1364/OE.23.018193.

[74] A. Ghrib, M. de Kersauson, M. El Kurdi, R. Jakomin, G. Beaudoin, S. Sauvage, G. Fishman, G. Ndong, M. Chaigneau, R. Ossikovski, I. Sagnes, and P. Boucaud. Control of tensile strain in germanium waveguides through silicon nitride layers. *Appl. Phys. Lett.*, 100(20):201104, 2012. doi: 10.1063/1.4718525.

[75] G. Capellini, G. Kozlowski, Y. Yamamoto, M. Lisker, C. Wenger, G. Niu, P. Zaumseil, B. Tillack, A. Ghrib, M. de Kersauson, M. El Kurdi, P. Boucaud, and T. Schroeder. Strain analysis in SiN/Ge microstructures obtained via Si-complementary metal oxide semiconductor compatible approach. *J. Appl. Phys.*, 113(1):013513, 2013. doi: 10.1063/1.4772781.

[76] G. Capellini, C. Reich, S. Guha, Y. Yamamoto, M. Lisker, M. Virgilio, A. Ghrib, M. El Kurdi, P. Boucaud, B. Tillack, and T. Schroeder. Tensile Ge microstructures for lasing fabricated by means of a silicon complementary metal-oxide-semiconductor process. *Opt. Express*, 22(1):399–410, 2014. doi: 10.1364/OE.22.000399.

[77] M. El Kurdi, A. Ghrib, M. de Kersauson, M. Prost, S. Sauvage, X. Checoury, G. Beaudoin, I. Sagnes, G. Ndong, M. Chaigneau, R. Ossikovski, and P. Boucaud. Tensile-strained germanium microdisks using Si_3N_4 stressors. pages 95–96, 2013. doi: 10.1109/Group4.2013.6644443.

[78] P. Velha, K. Gallacher, D. Dumas, D. Paul, M. Myronov, and D. Leadley. Tuning the electroluminescence of n-Ge LEDs using process induced strain. pages 337–339. IEEE, 2012. doi: 10.1109/GROUP4.2012.6324179.

[79] S. D. Senturia. *Microsystem Design.* Kluwer academic publishers, Boston, 2001.

[80] S. C. H. Lin and I. Pugacz-Muraszkiewicz. Local stress measurement in thin thermal sio_2 films on Si substrates. *J. Appl. Phys.*, 43(1):119–125, 1972. doi: 10.1063/1.1660794.

[81] C. W. Wilmsen, E. G. Thompson, and G. H. Meissner. Buckling of thermally-grown SiO_2 thin-films. *IEEE Trans. Electron Devices*, 19(1):122, 1972. doi: 10.1109/t-ed.1972.17381.

[82] W. Fang and J. A. Wickert. Post buckling of micromachined beams. *J. micromech. microeng.*, 4(3):116, 1994. ISSN 0960-1317. doi: 10.1088/0960-1317/4/3/004.

[83] W. Fang, C. H. Lee, and H. H. Hu. On the buckling behavior of micromachined beams. *J. micromech. microeng.*, 9(3):236, 1999. doi: 10.1088/0960-1317/9/3/304.

[84] D. Nam, D. Sukhdeo, A. Roy, K. Balram, S. L. Cheng, K. C. Y. Huang, Z. Yuan, M. Brongersma, Y. Nishi, D. Miller, and K. Saraswat. Strained germanium thin film membrane on silicon substrate for optoelectronics. *Opt. Express*, 19(27): 25866–25872, 2011. doi: 10.1364/oe.19.025866.

[85] D. S. Sukhdeo, D. Nam, J. H. Kang, M. L. Brongersma, and K. C. Saraswat. Bandgap-customizable germanium using lithographically determined biaxial tensile strain for silicon-compatible optoelectronics. *Opt. Express*, 23(13):16740–16749, 2015. doi: 10.1364/OE.23.016740.

[86] C. Boztug, J. R. Sánchez-Pérez, J. Yin, M. G. Lagally, and R. Paiella. Graiting-coupled mid-infrared light emission from tensilely strained germanium nanomembranes. *Appl. Phys. Lett.*, 103(20):201114, 2013. doi: 10.1063/1.4830377.

[87] D. Nam, D. S. Sukhdeo, J. H. Kang, J. Petykiewicz, J. H. Lee, W. S. Jung, J. Vučković, M. L. Brongersma, and K. C. Saraswat. Strain-induced pseudo-heterostructure nanowires confining carriers at room temperature with nanoscale-tunable band profiles. *Nano Lett.*, 13(7):3118–3123, 2013. doi: 10.1021/nl401042n.

[88] S. Ishida, S. Kako, K. Oda, T. Ido, S. Iwamoto, and Y. Arakawa. Suspended germanium cross-shaped microstructures for enhancing biaxial tensile strain. *Jpn. J. Appl. Phys.*, 55(4S):04EH14, 2016. doi: 10.7567/JJAP.55.04EH14.

[89] G. Shambat, S. L. Cheng, J. Lu, Y. Nishi, and J. Vuckovic. Direct band Ge photoluminescence near 1.6 μm coupled to Ge-on-Si microdisk resonators. *Appl. Phys. Lett.*, 97(24):241102, 2010. doi: 10.1063/1.3526732.

[90] Y. Suwa and S. Saito. First-principles study of light emission from silicon and germanium due to direct tranistions. In *IEEE 8th Int. Conf. Group IV Photonics* (GFP), pages 222–224, 2011. doi: 10.1109/GROUP4.2011.6053770.

[91] M. Virgilio, C. L. Manganelli, G. Grosso, T. Schroeder, and G. Capellini. Photoluminescence, recombination rate, and gain spectra in optically excited n-type and tensile strained germanium layers. *J. Appl. Phys.*, 114(24):243102, 2013. doi: 10.1063/1.4849855.

[92] M. Virgilio, C. L. Manganelli, G. Grosso, G. Pizzi, and G. Capellini. Radiative recombination and optical gain spectra in biaxially strained n-type germanium. *Phys. Rev. B*, 87(23):235313, 2013. doi: 10.1103/PhysRevB.87.235313.

[93] K. Wada, J. Liu, S. Jongthammanurak, D. D. Cannon, D. T. Danielson, D. Ahn, S. Akiyama, M. Popovic, D. R. Lim, K. K. Lee, H. C. Luan, Y. Ishikawa, J. Michel, H. A. Haus, and L. C. Kimerling. *Si Microphotonics for Optical Interconnection.* Springer Verlag, Berlin, 2006.

[94] P. Boucaud, M. El Kurdi, A. Ghrib, M. Prost, M. de Kersauson, S. Sauvage, F. Aniel, X. Checoury, G. Beaudoin, L. Largeau, I. Sagnes, G. Ndong, M. Chaigneau, and R. Ossikovski. Recent advances in germanium emission. *Photon. Res.*, 1(3):102–109, 2013. doi: 10.1364/PRJ.1.000102.

[95] M. E. Kurdi, H. Bertin, E. Martincic, M. de Kersauson, G. Fishman, S. Sauvage, A. Bosseboeuf, and P. Boucaud. Control of direct band gap emission of bulk germanium by mechanical tensile strain. *Appl. Phys. Lett.*, 96(4):041909, 2010. doi: 10.1063/1.3297883.

[96] J. Liu. Monolithically integrated Ge-on-Si active photonics. *Photonics*, 1(3):162–197, 2014. doi: 10.3390/photonics1030162.

[97] E. Gaubas and J. Vanhellemont. Dependence of carrier lifetime in germanium on resistivity and carrier injection level. *Appl. Phys. Lett.*, 89(14):142106, 2006. doi: 10.1063/1.2358967.

[98] T. Okumura, K. Oda, J. Kasai, M. Sagawa, and Y. Suwa. Optical net gain measurement in n-type doped germanium waveguides under optical pumping for silicon monolithic laser. *Opt. Express*, 24(9):9132–9139, 2016. doi: 10.1364/OE.24.009132.

[99] M. El Kurdi, T. Kociniewski, T. P. Ngo, J. Boulmer, D. Dbarre, P. Boucaud, J. F. Damlencourt, O. Kermarrec, and D. Bensahel. Enhanced photoluminescence of heavily n-doped germanium. *Appl. Phys. Lett.*, 94(19):191107, 2009. doi: 10.1063/1.3138155.

[100] D. Nam, J. H. Kang, M. L. Brongersma, and K. C. Saraswat. Observation of improved minority carrier lifetimes in high-quality Ge-on-insulator using time-resolved photoluminescence. *Opt. lett.*, 39(21):6205–6208, 2014. ISSN 1539-4794. doi: 10.1364/OL.39.006205.

[101] S. Brotzmann and H. Bracht. Intrinsic and extrinsic diffusion of phosphorus, arsenic, and antimony in germanium. *J. Appl. Phys.*, 103(3):033508, 2008. doi: 10.1063/1.2837103.

[102] A. Chroneos and H. Bracht. Diffusion of n-type dopants in germanium. *Appl. Phys. Rev.*, 1(1), 2014. doi: 10.1063/1.4838215.

[103] S. Kako, T. Okumura, K. Oda, Y. Suwa, S. Saito, T. Ido, and Y. Arakawa. Time-resolved photoluminescence study of highly n-doped germanium grown on silicon. In *IEEE 9^{th} Int. Conf. Group IV Photonics* (GFP), pages 340–342, 2012. doi: 10.1109/GROUP4.2012.6324180.

[104] C. Claeys and E. Simoen, editors. Elsevier, Oxford, 1 edition, 2007. ISBN 978-0-08-044953-1. doi: 10.1016/B978-008044953-1/50000-4.

[105] S. C. Jain and D. J. Roulston. A simple expression for band gap narrowing (BGN) in heavily doped Si, Ge, GaAs and Ge_xSi_{1x} strained layers. *Solid-State Electron.*, 34(5):453–465, 1991. doi: 10.1016/0038-1101(91)90149-S.

[106] R. Camacho-Aguilera, H. Zhaohong, Y. Cai, L. C. Kimerling, and J. Michel. Direct band gap narrowing in highly doped Ge. *Appl. Phys. Lett.*, 102(15):152106, 2013. doi: 10.1063/1.4802199.

[107] X. Wang, H. Li, R. Camacho-Aguilera, Y. Cai, L. C. Kimerling, J. Michel, and J. Liu. Infrared absorption of n-type tensile-strained Ge-on-Si. *Opt. Lett.*, 38(5): 652–654, 2013. doi: 10.1364/OL.38.000652.

[108] N. E. Posthuma, J. Van der Heide, G. Flamand, and J. Poortmans. Emitter formation and contact realization by diffusion for germanium photovoltaic devices. *IEEE Trans. Electron Devices*, 54(5):1210–1215, 2007. doi: 10.1109/TED.2007.894610.

[109] J. T. Bessette, R. Camacho-Aguilera, Y. Cai, L. C. Kimerling, and J. Michel. Optical characterization of Ge-on-Si laser gain media. In *IEEE* 8^{th} *Int. Conf. Group IV Photonics* (GFP), pages 130–132. IEEE, 2011. doi: 10.1109/GROUP4.2011.6053739.

[110] S. Matsumoto and T. Niimi. Concentration dependence of a diffusion coefficient at phosphorus diffusion in germanium. *J. Electrochem. Soc.*, 125(8):1307–1309, 1978. doi: 10.1149/1.2131668.

[111] A. Axmann, M. Schulz, and C. R. Fritzsche. Implantation doping of germanium with Sb, As, and P. *Appl. Phys.*, 12(2):173–178, 1977. doi: 10.1007/BF00896143.

[112] J. Kim, S. W. Bedell, and D. K. Sadana. Improved germanium n+/p junction diodes formed by coimplantation of antimony and phosphorus. *Appl. Phys. Lett.*, 98(8):082112, 2011. doi: 10.1063/1.3558715.

[113] H. C. Luan, D. R. Lim, K. K. Lee, K. M. Chen, J. G. Sandland, K. Wada, and L. C. Kimerling. High-quality Ge epilayers on Si with low threading-dislocation densities. *Appl. Phys. Lett.*, 75(19):2909, 1999. doi: 10.1063/1.125187.

[114] H. Y. Yu, E. Battal, A. K. Okyay, S. Jaewoo, J. H. Park, J. W. Baek, and K. C. Saraswat. Experimental and theoretical investigation of phosphorus $in-situ$ doping of germanium epitaxial layers. *Curr. Appl. Phys.*, 13(6):1060, 2013. doi: 10.1016/j.cap.2013.02.021.

[115] J. M. Hartmann, J. P. Barnes, M. Veillerot, J. M. Fédéli, Q. A. La Guillaume, and V. Calvo. Structural, electrical and optical properties of $in-situ$ phosphorous-doped Ge layers. *J. Cryst. Growth*, 347(1):37–44, 2012. doi: 10.1016/j.jcrysgro.2012.03.023.

[116] E. Kasper, M. Oehme, T. Arguirov, J. Werner, M. Kittler, and J. Schulze. Room temperature direct band gap emission from Ge p-i-n heterojunction photodiodes. *Adv. OptoElectron.*, 2012(1):4, 2012. doi: 10.1155/2012/916275.

[117] M. Takenaka, K. Morii, M. Sugiyama, Y. Nakano, and S. Takagi. Dark current reduction of Ge photodetector by GeO_2 surface passivation and gas-phase doping. *Opt. Express*, 20(8):8718–8725, 2012. doi: 10.1364/OE.20.008718.

[118] W. M. Klesse, G. Scappucci, G. Capellini, J. M. Hartmann, and M. Y. Simmons. Atomic layer doping of strained Ge-on-insulator thin films with high electron densities. *Appl. Phys. Lett.*, 102(15):151103, 2013. doi: 10.1063/1.4801981.

[119] R. E. Camacho-Aguilera, Y. Cai, J. Bessette, L. C. Kimerling, and J. Michel. High active carrier concentration in n-type, thin film ge using delta-doping. *Opt. Mater. Express*, 2(11):1462–1469, 2012. doi: 10.1364/OME.2.001462.

[120] D. Cammilleri, F. Fossard, D. Dbarre, C. Tran Manh, C. Dubois, E. Bustarret, C. Marcenat, P. Achatz, D. Bouchier, and J. Boulmer. Highly doped Si and Ge formed by GILD (gas immersion laser doping); from GILD to superconducting silicon. *Thin Solid Films*, 517(1):75–79, 2008. doi: 10.1016/j.tsf.2008.08.073.

[121] V. Sorianello, A. De Iacovo, L. Colace, A. Fabbri, L. Tortora, and G. Assanto. Spin-on-dopant phosphorus diffusion in germanium thin films for near-infrared detectors. *Phys. Status Solidi*, 11(1):57–60, 2014. doi: 10.1002/pssc.201300114.

[122] M. Jamil, J. Mantey, E. U. Onyegam, G. D. Carpenter, E. Tutuc, and S. K. Banerjee. High-performance Ge nMOSFETs with n^+-p junctions formed by "spin-on dopant ". *IEEE Electron Device Lett.*, 32(9):1203–1205, 2011. doi: 10.1109/LED.2011.2160142.

[123] X. Xu, K. Nishida, K. Sawano, T. Maruizumi, and Y. Shiraki. Resonant photoluminescence from Ge microdisks on Ge-on-insulator. In *7th Int. Si-Ge Tech. & Dev. Meeting* (ISTDM), pages 135–136, 2014. doi: 10.1109/ISTDM.2014.6874670.

[124] J. R. Jain, D. S. Ly-Gagnon, K. C. Balram, J. S. White, M. L. Brongersma, D. A. B. Miller, and R. T. Howe. Tensile-strained germanium-on-insulator substrate fabrication for silicon-compatible optoelectronics. *Opt. Mater. Express*, 1 (6):1121–1126, 2011. doi: 10.1364/PRJ.2.0000A8.

[125] E. M. Purcell. Spontaneous emission probabilities at radio frequencies. *Phys. Rev.*, 69:681, 1946. doi: 10.1103/PhysRev.69.674.2.

[126] N. Hauke, A. Tandaechanurat, T. Zabel, T. Reichert, H. Takagi, M. Kaniber, S. Iwamoto, D. Bougeard, J. Finley, G. Abstreiter, and Y. Arakawa. A three-dimensional silicon photonic crystal nanocavity with enhanced emission from embedded germanium islands. *New J. Phys.*, 14(8):083035, 2012. doi: 10.1088/1367-2630/14/8/083035.

[127] T. P. Ngo, M. El Kurdi, X. Checoury, P. Boucaud, J. F. Damlencourt, O. Kermarrec, and D. Bensahel. Two-dimensional photonic crystals with germanium on insulator obtained by a condensation method. *Appl. Phys. Lett.*, 93(24):241112, 2008. doi: 10.1063/1.3054332.

[128] M. El Kurdi, S. David, X. Checoury, G. Fishman, P. Boucaud, O. Kermarrec, D. Bensahel, and B. Ghyselen. Two-dimensional photonic crystals with pure germanium-on-insulator. *Opt. Commun.*, 281(4):846–850, 2008. doi: 10.1016/j.optcom.2007.10.008.

[129] X. Xu, T. Chiba, T. Nakama, T. Maruizumi, and Y. Shiraki. High-quality-factor light-emitting diodes with modified photonic crystal nanocavities including Ge self-assembled quantum dots on silicon-on-insulator substrates. *Appl. Phys. Express*, 5(10):102101, 2012. doi: 10.1143/APEX.5.102101.

[130] T. Tsuboi, X. Xu, J. Xia, N. Usami, T. Maruizumi, and Y. Shiraki. Room-temperature electroluminescence from Ge quantum dots embedded in photonic crystal microcavities. *Appl. Phys. Express*, 5(5):052101, 2012. doi: 10.1143/APEX.5.052101.

[131] P. H. Lim, Y. Kobayashi, S. Takita, Y. Ishikawa, and K. Wada. Enhanced photoluminescence from germanium-based ring resonators. *Appl. Phys. Lett.*, 93(4):041103, 2008. doi: 10.1063/1.2950087.

[132] S. L. McCall, A. F. J. Levi, R. E. Slusher, S. J. Pearton, and R. A. Logan. Whispering gallery mode microdisk lasers. *Appl. Phys. Lett.*, 60(3):289–291, 1992. doi: 10.1063/1.106688.

[133] J. Xia, Y. Takeda, N. Usami, T. Maruizumi, and Y. Shiraki. Room-temperature electroluminescence from Si microdisks with Ge quantum dots. *Opt. Express*, 18(13):13945–13950, 2010. doi: 10.1364/OE.18.013945.

[134] A. Andronico, X. Caillet, I. Favero, S. Ducci, V. Berger, and G. Leo. Semiconductor microcavities for enhanced nonlinear optics interactions. *J. Eur. Opt. Soc. Rapid*, 3(8):08030, 2008. doi: 10.2971/jeos.2008.08030.

[135] J.A. Stratton. *Electromagnetic Theory*. Wiley, 2007. ISBN 9780470131534. URL https://books.google.co.uk/books?id=zFeWdS2luE4C.

[136] S. V. Gaponenko. *Introduction to nanophotonics*. Cambridge University Press, New York, 2010. ISBN 9780521763752.

[137] B. Jones, M. Oxborrow, V. Astratov, M. Hopkinson, A. Tahraoui, M. Skolnick, and A. Fox. Splitting and lasing of whispering gallery modes in quantum dot micropillars. *Opt. Express*, 18(21):22578–22592, 2010.

[138] M. Gorodetsky, A. Savchenkov, and V. Ilchenko. Ultimate Q of optical microsphere resonators. *Opt. Lett.*, 21(7):453–455, 1996. doi: 10.1364/OL.21.000453.

[139] S. W. Chang and S. L. Chuang. Theory of optical gain of Ge-$Si_xGe_ySn_{1xy}$ quantum-well lasers. *IEEE J. Quant. Electron.*, 43(3):249–256, 2007. doi: 10.1109/JQE.2006.890401.

[140] G. E. Chang and H. Cheng. Optical gain of germanium infrared lasers on different crystal orientations. *J. Phys. D: Appl. Phys.*, 46(6):065103, 2013. doi: 10.1088/0022-3727/46/6/065103.

[141] G. Pizzi, M. Virgilio, and G. Grosso. Tight-binding calculation of optical gain in tensile strained 001 -Ge/SiGe quantum wells. *Nanotechnology*, 21(5):055202, 2010. doi: 10.1088/0957-4484/21/5/055202.

[142] M. de Kersauson, M. El Kurdi, S. David, X. Checoury, G. Fishman, S. Sauvage, R. Jakomin, G. Beaudoin, I. Sagnes, and P. Boucaud. Optical gain in single tensile-strained germanium photonic wire. *Opt. Express*, 19(19):17925–17934, 2011. doi: 10.1364/OE.19.017925.

[143] X. Xu, X. Wang, K. Nishida, K. Takabayashi, K. Sawano, Y. Shiraki, H. Li, J. Liu, and T. Maruizumi. Ultralarge transient optical gain from tensile-strained, n-doped germanium on silicon by spin-on dopant diffusion. *Appl. Phys. Express*, 8(9):092101, 2015. doi: 10.7567/APEX.8.092101.

[144] B. Dutt, D. S. Sukhdeo, D. Nam, B. M. Vulovic, Z. Yuan, and K. C. Saraswat. Roadmap to an efficient germanium-on-silicon laser: strain vs. n-type doping. *IEEE Photon. J.*, 4(5):1–9, 2012. doi: 10.1109/JPHOT.2012.2221692.

[145] Zh. I. Alferov. The history and future of semiconductor heterostructures from the point of view of a russian scientist. *Phys. Scripta*, 1996(T68):32, 1996. doi: 10.1088/0031-8949/1996/T68/005.

[146] N. N. Ledentsov, M. Grundmann, F. Heinrichsdorff, D. Bimberg, V. M. Ustinov, A. E. Zhukov, M. V. Maximov, Zh. I. Alferov, and J. A. Lott. Quantum-dot heterostructure lasers. *IEEE J. Sel. Top. Quantum Electron.*, 6(3):439–451, 2000. doi: 10.1109/2944.865099.

[147] H. Kroemer. A proposed class of hetero-junction injection lasers. *Proc. IEEE*, 51 (12):1782–1783, 1963. doi: 10.1109/PROC.1963.2706.

[148] R. Hall, G. Fenner, J. Kingsley, T. Soltys, and R. Carlson. Coherent light emission from GaAs junctions. *Phys. Rev. Lett.*, 9(9):366–368, 1962. doi: 10.1103/PhysRevLett.9.366.

[149] M. Asada, Y. Miyamoto, and Y. Suematsu. Gain and the threshold of three-dimensional quantum-box lasers. *IEEE J. Quant. Electron.*, 22(9):1915–1921, 1986. doi: 10.1109/JQE.1986.1073149.

[150] J. Wilson and J. Hawkes. *Optoelectronics - an introduction*. Prentice Hall, Englewood Cliffs, NJ, 1989.

[151] K. Zinoviev, L. G. Carrascosa, J. S. del Río, B. Sepúlveda, C. Domínguez, and L. M. Lechuga. Silicon photonic biosensors for lab-on-a-chip applications. *Adv. Opt. Technol.*, 2008:6, 2008. doi: 10.1155/2008/383927.

[152] S. Franssila. *Introduction to microfabrication*. John Wiley & Sons, 2010. ISBN 1119991897.

[153] P. W. Atkins and J. de Paula. *Physical Chemistry*, chapter 21. W. H. Freeman and Company, New York, 8^{th} edition, 2006. ISBN 0716787598.

[154] H. Bracht, S. Schneider, and R. Kube. Diffusion and doping issues in germanium. *Microelectron. Eng.*, 88(4):452–457, 2011. doi: 10.1016/j.mee.2010.10.013.

[155] C. O. Chui, K. Gopalakrishnan, P. B. Griffin, J. D. Plummer, and K. C. Saraswat. Activation and diffusion studies of ion-implanted p and n dopants in germanium. *Appl. phys. lett.*, 83(16):3275–3277, 2003. doi: 10.1063/1.1618382.

[156] Filmtronics webpage, . http:/www.filmtronics.com [Accessed: 2014 - 2016].

[157] Emulsitone webpage, . http:/www.Emulsitone.com [Accessed: 2014 - 2016].

[158] D. Mathiot, A. Lachiq, A. Slaoui, S. Noel, J. C. Muller, and C. Dubois. Phosphorus diffusion from a spin-on doped glass (SOD) source during rapid thermal annealing. *Mater. Sci. Semicond. Process.*, 1(3-4):231–236, 1998. doi: 10.1016/s1369-8001(98)00045-6.

[159] C. Heinz. Diffusion from zinc-doped spin-on sources into n-gallium antimonide. *Solid-State Electron.*, 36(12):1685–1688, 1993. doi: 10.1016/0038-1101(93)90214-B.

[160] X. Xu, K. Nishida, K. Sawano, T. Maruizumi, and Y. Shiraki. Resonant photoluminescence from microdisk based on n-doped, tensile-strained Ge on Si. pages 1034–1035, 2013. doi: -.

[161] L. B. Valdes. Resistivity measurements on germanium for transistors. *Proc. IRE*, 42(2):420–427, 1954. doi: 10.1109/JRPROC.1954.274680.

[162] D. B. Cuttriss. Relation between surface concentration and average conductivity in diffused layers in germanium. *Bell Syst. Tech. J.*, 40(2):509–521, 1961. doi: 10.1002/j.1538-7305.1961.tb01627.x.

[163] R. B. Fair. *Chapter: Concentration profiles of diffused dopants in silicon,* in F. F. Y. Wang, Elsevier Ed., *Impurity doping processes in silicon*, volume 2, chapter 10. Amsterdam, The Netherlands: North Holland, 1981.

[164] C. Y. Peng, C. F. Huang, Y. C. Fu, Y. H. Yang, C. Y. Lai, S. T. Chang, and C. W. Liu. Comprehensive study of the raman shifts of strained silicon and germanium. *J. Appl. Phys.*, 105(8):083537, 2009. doi: 10.1063/1.3110184.

[165] X. Sun, J. Liu, L. C. Kimerling, and J. Michel. Direct gap photoluminescence of n-type tensile-strained Ge-on-Si. *Appl. Phys. Lett.*, 95(1):011911, 2009. doi: 10.1063/1.3170870.

[166] M. A. Parker. *Physics of Optoelectronics*. Taylor & Francis Group CRC Press, New York, 2005.

[167] A. D. Andreev and E. P. OReilly. Theoretical study of Auger recombination in a GaInNAs 1.3 μm quantum well laser structure. *Appl. Phys. Lett.*, 84(11):1826–1828, 2004. doi: 10.1063/1.1664033.

[168] J. Piprek, F. Rmer, and B. Witzigmann. On the uncertainty of the Auger recombination coefficient extracted from InGaN/GaN light-emitting diode efficiency droop measurements. *Appl. Phys. Lett.*, 106(10):101101, 2015. doi: 10.1063/1.4914833.

[169] I. P. Marko, A. D. Andreev, A. R. Adams, R. Krebs, J. P. Reithmaier, and A. Forchel. The importance of Auger recombination in InAs 1.3 μm quantum dot .asers. *Electron. Lett.*, 58(59), 2003. doi: 10.1049/el:20030014.

[170] E. Gaubas and J. Vanhellemont. Comparative study of carrier lifetime dependence on dopant concentration in silicon and germanium. *J. Electrochem. Soc.*, 154(3): H231–H238, 2007. doi: 10.1149/1.2429031.

[171] W. C. Dunlap. Diffusion of impurities in germanium. *Phys. Rev.*, 94(6):1531–1540, 1954. doi: 10.1103/PhysRev.94.1531.

[172] N. R. Zangenberg, J. Fage-Pedersen, J. Lundsgaard Hansen, and A. Nylandsted Larsen. Boron and phosphorus diffusion in strained and relaxed Si and SiGe. *J. Appl. Phys.*, 94(6):3883–3890, 2003. doi: 10.1063/1.1602564.

[173] A. Pakfar, A. Poncet, T. Schwartzmann, and H. Jaouen. *A unified model of dopant diffusion in SiGe*, pages 62–65. Springer, 2001.

[174] W. R. Thurber. *The relationship between resistivity and dopant density for phosphorus-and boron-doped silicon*, volume 400. US Department of Commerce, National Bureau of Standards, 1981. URL https://books.google.co.uk/books?id=gXCDKm4H138C.

[175] Solecon Laboratories. Silicon/germanium resistivity and carrier concentration calculators, 2016. http://www.solecon.com/sra/rho2ccal.htm [Accessed: 2014 - 2016].

[176] D. Nam, D. S. Sukhdeo, S. Gupta, J. H. Kang, M. L. Brongersma, and K. C. Saraswat. Study of carrier statistics in uniaxially strained Ge for a low-threshold Ge laser. *IEEE J. Sel. Top. Quantum Electron.*, 20(4):1–7, 2014. doi: 10.1109/jstqe.2013.2293764.

[177] J. Laconte, D. Flandre, and J. P. Raskin. *Micromachined thin-film sensors for SOI-CMOS co-integration*. Springer US, 2006. ISBN 978-0-387-28842-0. doi: 10.1007/0-387-28843-0. URL http://www.springer.com/gb/book/9780387288420.

[178] J. Greil, A. Lugstein, C. Zeiner, G. Strasser, and E. Bertagnolli. Tuning the electro-optical properties of germanium nanowires by tensile strain. *Nano Lett.*, 12(12):6230–6234, 2012. doi: 10.1021/nl303288g.

[179] BYU Cleanroom. Optical absorption coefficient calculator, based on the handbook of optical constants of solids (e. d. palik, 1985). http://www.cleanroom.byu.edu/OpticalCalc.phtml [Accessed: 2014 - 2016].

[180] E. D. Palik. *Handbook of optical constants of solids*, volume 3. Academic Press, 1998. ISBN 0125444230.

[181] S. L. Cheng, G. Shambat, J. Lu, H. Y. Yu, K. Saraswat, T. I. Kamins, J. Vuckovic, and Y. Nishi. Cavity-enhanced direct band electroluminescence near 1550 nm from germanium microdisk resonator diode on silicon. *Appl. Phys. Lett.*, 98(21):211101, 2011. doi: 10.1063/1.3592837.

[182] X. J. Xu, H. Hashimoto, K. Sawano, H. Nohira, and T. Maruizumi. Enhanced light emission from germanium microdisks on silicon by surface passivation through thermal oxidation. *Appl. Phys. Express*, 9(5):4, 2016. doi: 10.7567/apex.9.052101.

[183] M. Prost, M. El Kurdi, A. Ghrib, S. Sauvage, X. Checoury, N. Zerounian, F. Aniel, G. Beaudoin, I. Sagnes, F. Boeuf, and P. Boucaud. Tensile-strained germanium microdisk electroluminescence. *Opt. Express*, 23(5):6722–6730, 2015. doi: 10.1364/OE.23.006722.

[184] S. Sun, Y. Sun, Z. Liu, D. I. Lee, S. Peterson, and P. Pianetta. Surface termination and roughness of Ge(100) cleaned by HF and HCl solutions. *Appl. Phys. Lett.*, 88 (2):21903, 2006. doi: 10.1063/1.2162699.

[185] V. Passi, A. Lecestre, C. Krzeminski, G. Larrieu, E. Dubois, and J. P. Raskin. A single layer hydrogen silsesquioxane (HSQ) based lift-off process for germanium and platinum. *Microelectron. Eng.*, 87(10):1872–1878, 2010. doi: 10.1016/j.mee.2009.11.022.

[186] M. A. Hopcroft, W. D. Nix, and T. W. Kenny. What is the young's modulus of silicon? *J. Microelectromech. Syst.*, 19(2):229–238, 2010. doi: 10.1109/JMEMS.2009.2039697.

[187] H. A. Tahini, A. Chroneos, R. W. Grimes, and U. Schwingenschlgl. Co-doping with antimony to control phosphorous diffusion in germanium. *Journal of Applied Physics*, 113(7):073704, 2013. doi: 10.1063/1.4792480.

[188] J. Scheuer, W. Green, G. DeRose, and A. Yariv. Lasing from a circular bragg nanocavity with an ultrasmall modal volume. *Appl. Phys. Lett.*, 86(25):251101, 2005. doi: 10.1063/1.1947375.

[189] J. D. Joannopoulos, S. G. Johnson, J. N. Winn, and R. D. Meade. *Photonic crystals: molding the flow of light*. Princeton university press, 2011. ISBN 1400828244.

[190] M. Fujita and T. Baba. Microgear laser. *Appl. phys. lett.*, 80(12):2051–2053, 2002. doi: 10.1063/1.1462867.

[191] K. Nozaki, A. Nakagawa, D. Sano, and T. Baba. Ultralow threshold and single-mode lasing in microgear lasers and its fusion with quasi-periodic photonic crystals. *IEEE J. Sel. Top. Quantum Electron.*, 9(5):1355–1360, 2003. doi: 10.1109/JSTQE.2003.819465.

[192] Y. Liu, M. D. Deal, and J. D. Plummer. High-quality single-crystal Ge on insulator by liquid-phase epitaxy on Si substrates. *Appl. Phys. Lett.*, 84:2563, 2004. doi: 10.1063/1.1691175.